SHOCK COMPACTION AND IMPACT RESPONSE OF THERMITE POWDER MIXTURES

A Thesis
Presented to
The Academic Faculty

by

David Anthony Fredenburg

In Partial Fulfillment
of the Requirements for the Degree
Doctor of Philosophy in the
School of Materials Science and Engineering

Georgia Institute of Technology
December 2010

SHOCK COMPACTION AND IMPACT RESPONSE OF THERMITE POWDER MIXTURES

Approved by:

Professor Naresh N. Thadhani, Advisor
School of Materials Science and Engineering
Georgia Institute of Technology

Professor Joe Cochran
School of Materials Science and Engineering
Georgia Institute of Technology

Professor Thomas H. Sanders
School of Materials Science and Engineering
Georgia Institute of Technology

Professor Min Zhou
School of Mechanical Engineering
Georgia Institute of Technology

Dr. Tracy J. Vogler
Sandia National Laboratories

Date Approved: August, 26 2010

To Pops,

I can see you smiling now.

ACKNOWLEDGEMENTS

The author would like to acknowledge first and foremost the funding sources for this research, which include the Defense Threat Reduction Agency through grant HDTRA1-07-1-0018, and the Laboratory Directed Research and Development Program of Sandia National Laboratories under Contract DE-AC04-94AL85000.

Thanks is also extended to all the members of the High Strain Rate Lab, present and past. Dr. Thadhani, your counsel and advice has been extremely valuable in shaping the foundations on which I have built my knowledge of shock physics. Specifically, Dan Eakins, Lou Ferranti, and Morgana Trexler for an efficient and extremely helpful introduction the HSR facility. Also, Kit Kneel, Chris Wherenberg, Brad White, Adam Jakus, and Paul Specht for continued excellence in all things shock. And to the newer members, Sean Kelly, Brady Aydelotte, Mike Tucker, and Jonathan Tooker, may the spirit of the HSR lab live and thrive in you. A special thanks also is extended to the numerous undergraduate students who have worked with the HSR lab over the years. In addition, thanks goes out to all those in the Dynamic Material Properties group at Sandia for their advice, guidance, and technical assistance.

Lastly, the author would like to thank the continued support of family and friends, whose encouragement and continued belief has helped tremendously along the way. And to Stephanie, thanks for all the help and understanding, especially through this final stretch; your faith and devotion has been, and continues to be, of invaluable measure.

TABLE OF CONTENTS

DEDICATION iii

ACKNOWLEDGEMENTS iv

LIST OF TABLES ix

LIST OF FIGURES x

LIST OF SYMBOLS OR ABBREVIATIONS xiv

SUMMARY xiv

I INTRODUCTION 1

II SHOCK FUNDAMENTALS FOR SOLID MATERIALS 10

2.1 Shock Response of Solid Materials 10

2.2 Mie-Gr*ü*neisen Equation of State 15

2.3 Hugoniots and Isotherms 17

2.3.1 The Zero K Isotherm 21

2.4 Hugoniots and Isentropes 23

2.5 Mixture Hugoniots 25

2.5.1 Basic Mass Averaged Equation of State 26

2.5.2 Zero Kelvin (Isothermal) Mass Averaged Equation of State . . . 26

2.5.3 Material Velocity Mass Averaged Equation of State 27

2.5.4 Energy Partitioned Equation of State 28

2.5.5 Comparison of Mixture Models 31

III SHOCK FUNDAMENTALS FOR PARTICULATE MATERIALS 34

3.1 Particle Packing 34

3.2 Quasi-Static Compaction of Powders 38

3.3 Dynamic Compaction of Powders 48
3.3.1 Energy Considerations 48
3.3.2 Configurational Considerations 52
3.4 Equations of State for Particulate Materials 56
3.4.1 Isochoric Approach 57
3.4.2 Isobaric Approach 62
3.4.3 Comparison of Porous Equations of State 68
IV COMPACTION MODELS AND THEIR COMPARISON 72
4.1 The P-σ_Y Model 73
4.2 The P-P_{Act} Model 76
4.3 The P-α Model 80
4.4 The P-λ Model 85
4.5 Comparison of Compaction Models 88
V THERMITES AS ENERGETIC COMPONENTS 97
5.1 Impact Initiated Reactions 98
VI POWDER MIXTURES AND EXPERIMENTAL METHODS 103
6.1 Starting Powders 104
6.2 Characterization of Bismuth Oxide 106
6.3 Powder Properties 115
6.4 The Ta + Fe_2O_3 and Ta + Bi_2O_3 Powder Mixtures 117
6.4.1 Energetic Considerations 119
6.5 Mixture Preparation 121
6.6 Quasi-Static Compression Technique 123
6.7 Parallel Plate Impact Experiments 126
6.7.1 Polyvinlyidene Fluoride Stress Guages 126

6.7.2 Target assembly 127
6.7.2.1 Ta + Fe_2O_3 Compaction Fixture 127
6.7.2.2 Ta + Bi_2O_3 Compaction Fixture 129
6.7.3 Performing the Measurements 131
6.8 Impedance Matching - Interpreting Measured Quantities 134
6.9 Error Analysis 139
6.9.1 Systematic Uncertainties in Impedance Matching for Three Materials 139
6.9.2 Remaining Uncertainties 144
VII COMPRESSION OF THERMITE POWDER MIXTURES 147
7.1 Results of Quasi-Static Compaction of Reactant Powders 147
7.2 Dynamic Compaction Results 162
7.2.1 Equilibrium Equation of State Response 163
7.2.1.1 Solid Mixture EOS 164
7.2.1.2 Porous Mixture EOS 168
7.2.2 Initial Powder Configuration 169
7.2.3 Experimental Data 173
7.3 Hugoniot Response of Ta + Fe_2O_3 181
7.3.1 Equations of State 181
7.3.2 Compaction Model Fits 188
7.3.3 Concluding Remarks 192
7.4 Hugoniot Response of Ta + Bi_2O_3 194
7.4.1 Equations of State 194
7.4.2 Compaction Model Fits 200
7.4.3 Concluding Remarks 205
7.5 Summation of Results and Trends 205

VIII ANALYSIS AND DISCUSSION OF RESULTS 207
8.1 Analysis Framework 208
8.1.1 Configurational Considerations 209
8.1.2 Densification Strength Properties 213
8.1.3 Application to Dynamic Compaction Data 220
8.2 Model Extension 230
8.3 Significance of the Crush Strength 244
IX SUMMARY OF RESULTS, CONCLUSIONS, AND FUTURE WORK 248
9.1 Summary of Results 248
9.2 Conclusions 250
9.3 Future Work 253
APPENDIX A MATLAB SCRIPTS FOR DATA CALCULATIONS 256
REFERENCES 293

LIST OF TABLES

2.1 Component material properties of Elkonite 10W3 31

4.1 Fits of Ta and WC to P-σ_Y and P-P_{Act} models 91

6.1 Elastic properties and soundspeed data for Bi_2O_3 111

6.2 Parallel plate impact data for pure Bi_2O_3 113

6.3 Material properties of Ta, Fe_2O_3, and Bi_2O_3 116

6.4 Shock parameters for Ta, Fe_2O_3, and Bi_2O_3 117

6.5 Heterogeneity of mixtures 118

6.6 Cu and W-6Ni-4Cu shock properties 136

6.7 Systematic uncertainty parameters for Cu and W-6Ni-4Cu 142

7.1 Quasi-static model fitting parameters for constituents 152

7.2 Quasi-static fitting parameters for Ta + Fe_2O_3 and Ta + Bi_2O_3 156

7.3 Average and initial properties of mixtures 164

7.4 Solid isothermal and energy partitioning mixture model parameters 165

7.5 Equation of state for solid mixtures 166

7.6 Hugoniot data for Ta + Fe_2O_3 182

7.7 Hugoniot data for Ta + Bi_2O_3 195

8.1 Non-rearrangement quasi-static model fitting parameters of components and mixtures 217

8.2 Non-rearrangement and 53 % TMD densification moduli 240

LIST OF FIGURES

1.1 Effect of crush strength on reaction initiation stress 7

2.1 Plate impact schematic and resultant shock wave 11

2.2 Solid Cu material behavior in various phase space 14

2.3 σ-V relationship between Hugoniot and isotherm 18

2.4 σ-V relationship between Hugoniot and isentrope 24

2.5 Mixture comparison without porosity 32

3.1 Packing fraction as a function of weight fraction OF larger particles 36

3.2 Particle settling in ternary system 37

3.3 Three stages of compaction 39

3.4 Characteristic quasi-static compact 41

3.5 Evolution of plastic strain in quasi-static compaction 42

3.6 Balance of forces in powder compaction die 43

3.7 Density gradients for single and double action pressing 45

3.8 Particle size effect on density and strength (quasi-static) 46

3.9 Energy deposition in quasi-statically and dynamically loaded powder systems 49

3.10 Energy dissipation mechanisms in powders 50

3.11 Morphology affect on turbulent flow 54

3.12 Morphology affect on compaction wave 55

3.13 Solid and porous σ-V Hugoniot 58

3.14 Hugoniots for distended Inconel 718 with γ/V = constant 60

3.15 Comparison of anomalous and non-anomalous particulate Hugoniots 62

3.16 Isochoric and Isobaric comparison in σ-E plane 63

3.17 Isochoric and Isobaric comparison for highly distended copper 65

3.18 Schematic of isochoric and isobaric paths to distended Hugoniot 67

3.19 Porous EOS predictions for Elkonite 10W3 69
4.1 Unconstrained deformation in P-σ_Y model 73
4.2 Linear stress-density relationship in granular ceramics 78
4.3 Data fit of granular ceramics to P-P_{Act} model 81
4.4 General P-α compaction response 83
4.5 General P-λ compaction response 88
4.6 Ta and WC fits to P-σ_Y and P-P_{Act} models 90
4.7 P-α and P-λ fits to Ni-Al powder mixture 94
4.8 P-α and P-λ fits to Ti-Si powder mixture 95
5.1 Effect of particle size on reactivity of Nb-Si 100
5.2 Effect of pulse duration on reactivity of Ti-Si 102
6.1 Micrographs of starting powders 105
6.2 Testing apparatus for hot pressing 107
6.3 X-Ray of Bi_2O_3 powder and hot-pressed pellet 109
6.4 Typical soundspeed measurement waveform 110
6.5 Schematic of Bi_2O_3 experimental setup 112
6.6 U_S-u_P fits of pure Bi_2O_3 114
6.7 SEM images of Ta + Fe_2O_3 and Ta + Bi_2O_3 mixtures 122
6.8 Quasi-static punch and die 125
6.9 PVDF gauge 127
6.10 Unfilled PVDF fixture and target assembly 128
6.11 Dual ring target assembly used in Ta + Bi_2O_3 compaction experiments . . . 130
6.12 Schematic of 80 mm gas-gun 132
6.13 Schematic of loaded PVDF fixture 134
6.14 Impedance match technique 138
6.15 Systematic uncertainty in flyer and driver 142

6.16 Systematic uncertainty in release isentrope 143
7.1 P-σ_Y compaction of Ta, Fe_2O_3, and Bi_2O_3 149
7.2 P-P_{Act} compaction of Ta, Fe_2O_3, and Bi_2O_3 150
7.3 Modified Kawikata fit to Ta, Fe_2O_3, and Bi_2O_3 151
7.4 Quasi-static compaction of Ta + Fe_2O_3 154
7.5 Quasi-static compaction of Ta + Bi_2O_3 155
7.6 Solid mixture predicted Hugoniots 167
7.7 Ta + Fe_2O_3 initial powder configuration 171
7.8 Ta + Bi_2O_3 initial powder configuration 172
7.9 Voltage signal from velocity pin 175
7.10 Input and propagated PVDF traces 177
7.11 Schematic of gauge locations for adjusted TOF 180
7.12 Ta + Fe_2O_3 σ-V plotted results 183
7.13 Ta + Fe_2O_3 U_S-u_P plotted results 185
7.14 Ta + Fe_2O_3 σ-V data and model results 186
7.15 P-α fits of Ta + Fe_2O_3 190
7.16 P-λ fit of Ta + Fe_2O_3 193
7.17 Ta + Bi_2O_3 σ-V plotted results 196
7.18 Ta + Bi_2O_3 U_S-u_P plotted results 197
7.19 Ta + Bi_2O_3 σ-V plotted results 198
7.20 P-α fits of Ta + Bi_2O_3 202
7.21 P-λ fit of Ta + Bi_2O_3 204
8.1 Powder mixtures in loose and pre-compacted states 211
8.2 Non-rearrangement modified P-σ_Y compaction of Ta, Fe_2O_3, and Bi_2O_3 . . 218
8.3 Non-rearrangement modified P-σ_Y compaction of Ta + Fe_2O_3 and Ta + Bi_2O_3 219
8.4 Wu-Jing model fit with densification moduli of the Ta + Fe_2O_3 mixture . . 222

8.5 Wu-Jing model fits with densification moduli of the powders, Ta + Fe_2O_3 . 224
8.6 Wu-Jing model fits with densification moduli of the powders, Ta + Bi_2O_3 . 226
8.7 Effect of Ta rate dependence on Wu-Jing prediction, Ta + Bi_2O_3 228
8.8 Volumetric densification dependency of Ta + Fe_2O_3 232
8.9 Volumetric densification dependency of Ta + Bi_2O_3 233
8.10 Dependency of crush strength on reaction threshold 234
8.11 Al 6061 initial configuration and modified P-σ_Y fit 236
8.12 Effect of components on predicted crush strength 237
8.13 Crush response of equivolumetric Al + Fe_2O_3 241

SUMMARY

This dissertation focuses on developing a predictive method for determining the dynamic densification behavior of thermite powder mixtures consisting of equivolumetric mixtures of Ta + Fe_2O_3 and Ta + Bi_2O_3. Of primary importance to these highly reactive powder mixtures is the ability to characterize the stress at which full compaction occurs, the crush strength, which can significantly influence the stress required to initiate reaction during dynamic or impact loading. Examined specifically are the quasi-static and dynamic compaction responses of these mixtures. Experimentally obtained compaction responses in the quasi-static regime are analyzed using available compaction models, and an analysis technique is developed that allows for a correct measurement of the apparent yield strength of the powder mixtures. The correctly determined apparent yield strength is combined with an equation of state to yield a prediction of the shock densification response, including the dynamic crush strength of the thermite powder mixtures. The validated approach is also extended to the Al + Fe_2O_3 thermite system. It is found that accurate predictions of the crush strength can be obtained through determination of the apparent yield strength of the powder mixture when incorporated into the equation of state. It is observed that the predictive ability in the incomplete compaction region is configurationally dependent for highly heterogeneous thermite powder systems, which is in turn influenced by particle morphology and differences in intrinsic properties of constituents (density, strength, etc.).

CHAPTER I

INTRODUCTION

The shock compression of porous and powder materials has been an on-going field of research for many years. Early work in the field was concerned largely with experimentally determining the equilibrium equation of state response of porous solids and powders at extremely high pressures and temperatures where strengths of the materials could be neglected [1–3]. From these types of experiments, thermodynamic states that were not obtainable in solid materials could be reached in the corresponding distended material; thus offering validation of the equations of state [4] which extrapolated data from one thermodynamic state to another, e.g. from the Hugoniot to the isotherm (see Sect. 2.3). Another separate, but equally important, area of early research was concerned with the response of these similar materials to much lower amplitude stresses, where strengths of the distended bodies could not be neglected. Here, much of the focus was directed toward developing model formulations that could describe the densification response of distended materials in the incomplete compaction region. Significant contributions in this area were made by Herrmann [5], Butcher and Karnes [6], and others [7, 8] in early development of the P-α model.

As time progressed, so too has our understanding of the complex phenomena involved in the densification processes that occur during the passage of shock waves in distended

materials. Extending the work of Herrmann [5], the P-α model has been modified to include appropriate stress averaging [9], rate effects [10], viscosity [11], and deformable/non-deformable material responses [11]. Other models seeking to describe similar phenomena have been developed over the years, such as those by Grady et al. [12], Petrie and Page [13], and Simons and Legner [14], and have met with varying degrees of success. Inherent in each of these models is the ability to incorporate certain aspects of the compaction process that result in an accurate description of densification for the particular system being investigated.

For example, the Mie-Gr*ü*neisen equation of state extrapolation [15], which neglects strength effects and can predict an anomalous Hugoniot response for high initial porosity materials of decreasing density with increasing stress for highly porous materials (not observed for lower initial porosity materials), presents a unique case for one seeking to model the compaction process at both low and high stresses. Experimental work on highly distended copper [14] and iron [16] powders has shown that at low stresses density increases proportionally with stress, while at higher stresses density either remains approximately constant or decreases. In an attempt to capture these trends in model formulation, Petrie and Page [13] combined quasi-static analysis techniques valid at low stresses with an equilibrium equation of state formulation valid at high stresses to form a unified theory which does not result in the anomalous Hugoniot response. While overcoming the anomalous response predicted by the other models, the formulation of Petrie and Page [13] is forced to become deficient in other areas. Specifically, it has been shown that complete densification is not predicted by this model in highly porous materials [13], even at very high stresses.

From this example, one can see that by incorporating the necessary means to describe the compaction behavior at low stresses, model predictions at higher stresses can suffer.

These types of scenarios are often encountered when modeling the densification response of porous and powdered bodies over a wide range of initial and impact conditions. What works well at low stresses, may not work well at higher stresses. Similarly, what works well for one material system, may not be well suited to others; there has yet to be formulated a 'one size fits all' model. As such, the experimentalist seeking to employ a compaction model to either describe or predict the dynamic (shock) densification response of a distended body must consider carefully the most important trait(s) of compaction that need to be represented.

Taking into account the many different formulations of dynamic compaction models available, most of these models can be divided into two main categories, predictive and descriptive. Much of the available literature in this area has been focused on the descriptive type. Models of this type are the popular P-α model, developed by Herrmann [5] and the P-λ model developed by Grady et al. [12]. These models combine properties of the material whose densification behavior is being described with experimentally determined compaction data to obtain a best fit of the model to the data. Though varying in form and function, a common trait shared between these types of models is the inclusion of one or more empirical fitting parameters. Often, these parameters have little or no correlation with measurable physical properties, and serve only to allow for better fits of model predictions to experimental data. Because the flexibility of a fitting parameter(s) often allows these models to describe the compaction process in a particular distended system quite well, descriptive models have found widespread use in various computational shock physics codes [17, 18]. With knowledge of only a few key material and model parameters, these models have been used successfully to describe the behavior of distended bodies and other bodies of interaction under various impact conditions and geometries.

What has been explored and employed successfully to a lesser extent are models of the predictive type. These models seek to predict some aspect of the dynamic compaction response, be it the incremental compaction response as density approaches theoretical, the stress at which full compaction occurs (i.e., the crush strength [19]), or both. Of primary importance to this subset of compaction models is the availability of measured (deformation or yield) properties of the bulk and/or porous material. The model of Petrie and Page [13] discussed earlier is one such model in that it uses quasi-static compaction data to predict the dynamic crush-up response and the high stress equation of state response. Another model which has been utilized with moderate success to predict the crush strength of distended materials is P-σ_Y model of Fischmeister and Artz [20]. The P-σ_Y model also relies on densification behavior in the quasi-static regime; however in keeping with its basis in rate independent compaction, straightforward application of this model in the dynamic regime has been found to under predict experimentally determined compaction responses and crush strengths.

Furthermore, many of the compaction models developed to date have been focused primarily on describing and/or predicting the dynamic (shock) loading response of systems composed of a single component plus voids. With the addition of a second component, such as in a mixture, the mechanisms by which deformation, yielding, and the removal of voids occurs becomes more complicated. Consider the consolidation of a mixture of two materials with similar yield strengths, where the yield properties of one material are rate sensitive. Upon application of a dynamic load of moderate strength, the threshold for material deformation may differ between the two materials, resulting in one stiff and one compliant component. Depending on the relative volume percentage of each material present, the densification response of the mixture can be expected to vary significantly.

However, if the applied load is such that it is well above the yield strengths of either material, rate dependent effects diminish and the mixture responds in a more homogeneous fashion.

One can see that many different aspects affect what is collectively called the 'compaction response' of distended materials and mixtures. In addition to what has been mentioned previously, other factors include: particle size, particle morphology, surface roughness, the location of voids, the dominant deformation mechanism (plastic deformation vs. fracture), etc. Note that the influence of these factors decreases with increased levels of stress. For practical application, a model must limit the number of variables it employs if it is to be successfully applied. As such, models are often restricted to describing/predicting well only certain aspects of the compaction process, and one must determine what the most important trend(s) that a specific model must be able to capture.

In this work the author seeks to develop a methodology that will allow an experimentalist to determine specific information about the dynamic (shock) compaction response of highly heterogeneous thermite powder mixtures. This methodology is developed as predictive in nature, with the expectation that through a systematic investigation of the initial powder configuration and quasi-static densification response, an accurate estimate of the crush strength can be determined for mixtures of this type. Examined in detail are the quasi-static and dynamic responses of Ta + Fe_2O_3 and Ta + Bi_2O_3 powder mixtures.

Mixtures of this type, which are composed of metal(1) + metal(2) oxide, are collectively known as thermite mixtures. These mixtures have the potential to undergo reaction and release a large amount of exothermic heat. Historically, these types of mixtures have been used in large scale metal welding and fabrication operations [21]. More recently, their potential to be used as components in kinetic energy penetrators (shell casings) has been

realized, which has led to renewed interest in the mechanisms by which these mixtures both compact and react. As such, there have been many developments in the area of reaction models [22, 23] which seek to describe the conditions necessary to initiate reactions in thermite mixtures. What has been explored to a lesser extent is the compaction behavior of these mixtures and what effect the compaction response has on the reactivity of a system. Is there some correlation between the stress at which the mixture consolidates to full density (crush strength) and its reaction initiation threshold?

To determine if a correlation of this sort exists, consider the hypothetical scenario shown in Fig. 1.1, which illustrates three separate reactive mixtures with varying levels of crush strength. Also, suppose that each of these mixtures consists of the same reactive materials (e.g. Al + Fe_2O_3) at the same initial density ($V/V_0 = 2$), and the variation in crush strength results from differences in the initial configuration (particle size and morphology). In this case the theoretical energy product resulting from the thermite reaction is the same for all mixtures. For mixtures where compaction precedes reaction, the greatest amount of energy (work) is consumed during compaction of the highest crush strength mixture, Fig. 1.1(c). Correspondingly, the least amount of energy (work) is consumed to fully densify the mixture with the lowest crush strength, Fig. 1.1(a).

If a stress σ_i is applied to all of the mixtures, as shown in Fig. 1.1, the Hugoniot responses of the mixtures varies. For the mixture with the lowest crush strength $\sigma_C = 2$ GPa (Fig. 1.1(a)), application of stress σ_i results in a reaction between the components as shown by the deviation in Hugoniot response (shown by the black boxes) from the inert curve. For the mixtures with higher crush strengths $\sigma_C = 4$ and 6 GPa, reaction is not observed to occur at stress σ_i. In these hypothetical mixtures, the variation in reaction initiation stress results from the largely different amount of energy (work) consumed during consolidation

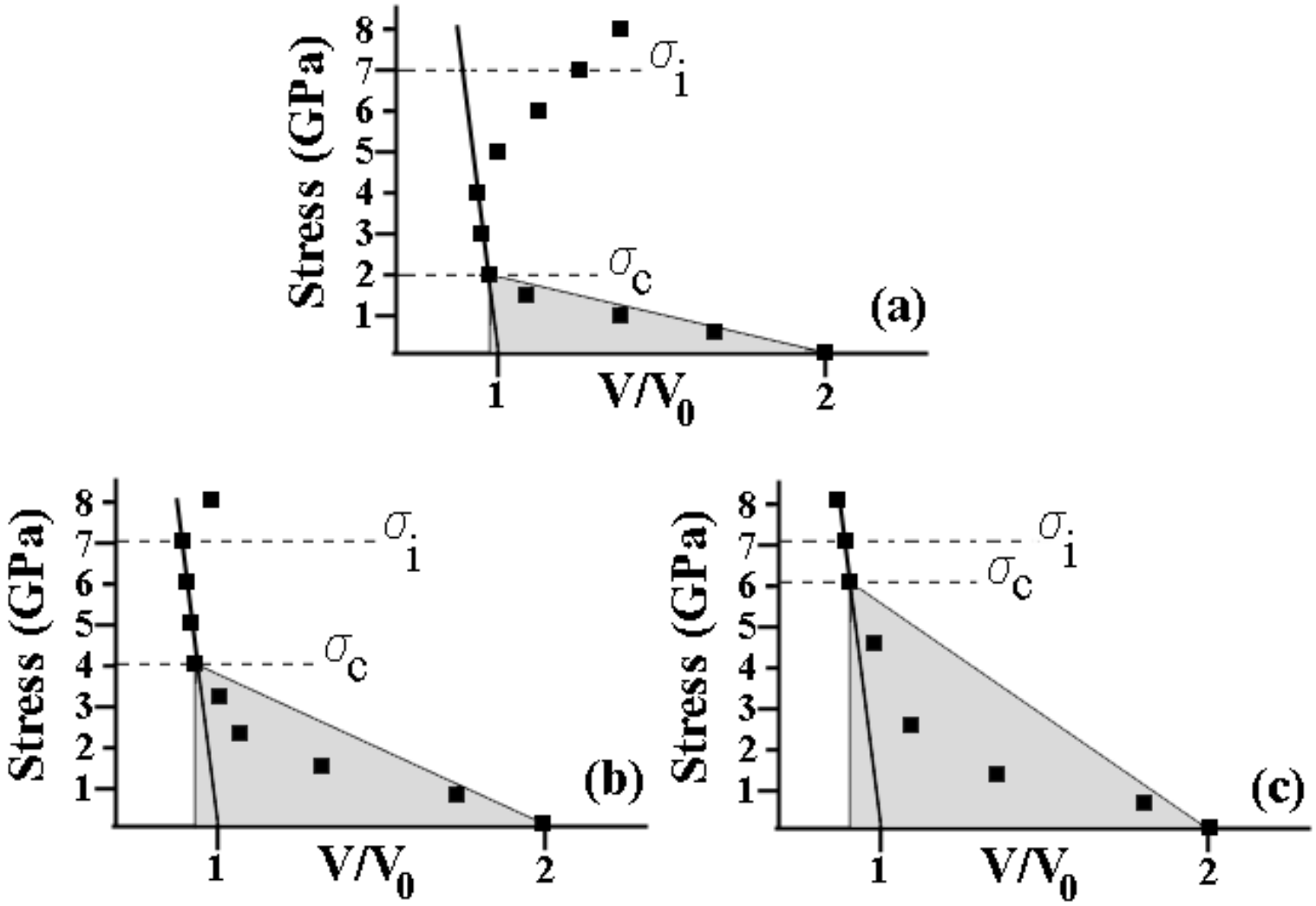

Figure 1.1: Schematic illustrating the different amounts of energy (work) associated with fully densifying a mixture with a crush strength (σ_C) of (a) 2 GPa, (b) 4 GPa, and (c) 6 GPa. The inert Hugoniot of the solid mixture is shown by the solid line originating at $V/V_0 = 1$, and the energy consumed during compaction is shown as the shaded region, which is based on $1/2PdV$. The stress applied to each mixture is σ_i.

of the mixtures to full density. With the least amount of energy consumed to compact the mixture in Fig. 1.1(a), there exists a sufficient amount of energy remaining to initiate reaction. This is not the case for the remaining two mixtures, for which consolidation to full density requires a significantly larger amount of energy.

To determine if a correlation between crush strength and reaction initiation stress of the sort illustrated by Fig. 1.1 exists, one would need to perform a multitude of experiments to establish values for both the crush strength as well as the threshold for reaction initiation. Current methods of determining the dynamic crush strength of powders and powder mixtures are often experimentally intensive. Hence, a need exists to develop methods that can accurately determine the crush strength in these highly heterogeneous thermite powder mixtures. The focus of this dissertation is to develop such a methodology, one that uses limited experimental resources to accurately predict the crush strength in thermite powder mixtures.

In establishing this methodology it is necessary to have an understanding of the relevant shock responses of the materials involved. As such, this dissertation begins with a discussion of the fundamentals of shock propagation in solids and distended (porous solids and powder compacts) materials. Of specific interest to the method developed are the different formulations for estimating the Hugoniot response of solid and porous mixtures and some of the various compaction models available in the literature. In addition to presenting the fundamentals on which these formulations and models were built, analysis of their application to specific material systems is given, with the intent of discovering strengths and weakness of the different approaches. Following the necessary technical background,

details of the powder mixtures are presented, with emphasis on individual constituent properties as well as the heterogeneities within the mixture. This is followed by the experimental methods used to obtain the compaction characteristics of the mixtures, exploring both quasi-static and dynamic approaches and analysis techniques.

Results of the experiments are covered in the subsequent chapter, beginning with a presentation of those obtained quasi-statically. Focus is then shifted toward those obtained dynamically, with particular attention directed toward the applicability of specific equations of state and compaction models to each of the two mixtures. Subsequently, the appropriate equations of state and compaction models are applied to each of the two systems (Ta + Fe_2O_3 and Ta + Bi_2O_3), and results of model calculations are presented in conjunction with experimental results. The chapter is concluded with a summary of the results and trends observed. Next, experimental results are analyzed and the methodology for predicting the compaction response of the thermite powder systems is presented. Detailed within this chapter are the configurational considerations pertaining to the initial microstructure and the methodology for determining an appropriate estimate of the yield strength of the components and mixtures. The methodology is then applied to the thermite systems investigated, and results are discussed. This approach is then extended to the more popular Al + Fe_2O_3 thermite system, and a comparison of the predicted and observed compaction response is given. Finally, concluding remarks are offered as to the development of the methodology and its extension to systems outside of the framework within which it was originally developed.

CHAPTER II

SHOCK FUNDAMENTALS FOR SOLID MATERIALS

Prior to delving into the complex response of heterogeneous powder mixtures to dynamic loading, which is the major focus of this dissertation, it is instructive to first examine the fundamentals of shock compression of solid materials. This chapter describes the basic fundamentals of shock wave propagation in solids, followed by the foundations of the Mie-Grüneisen equation of state, which is used for both solid and porous materials. Next, the relationships between different thermodynamic response curves with regard to shock loading will be examined, including different methods of determining these response curves for mixtures of materials. Finally, different mixture methods will be discussed and their predictions will be compared with published experimental results.

2.1 Shock Response of Solid Materials

When two solid bodies collide at high velocity, stress waves are generated at the point/plane of impact and travel into the bodies interior. The waves can take many forms including purely elastic, elastic-plastic, or perfectly plastic, where characteristics of the waves depend largely on the velocity of impact and properties of the materials [24].

For the case of high velocity impact, as can be produced by accelerating an impactor with explosives or compressed gas, large amplitude stress waves are produced in both the impactor and target material. A schematic of an idealized planar impact loading situation is given in Figure 2.1. In this configuration, an impactor (I) is accelerated at a stationary target (T) and impact occurs along the planar interface between the two. As the stress wavefront

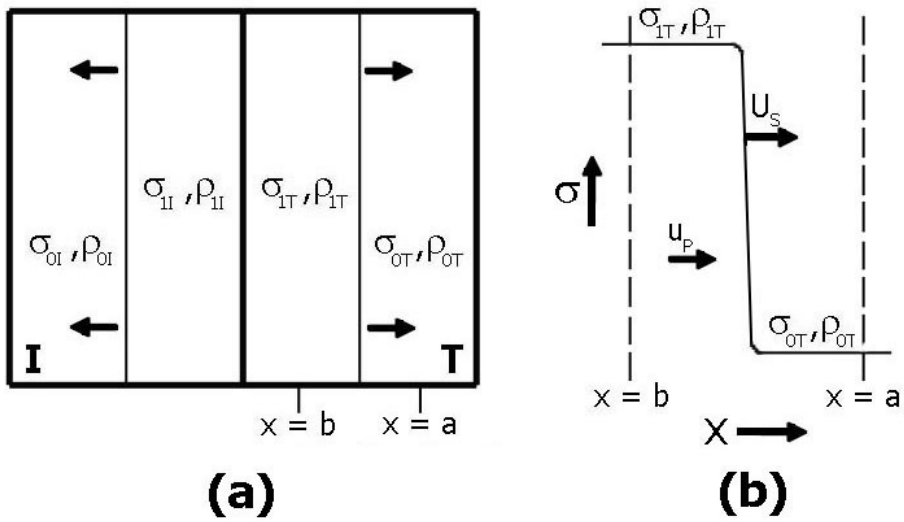

Figure 2.1: Schematic showing (a) parallel plate impact of impactor I with target T, and (b) resulting shock wave at a given instant in time.

propagates into the target material at speed U_S, it transforms the material from an initial stress σ_0 and density ρ_0 state, to an elevated stress σ_1 and density ρ_1 state (Fig. 2.1(a)). Material behind the front moves at a velocity u_P, which is slower than U_S and is responsible for the buildup of stress behind the front. If the wave front is sufficiently thin such that material properties can be treated as discontinuous across the front, and the material is in a state of equilibrium behind the front, the stress wave is called a shock wave [4].

The equations to relate stress, σ, temperature, θ, and energy, E, (thermodynamic variables) behind a shock front were originally developed by Rankine [25] and Hugoniot [26] for fluids; however, their analysis can also be extended to solids. It should be noted that in the strict sense of application to solids, σ used here to describe stress, is actually a measure of the applied pressure, or hydrostatic component of stress. This definition of stress (σ) is used throughout the remainder of this chapter to describe the Mie-Grüneisen equation of state (Sect. 2.2 and the various thermodynamic response curves (Sects. 2.3 and 2.4).

For shock waves of constant amplitude traveling into a material which is initially undisturbed ($U_{S0} = 0$), the conservations equations of mass (1), momentum (2), and energy (3) are [1]

$$\rho_0 U_S = \rho(U_S - u_P) \tag{1}$$

$$\sigma - \sigma_0 = \rho_0 U_S u_P \tag{2}$$

$$E - E_0 = 1/2(\sigma + \sigma_0)(V_0 - V) \tag{3}$$

where the subscript 0 denotes material properties prior to the arrival of the shock front, and V is the volume. The product of the initial density and shock velocity, $\rho_0 U_S$, in Eqns. 1 and 2 is commonly known as the shock impedance, and is an important parameter that will be discussed later in greater detail. Equations 1-3 are known as the Hugoniot equations or 'jump equations', and are applicable not only to shock waves, but to any wave propagating with a constant speed and shape [27]. A fourth equation relating any of the two quantities in Eqns. 1-3, an equation of state (EOS), is needed for closure such that all unknowns in Eqns. (1-3) can be determined from a single measurement. One such equation which has found widespread use is the relationship between shock and particle velocities. This relationship has to be determined experimentally, and is often described empirically for solids by the linear relationship [28]

$$U_S = C_0 + S u_P \tag{4}$$

where C_0 is the zero pressure soundspeed of a material and S is a fitting parameter.

The conservation equations, together with the equation of state, allow for the complete representation of a material in thermodynamic space. To demonstrate the applicability of these equations to solid materials, experimental results on the shock response of copper are examined. The experimental data shown in Fig. 2.2 was obtained from Marsh [29],

and shown are every fifth data point beginning with the first impact experiment spanning a stress range from 8 - 217 gigapascals (GPa). For the data reported, the shock velocity U_S was experimentally measured and the material (particle) velocity u_P was inferred through either impedance matching or a measurement of the free surface velocity. Figure 2.2(a) shows the experimental $U_S - u_P$ relationship for copper as well as a linear least squares fit of the data which yields values of $C_0 = 3.9312$ km/s and $S = 1.4895$ for the EOS of the form of Eq. 4. With C_0 and S determined, the linear equation of state can be used to calculate the volume V under shock loading through [28]

$$V = V_0\left(1 - \frac{1}{S} + \frac{C_0}{S\,U_S}\right) \quad = \quad V_0\left(1 - \frac{u_P}{C_0 + S\,u_P}\right) \tag{5}$$

With the volume so determined, the shocked stress is calculated by [28]

$$\sigma = \frac{C_0^2(V_0 - V)}{[V_0 - S(V_0 - V)]^2} \tag{6}$$

where the fit of Eq. 6 to the data of Marsh [29] is shown in Figs. 2.2(b) and (c). One can see that once C_0 and S are determined, the complete Hugoniot response of a material can be predicted. Also shown in Fig. 2.2(b) is the Rayleigh line, the line which connects the initial state (ρ_0, U_{S0}, u_{P0}) to the final Hugoniot state achieved during impact (ρ, U_S, u_p). Under impact conditions the material will not follow the Hugoniot path; rather, it follows the Rayleigh line to reach its final state on the Hugoniot. Furthermore, it can be shown through Eqns. 1-3 that the slope of the Rayleigh line in the σ-V plane is proportional to the square of the shock impedance.

Having described some of the more fundamental relationships regarding the shock loading of solid materials, and their relationships between experimentally determined parameters through the linear equation of state, attention now shifts toward an alternate equation

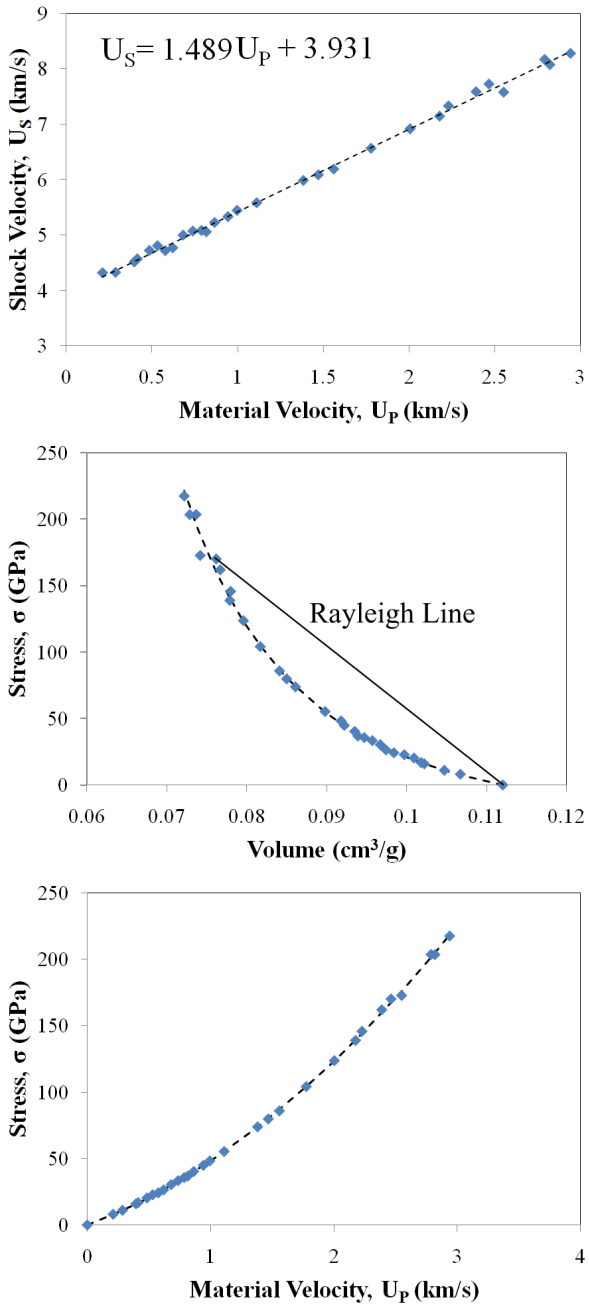

Figure 2.2: Schematic showing Cu material behavior from [29] in (a) $U_S - u_P$, (b) $\sigma - V$, and (c) $\sigma - u_P$ space

of state which allows for prediction of material behavior in 'off Hugoniot' states. This equation of state is the commonly used Mie-Grüneisen EOS.

2.2 Mie-Grüneisen Equation of State

When examining the behavior of materials under shock loading, it is often desirable to obtain information about the behavior of the material in an off-Hugoniot state. For example, mixing routines used to predict the Hugoniot response of mixtures composed of two or more materials with known Hugoniots requires knowledge of the materials 0 K isotherms ($\sigma - V$ response at zero Kelvin). Furthermore, unloading from the shocked state is assumed to occur isentropically (at constant entropy) such that accurately predicting the stresses in successive impedance matching calculations (see Sect. 6.8) requires knowledge of the release isentrope. However, in many instances, only information about the Hugoniot response of a material is known and can be determined experimentally. In instances such as these, the Mie-Grüneisen EOS can be used to determine the off-Hugoniot response.

The Mie-Grüneisen EOS is statistical in character and uses the oscillatory nature of atomic vibrations to relate two pressure and energy states [15]. The underlying assumption in this approximation is that at a given volume, all the atomic oscillators are assumed to vibrate at the same frequency, making the Grüneisen parameter a function of only volume. In its most basic form, the Grüneisen approximation can be represented as [15]

$$\gamma(V) = -(\frac{\delta \ ln \ \nu}{\delta \ ln \ V})_\theta \tag{7}$$

where ν is the vibrational frequency of an atom, $\gamma(V)$ is the Grüneisen parameter, and the relation is taken at constant temperature. This relation is of practical importance because if one can assume that all atomic oscillators are vibrating at the same frequency at a particular volume, then one can relate the stress and energy in some known reference state to the stress

and energy in another state, where these values are unknown. Utilizing the Grüneisen parameter to this end allows for the known and unknown stress and energy states to be related through [15]

$$\sigma - \sigma_R = \frac{\gamma(V)}{V}(E - E_R). \tag{8}$$

One can see that Eq. 8 serves to relate an unknown (σ, V, E) state of interest to the stress and internal energy of some known reference state (σ_R, V, E_R) at the same volume. Equation 8 can also take the differential form [15]

$$d\sigma = \frac{\gamma(V)}{V}dE \tag{9}$$

which upon rearrangement and appropriate substitution using Maxwell's relations allows for the Grüneisen coefficient to be expressed in terms of the volumetric thermal expansion, 3α, and the isothermal compressibility, K [15]

$$\frac{\gamma(V)}{V} = \frac{3\alpha}{C_V K}. \tag{10}$$

Another form of $\gamma(V)$ was developed by Slater [30] and extended by Dugdale and McDonald [31] and uses Debye's theory of atomic vibrations to account for vibrational velocities at pressures other than zero. Their work resulted in the relation for the Grüneisen parameter as a function of stress and volume [32]

$$\gamma(V) = -\frac{V}{2} * \frac{d^2(\sigma\, V^{\frac{2}{3}})/dV^2}{d(\sigma\, V^{\frac{2}{3}})/dV} - \frac{1}{3}. \tag{11}$$

Though the Dugdale-MacDonald relation, Eq. 11, has been shown to match sufficiently well with calculations of the Grüneisen parameter [32], the approximation

$$\frac{\gamma}{V} = \frac{\gamma_R}{V_R} = constant \tag{12}$$

is often used to simplify calculations, and has been shown to give sufficiently accurate results for many materials for stresses up to several hundred gigapascals [1, 15]. Using the approximation given by Eq. 12, calculations have been developed using the Mie-Grüneisen EOS to determine relationships between the different thermodynamic response curves of a material, specifically, relations between Hugoniots, isotherms, and isentropes. The underlying principles in the derivations relating the aforementioned thermodynamic responses will be presented in the next few sections.

2.3 Hugoniots and Isotherms

The general Mie-Grüneisen EOS given by Eq. 8 can be used to calculate the (σ-V-E) response of a material from a known reference curve. Thus if the Hugoniot of a material is known, one can use this, in conjunction with the Grüneisen EOS, to determine an isothermal loading response. Similarly, if the isotherm is known, the Hugoniot can be calculated. The relationship between a Hugoniot and an isotherm, calculated based on a pressure offset is shown in Fig. 2.3.

If the Hugoniot of a material is known, Eq. 8 takes the general form [33]

$$\sigma_H(V) = \sigma_\theta(V, \theta_0) + \frac{\gamma(V)}{V}[E_H(V) - E_\theta(V, \theta_0)], \tag{13}$$

where $\sigma_H(V)$ and $\sigma_\theta(V, \theta_0)$ are the known Hugoniot and unknown isothermal hydrostatic stress responses. Similarly $E_H(V)$ and $E_\theta(V, \theta_0)$ are the specific internal energy on the Hugoniot and isotherm, where θ represents temperature. To determine the stress response along the isotherm, $\sigma_\theta(V, \theta_0)$, relations for the energy terms must be developed first. The Rankine-Hugoniot energy relation can be used to represent the energy along the Hugoniot as [33]

$$E_H(V) = E_R + \frac{1}{2}\sigma_H(V)(V_R - V) \tag{14}$$

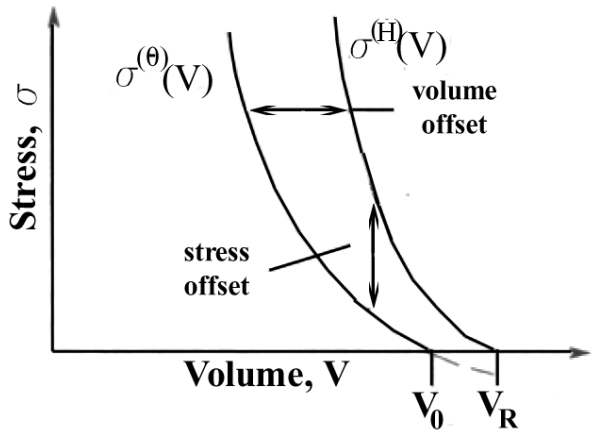

Figure 2.3: σ-V relationship between a Hugoniot and isotherm (from Davison [33]).

where the reference state is such that when $\sigma_H = 0$, $V = V_R$. The specific internal energy along the isotherm can be represented by the equation [33]

$$E_\theta(V,\theta_0) = E_0 - \int_{V_0}^{V} \sigma_\theta(V,\theta_0)dV + \theta_0 \int_{V_0}^{V} \frac{\gamma(V)}{V} C_V(V,\theta_0)dV \tag{15}$$

where E_0 is the reference internal energy at zero stress and $\theta = \theta_0$, $C_V(V,\theta_0)$ is the constant volume heat capacity. It should be noted that the general form of Eq. 15 follows from the first law of thermodynamics. Inserting Eq. 14 and 15 into Eq. 13, and assuming the specific heat and ratio γ/V are constant results in the following relation for the isotherm in terms of a known Hugoniot [33].

$$\sigma_\theta(V,\theta_0) + \frac{\gamma}{V}\int_{V_0}^{V} \sigma_\theta(V,\theta_0)dV = \sigma_H(V)[1 - \frac{\gamma}{2V}(V_R - V) - \frac{\gamma}{V}(E_R - E_0 - \theta_0 \frac{\gamma}{V} C_V(V_0 - V))] \tag{16}$$

Equation 16 can be manipulated to yield a first order differential equation to solve for $\sigma_\theta(V,\theta_0)$ as a function of volume as will be shown later. Similarly, one can solve for an unknown Hugoniot as a function of a known isotherm through [33]

$$\sigma_H(V) = \frac{\sigma(\theta)(V,\theta_0) + \frac{\gamma}{V}[E_R - E_0 + \int_V^{V_0} \sigma_\theta(V,\theta_0) - \theta_0 \frac{\gamma}{V} C_V(V - V_0)]}{1 - \frac{\gamma}{2V}(V_0 - V)} \tag{17}$$

Evaluating Eq. 16 for the isotherm requires knowledge of the reference internal energies at zero stress for the Hugoniot and the isotherm, as well as the zero stress specific volume of the isotherm, see Fig. 2.3. Davison [33] gives the following approximate relations to determine V_0 and E_0 along the isotherm in terms of known V_R and E_R [33]

$$V_0 = V_R exp[\beta(\theta_0 - \theta_R)] \tag{18}$$

and

$$E_R - E_0 = \int_{\theta_R}^{\theta_0} C_P d\theta \tag{19}$$

where β is the volumetric thermal expansion coefficient and C_P is the specific heat at constant pressure ($\sigma = 0$). A more rigorous method of determining these parameters utilizing Debye's atomic theory has been developed by McQueen et al. [1] and is presented next.

The simplest form of the Debye theory [34], in which a single Debye theta, θ_D, is used to describe the atomic vibrations of a solid, can be used to accurately represent the specific heat and thermal energy of many solids. Within this framework, McQueen et al. [1] define the specific heat at constant volume, C_V, and the thermal energy, E_T, as

$$C_V = 3nk[4D_3(x) - 3x/(e^x - 1)] \tag{20}$$

where

$$D_3(x) = \frac{3}{x^3}\int_0^x \frac{z^3}{e^z - 1} dz, x = \theta_D/T \tag{21}$$

and

$$E_T = 3nkTD_3(x). \tag{22}$$

In the foregoing equations, n is the number of atoms per gram of material and k is Boltzmann's constant. The thermal energy E_T can represent the zero stress energy along the Hugoniot, E_R, if the zero stress reference energy along the isotherm is arbitrarily set to

zero. If adequate material properties exist, Eq. 20 can be used to solve for θ_D in terms of the known specific heat, provided the specific heat is less than the quantity $3nk$. In instances where the specific heat exceeds $3nk$, the above relations do not hold and θ_D can be approximated using Lindemann's melting law by [34]

$$\theta_D \approx B T_M^{\frac{1}{2}} \overline{A}^{-\frac{5}{6}} \rho_0^{\frac{1}{3}} \tag{23}$$

where $\overline{A}$ is the mean atomic weight, T_M is the melting temperature of the solid, ρ_0 is the mean density, and B is an empirical constant found to be approximately 120. Once a value for the Debye theta θ_D is known, E_T can be calculated using Eqns. 21 and 22. For the special case of the $0K$ isotherm, V_0 can be determined by solving the Mie-Grüneisen EOS in the form of

$$\sigma_H(V_0) = \frac{\gamma_{0K}}{V_0} E_H \tag{24}$$

where $\gamma_{0K} = (\gamma_R / V_R) V_0$ and E_H is given by Eq. 3, with V_0 and V set to V_R and V_0, respectively, and $P_0 = E_0 = 0$. For isotherms other than $0K$, Eqns. 18 and 19 can be used to solve for V_0 and E_0. With values for V_0 and E_0 known, one can now differentiate Eq. 16 to yield [33]

$$\frac{d\sigma_\theta(V,\theta_0)}{dV} + \frac{\gamma(V)}{V}\sigma_\theta(V,\theta_0) = \overline{K}(V) + (\frac{\gamma(V)}{V})^2 C_V \theta_0 \tag{25}$$

where

$$\overline{K}(V) = [1 - \frac{\gamma(V)}{2V}(V_R - V)]\frac{d\sigma_H(V)}{dV} + \frac{\gamma(V)}{2V}\sigma_H(V). \tag{26}$$

Equation 25 is a first order differential equation which can be solved numerically to yield the stress as a function of volume along the isotherm. Having solved for the $\sigma - V$ isotherm, the specific internal energy along the isotherm can then be determined by inserting the known σ and V quantities into Eq. 13 and solving for $E_\theta(V,\theta_0)$ which gives [33]

$$E_\theta(V,\theta_0) = E_R + \frac{\gamma(V)}{V}\sigma_\theta(V,\theta_0) + \sigma_H(V)[\frac{1}{2}(V_R - V) - \frac{V}{\gamma(V)}] \tag{27}$$

By implementing Eqns. 25 and 27, one can determine the (σ-V-E) relations for any isotherm of a material from a known Hugoniot. In many instances the $0K$ isotherm is of particular interest, and the next section examines two different methods to determine the $0\ K$ isotherm of a material in greater detail.

2.3.1 The Zero K Isotherm

In the foregoing analysis, general equations for an isotherm of any temperature were developed, and the $0K$ isotherm is merely a special case in which $\theta = 0$. As such, one means of arriving at the $0K$ isotherm is by substituting $\theta = 0$ into either Eq. 16 or Eq. 25 which yields [33]

$$\sigma_\theta(V,\theta_0) + \frac{\gamma}{V}\int_{V_0}^{V} \sigma_\theta(V,\theta_0)dV = \sigma_H(V)[1 - \frac{\gamma}{2V}(V_R - V) - \frac{\gamma}{V}(E_R - E_0)] \tag{28}$$

and

$$\frac{d\sigma_\theta(V,\theta_0)}{dV} + \frac{\gamma}{V}\sigma_\theta(V,\theta_0) = \overline{K}(V) \tag{29}$$

where $\overline{K}(V)$ takes the same value as in Eq. 25. Recall that Eqns. 22 and 24 can be used to determine E_R at $V = V_R$ and $P = 0$ along the Hugoniot and V_0 at $P = 0$ along the isotherm.

An alternative method to determine the $0K$ isotherm has been developed by McQueen et al. [1]. This approach assumes a material can be adequately described by a two term EOS such that

$$\sigma_H(V,\theta) = \sigma_K(V) + \sigma_\theta(V,\theta) \quad and \quad E_H(V,\theta) = E_K(V) + E_\theta(V,\theta) \tag{30}$$

where $\sigma_H(V,\theta)$, $\sigma_K(V)$, and $\sigma_\theta(V,\theta)$ and $E_H(V,\theta)$, $E_K(V)$, and $E_\theta(V,\theta)$ are the Hugoniot, isotherm, and thermal stress and energies, respectively. By representing a material with a two term equation of state, one effectively neglects any electronic behavior. Such equations of state have been shown to not be entirely accurate by Al'tshuler [3]; however, electronic

terms are sufficiently small below approximately ten thousand degrees such that they may be neglected in the analysis of materials under moderate shock stresses up to several hundred GPa [35]. With knowledge of a materials Hugoniot, $\sigma_H(V)$, the energy along the Hugoniot is calculated using Eq. 14, with E_R representing the reference energy along the Hugoniot at $\sigma = 0$, $V = V_R$. Calculation of the thermal energy, $E_\theta(V, \theta)$ requires knowledge of the temperature along the Hugoniot which can be determined by first taking the derivative of the Rankine-Hugoniot energy equation, Eq. 14, expanded to include the initial stress σ_0 which gives [33]

$$\frac{dE_H(V)}{dV} = \frac{1}{2}[\frac{d\sigma_H(V)}{dV}(V_0 - V) - \sigma_H(V) - \sigma_0] \tag{31}$$

where the Hugoniot is centered at the points $\sigma = \sigma_0$ and $V = V_0$. Recalling the first law of thermodynamics, $dE = \theta\, dS - \sigma\, dV$ where S is entropy, it can be rearranged to yield

$$\frac{dE_H(V)}{dV} = \theta_H(V)\frac{dS_H(V)}{dV} - \sigma_H(V). \tag{32}$$

Combining Eqns. 31 and 32 results in [33]

$$\frac{dS_H(V)}{dV} = \frac{\frac{d\sigma_H(V)}{dV}(V_0 - V) + \sigma_H(V) - \sigma_0}{2\theta_H(V)} \tag{33}$$

which can be solved for temperature if one recalls that temperature is a function of both volume and entropy such that its total derivative can be expressed (using the thermodynamic derivatives $(d\theta/dV)_S = -(\gamma/V)\theta$ and $(d\theta/dS)_V = \theta/C_V$) as

$$d\theta = -\frac{\gamma}{V}\theta\, dV + \frac{\theta}{C_V}dS_H(V) \tag{34}$$

which when divided by dV yields

$$\frac{d\theta_H(v)}{dV} = -\frac{\gamma}{V}\theta + \frac{\theta}{C_V}\frac{dS_H(V)}{dV} \tag{35}$$

Finally, substituting Eq. 33 into Eq. 35 yields [33]

$$\frac{d\theta_H(V)}{dV} + \frac{\gamma}{V}\theta_H(V) = \frac{\frac{d\sigma_H(V)}{dV}(V_0 - V) + \sigma_H(V) - \sigma_0}{2C_V} \tag{36}$$

which is a first order differential equation that can be solved for temperature. In the foregoing analysis, it is assumed that both the ratio γ/V and C_V are constants. With the temperature along the Hugoniot known, the thermal energy $E_\theta(V, \theta)$ along the Hugoniot can be calculated using Eqns. 21 and 22, and with the thermal energy so calculated the thermal stress can be calculated using the Mie-Grüneisen EOS through $\sigma_\theta(V, \theta) = \frac{\gamma}{V}E_\theta(V, \theta)$. Having solved for the thermal stress and thermal energy one can then determine the energy and stress along the $0K$ isotherm using Eq. 30 to yield

$$\sigma_K(V) = \sigma_H(V, \theta) - \sigma_\theta(V, \theta) \quad \textit{and} \quad E_K(V) = E_H(V, \theta) - E_\theta(V, \theta) \tag{37}$$

such that a complete (σ_K-V-E_K) representation of the material at $0K$ is known.

2.4 Hugoniots and Isentropes

The isentrope is another thermodynamic curve of interest. It is the compressional response of a material under the condition that entropy is held constant. Conventionally, the isentrope has been used to describe the unloading behavior of a material from its Hugoniot state [36]. However, recent advancements in ramp loading [37] have allowed for the determination of material strength properties under quasi-isentropic loading conditions [38, 39] and have increased interest in isentropic loading phenomena. A schematic representation of the Hugoniot and an isentrope is shown in Fig. 2.4.

Generally, experimentally determining isentropic (quasi-isentropic) loading curves requires extremely specialized equipment [37], and it is often desirable to derive the isentropic loading and unloading response of a material from its known Hugoniot. Similar to

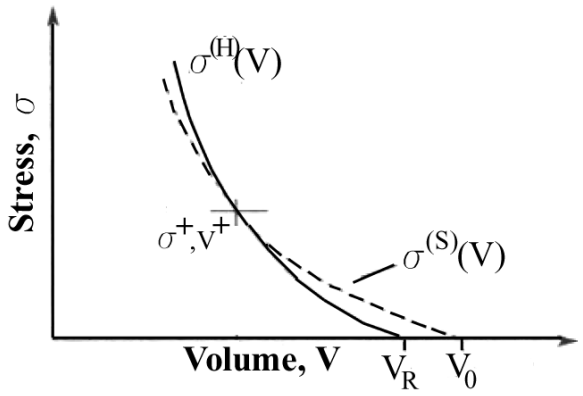

Figure 2.4: σ-V relationship between a Hugoniot (solid curve) centered at $\sigma = 0, V = V_R$ and an isentrope through the point (σ^+, V^+)(from Davison [33]).

the method for calculating the isotherm of a material, the isentrope can also be derived from the known Hugoniot using a pressure (hydrostatic stress) offset (Fig. 2.3) at a given volume. Beginning with the Mie-Grüneisen EOS and inserting the Rankine-Hugoniot energy equation as well as the expression for energy along an isentrope, which can be represented as [33]

$$E_S(V, S^+) = E^+ - \int_{V+}^{V} \sigma_S(V, S^+) dV \tag{38}$$

one arrives at the equation for stress as a function of volume along the isentrope with respect to the known Hugoniot

$$\sigma_S(V, S^+) = \frac{\gamma(V)}{V}[\frac{1}{2}\sigma^+(V_R - V^+) - \int_{V^+}^{V} \sigma_S(V, S^+) dV] + \sigma_H(V)[1 - \frac{\gamma(V)}{2V}(V_R - V)]. \tag{39}$$

In Eq. 38, E^+ is simply shock energy along the Hugoniot at (σ^+, V^+). Figure 2.4 shows schematically the meaning of the quantities given in the foregoing equations. Equation 39 can be solved by differentiating with respect to volume, which results in, if $\frac{\gamma(V)}{V} = \frac{\gamma_R}{V_R} =$ *constant*, the first order differential equation [33]

$$\frac{d\sigma_S(V, S^+)}{dV} + \frac{\gamma_R}{V_R}\sigma_S(V, S^+) = \frac{\gamma_R}{2V_R}\sigma_H(V) + \frac{d\sigma_H(V)}{dV}[1 - \frac{\gamma_R}{2V_R}(V_R - V)] \tag{40}$$

Equation 40 allows one to determine the stress as a function of volume along the isentrope passing through the point (σ^+, V^+) in terms of a Hugoniot centered at $(\sigma = 0, V = V_R)$ which also passes through the same point (σ^+, V^+).

Another important quantity related to an isentropic compression or decompression is the steady-state mass flow, or material velocity. Because isentropic flow occurs gradually, direct application of the Rankine-Hugoniot 'jump equations' cannot be used. Instead, one must use differential forms of the mass (41) and momentum (42) continuity equations [40]

$$\frac{\partial \rho}{\partial t} + \frac{\partial \rho}{\partial x}u + \rho \frac{\partial u}{\partial x} = 0 \tag{41}$$

$$\frac{\rho}{c}(\frac{\partial u}{\partial t} + u\frac{\partial u}{\partial x}) + \frac{\partial \rho}{\partial x}c = 0 \tag{42}$$

to determine the characteristics of mass flow [41], where t, x, and u are time, position, and displacement, and c is the speed of sound in the material. Using this technique, the mass velocity behind a steady-state isentropic flow is shown to be [40]

$$u = \int_{\rho_0}^{\rho_1} \frac{c\partial \rho}{\rho} = \int_{\sigma_0}^{\sigma_1} (-\frac{\partial V}{\partial \sigma})_S^{1/2} d\sigma. \tag{43}$$

Thus one can determine the material velocity directly from the stress-volume response along the isentrope. Equation 43 will be used explicitly in impedance matching techniques, where stress and material velocity are of primary importance.

2.5 Mixture Hugoniots

It is often desirable to predict the high-pressure response of mixtures of materials. In the case of simple mixtures, which are composed of structurally varying components inter dispersed within some volume, several different methods of estimating mixture Hugoniots

have been developed. Overall, the goal of the various mixture routines is to predict the Hugoniot response of the mixture with knowledge of the compressional responses of the individual components. In this section, several different means by which the Hugoniot responses of mixtures are obtained are examined, and their results are compared to published data.

2.5.1 Basic Mass Averaged Equation of State

The simplest method of estimating an equation of state (EOS) for a mixture is by averaging the EOS of each material present within the mixture. Averaging can be carried out on the basis of the mass fractions of the individual components such that the EOS for the mixture is determined through the relations

$$\rho_0 = \sum X_i \rho_{0i} \quad C_0 = \sum X_i C_{0i} \quad S = \sum X_i S_i \tag{44}$$

where X_i is the mass fraction of component i. This method is simple and straightforward, and is considered satisfactory as a first approximation for mixtures of many materials. However, as shock stress increases, so to do temperature effects, and when constituents possess significantly different thermal properties the method of simple mass averaging may be insufficient to adequately describe the Hugoniot response mixtures. To address this issue, McQueen and co-workers [1] developed a modified mass averaging technique based on zero Kelvin isotherms.

2.5.2 Zero Kelvin (Isothermal) Mass Averaged Equation of State

Realizing the compressional response of a simple mixture is influenced by variations in shock heating between the individual components, McQueen and co-workers [1] sought to minimize these effects by formulating a mixture EOS based on the zero Kelvin isotherms

(cold curves) of the constituents. In this method, a zero Kelvin isotherm for each constituent is calculated, by either extending low pressure quasi-static data of the type obtained by Bridgman [42] or by calculation from the known Hugoniot as presented in Sect. 2.3.1. Once the zero Kelvin compression curves for the constituents are known, the zero Kelvin curve for the mixture is obtained using the following relations for volume and energy

$$V_k = \sum X_i V_i(\sigma) \qquad E_k = \sum X_i E_i(\sigma) \tag{45}$$

where the subscript k indicates the quantity is taken along the zero Kelvin isotherm. Inherent in these equations is that stress is equilibrated in the constituents behind the shock front. To determine the Hugoniot response of the mixture, the zero Kelvin isotherm for the mixture described by Eq. 45 must be heated up. To accomplish this, values for the Grüneisen parameter of the mixture, or equivalently $(\partial E/\partial P)_V = V/\gamma$ which in their analysis is assumed constant, and the specific heat at constant volume C_V of the mixture must be determined. McQueen and co-workers [1] assume these quantities for the mixture can be described adequately well by

$$V/\gamma = \sum X_i (V/\gamma)_i \qquad C_V = \sum X_i C_{Vi} \tag{46}$$

With these quantities known, the Hugoniot of the mixture is determined using the Mie-Grüneisen EOS of the form of Eq. 8.

2.5.3 Material Velocity Mass Averaged Equation of State

Another method of determining the EOS of a simple mixture is presented by Batsanov [43], and is based on mass averaged material velocities of the constituents. Within this framework, the mass velocity of a two component mixture is related to the mass velocities

of the individual constituents through the relation

$$u(\sigma)^2_{\sigma,m} = X_1 u(\sigma)^2_{\sigma,1} + (1 - X_1) u(\sigma)^2_{\sigma,2} \tag{47}$$

where the subscripts m and $i = 1, 2$ indicate values for the mixture and the individual constituents. If the equation of state relating $U_S - u_P$ is linear, the material velocity of constituent i can be expressed as a function of stress as [43]

$$u_{P,i} = \frac{C_{0,i}}{2S_i}\left(\sqrt{1 + \frac{4S_i V_{0,i}\sigma}{C^2_{0,i}}} - 1\right) \tag{48}$$

where $C_{0,i}$ and S_i are the same fitting parameters found in Eq. 4. Substituting Eq. 48 into Eq. 47, one can determine the material velocity at a given stress for a two component mixture. Again, in this description stress is assumed equilibrated between the constituents. With knowledge of the $\sigma - u_P$ behavior of the mixture, the conservation relations given by Eqns. 1-3 can be used to convert the $\sigma - u_P$ response to the $\sigma - V$ plane. Extension to systems with more than two components is apparent.

2.5.4 Energy Partitioned Equation of State

An approach taken by Krueger and Vreeland [44] stems from the idea that different components in the mixture will absorb different amounts of energy (temperature) immediately behind the shock front. In their model, it is assumed that stress and material velocity are equilibrated between the constituents at or within close proximity to the rise time to peak stress. Conversely, thermal equilibrium is not reached during the shock rise time, and is supposed to occur orders of magnitude more slowly than stress equilibrium. Within this framework, the total specific internal energy of a shock wave of stress σ_1 can be partitioned to each of the components through

$$XE_A + (1 - X)E_B = \frac{1}{2}\sigma_1(V_{00,M} - V_{1,M}) \tag{49}$$

where X is the mass fraction of component A, $V_{00,M}$ and $V_{1,M}$ are the initial volume and volume at stress σ_1 of the mixture. Here, the ambient energy for each component is taken as the reference energy, and the initial stress of the mixture is assumed to be zero. The energy and stress can be further partitioned into thermal and elastic components

$$E_A = E_{T,A} + E_{E,A}, \qquad E_B = E_{T,B} + E_{E,B} \tag{50}$$

$$\sigma_A = \sigma_{T,A} + \sigma_{E,A} = \sigma_B = \sigma_{T,B} + \sigma_{E,B} \tag{51}$$

where the subscripts T and E signify the thermal and elastic components. Employing the definition of the Grüneisen parameter given by Eq. 9, and assuming a constant γ/V ratio the thermal stress can be defined in terms of the thermal energy for each component i as

$$d\sigma_{T,i} \approx \frac{\gamma_{0,i} dE_{T,i}}{V_{0,i}} \Rightarrow \sigma_{T,i} \approx \frac{\gamma_{0,i} E_{T,i}}{V_{0,i}}. \tag{52}$$

By substituting Eqns. 50-52 into Eq. 49 the equation for the equilibrated stress becomes [44]

$$\sigma_1 = \frac{\omega_A \sigma_{E,A}(\lambda_A) + \omega_B \sigma_{E,B}(\lambda_B) - X E_{E,A}(\lambda_A)/V_{0,A}V_{0,B} - (1-X) E_{E,B}(\lambda_B)/V_{0,A}V_{0,B}}{\omega_A + \omega_B - (1/2)[\varphi - \eta_A \lambda_A - \eta_B \lambda_B]} \tag{53}$$

where

$$\omega_A = \frac{X}{\gamma_{0,A} V_{0,B}}, \qquad \omega_B = \frac{(1-X)}{\gamma_{0,B} V_{0,A}} \tag{54}$$

$$\eta_A = \frac{X}{V_{0,B}}, \qquad \eta_B = \frac{(1-X)}{V_{0,A}} \tag{55}$$

$$\lambda_A = \frac{V_{1,A}}{V_{0,A}}, \qquad \lambda_B = \frac{V_{1,B}}{V_{0,B}}, \qquad \varphi = \frac{V_{00,M}}{V_{0,A} V_{0,B}} \tag{56}$$

In the foregoing equations, $V_{1,A}$ and $V_{1,B}$ are the specific volumes of components A and B at stress σ_1, and a volume dependence (λ_i) is indicated for the elastic stresses and energies.

Yet to be defined are relations for the elastic components of stress and energy, $\sigma_{E,i}(\lambda_i)$ and $E_{E,i}(\lambda_i)$. These are assigned to an isentropic Murnaghan [45] relation of the form [44]

$$\sigma_E = \frac{\beta_{0S}}{\beta'_{0S}}\left[\left(\frac{V_0}{V_1}\right)^{\beta'_{0S}} - 1\right] \tag{57}$$

which can be integrated to yield the elastic energy

$$E_E = -\int_{V_0}^{V} \sigma_C dV = \frac{\beta\, V}{\beta'_{0S}}\left(\frac{(V_0/V)^{\beta'_{0S}}}{\beta'_{0S} - 1} + 1\right) - \frac{\beta_0\, V_0}{\beta'_{0S} - 1} \tag{58}$$

In Eqns. 57 and 58, β_{0S} is the isentropic bulk modulus and β'_{0S} is its first derivative with respect to stress taken at constant entropy. In light of the fact that the stress derivative of the isentropic bulk modulus is difficult to obtain experimentally and theoretically, the assumption $\beta'_S \approx \beta'_T$ is made, where β'_T is the isothermal pressure derivative of the bulk modulus which is more easily obtained. Similarly, the thermal energy of a mixture can also be difficult to determine, thus Krueger and Vreeland [44] postulated that there existed some ratio of the thermal energies

$$\xi(\sigma_1, U_S, u_P) \equiv E_{T,B}/E_{T,A} \tag{59}$$

which, when combined with the relation

$$\sigma_1(1 - \xi/\epsilon) = \sigma_{E,B}(\lambda_B) - (\xi/\epsilon)\sigma_{E,A}(\lambda_A) \tag{60}$$

makes it convenient to examine the two extremes of energy partitioning, where either component A or B absorbs all the energy, or any other intermediate partitioning. To determine the Hugoniot response of the mixture, Eqns. 53 and 60 must be combined with the continuity equations of mass and momentum, Eqns. 1 and 2, to yield a system of four equations with five unknowns ($\sigma_1, U_S, u_P, V_{1,A}$,and$V_{1,B}$), which can be solved simultaneously if a value for one of the variables is assumed.

2.5.5 Comparison of Mixture Models

To look at the robustness of each of the aforementioned mixture models, it is intuitive to compare model predictions with results from actual Hugoniot experiments. Unfortunately, for simple mixtures of the type for which these models were developed, where individual constituents are structurally distinct (i.e. not a single phase alloy), published data for fully dense mixtures is sparse. Instead we examine a nearly fully dense mixture of tungsten and copper, which is commercially designated as Elkonite 10W3 and is composed of tungsten with 24 weight percent copper. The material properties of the constituents are given in Table 2.1

Table 2.1: Material properties used to determine mixture response of Elkonite 10W3. Data with $*$ from [44], all else from [1] p. 532 and p. 543.

	Cu	W
$\rho_0\ (g/cm^3)$	8.930	19.224
$C_0\ (km/s)$	3.940	4.029
S	1.489	1.237
γ_0	1.99	1.54
$3Nk\ (at-J/kg-K)$	392.5	135.7
$C_V\ J/kg-K)$	371.8	131.0
$\theta_D\ (K)$	306	247
$E_{0H}\ (J/kg)$	77,000	29,000
$V_{0K}\ (m^3/kg)$	$1.10902x10^{-4}$	$5.58779x10^{-5}$
$P_{0H}\ (kg/m-s^2)$	0	0
$T_0\ (K)$	293	293
X_i	0.24	0.76
$\beta_{0S}\ (kg/m-s^2)$	$139.76x10^{9*}$	$308.1x10^{9*}$
β'_{0S}	4.994^*	3.996^*

The Elkonite 10W3 Hugoniot data used for comparison of model data is that of Marsh [29], which has an average initial density of $\rho_0 = 14.852\ g/cm^3$ [29]. The theoretical density of this composition, as determined from the mass averaged rule of mixtures, is

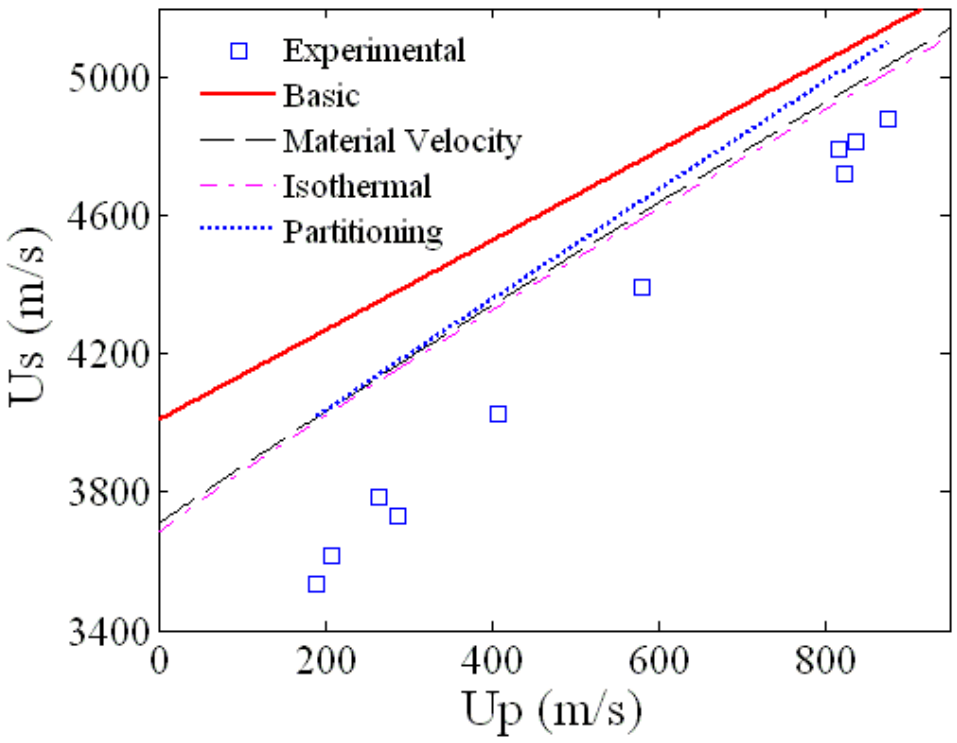

Figure 2.5: Comparison of different mixture routines with experimental Hugoniot data for Elkonite 10W3.

15.058 g/cm^3, resulting in a distention of 1.014, or equivalently, the mixture is 98.6 % of its calculated theoretical density. Neglecting porosity, the results of the four mixture models with the data of Marsh [29] are given in Fig. 2.5. Clearly visible in Fig. 2.5 is how the incorporation of even the slightest amount of porosity significantly effects the ability of these models to accurately predict the Hugoniot response. It should be noted that the energy partitioning ratio (Sect. 2.5.4) used in the calculation is $\xi = 1$. The basic mass averaging method (Sect. 2.5.1) is by far the worst at predicting the response, and differs significantly from the other predictions. The mass averaged, isothermal, and energy partitioning models all predict similar responses up to $u_P \approx 400$ m/s, at which point the energy partitioning

model diverges from the other two models. However, all methods without the explicit incorporation of porosity perform very poorly.

As many mixtures of interest often possess some level of inherent porosity, these models need to have the ability to incorporate porosity if they are to successfully predict the Hugoniot response. As developed thus far, only the energy partitioning model (Sect. 2.5.4) has a means to incorporate porosity; it does so through the parameter $V_{00,M}$. The influence of porosity and its effect on material response is the subject of the next chapter, at which point the the Elkonite 10W3 material system will be revisited.

CHAPTER III

SHOCK FUNDAMENTALS FOR PARTICULATE MATERIALS

Having covered the basic fundamentals needed to describe shock processes in solids, attention is now turned toward the shock response of distended materials (including porous solids and powder compacts), which adds additional elements of complexity to the analysis of shock wave propagation. In addition to bulk material response, factors such as powder particle and void size and shape and surface characteristics will influence the shock compression response. Although research on distended materials has been on-going for over 50 years [2, 46], many questions regarding the crush-up response, particularly in the case of powders, during dynamic loading still remain. For example, what role do the intrinsic and extrinsic properties of individual constituents play in the consolidation of highly heterogeneous powders and their mixtures? This chapter begins with general comments on the packing of powders. This is followed by an explanation of the static and dynamic consolidation techniques, with emphasis given to energetic and configurational considerations. Lastly, different methods to incorporate distention into the shock Hugoniot are described, focusing on several constant volume and constant stress extrapolations.

3.1 Particle Packing

The resting configuration of powder particles (and void space) is an important parameter in powder processing and depends on many factors including particle size distribution, shape, surface roughness, density, etc. For a random dense packing of monosized spherical powders, the maximum packing fraction is ≈ 0.6 [47]. However, by introducing a size

distribution in the powders, as is the case in most real-world powder systems, significant increases in packing fraction can be achieved [47, 48]. For different binary mixtures of particles, Santiso and M*ü*ller [47] have observed variations in the total packing fraction by changing the weight fraction of larger particles. Their results are shown in Fig. 3.1, with the solid and dotted lines giving the upper and lower bounds of packing fractions for infinite and mono disperse size ratios. One can see that as the size ratio of large to small particles increases, there is an optimal weight fraction of larger particles that results in maximal packing fraction. However, as the weight fraction of larger particles is further increased, total packing fraction decreases due to the amount of smaller particles being insufficient to completely fill the void spaces between the contiguous network of larger particles.

Introduction of a size distribution can also lead to significant segregation in powder mixtures. As particles move past one another during processing, it has been shown that smaller particles tend to settle toward the bottom of a mixture, shifting larger particles upward [49]. Lan, employing Monte Carlo methods to simulate shaking in a ternary powder system has observed preferential segregation of the smallest particles at early times [50]. Results of this work from Rosato [49] are shown in Fig. 3.2. Notice that settling of the smallest particles has occurred at cycles 60 and 120, where medium and large particles remain largely unsegregated. This phenomena can lead to significant heterogeneities in powder compacts with finite size distributions, especially if the particles also possess variant intrinsic properties.

As particle size is reduced to less than 100 μm, gravity is no longer the dominant force influencing particle motion; rather, attractive and repulsive forces between particles become dominant. For particles $< 100\ \mu$m van der Waals forces are the dominant forces, while as particle size decreases below $< 1\ \mu$m electrostatic forces become dominant. Interactions of

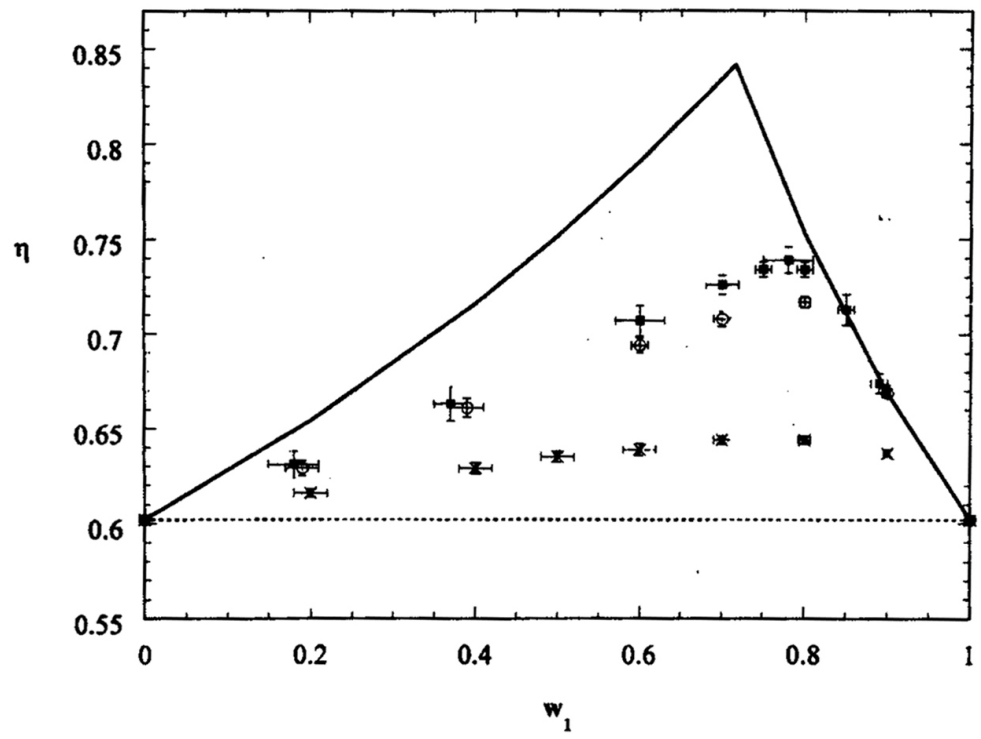

Figure 3.1: Packing fraction η of binary hard spheres as a function of volume fraction of larger particles w_1 for different size ratios R: crosses, $R = 2$; open circles, $R = 4$; closed squares, $R = 5$. Solid line represents infinite size ratio, and dashed line is for a mono disperse system ($R = 1$).(From Santiso and Muller [47])

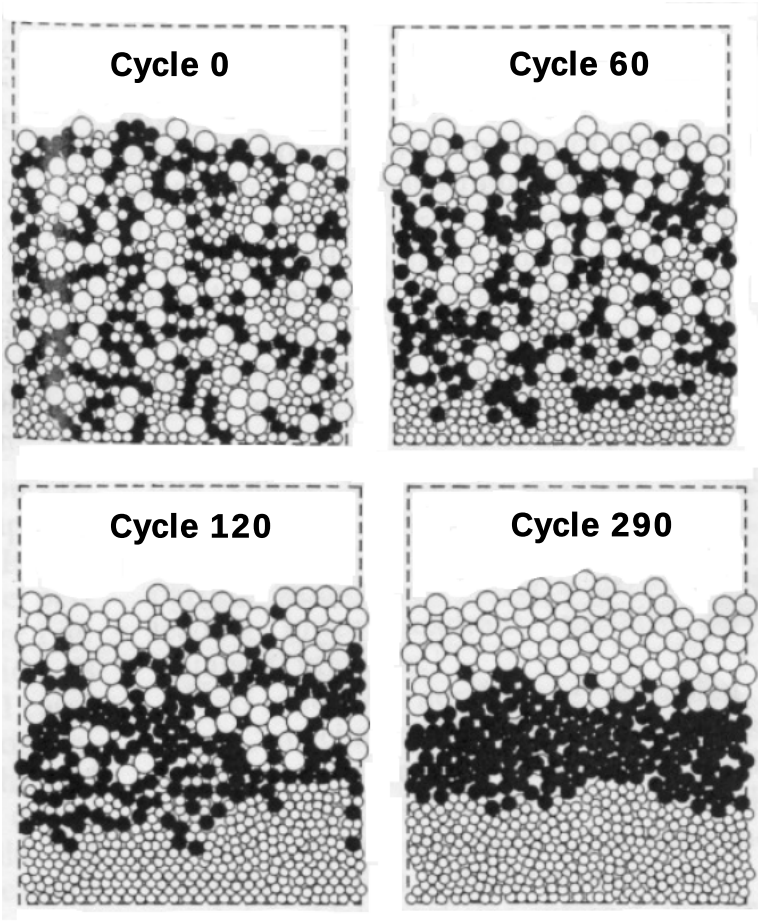

Figure 3.2: Particle configurations at 0, 60, 120, and 290 cycles for Monte Carlo simulation of ternary mixture with d_1:d_2:d_3 = 1:1.5:2 and shaking amplitude equal to diameter d_1 (From Rosato [49]).

these types can lead to decreased coordination and the formation of agglomerates, resulting in lower overall packing fractions [51]. Surface roughness can also affect packing fractions, especially as particle size decreases. As particle surfaces become increasingly rough, particle sliding and rolling becomes more difficult, which can lead to increased porosity [52]. Furthermore, deviation in particle shape from that of a sphere can also lead to less efficient packing and an increase in porosity [53].

Hence, it is evident that many different factors influence the resting configuration of a powder mixture. In an ideal mixture, the highest packing fractions might be achieved with smooth, spherical, bi-dispersed size powders with diameters greater than 100 μm. However, in reality powder mixtures rarely achieve this level of ideality. Particles often contain some level of surface roughness, are rarely perfect spheres, and almost always contain some finite size distribution. Furthermore, particle sizes in powder metallurgy and other applications are often much less than 100 μm [16, 54]. Though less than ideal, researchers and engineers alike work with real powder mixtures, and their relative arrangement (packing) is of primary importance because it can greatly influence both the quasi-static and dynamic compaction characteristics.

3.2 Quasi-Static Compaction of Powders

Conventional quasi-static compaction of powders occurs at relatively low loading rates, between 10^{-5} - 10^{-1}/s, where inertial effects can be neglected [55]. This type of compaction is facilitated by the transfer of stresses (which may be σ_x, σ_y, or σ_z and do not necessarily refer to the hydrostatic component of stress discussed in the previous chapter) along particle contact points or surfaces, and generally, as applied stresses exceed some critical value (equivalent to the Brinell hardness) at the contact points, the material deforms and contacts

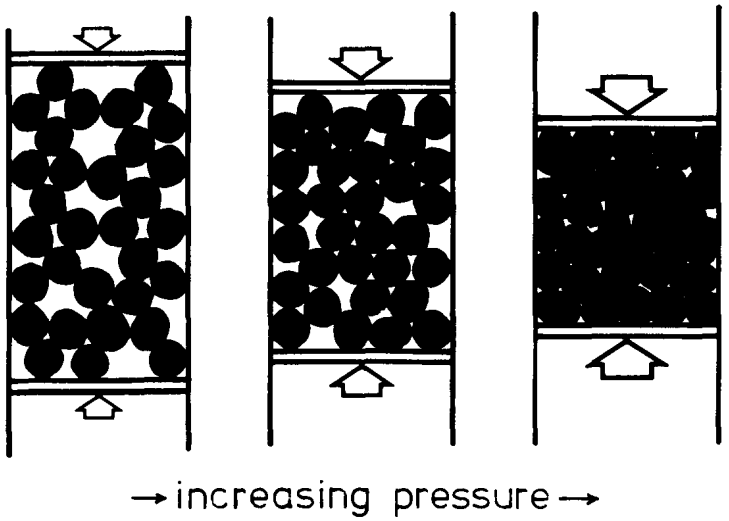

Figure 3.3: Three stages of uniaxial compaction of metal powders showing from left to right initial rearrangement, growth of contacts, and bulk deformation (from German [57]).

grow as compaction proceeds [56]. The process can be described by three distinct stages, which are shown schematically in Fig 3.3 [57].

With application of an initial applied stress, the powder configuration changes from its loosely associated state to a higher density, higher coordination configuration through the rearrangement of particles. Following rearrangement, as stress increases, the contact points between neighboring particles begin to deform and grow in number and size for ductile powders. Finally, as the applied stress increases further and contacts begin to impinge upon one another, deformation of the bulk occurs. It is supposed that all three of these processes occur simultaneously; however, each process is thought to dominate over a specific stress range [58].

At low stresses, particle rearrangement is the dominant mechanism responsible for compaction. This process is greatly influenced by extrinsic particle properties such as shape,

size, and surface roughness, and is responsible for an approximately 5 to 10 percent reduction in porosity [57]. The second stage of compaction is characterized by the growth of contact areas between particles, and Artz [59], assuming an initial random dense packing of monosized spherical powders, has developed equations to describe the increase in coordination and average contact area between particles as a function of a particle's center position. During this stage, deformation of the particles is located almost exclusively at the contact points, and as particle contacts grow, further increases in densification become more difficult. Finally, as contacts between particles begin to impinge upon one another, densification is dominated by deformation of the bulk [20]. Similar mechanisms occur for brittle ceramic powders, with the exception that during the final stage of compaction bulk deformation is replaced by particle fracture and further rearrangement [58].

One defining characteristic of quasi-static compaction is the non-existence of inertial effects. Consequently, this allows for the rearrangement of particles during consolidation, such that stresses are more evenly distributed throughout the powder network. This leads to the characteristic geometries observed for quasi-static compacts, which are comprised of straight lines of contact (2-D) and finite points of contacts (1-D) between neighboring particles [60]. An example of this configuration is shown schematically in Fig. 3.4 and is based on the results of a computational investigation by Kumar, Kumar, and Philip [61].

This investigation also demonstrated the evolution of plastic strain in the quasi-static regime, as illustrated in Fig. 3.5. Note how the strain originates at particle contact points, and grows laterally as time progresses, flattening particle contacts until the particle resembles the characteristic quasi-static hexagonal shape.

Another key aspect of quasi-static compaction are die wall effects. In uniaxial pressing, die walls not only cause localized regions of increased voids [62], but can also lead to

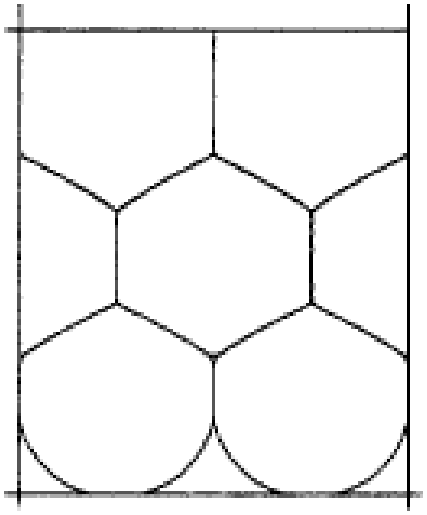

Figure 3.4: Characteristic quasi-static compact showing straight contact lines and finite contact points between particles (from Kumar [61]).

enhanced friction, causing gradients of stress and density within the compacts. If a powder of height H is compressed in a die with diameter D, as is shown in Fig. 3.6, forces must balance such that [57]

$$\Sigma F = 0 = A(P - P_b) + uF_n \tag{61}$$

where F_n is the normal force and u is the coefficient of friction between the die wall and the powder. With the incorporation of a proportionality constant, z, representing the ratio of radial to axial stress, the normal force can be written in terms of the applied stress as [57]

$$F_n = \pi\, zPDdH \tag{62}$$

where the frictional force is determined by combining Eq. 62 with the coefficient of friction as [57]

$$F_f = u\pi\, zPDdH \tag{63}$$

In the foregoing equations, dH is the thickness of the segment of powder and P is the

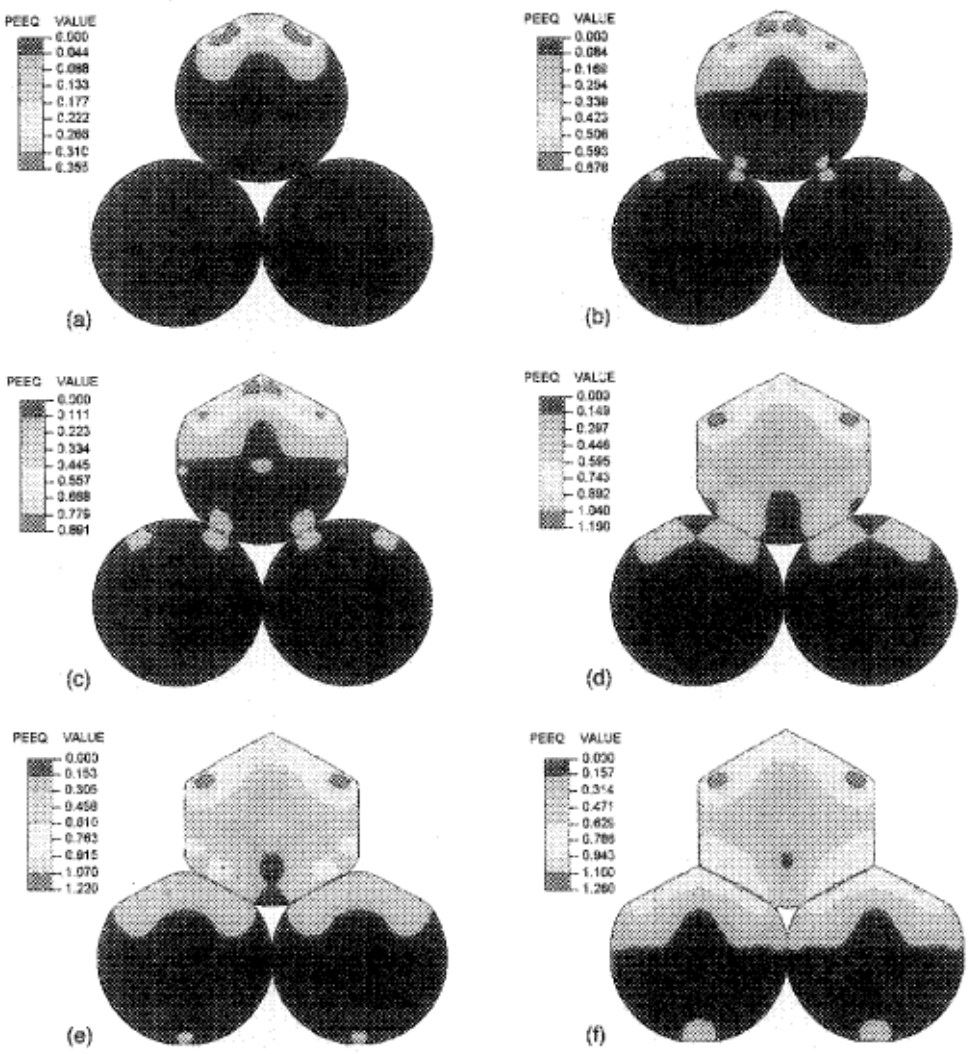

Figure 3.5: Equivalent plastic strain for compaction speed of 300 m/s at (a) 40, (b) 60, (c) 70, (d) 80, (e) 90, and (f) 100 ns (from Kumar [61]).

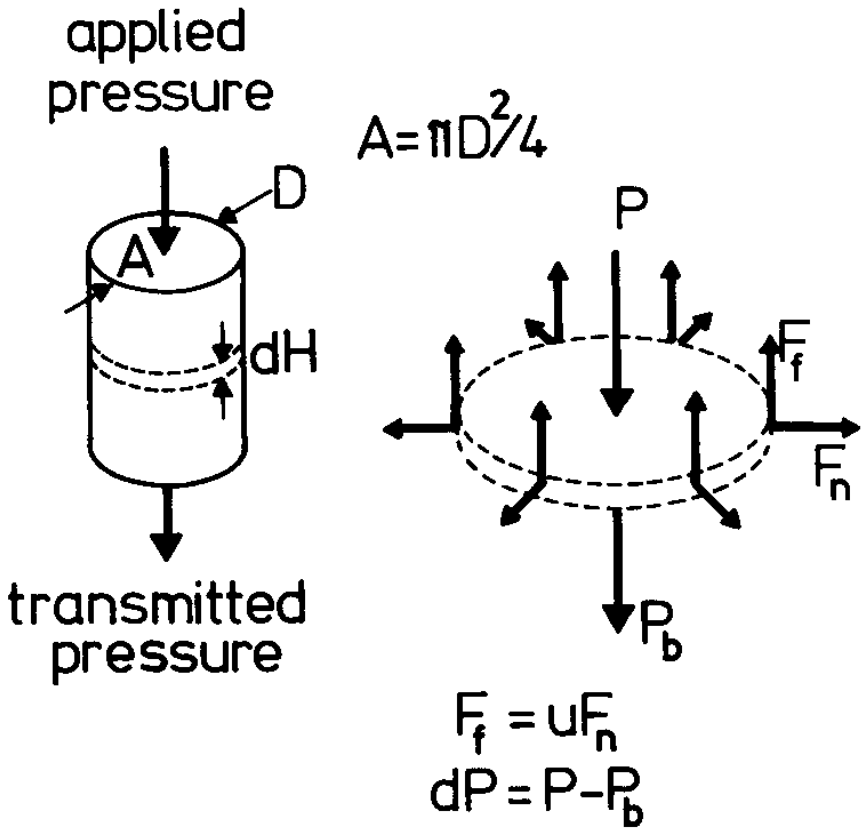

Figure 3.6: Schematic showing applied stress *P* and normal and frictional forces within a powder compact (from German [57]).

applied stress as shown in Fig. 3.6.

To minimize these effects, powders and/or dies may be lubricated and pressing geometries should be such that low height to diameter ratios are achieved. The method of uniaxial pressing (single or double action) also affects final compact density. For single action pressing, the highest densities are achieved near the mobile punch surface and decrease with distance toward the stationary punch. In contrast, for double action pressing,

the lowest densities are found in the center of the compact. This concept is shown schematically in Fig. 3.7 [63]. What is not explicitly shown in Fig. 3.7, is the difference in density variation throughout the compact thickness between pressing methodologies. For a copper powder pressed with a height to diameter ratio of one, German [57] has shown that density gradients for single and double action pressings can reach 15 and 5 percent, respectively. For powders which require specific compositional control such that lubricants may not be used, density gradients in the compact should be minimized by careful control of compact geometry and pressing methodology.

It is also important to note the relationships between applied load and resultant final compact density and structural integrity. Generally, as compaction pressure increases compact density and structural integrity tend to increase; how much depends on the intrinsic and extrinsic powder material properties. Numerous relations have been developed over the years to describe the stress-density, or compressibility, relationship for powder systems, and an excellent, though somewhat dated, review is provided by Kawikata and L*ü*dde [64]. Generally, it is observed that softer powders are compacted more readily than harder ones [65], thus for any given compaction stress a material with a higher hardness will result in a lower overall compact density. In addition to material hardness, particle size also affects the densification response, and compressibility is often found to be proportional to particle size. This results strictly from geometric considerations in that as particle size increases, the number of contact points supporting the applied load decreases, and the overall stress per contact increases. Higher stresses at the contacts leads to a greater amount of localized yielding for larger particles at lower overall applied stresses. The effect of particle size on the stress-density relationship is shown in Fig. 3.8 for an iron powder [66]. Figure 3.8 also shows the effect of particle size and applied stress on strength. For

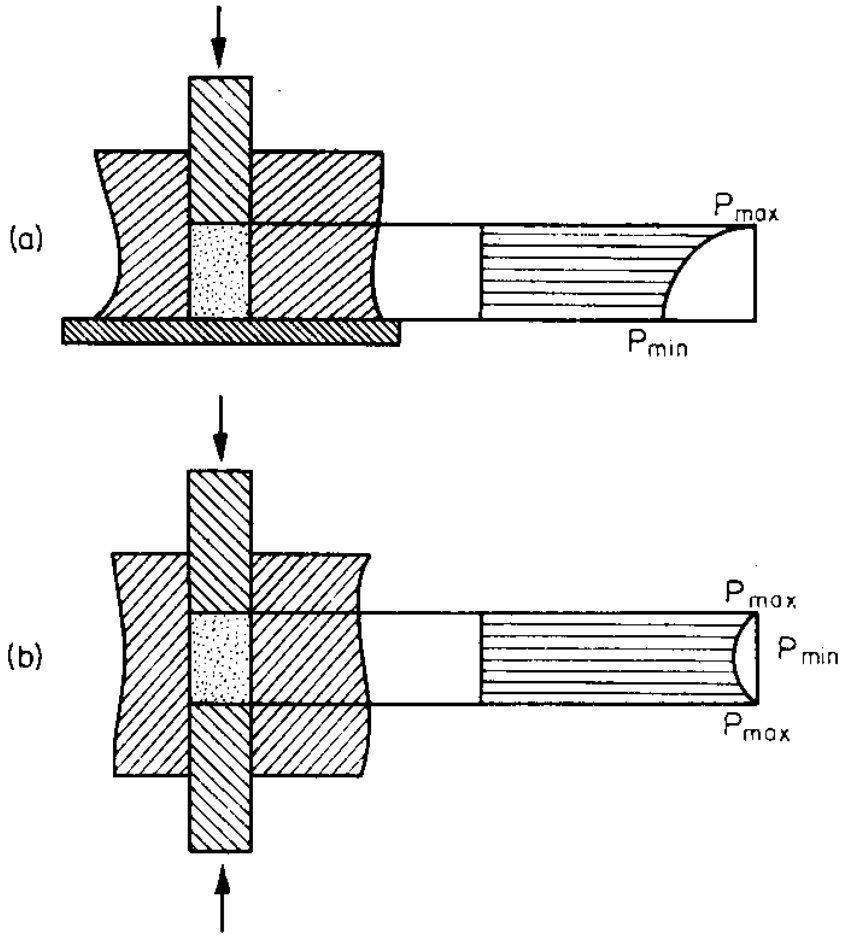

Figure 3.7: Variation in density (P) for (a) single action and (b) double action pressing (from Tsukerman [56]).

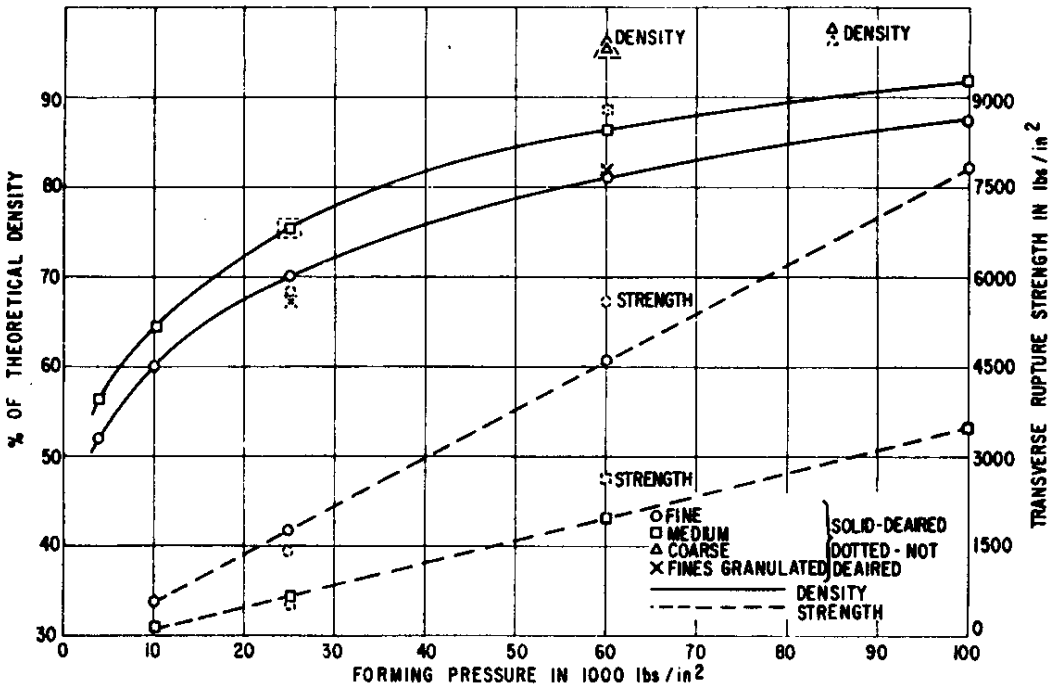

Figure 3.8: Density and strength versus forming pressure (applied stress) for hydrostatically pressed iron powder (from van Buren [66]).

a given particle size, an increase in applied stress results in an increase in compact strength. However, in contrast to its effect on density, particle size has an inverse relationship with compact strength. Thus, as particle size increases, compact strength decreases.

Particle shape also affects compact strength. For particles with identical intrinsic properties, compact strength depends largely on the average area of contacts and their respective cohesive forces, which are highly dependent on shape and surface roughness. Tsukerman [63] reports that tensile strengths for an identical composition of iron pressings with different particle structures can vary by as much as a factor of 100.

Through direct application of stress during quasi-static loading, ductile metallic powders can reach densities upwards of 90-95 % theoretical. Furthermore, ceramics and oxides, which are typically harder and more brittle than metals, can saturate at even lower densities. Under these conditions Benson et al. [60] notes that quasistatic deformation does not result in bonding between the particles even under high pressures, hence structurally sound compacts will not necessarily be produced even though densities approach theoretical. In order to achieve near full density compacts, with properties sufficient for structural applications, quasi-statically pressed compacts need to undergo further processing. For some materials, this can be a high temperature sintering process; which, for certain systems can result in unacceptable alterations in microstructures and their resultant material properties. For example, sintering at high temperatures can result in grain growth, phase transformations, and molecular decomposition or chemical reactions. Consequently, a low temperature full consolidation process is often desired; dynamic densification, or shock compaction, presents one such methodology.

3.3 Dynamic Compaction of Powders

Dynamic densification, or shock compaction, involves the consolidation of powders and porous materials through the rapid application of stresses where inertial effects dominate. Generally, this involves strain rates between 10^{-1}/s at the lower end, and up to 10^{5}/s and higher at the upper end [55]. In the high strain rate regime, the application and duration of stress is restricted to very short times, such that long distance atomic rearrangements do not have time to occur. This makes the dynamic method an attractive means of forming dense solids from powders with metastable or refined microstructures. The stresses necessary for consolidation can be generated by a number of different experimental techniques including (from low to high strain rates): standard mechanical testing, drop weight tests, Hopkinson pressure bars, rod on anvil impact (Taylor) tests, flyer plate impact, and explosive compaction. However, for true shock consolidation to occur, the velocity of the particles moving behind the compaction front must be greater than the sound velocity in the powder, effectively limiting this process to the higher velocity compaction techniques (e.g. flyer plate impact and explosive compaction) even though sound velocities in powders can be three orders of magnitude lower than those in solids [67].

3.3.1 Energy Considerations

One of the defining characteristics of dynamic consolidation which differentiates it from quasi-static compaction is the amount of energy deposited and its distribution during consolidation. For a stress P_1 applied quasi-statically, the stress-volume response of the powder body follows along the continuous path shown by the curve above the shaded region in Fig. 3.9(a). Hence, the energy deposited into the powder by loading to P_1 and unloading to zero stress is given by the shaded region in Fig. 3.9(a). Similar to the Hugoniot of the solid

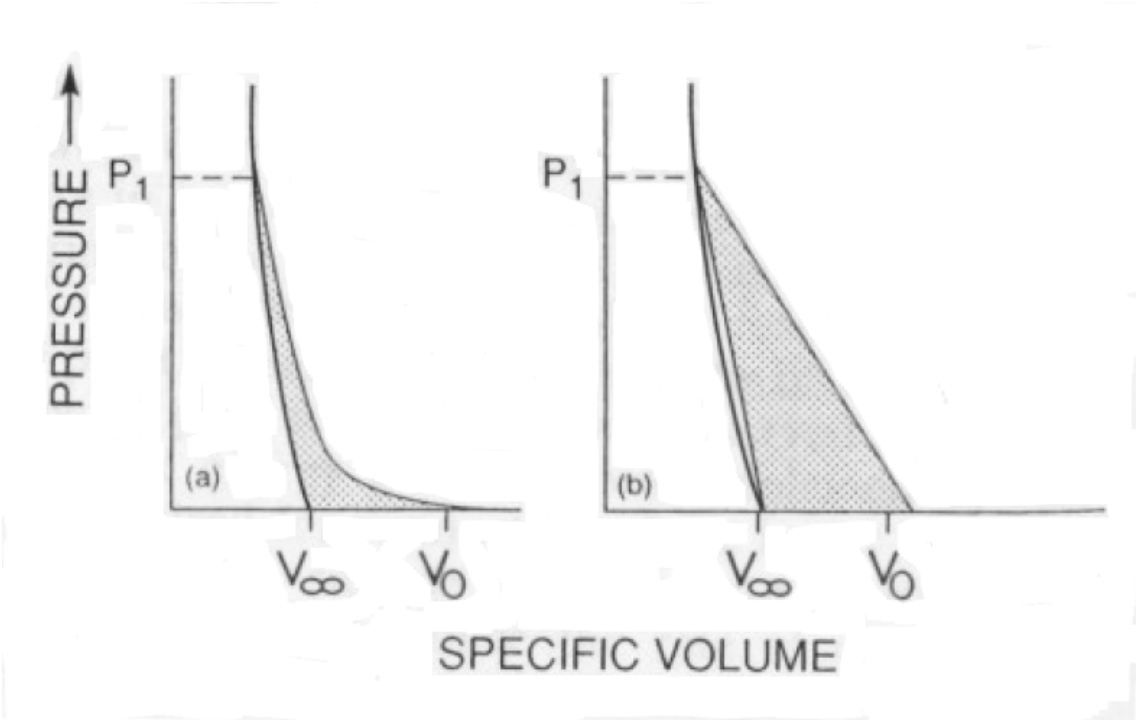

Figure 3.9: Schematic showing stress-volume relationships for (a) quasi-statically and (b) dynamically applied loads. Shaded regions indicate energy deposited during loading to P_1 and unloading(from Rosato [49]).

material (see Sect. 2.1), there also exists a porous Hugoniot which behaves in an analogous manner, and is shown schematically by the curved line in Fig. 3.9(b). For a powder body initially at volume V_0 compressed to volume V greater than the solid volume V_∞ by stress P_1, the energy deposited after unloading from the shocked state can be approximated by the shaded region in Fig. 3.9(b). Comparison of the two shaded regions in Fig. 3.9 clearly indicate that for a given applied stress, the energy deposited during shock consolidation is greater than in quasi-static compaction. Consequently, how this energy is distributed and dissipated in the porous body can greatly influence properties of the final compact.

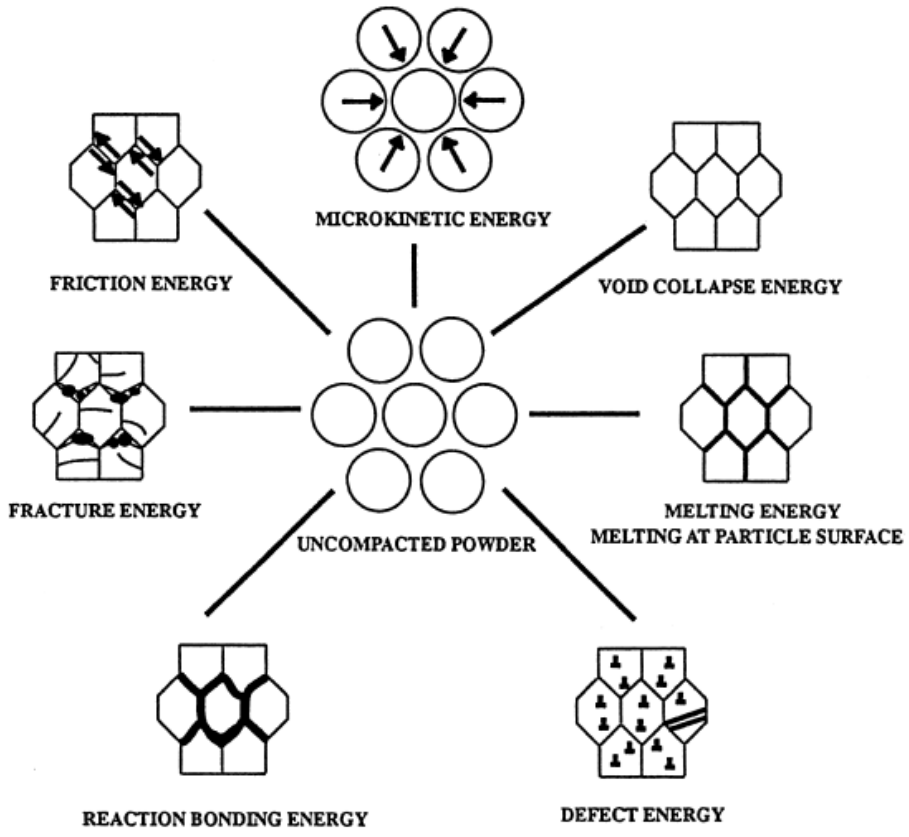

Figure 3.10: Energy dissipation mechanisms in the shock consolidation of powders(from Meyers [68]).

The dissipation of energy during dynamic (shock) consolidation is highly heterogeneous. As the compaction wave proceeds through a powder body in its loosely associated state, high amplitude stresses applied over a very short time period cause the rapid acceleration and deceleration of particles. As particles slide past and impact one another, the shock energy is transferred through particle contacts, and, depending on the magnitude of stress and the mechanical properties of the powder, can take many forms. Figure 3.10 shows some of the various forms of energy dissipation that can occur in a powder during transformation to its fully consolidated state, each of which is described below.

- *Microkinetic energy* is associated with the plastic flow occurring after complete pore collapse [11] and is responsible for the markedly different particle morphologies observed for quasi-static and dynamic compaction [60].

- *Void collapse energy* results in the rearrangement and plastic flow of particles during the complete closure of interparticle voids.

- *Friction energy* is the heat associated with particle contacts as they slide past one another during compaction.

- *Melting energy*, the energy resulting from localization of plastic flow near particle surfaces which causes melting. Gourdin [69] and Schwarz [70] have defined models to predict melting at particle surfaces based on this energy, and Williamson [71] has shown the distribution of this energy and how it results in localized temperature rises in simulated particle beds.

- *Fracture energy* is observed mainly in brittle materials, and has been shown by Thadhani et al. [72] to be particle size dependent in reactive mixtures of Ti-Si.

- *Defect energy* contributes to the formation and migration of point, line, and interfacial defects during passage of the shock, and a review of common microstructural features associated with dynamic deformation is given by Murr and Esquivel [73].

- *Reaction bonding energy* utilizes the exothermic heat release generated by reactive powders to aid interfacial bonding in inert powder mixtures.

3.3.2 Configurational Considerations

Producing not only fully dense, but also mechanically robust compacts by means of shock consolidation requires careful control of both shock loading conditions as well as intrinsic and extrinsic powder properties. In a study examining the shock consolidation of AISI 9310 steel with initial compaction stresses between 4-18 GPa, Kasiraj et al. [74] found that while fully dense compacts could be produced at the low shock stresses, ultimate tensile strength and diamond pyramid hardness of the compacts were found to increase, reach a maximum, and then decrease with increasing shock stress, indicating varying levels of interparticle bonding over the stress range investigated. In regard to extrinsic powder properties, particle size and shape have been shown to greatly influence consolidation as well as interparticle bonding.

According to Roman [75], it is not necessarily the amount of the energy expended in shock compression, but rather the nature of its distribution that exerts a governing influence on the formation of a compact. In a number of studies [27, 70, 75, 76], the effect of particle size on the distribution of shock energy has been investigated. Considering geometry alone, as particle size decreases, the number of contact points increases, and the distribution of compaction energy in the powder compact becomes more uniform. Consequently, a more uniform energy distribution results in a reduction in localized plastic flow, such that compacts composed of smaller particles require greater total energy input to reach a given density and level of interparticle bonding [75]. As particle size increases, so too does energy localization at contact points, and this can lead to increased temperatures and material flow for larger particles [71] which can lead to melting and strong interparticle bonds.

An opposing viewpoint is offered by Rusnak [76]. In studying the compaction behavior of fine and coarse copper powders, Rusnak [76] found that greater energies are required to

consolidate coarser copper powders. However, in Rusnak's work, energy is defined in terms of the total kinetic energy of the incoming projectile, while in most other investigations [27, 70, 75] energy is defined in terms of the total energy behind the shock front, given by Eqn. 3. The disparity in energy definition, as well as the relatively low velocity (≈91m/s) at which Rusnak's experiments were performed may lead to his opposing viewpoint; it is generally agreed upon that larger particles require less total energy to reach a given density and level of interparticle bonding than smaller particles during dynamic consolidation due to stresses being localized at fewer contact points.

The effects of particle shape on the consolidation behavior of powder mixtures has been studied to a lesser extent. Using direct numerical simulation, Benson [77] has shown that morphology does not significantly affect the bulk shock velocity - particle velocity relationship in beds of idealized cylindrical and rectangular copper powders. However, his work does show that micromechanical phenomena, like turbulent flow, is morphology dependent. As shown in Fig. 3.11, a constant velocity (1 km/s) boundary condition is applied to the upper boundary of the initial powder configuration and travels in the downward direction, which results in the deformed microstructures shown in Fig. 3.11. Also observed in Fig. 3.11 is the preferential deformation experienced by the rectangular particles which is not observed for the cylinders. This suggests that inhomogeneous distributions of interparticle bonds may be more readily observed as particle shape deviates from spherical.

Evidence supporting this suggestion is offered by Thadhani [78] who finds that irregularly shaped powder mixtures of Ti-Si promote plastic deformation and flow during consolidation. Examining the simulated response of experimental microstructures of spherical Ni + spherical Al and flake Ni + spherical Al, Eakins and Thadhani [79] have shown configurationally dependent variations in compressional response; results from this work are

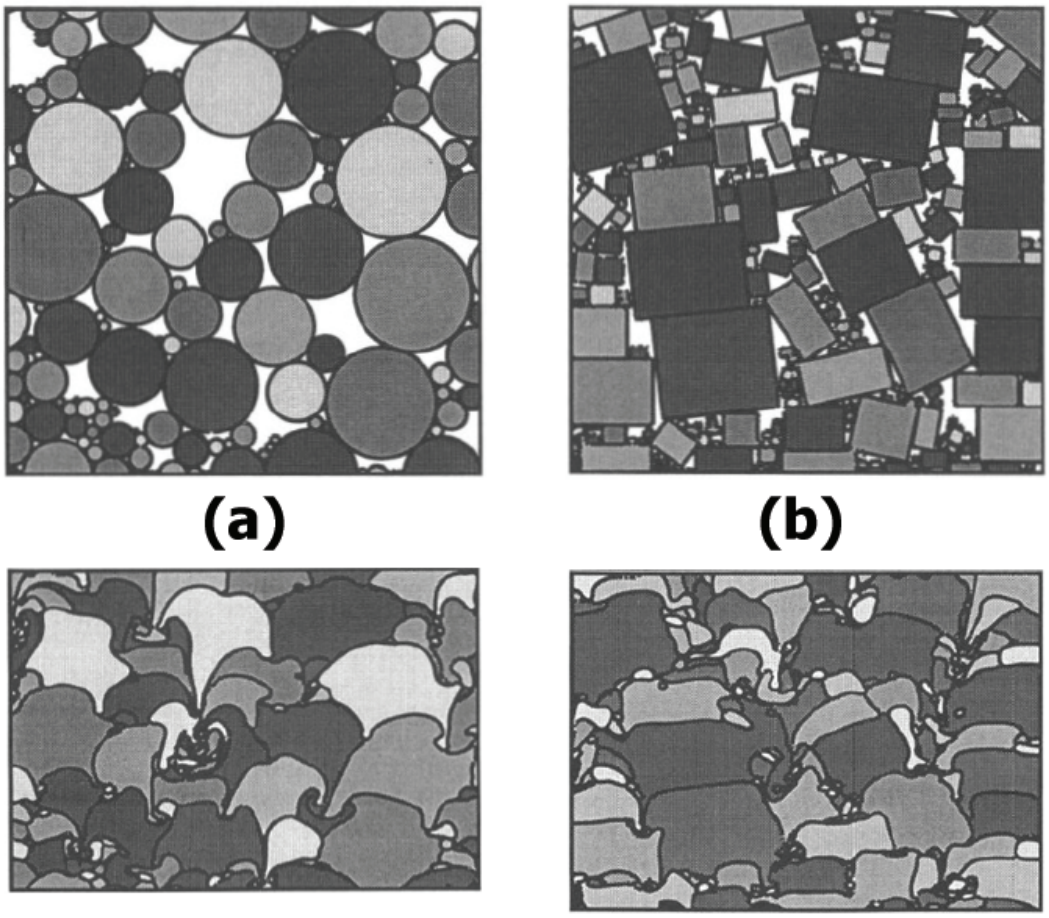

Figure 3.11: Two-dimensional simulated microstructures showing (top) initial conditions of copper (a) cylinders at initial porosity of 19% and (b) rectangles at 16% initial porosity. Deformed images (bottom) show microstructures following imposition of a shock wave with particle velocity 1 km/s (from Benson [77]).

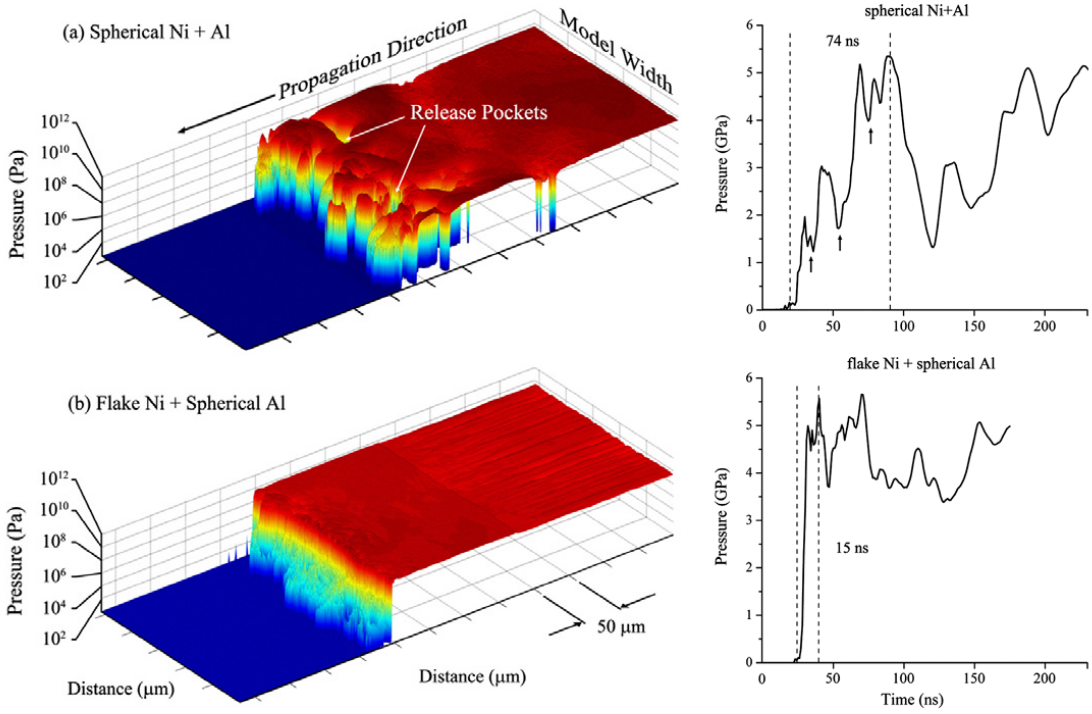

Figure 3.12: Comparison of stress surfaces and stress profiles for 45% TMD (a) spherical Ni+Al and (b) flake Ni + spherical Al at a particle velocity of 1 km/s (from Eakins [79]).

given in Fig. 3.12.

Notice the distinct difference in both the character and duration of the shock fronts between the two mixtures. The mixture composed entirely of spherical particles shows a very disperse shock front with a characteristic rise time of approximately 74 ns. In stark contrast, the mixture containing flakes shows a very distinct shock front with a much shorter rise time. The main factors governing variation in shock response are the size and location of void space. The spherical mixture is comprised of large voids, on the order of the particle diameter (tens of microns), which cause significant reflections and release waves during consolidation. In the flake mixture, void space is located primarily between the Ni flakes and is found to be no more than 600 nm thick, such that upon application of stress,

void closure can occur rapidly, resulting in increased shock stability in flake mixtures even at low densities.

Up to this point, basic ideas concerning particle packing and rearrangement as well as some of the more fundamental aspects of quasi-static and dynamic compaction have been introduced. In the next few sections, the focus shifts toward various methods of determining the high stress equation of state for particulate materials.

3.4 Equations of State for Particulate Materials

Section 2.5.5 has shown how the incorporation of even the slightest amount of porosity limits the predictive ability of the Hugoniot mixture models presented, see Fig. 2.5. In this section, several different methods for explicitly incorporating distention (porosity) into an equation of state are presented. This will be followed by a re-examination of the mixture models and material system examined in Sect. 2.5.5, with the explicit incorporation of porosity.

In addition to configurational considerations, one of the more distinct differences between distended and solid materials is the amount of energy dissipated at a given stress. If, for a moment, the temperature/entropy term in the first law of thermodynamics is disregarded, the change in internal energy for a system undergoing compression can be represented simply as $dE = -\sigma\, dV$, where here σ represents the mean hydrostatic stress (pressure) applied. For a material with initial solid volume V_0 and corresponding distended volume V_{00}, where $V_{00} > V_0$, a greater amount of energy is dissipated for the distended material at a given stress resulting from the larger dV term. The greater reduction in volume, in conjunction with the finite amount of energy required to eliminate voids and surfaces in

the distended material, results in a Hugoniot that is offset from that of the solid. An example of this is shown in Fig. 3.13; note the size of the shaded areas which are representative of the specific internal energies imparted into the solid and distended systems by passage of a shock of similar magnitude σ_H. Also, at stress σ_H one can see that the distended material is at a greater specific volume than that of the solid. For a solid and distended material to reach the same volume, V, the stress in the distended material must be greater than in the solid, as shown in Fig. 3.13. In this section several different formulations are presented for incorporating porosity into a general equation of state, which could be for a single component system or mixture. These formulations serve to extrapolate the distended Hugoniot from that of the solid through either an isobaric or isochoric approach.

3.4.1 Isochoric Approach

A convenient method of predicting the Hugoniot response of particulate (porous or distended) materials is by using the Mie-Grüneisen equation of state to offset the solid Hugoniot curve by some increment of stress at a constant volume, i.e. along an isochoric path. Again, σ represents the mean hydrostatic stress (pressure) applied to the system. If the Hugoniot of the solid material is chosen as the reference state, the Mie-Grüneisen EOS takes the form

$$\sigma_P = \sigma_H + \frac{\gamma}{V}(E_P - E_H) \tag{64}$$

where the subscripts P and H denote values taken along the distended and solid Hugoniots. Inherent in this formulation is that the Grüneisen coefficient γ does not change appreciably from its value for solid materials with the additional energy (temperature) associated with the consolidation of particulate materials. McQueen and co-workers [1] have shown this to be the case as they found little variation in γ with temperature, such that Eq. 12 holds true

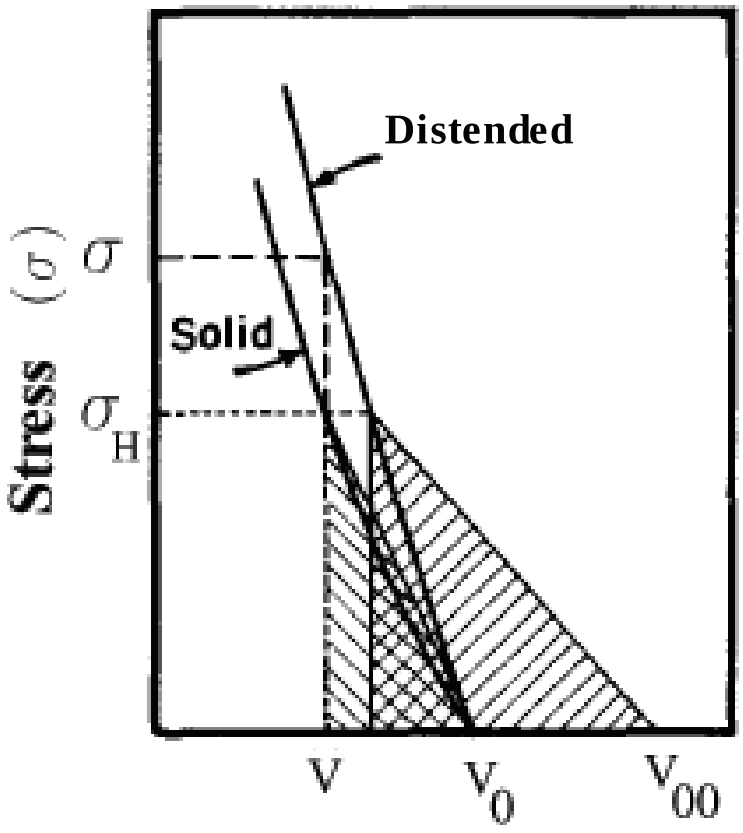

Figure 3.13: Schematic of the porous and solid Hugoniot for a material, where the shaded areas under the Rayleigh lines show the energy input to reach a given stress (from Meyers [15]).

for particulate materials.

In choosing the Hugoniot of the solid as the reference state, one can completely describe the stress and energy along this reference state (σ_H, E_H) using Eqns. 1 - 3 and Eq. 4. If the reference energy for the particulate material is set to zero, the internal energy imparted by a shock of magnitude σ_P can be represented as

$$E_P = (1/2)\sigma_P(V_{00} - V) \tag{65}$$

Using these relations, the equation for stress as a function of volume in a porous material can be written as [15]

$$\sigma_P = \frac{[2V - \gamma(V_0 - V)]C_0^2(V_0 - V)}{[2V - \gamma(V_{00} - V)][V_0 - S(V_0 - V)]^2}. \tag{66}$$

In Eq. 66 it should be noted that $\gamma = \gamma(V)$ where the ratio γ/V is assumed constant. Using this relation, one can construct Hugoniots for different initial density configurations simply by changing the parameter V_{00}. It should be noted that this formulation assumes the porous material has a crush strength of zero; that is, at any stress $\sigma > 0$ the volume changes from its initial volume V_{00} to the initial volume of the solid V_0. As initial density decreases, the calculated distended Hugoniots shift further and further from the solid Hugoniot, and at some critical distention, it begins to exhibit an anomalous behavior where increases in stress result in decreases in density. This behavior occurs when the ratio of initial density of the distended material to that of the solid reaches [80]

$$\frac{\rho_{00}}{\rho_0} = \frac{\gamma}{2 + \gamma} \tag{67}$$

The anomalous behavior is shown schematically as the right most Hugoniot curve in Fig. 3.14. For many materials this occurs for initial densities at or below 50% theoretical

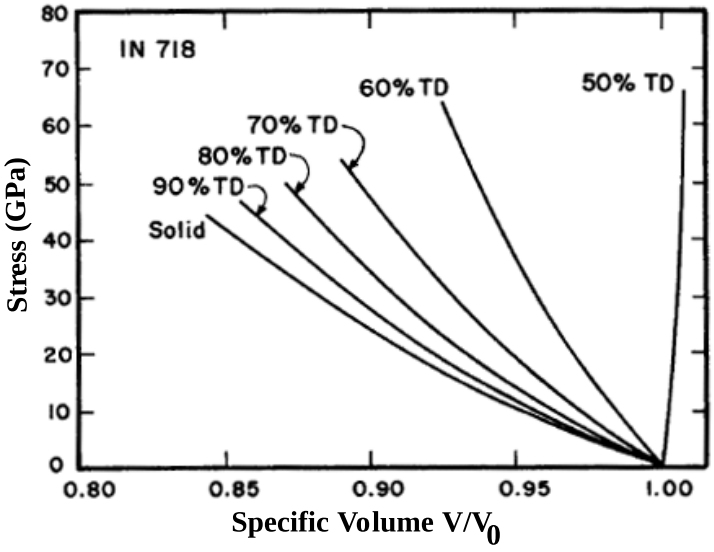

Figure 3.14: Predicted Hugoniots for Inconel 718 at different initial theoretical densities (TD) (from Meyers [15]).

density. This anomalous behavior is thought to result from the increased role that thermal stresses play during consolidation of highly distended and porous materials.

To examine the roles of the cold (isothermal) and thermal stresses during compaction, Zeldovich and Raizer [81] developed a framework for an EOS that deals explicitly with both the cold and thermal components. Similar to the previous case, this approach [81] also operates under the constant volume approximation such that the Mie-Gr*ü*neisen EOS may be used. Here the total internal energy in the porous or distended material is denoted by Eq. 65 and is separated into cold and thermal components via Eq. 30. The constant volume approximation is incorporated through the definition of thermal energy $E_T = \sigma_T/\rho\,\gamma$, which after appropriate substitution and rearrangement of E_T and Eq. 30 into Eq. 65 results in a Hugoniot for a distended material of the form [81]

$$\sigma_P(\rho, \rho_{00}) = \frac{2\sigma_C/\gamma - 2\rho\, E_C}{2/\gamma - \rho/\rho_{00} + 1} \tag{68}$$

where the subscript C represents properties on the cold curve. This equation is general in the sense that no specific relations for σ_C and E_C are given. Simons and Legner [14] propose a piecewise formulation for Eq. 68. At high stresses, they suppose thermal terms dominate, such that the elastic (cold) components need only be accurate at low stresses. Their simplified equation neglects higher order terms for the elastic energy and shows moderate success in describing the Hugoniots of materials with initial densities as low as 42% theoretical density. However, similar to the previous constant volume based approach this model also assumes that the material's crush strength is zero and does not describe well the low stress data.

Extending this work, Petrie and Page [13] modified the Kawikata [64] equation (which is used to represent the cold compaction curve at low stresses) to asymptotically approach the solid density at high stresses. Their modified Kawikata equation [13]

$$\rho = \rho_{00}\left(\frac{1 + b\sigma_C}{1 + ab[(K - \sigma_C)/K]\sigma_C}\right) \tag{69}$$

appropriately bridges the cold (low stress) and thermal (high stress) components into a single continuous curve. The variables to be solved for in Eq. 69 are the initial density and stiffness parameters ρ_{00} and b. Here K is the bulk modulus of the material and a is assigned the value $a = \rho_{00}/\rho_{S0}$ where ρ_{S0} is the initial density of the solid material at zero stress. Utilizing the work of Carroll and Holt [9] to describe the effective area on which stresses act through the parameter $\alpha = V/V_S$, where V_S is the volume of the solid, Petrie and Page [13] modified Eq. 68 to account for the associated increase in stress applied to the actual solid component:

$$\sigma_P(\rho, \rho_{00}, \alpha) = \frac{2\alpha\sigma_C/\gamma - 2\rho\, E_C}{2\alpha/\gamma - \rho/\rho_{00} + 1}\ . \tag{70}$$

By incorporating the idea of apparent density, they removed the anomalous behavior that

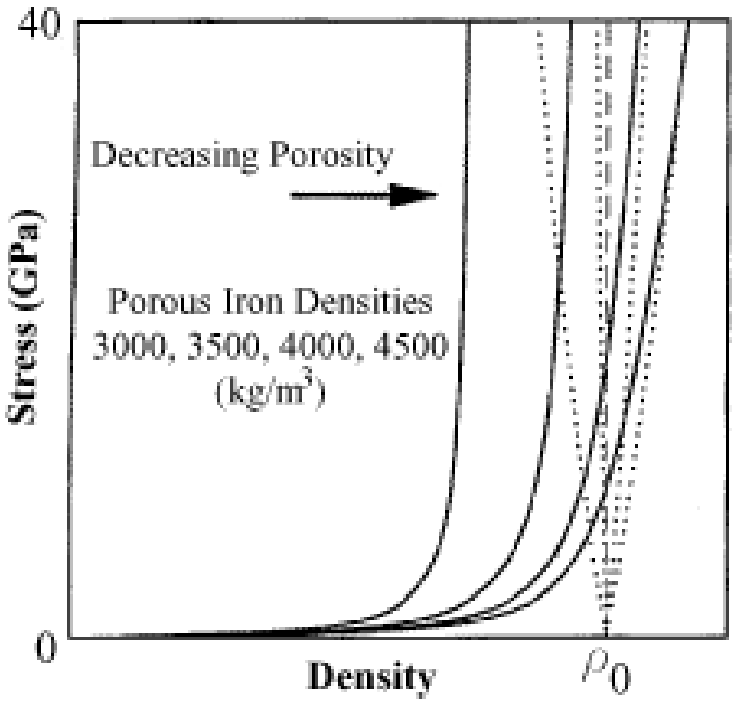

Figure 3.15: Predicted Hugoniots for different initial densities of Iron using approach of Petrie and Page (solid) and Simons and Legner (dotted) (from Petrie and Page [13]).

predicts a decrease in density with an increase in stress. This approach also is unique with respect to the previous two model formulations in that it does not assume a zero crush strength for the material; rather it accounts for the crush up to solid density through the modified Kawikata equation. A schematic showing the anomalous Hugoniot response predicted by Simons and Legner [14] and the non-anomalous behavior of Petrie and Page [13] is shown for porous iron at different initial densities in Fig. 3.15.

3.4.2 Isobaric Approach

The isobaric approach differs from that previously presented in that it uses a constant (hydrostatic) stress approach to extrapolate the distended Hugoniot from that of the solid.

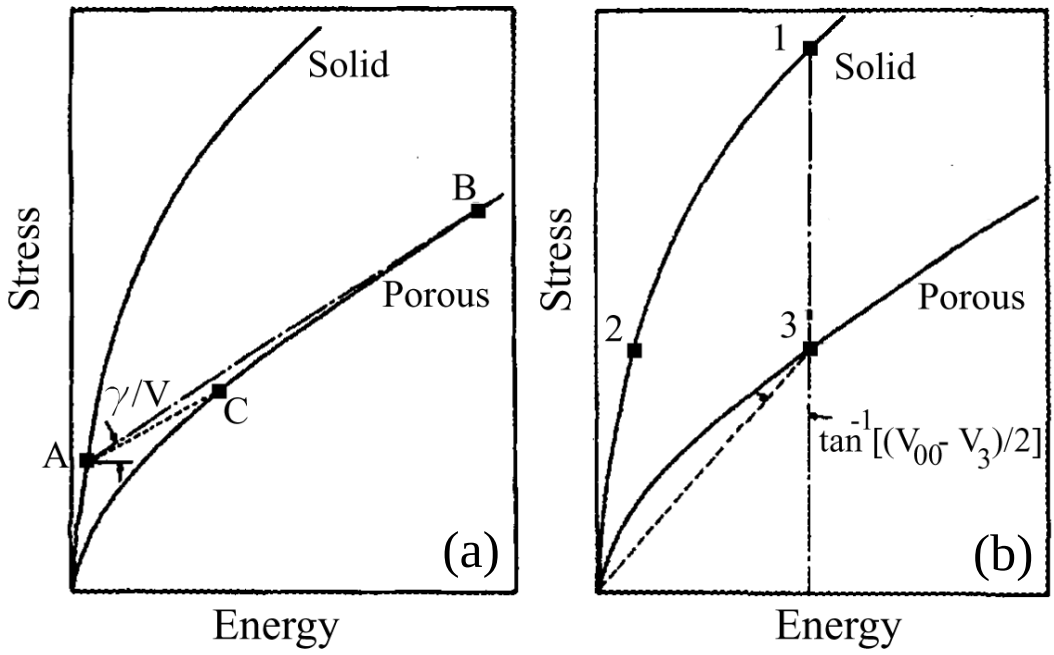

Figure 3.16: Distended Hugoniot prediction based on (a) isochoric and (b) isobaric approach in the σ-E plane (from Oh and Persson [82]).

In the previous approach γ was assumed to be a function of volume only such that Eq. 12 holds, and for materials with very different internal energies (e.g. solid and highly distended materials) small uncertainties in the Grüneisen coefficient can lead to large discrepancies in extrapolated distended Hugoniots. This concept is shown schematically in Fig. 3.16(a), where the points A on the solid Hugoniot and B on the distended Hugoniot have the same volume. As density decreases, the slope of the distended Hugoniot in the σ-E plane flattens out, and even the slightest change in stress will result in substantial changes in internal energy. From Eq. 9 the slope of A-B is γ/V, such that a slight reduction in γ from its actual value can result in an extrapolation of A to point C, not B, an effect that is magnified as porosity increases. In an effort to reduce the uncertainties associated with extrapolating a distended Hugoniot at constant volume which relies on an accurate γ function, Oh and

Persson [82] used an isobaric approach to develop the approximate equation of state for a powder

$$\left(\frac{\partial E}{\partial V}\right)_P \approx -\left(\frac{\partial E}{\partial V}\right)_H \tag{71}$$

where the subscripts P and H denote that derivatives are taken along the distended and solid Hugoniots. Using this crude approximation, which requires the U_S-u_P relationship for the solid to be linear, the extrapolation of a point on the distended Hugoniot (point 3 in Fig. 3.16(b)) is determined through the angle $tan^{-1}[(V_{00} - V_3)/2]$ which is far less sensitive to uncertainties than γ/V. By specifying the state points on the solid and distended Hugoniots such that

$$E_1 = E_3 \tag{72}$$

$$P_2 = P_3 \tag{73}$$

Eq. 71 results in

$$V_3 - V_2 \approx V_2 - V_1 \tag{74}$$

where the meaning of the subscripts are shown in Fig. 3.16(b). Using the jump equations with the conditions σ_1 and $\sigma_2 > \sigma_0$, E_1 and $E_2 > E_0$, and $E_3 > E_{00}$, the following relations for stress and energy at each state point are defined [82]

$$\sigma_1 = C_0^2(V_0 - V_1)/[V_0 - S(V_0 - V_1)]^2 \tag{75}$$

$$\sigma_2 = C_0^2(V_0 - V_2)/[V_0 - S(V_0 - V_2)]^2 \tag{76}$$

$$E_1 = \frac{1}{2}\sigma_1(V_0 - V_1) \tag{77}$$

$$E_2 = \frac{1}{2}\sigma_2(V_0 - V_2) \tag{78}$$

$$E_3 = \frac{1}{2}\sigma_3(V_{00} - V_3)\,. \tag{79}$$

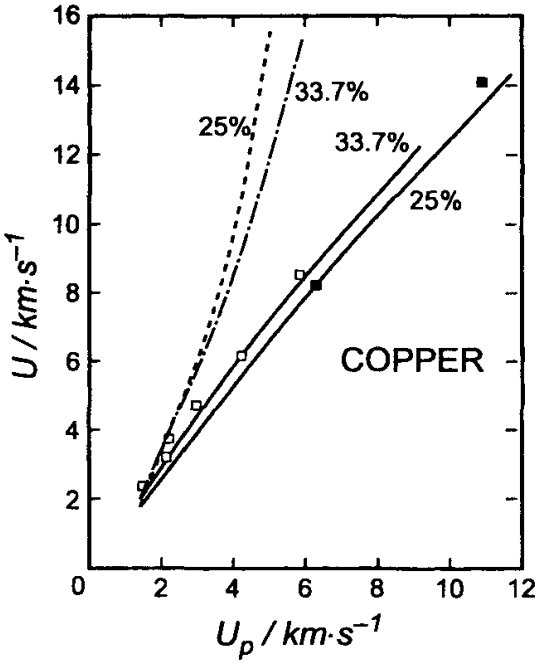

Figure 3.17: Hugoniot predictions for distended copper at 25% and 33.7% theoretical density, showing improvement of isobaric approach (solid lines) over isochoric approach (dotted lines) (from Oh and Persson [82]).

Equations 72-79 serve as a system of eight equations with nine unknowns, which may be solved simultaneously to determine the distended Hugoniot if one of the unknowns is specified and the remaining eight are determined. The strength of the isobaric approach is exemplified when describing the Hugoniots of highly distended materials, those whose initial densities fall below the limit of anomalous behavior for the isochoric approach given by Eq. 67. A comparison of the isochoric and isobaric predictions for distended copper at 25% and 33.7% theoretical density is shown in Fig. 3.17, where the isobaric approach clearly approximates the experimental data much better than the isochoric approach.

An alternative isobaric approach which extrapolates the distended Hugoniot from the

zero Kelvin isotherm is offered by Wu and Jing [83]. In their approach, a point along the distended Hugoniot (point A in Fig. 3.18) can be determined precisely if the σ-V relationship along the zero Kelvin isotherm is known. In a manner analogous to the isochoric approach which relates stress and energy through γ at constant volume through the Mie-Grüneisen EOS, the isobaric approach of Wu and Jing [83] relates volume and enthalpy through the parameter R at constant (hydrostatic) stress through the relation

$$V - V_C = \frac{R}{\sigma}(H - H_C) \tag{80}$$

which after differentiating with respect to enthalpy at constant stress gives the leftmost term of Eq. 81

$$R = \sigma \left(\frac{\partial V}{\partial H} \right)_\sigma = \frac{\sigma \gamma}{K_S} = \frac{\sigma \gamma}{\rho C^2} \tag{81}$$

In the foregoing equations the subscript C indicates values along the zero Kelvin isotherm, H is enthalpy, γ is the Grüneisen coefficient, K_S is the isentropic bulk modulus, and C is the sound speed at density ρ. The model assumes specific heat at constant stress (pressure) C_P is constant, such that through application of the appropriate thermodynamic relations one can derive the two rightmost definitions of R, the parameter relating two volume and enthalpy states at constant stress.

Equation 80 is general in the sense that it can relate both the solid and distended Hugoniots to their respective zero Kelvin isotherms, and Wu and Jing [83] define an effective R such that it describes both the solid and distended materials. Operating under the assumption that specific internal energy for the distended and solid materials is the same, and incorporating the elastic-plastic effect often observed during the compaction of distended

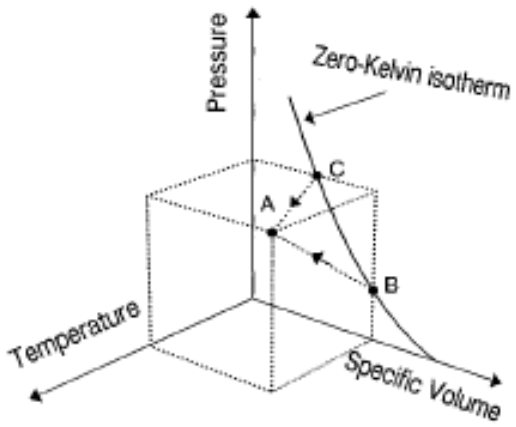

Figure 3.18: Schematic illustrating that state point A along distended Hugoniot can be determined along isobaric (C-A) and isochoric (B-A) path. (from Wu and Jing [83]).

materials the equation for the porous Hugoniot is found to be [83]

$$V'_H = \frac{1-(R/2)}{1-(R/2)[1-(\sigma_1/\sigma)]}V_H + \frac{(R/2)}{1-(R/2)[1-(\sigma_1/\sigma)]}\left((V_1 - V_0) + \frac{\sigma_1}{\sigma}V_{00} + \frac{1-R}{(R/2)}(V'_C - V_C)\right) \tag{82}$$

where the prime denotes quantities for the distended material and terms with the subscript $'1'$ are values taken at the Hugoniot elastic limit of the distended material. From Eq. 82 it is shown that one needs σ-V relations for the solid Hugoniot as well as along the zero Kelvin isotherms of the distended and solid materials. For many solids, an accurate representation of the Hugoniot is given by

$$\sigma_H = \frac{C_0^2(V_0 - V)}{[V_0 - S(V_0 - V)]^2} \tag{83}$$

which was defined previously in Sect. 2.1. To define the zero Kelvin isotherm of the solid V_C, Wu and Jing [83] use the Born-Mayer potential [40]; however this relation may also be determined using the methodology presented in Sect. 2.3. The distended cold curve is

defined in terms of the solid cold curve through the distention parameter α as

$$V_C' = \alpha_C \, V_C \tag{84}$$

where α_C is defined in the manner put forth by Carroll and Holt [10] which gives $\alpha_C \approx \alpha_0$ for $\sigma < \sigma_{crit}$, and $\alpha_C \approx 1/[1 - exp(-3\sigma/2Y)]$ for $\sigma > \sigma_{crit}$, where $\alpha_0 = V_{00}/V_0$ and $\sigma_{crit} = (2/3)Yln(\alpha_0/(\alpha_0 - 1))$. Here σ_{crit} is the critical stress at which plastic deformation occurs, and is Y is the yield strength of the solid material. By defining distention through α_C, the model specifically incorporates the crush up response in the incomplete compaction region observed in many distended materials at low stresses. At this point, all that is left to define are specific relations for the Grüneisen coefficient and the isentropic bulk modulus. Wu and Jing [83] define γ using the Dugdale-MacDonald [31] relation given in Eq. 11 for the cold curve, which relates $\gamma = f(V_C)$ and inherently also yields a relation for $\gamma = f(\sigma)$. The isentropic bulk modulus K_S is given as [83]

$$K_S = \frac{\sigma\,\gamma}{2} - \frac{d\sigma}{dV_H}\left(V_H - \frac{\gamma}{2}(V_0 - V_H)\right) \tag{85}$$

where σ is that given by Eq. 83. In defining γ and K_S as such, both γ and K_S are defined from $\sigma = 0$ up to some finite value of stress. However, the volume increment over which the corresponding stresses are determined differs for γ and K_S in that $\gamma : V_{0K} \rightarrow V$ and $K_S : V_{0H} \rightarrow V$ where $V_{0K} < V_{0H}$. This can lead to anomalous behavior of the model at low stresses, and care must be taken when applying this model in the extremely low stress regime.

3.4.3 Comparison of Porous Equations of State

When determining which type of model is best suited to describe/predict different distended material Hugoniots, one must examine the full range of initial and final conditions of the

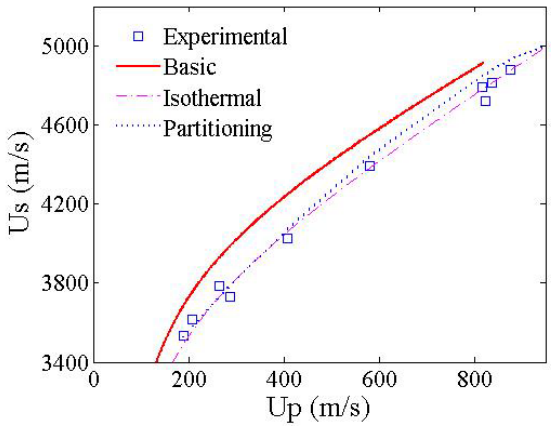

Figure 3.19: Porous EOS predictions for mass averaged, isothermal, and energy partitioning mixture routines compared with experimental data on Elkonite 10W3.

system to be modeled, as well as the assumptions under which each model is developed. For materials with low initial distentions (below the limit given by Eq. 67), an isochoric approach may be best suited; however in choosing an isochoric approach one must also consider the stress range at which compaction is being modeled and whether or not material strength effects need be to be taken into account. As initial distention (porosity) increases the isobaric approach becomes more desirable, as shown in Fig. 3.17. Also of importance is the stress range over which the model has been validated. Of the models presented, none consider electronic contributions, and as such they should only be applied up to stresses at which the electronic contributions to material response are small enough to be neglected (up to several hundred GPa).

Returning to the example presented in Sect. 2.5, after distention is explicitly incorporated into the mixture models used to describe the Elkonite system the models more closely predict experimental results as can be seen by comparing Fig. 3.19 with Fig. 2.5. As distention in the Elkonite system is low, the Mie-Gr*ü*neisen isochoric approach (Eq. 66) is chosen

to incorporate porosity in the basic mass averaged and isothermal mixture Hugoniots, while for the energy partitioning model, distention is incorporated through the parameter φ given in Eq. 56. Similar to the non-distended predictions, after the inclusion of distention the basic mass averaged EOS is again the furthest from predicting experimental results. This results from the crude approximations under which the mixture model was developed, and is not a result of the isochoric Mie-Gr*ü*neisen extrapolation. The energy partitioning and isothermal predictions overlap at material velocities up to $\approx$ 400 m/s, at which point the isothermal prediction continues to follow the experimental data closely while the energy partitioning model diverges to slightly higher predicted shock velocities. Thus, for the mixture models presented in Sect. 2.5.5, the isothermal mixture method of McQueen and co-workers [1] seems to best replicate the experimental results.

Furthermore, the isochoric model used to incorporate porosity into the Elkonite system did not account for any elastic-plastic behavior which may have occurred during consolidation, and assumes the distended material fully densifies at any stress greater than zero. These types of models work well for predicting the dynamic response of initially distended materials at higher stresses, where full compaction has occurred. However, at lower stresses where the material is still in the incomplete compaction regime, models which do not explicitly incorporate the crush-up response yield predictions that are far from experimentally observed results.

In instances where the crush response is of interest, one would want to choose a model for the distended EOS that explicitly incorporates this response, such as the isochoric approach put forth by Petrie and Page [13] or the isobaric approach of Wu and Jing [83]. Alternatively, one might want to examine the various compaction models used to explicitly describe the process of consolidation to full density. The next chapter focuses solely

on these types of compaction models, which might be combined with an EOS that does not specifically incorporate the crush-up response of a material to yield a complete σ-V response at both low and high stresses.

CHAPTER IV

COMPACTION MODELS AND THEIR COMPARISON

The compaction of powders to full density is a complex process in which it has been shown that both intrinsic and extrinsic powder properties play a major role. For a model to completely describe the intricacies of compaction, it would have to contain an unreasonably large number of fitting parameters, i.e. a parameter to describe shape effects, strength effects, surface effects, etc., and application of this type of model would be extremely cumbersome, even with the aid of modern computational procedures. As such, certain simplifying assumptions about the compaction behavior are made when attempting to quantify the compaction process into a model. Furthermore, application of any compaction model to a material system outside of the scope under which its respective simplifying assumptions are made can lead to poor fits between the models and experimental data [84].

Two quasi-static compaction models, one developed for ductile metal powders (P-σ_Y) [20] and the other for brittle ceramic powders (P-P_{Act}) [58] are examined below. Next, the slightly more complex phenomena of dynamic compaction is described, including the popular P-α model [5], which treats powder particles and void space as a single homogeneous media, and the more recent P-λ model [12], which takes into account individual constituent material properties. This chapter concludes by discussing similarities, differences, and limitations between the various compaction models. It should be noted that all of these models were developed to describe the pressure-density or pressure-volume

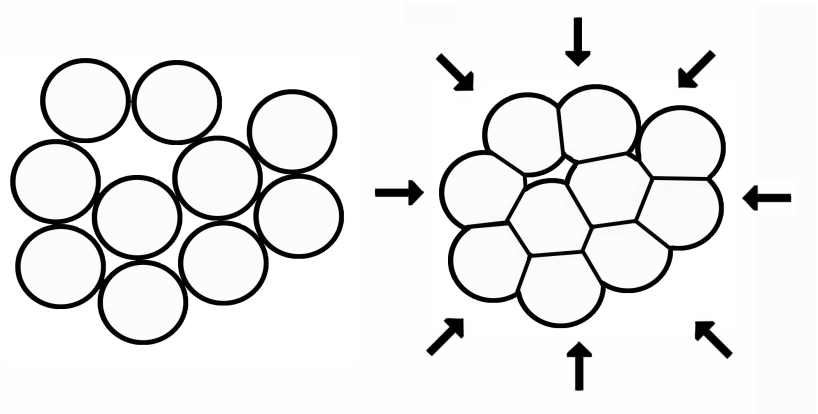

Figure 4.1: Initial configuration of particles after rearrangement has occurred (left), and after the application of an applied stress (right), showing growth of the contact points/areas.

response of porous or distended materials. As such, the definition of stress in this chapter refers to the mean hydrostatic stress applied to the distended materials. As a naming convention, the variable $'P'$ is used to define the mean hydrostatic stress is in these models.

4.1 The P-σ_Y Model

The P-σ_Y model, originally developed by Fischmeister and Artz [20], is a physically based model that describes the compaction of powders during the latter two stages of compaction, through contact point and bulk deformation mechanisms. The model attributes the gradual increase in resistance to densification observed in powder mixtures to the following phenomena: growth of contact areas between neighboring particles, creation and growth of additional contact areas, and the increasing constraint under which particles deform as densification proceeds. Assumptions in this model include, (a) the powder is composed of monosized spheres at an initial random dense packing of $\approx 0.64\%$, and (b) initial deformation and densification occurs after the complete rearrangement of particles has occurred. The full model is formulated into two sub models, and the first operates under the assump-

tion that growth of contact points occurs independently and without influence from neighboring contacts. The first sub model is termed the model of unconstrained deformation, and a schematic showing the growth of contact points in this region is shown in Fig. 4.1. The model of unconstrained deformation takes the form [20]

$$P_S(\rho) = \frac{3}{4\pi}\frac{a(\rho)Z(\rho)}{R^2}\rho\ \sigma_Y(\rho) \tag{86}$$

Here, P_S is the stress necessary to achieve compaction to a given relative density ρ, $a(\rho)$ and $Z(\rho)$ are the average contact area and coordination of the particles, R is the particle radius, and $\sigma_Y(\rho)$ is the yield strength of the contacts. The model of unconstrained deformation is shown to work well for densities up to $\approx 90\%$ theoretical maximum density (TMD); however, with further densification the impingement of neighboring particles causes geometric constraints and the first submodel begins to break down. To account for this constraint, Fischmeister and Artz propose the second submodel which operates under constrained deformation [20]

$$P_H(\rho) = k\sigma_Y\ ln\left\{\frac{a(1)Z(1)}{a(1)Z(1) - a(\rho)Z(\rho)}\right\} \tag{87}$$

where k is a geometric constant approximated as 2. The complete densification relation is expressed as a linear combination of the unconstrained and constrained models through the relationship $P = f_S P_S + f_H P_H$, where f_S and f_H are the volume fractions of the 'soft' (unconstrained) and 'hard' (constrained) components yielding

$$P(\rho) = \sigma_Y(\rho)\left(\frac{3a(\rho)Z(\rho)}{4\pi\ R^2}\rho\ f_S + 2f_H ln\left\{\frac{a(1)Z(1)}{a(1)Z(1) - a(\rho)Z(\rho)}\right\}\right) \tag{88}$$

At compactions below $\approx 90\%$ theoretical, f_H, and consequently the second term is approximately zero and the compaction response is dominated by the unconstrained portion of the model. As compaction proceeds, f_H increases and the response becomes dominated by the

second term, which allows for an asymptotic approach to full density. Functional values for $a(\rho)Z(\rho)$ have been assigned in [20] for monosized spheres.

Many particle mixtures are, however, not composed of monosized spherical powders, and variations in particle size and shape can lead to changes in initial density and coordination. Therefore, Fischmeister and Artz [20] compared the results of their densification relationship developed for monosized spheres with compaction data available in the literature for particles with different sizes and shapes. For different size particles they postulated that an increase in coordination, $Z(\rho)$, will be offset by a decrease in contact area, $a(\rho)$, and found that the product $a(\rho)Z(\rho)$ for bronze particles with a size distribution between 100-350 μm coincides well with similar data for particles with a very narrow size distribution. Thus, for particles within this size range, they suggest that it is not simply the contact area or the coordination that has a large influence on compaction, but rather it is the product of the two which dictates the compaction response.

With regard to particle shape, Fischmeister and Artz [20] also found significant deviations in compaction characteristics compared with the spherical model. Not surprisingly, the more spherical a particle was, the more closely it correlated with model predictions. Thus one can envision some measure of 'irregularity' to account for the deviation of a particles shape from spherical which might be incorporated to better predict the compaction behavior of irregular shaped particles. However, they also found that the effects of particle shape diminish as stress increases.

A practical extension of this model has been developed by Meyers and co-workers [85], which relies on the ability to calculate the force transmitted to the contact areas and the total contact area as a function of relative density. From Fischmeister and Artz the force

transmitted to the contact areas is [20]

$$f = \frac{4\pi R^2}{\rho Z} P \tag{89}$$

where P is the pressure, or stress, applied to the particles. As stress applied to the particles is increased, the total contact area between particles increases such that the total average contact area per particle is defined as [85]

$$ZA_C = 4\pi \rho \left(\frac{\rho - \rho_0}{1 - \rho_0} \right) R^2 \tag{90}$$

Noting that the effective stress on each particle contact is $P_{eff} = f/A_C$, and using the yielding criteria developed by Artz [59], $P_{eff} \geq 2.97\ \sigma_Y$, where σ_Y is the yield (flow) strength of the material, the equation for the external stress required to induce plastic flow in a powder material is [85]

$$P_Y = 2.97\rho^2 \left(\frac{\rho - \rho_0}{1 - \rho_0} \right) \sigma_Y. \tag{91}$$

In this form, Eq. 91 can determine the stress necessary to reach a given density if the yield strength of the powder material or mixture is known. Conversely, the yield strength of a compact can be determined by fitting Eq. 91 to experimental stress-density data. The latter formulation is of particular interest in the case when the stress-density relationship for a powder body is only known over a limited (low stress) range. Using this method, after one determines a value for the yield strength, extrapolations to higher densities can be made and one can estimate the stress required for the powder to reach near full density.

4.2 The P-P_{Act} Model

The previous model, based on contact point and bulk deformation [20], is suited well for ductile metallic powders. However, the foundations of the P-σ_Y model break down when

one attempts to describe the consolidation of brittle particles. For these types of particles, it is not contact point or bulk deformation which are the key mechanisms for compaction; rather it is the successive fracture and rearrangement of particles which govern densification. As such, the P-P$_{Act}$ model seeks to develop a theoretical framework under which to describe the compaction of hard, brittle particles.

Originally proposed by Kenkre and co-workers [58], the P-P$_{Act}$ model uses stress activated and non-stress activated terms to describe the stress-density relationship in granular ceramics. It takes advantage of the linear compaction regions in the stress-density plane that are commonly observed in granular ceramics when density is plotted against the logarithm of compaction stress (see Fig. 4.2). The breakpoint in linearity is often associated with the onset of particle fracture, and is assigned such in the development of this model. At compaction stresses below the breakpoint, increases in stress are accompanied by minimal increases in density. This is considered the non-stress activated region, and is thought to describe the rearrangement of particles prior to the onset of fracture. In this region, the number of voids filled follows a linear relationship up to some saturation stress, and then becomes independent of pressure at values in excess of this saturation. The independence of stress at values above saturation results from the cessation of particle rearrangement and the inability of compacts to increase in density in the absence of some other process (deformation or fracture). For the non-stress activated regime, the process of filling voids is proportional to the factor f_l which is prescribed the following relation [58]

$$f_l = (constant)\left[1 - exp\left(-\frac{P}{P_l}\right]\right) \tag{92}$$

where P and P_l are the applied stress and the saturation stress for rearrangement, respectively.

To reach densities above those which can be obtained solely through rearrangement, the

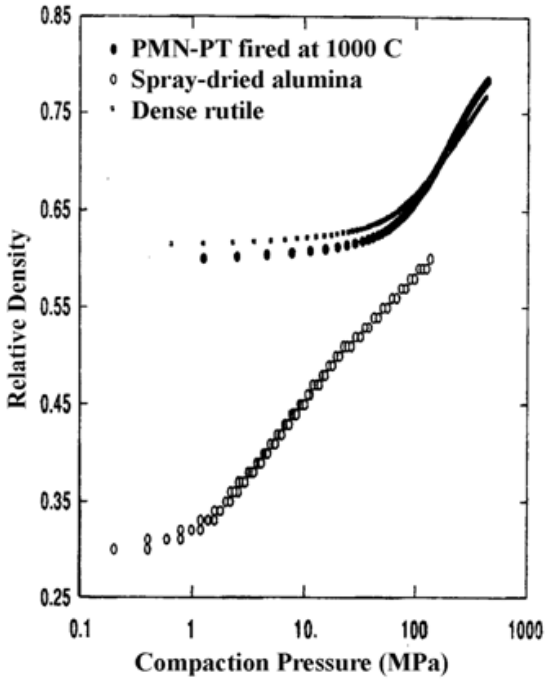

Figure 4.2: Semi-logarithmic compaction response of lead magnesium niobate-lead titanate (PMN-PT), spray dried alumina, and rutile showing two linear compaction regions (from Kenkre [58]).

model proposes that a stress activated process also occurs. In classical statistical mechanics, rate activated processes are often of the Arrhenius type, where the system of interest exchanges energy/temperature with its surroundings and must overcome some characteristic energy barrier to become activated. Mehta and Edwards [86] have extended the energy-based approach to a volume-based approach for dealing with powder mixtures, where volume is considered the quantity exchanged between the system and its surroundings, not energy. Within this framework, and through the first law of thermodynamics, pressure (stress) and volume are considered conjugate variables [87] similar to energy and temperature in classical statistical mechanics. As such, the probability of overcoming some volume barrier and filling a void in the pressure activated region is described by the equation [58]

$$f = (constant) exp\left(-\frac{P_a}{P}\right) \tag{93}$$

where P_a is a single stress barrier. When $P \leq P_a$, little variation in f is observed; however, as P increases beyond P_a the probability of overcoming the volume barrier increases and the filling of voids occurs. Physically, the filling of voids in the stress activated regime is attributed to processes such as crushing, chipping, or fracture for ceramic powders. In real powder systems, there may be many such stress activated barriers, and the number of voids filled is proportional to the sum of the probabilities for each barrier.

It is presumed that both the stress activated and non-stress activated process occur simultaneously during loading such that the entire densification relation takes the form [58]

$$\rho = \frac{\rho_0}{1 - \left(\frac{\rho_\infty - \rho_0}{\rho_\infty}\right)\left\{c\left[1 - exp\left(-\frac{P}{P_l}\right)\right] + (1-c) exp\left(-\frac{P_a}{P}\right)\right\}} \tag{94}$$

In Eq. 94, ρ_0 is the initial density at zero stress, ρ_∞ is the theoretical density at infinite stress, and c is the fraction of compaction as a result of rearrangement. The form of Eq. 94 assumes that a single stress barrier P_a and rearrangement saturation stress P_l exist, where

experimentally, variations in particle configuration, mechanical properties, and stress distribution may actually cause the single stress barrier assumption to break down. As a result, Kenkre and co-workers [58] examine the effect of various distribution functions for P_a on the compaction behavior of granular ceramics. Fits of their experimental data with the theory are shown in Fig. 4.3, where it can be seen that the theory agrees quite well with experimental data.

4.3 The P-α Model

The P-α model originally proposed by Herrmann [5] was developed to describe the compaction behavior of ductile porous materials under dynamic (shock) loading. To adequately describe the compaction process over such a wide range of stress, the model decomposes the compaction process at lower stresses into separate elastic and plastic components. Assumptions in this model include, (a) shear strengths are neglected, and (b) specific internal energy for the porous and solid materials are assumed to be the same under identical conditions of pressure and temperature. Neglecting shear strength of the powders limits the model to describe only the irreversible process of compaction through the closure of voids, which may not be entirely true, especially at low compaction stresses when individual powder strength properties may influence compaction behavior. The second assumption neglects surface energy of the pores. This may be a fair assumption for larger particles; however, as particle size enters the nano-regime, as has been shown by Dai and co-workers [16], the surface energy indeed has a significant influence on the compaction response.

The equation of state (EOS) of the porous material is derived from that of the solid material through the distention parameter α, which is a measure of porosity through the

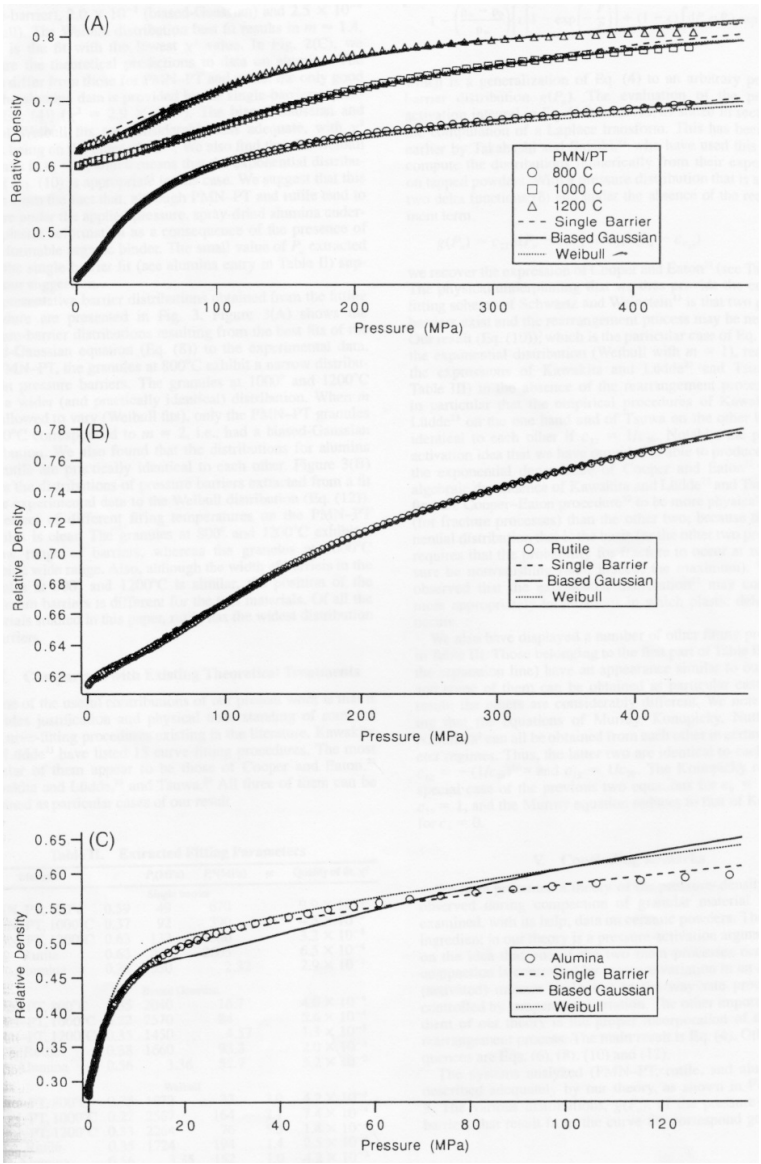

Figure 4.3: Fit of experimental data to model prediction for single-barrier, biased-Gaussian, and Weibull distributions in P_a for powder mixtures of (A) PMN-PT (B) rutile and (C) alumina (from Kenkre [58]).

relation

$$\alpha = \frac{V}{V_S} \tag{95}$$

where V and V_S are the specific volume of the porous and solid material. The EOS for the solid material can be defined generally as a function of specific volume (V_S) and specific internal energy E as $P = f(V_S, E)$. Making use of Eq. 95, Carroll and Holt modified Herrmann's [5] original EOS for the porous material to account for stress averaging over the particle contacts to yield [9]

$$P = \alpha^{-1} f(\frac{V}{\alpha}, E) \tag{96}$$

where the same function f is implied for both the solid and porous materials. For closure, the pore collapse relation must be defined as a function of pressure and energy; however, since pressure and specific internal energy are related along the normal Hugoniot of a material, α can be defined by the simplified relation $\alpha = g(P)$. In the elastic regime, $\alpha = g_e(P)$ is expected to have the following properties [5]

$$\begin{array}{ccc} p = 0 & \alpha = \alpha_e & d\alpha/dp = \alpha_e^{'} \\ 0 < p < p_e & \alpha_e > \alpha > 1 & d\alpha/dp < 0 \\ p = p_e & \alpha = 1 & d\alpha/dp = 0 \end{array}$$

where the meaning of these variables, as well as those that will be given to describe α in the plastic regime, are shown in Fig. 4.4. In Fig. 4.4 the material is initially at a porosity α_e, which upon application of an applied stress will deform elastically until stress P_e is reached, at which point all further deformation is plastic. One unique element of this model is its ability to predict the reloading behavior of porous materials. If, for instance, a material is subjected to a stress P_p which is above the elastic threshold stress P_e but below the crush stress P_s and then unloaded to zero stress, the P-α model allows one to predict its compaction response upon reapplication of stress. Initial reapplication of stress is elastic,

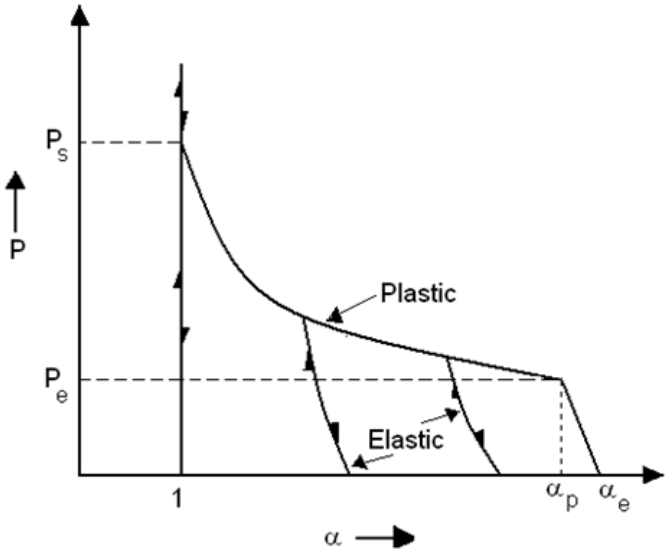

Figure 4.4: General schematic depicting the predicted P-α compaction response (from Herrmann [5]).

and will follow the elastic loading path (see arrows in Fig. 4.4) until the stress exceeds the value P_p at which point it will follow along the plastic path until solid density is reached. Specific relations describing the elastic response of porous media can be found in works by Herrmann [5], Butcher and Karnes [6], and Carroll and Holt [10], and will not be discussed further due to the relatively minor change in porosity that occurs in the elastic region for powder bodies.

Of primary importance to the compaction of powders is the plastic response, for which the compaction behavior $\alpha = g_p(P)$ is thought to follow the relations [5]

$$\begin{aligned} p = p_e \qquad & \alpha = \alpha_p \qquad & d\alpha/dp = \alpha_p' \\ p_e < p < p_s \quad & \alpha_p > \alpha > 1 \quad & d\alpha/dp < 0 \\ p = p_s \qquad & \alpha = 1 \qquad & d\alpha/dp = 0 \end{aligned}$$

Several different formulations for $\alpha = g_p(P)$ have been proposed over the years, of which a

few will now be examined. If rate effects are ignored and compaction is assumed to occur quasi-statically, Carroll and Holt [10] propose that α can be well represented by

$$\alpha = \frac{1}{1 - e^{-3P/2Y}} \tag{97}$$

for values of stress $P_{crit} \leq P \leq \infty$, where

$$P_{crit} = \frac{2}{3} Y ln\left[\alpha_0/(\alpha_0 - 1)\right] \tag{98}$$

and Y is the yield strength of the matrix material. Recall this was the formulation for α used in the Wu-Jing [83] model. This formulation is convenient because it contains the experimentally measurable, or alternatively, the fitting parameter Y. In this approximation, the porosity α is assumed to remain at its initial value α_0 until some critical stress P_{crit} is reached. This effectively neglects any compaction that may occur elastically, and prescribes all observed compaction to be plastic. Notice this formulation does not explicitly contain any of the variables defined in the original model by Herrmann [5]. Butcher and Karnes [6] proposed a simplified representation of α through the quadratic equation:

$$\alpha = \alpha_0 + \alpha_1 \, P + \alpha_2 \, P^2 \tag{99}$$

which, if appropriate values for α_0, α_1, and α_2 are inserted into Eq. 99, results in the simplified relation for the plastic response [5]

$$\frac{\alpha - 1}{\alpha_p - 1} = \left(\frac{(P_s - P)}{(P_s - P_e)}\right)^n \tag{100}$$

Equation 100 has been shown to describe the compaction behavior of ductile porous metals quite well. However, deficiencies in this type of formulation have been shown to exist in other types of material systems, specifically, dry sand and other ceramic powders. For these types of powders, a power law relation of the form

$$\alpha = \left(\frac{P_s}{P}\right)^{1/n} \tag{101}$$

has been suggested by Grady [88], and has been shown to agree quite well with experimental data for dry sand [89]. In this formulation, n is simply a fitting parameter; however, upon careful examination of this formulation with various material systems a correlation of n with some type of strength parameter may be possible. The attractiveness of the P-α formulation is due largely to the fact that (a) it can be easily implemented into computer codes, (b) it requires minimal experimentally determined model parameters, and (c) it can be used to predict the compression/recompression response with relative ease. It is important to note at this that time all of the P-α formulations previously covered did not consider any rate effects, which in many instances are central to the compaction phenomena. For an in-depth review of rate dependent P-α model behavior, the reader is directed to works by Carroll and Holt [10], Nesterenko [11], and Tong and Ravichandran [19].

4.4 The P-λ Model

A more recent compaction model that explicitly incorporates material properties of individual constituents in heterogeneous mixtures is the P-λ model developed by Grady et al. [12]. Similar in formulation to the P-α model, this model describes the compaction process through a single internal state variable, λ. The model also neglects shear strengths in the mixtures and examines only the general pressure-volume response; thus in developing the framework for this model the terms pressure and stress are used interchangeably to define the mean hydrostatic stress applied to the mixture. The model is separated into three distinct regions, the unequilibrated elastic response, the pressure equilibrated equation of state response, and the transition region between the two.

When the magnitude of applied stress is low, deformation of the mixture is presumed elastic, and Grady et al. [12] give two different additive models to define the elastic response

of the mixture. The equations developed here are for a two component mixture where f_1 and f_2 are the volume fractions of each of the component, but can easily be extended to mixtures with more than two components. The total volume strain and total pressure in the mixture are defined by simple volume fraction additions of each component. Similarly, each component has its own bulk moduli K_1 and K_2 such that one can define a mixture modulus based on either an iso-pressure (Reuss) or iso-strain (Voight) response. The iso-pressure bulk modulus, K_p, is a lower bound for the mixture modulus, and details of its formulation can be found in Grady et al. [12] and will not be discussed further. The iso-strain response provides an upper bound for the elastic response and is defined as

$$K_\mu = f_1 K_1 + f_2 K_2 \tag{102}$$

From this modulus, the pressure-volume response of the mixture in the unequilibrated elastic region can be determined through an appropriate definition of strain (e.g. true $\epsilon_T = ln(V/V_0)$ or engineering $\epsilon_E = (\Delta\ V/V_0)$ assuming linear elasticity, $P = K_\mu\ \epsilon$.

At the other extreme is the equilibrium equation of state response, where individual components are in a state of pressure equilibrium. Grady et al. [12] propose a simple mass fraction additive equation of state for the mixture. However, alternative methods of determining the equation of state for a solid mixture have been presented in Sect. 2.5 which upon incorporation of porosity can be formulated into the equilibrium equation of state for initially porous materials in the manner presented in Sect. 3.4. The exact formulation for the equilibrium equation of state is not a central concern of this model; rather it is important only that some formulation is chosen to represent the fully compacted pressure equilibrated state.

The crux of this model comes in the description of the partially compacted state, where

the material is assumed to exist in some combination of the unequilibrated elastic and pressure equilibrated states. The amount of each state present is assigned through the variable λ, which defines the mass fraction of material in the fully compacted state. Lambda varies from $0 \leq \lambda \leq 1$ such that when $\lambda = 0$ the material is entirely in the unequilibrated elastic state and when $\lambda = 1$ it is in its pressure equilibrated state. The specific volume of the mixture can thus be represented as

$$V_m(p) = \lambda\, V_h(p) + (1 - \lambda) V_x(p) \tag{103}$$

where $V_h(p)$ and $V_x(p)$ are the specific volumes of the mixture in its pressure equilibrated and unequilibrated elastic states, respectively. For λ, Grady et al. have chosen the functional relationship [12]

$$\lambda = 1 - e^{-(p_l/y_l)^n} \tag{104}$$

where p_l is defined as a measure of the local stress difference resulting from varying component compliance through $p_l = (1 - K_p/K_\mu)p$, where p is the global pressure. The parameter y_l is a measure of the local yield strength which, when overcome, will initiate yielding and compaction in the mixture, and n is defined as a measure of the homogeneity of compaction which dictates the pressure interval over which compaction will occur. As developed, n is the only parameter which can not be defined from individual component properties and must be determined from properties of the mixture. Thus n can be thought of as a fitting parameter to align experimental data to theoretical prediction. In a similar manner, y_l can also be used as a fitting parameter if a direct functional relationship is not applied.

Through Eqns. 103 and 104, the compressional response of a mixture can be obtained. A graphical representation of this model is taken from [12] and reproduced as Fig. 4.5. Here the unequilibrated elastic response ($\lambda = 0$) is given by the iso-strain (Eq. 102) response and

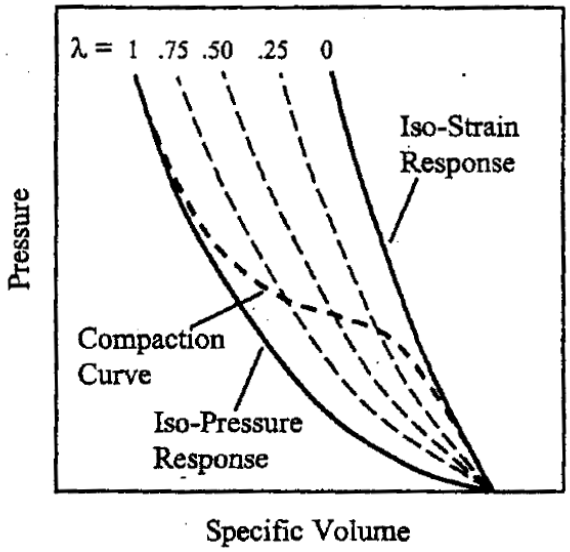

Figure 4.5: Schematic showing the compressional response for a generic P-λ mixture (from Grady et al. [12]).

the iso-pressure response is some chosen form of the pressure equilibrated equation of state for the solid mixture. Figure 4.5 shows the general compression response for an initially solid mixture, however, if one component in the mixture is air or some other entrapped gas, as is the case for porous materials, the iso-strain response curve for $\lambda = 0$ is simply shifted such that its origin is at the initial specific volume of the porous body (V_{00}).

4.5 Comparison of Compaction Models

In the previous few sections four different compaction models for porous and powdered systems were examined. The first two, the P-σ_Y and the P-P_{Act} models, were developed explicitly to describe the quasi-static compaction behavior of very different powder types. The P-σ_Y model is based on contact point deformation mechanisms, which ascribes the densification response to an applied load to occur through the growth of particle contact

points and significant plastic deformation. This framework works well when describing the compaction response of ductile powders; however, when particles undergo little deformation prior to the onset of fracture as is the case in many ceramic powders, the physical basis under which the P-σ_Y model was built decreases. Thus one would expect that the P-σ_Y model might do a poor job of describing the compaction response of brittle powders. Similarly, as the P-P_{Act} model was developed explicitly for brittle powders where the main mechanisms of densification are rearrangement and fracture, one would not expect this model to describe well the compaction response of ductile powders.

To see how well these models operate in describing the compaction behavior for configurations which are out of the framework under which the models were originally developed, the tungsten carbide (WC) and tantalum (Ta) powder systems are examined. Details of the WC powder and quasi-static compaction method used to compact it can be found in Vogler et al. [90] and will not be discussed further, with the exception that the powder WC-SA5 (in [90]) was subjected to vibrations prior to compaction and that its morphology was blocky. The Ta powder used for model comparison is that which was used in the current investigation, and a detailed description of the powder and its quasi-static loading conditions can be found in the experimental portion of this document. At this time it should be noted that for the Ta powder, no settling procedure has been used, and the powder morphology is rounded/globular. The experimental stress-density results as well as the fit of these results to the P-σ_Y and P-P_{Act} models for Ta and WC are shown in Fig. 4.6, where fits were made using the nonlinear least squares method of the curve fitting toolbox in MATLAB [91]. The fitting parameters for Ta and WC thus obtained are given in Table 4.1, where χ^2 is the sum of the square of the errors between the experimentally measured and model predicted values.

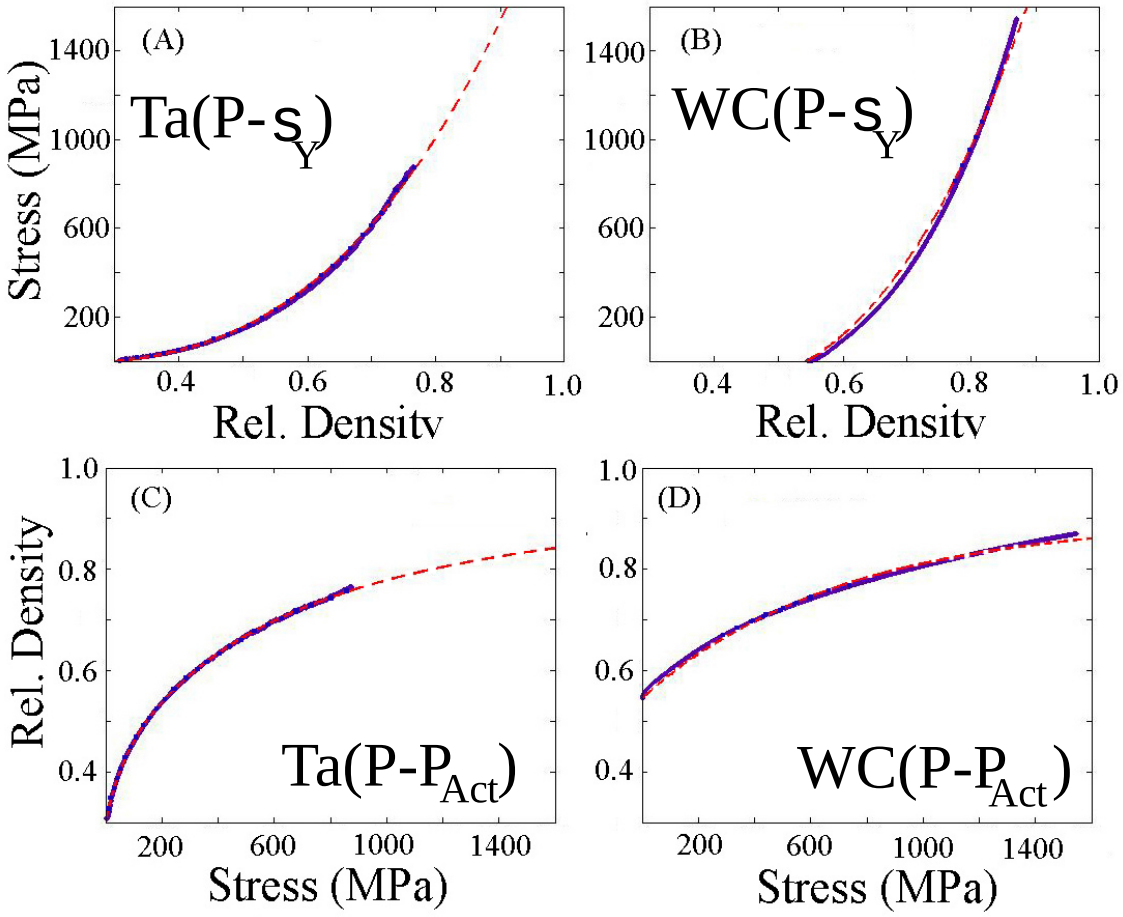

Figure 4.6: Plots showing stress vs. relative density comparing experimental data to fits of the P-σ_Y model for (a) Ta and (b) WC, and fits of the P-P_{Act} model for (c) Ta and (d) WC. The experimental data is denoted by the thicker points and the fits are given by the thinner dashed lines.

Table 4.1: Fitting parameters for Ta and WC to the P-σ_Y and P-P_{Act} models.

Property	Ta	WC
ρ_{00}	0.306 (%TMD)	0.545 (%TMD)
σ_Y	746 (MPa)	913 (MPa)
$\chi^2(P-\sigma_Y)$	2.57 x10^5	8.74 x10^5
C	0.526	0.669
P_a	309 (MPa)	1346 (MPa)
P_l	49 (MPa)	332 (MPa)
$\chi^2(P-P_{Act})$	5.70 x10^{-3}	2.68 x10^{-2}

Shown in Fig. 4.6(A) and (B) are the P-σ_Y fits to Ta and WC quasi-static compression data. Recalling the two assumptions in the P-σ_Y model (particles are spherical and initial relative density is 0.64) it is observed that relaxation of these assumptions does not seem to have an overly deleterious effect for fitting the Ta powder. Conversely, the fit of the WC powder is less accurate, even though the initial density for the WC powder is much closer to the ideal model assumption. The better fit for Ta is attributed mainly to the underlying physical process for which this model was developed, i.e. deformation by contact point growth and coalescence. These mechanisms are more likely to occur in the ductile Ta powder than in the brittle WC powder; Vogler et al. [90] found cracking in the post quasi-statically compacted powders. They also observed that the overall size of the particles had been reduced. Thus it seems that in using the P-σ_Y model, restrictions on morphology and initial density can be relaxed while still allowing for a good fit between model and experimental results. However, accuracy of the model tends to decrease slightly for brittle particles which undergo little plastic deformation during consolidation.

Figure 4.6 also shows fits of the P-P_{Act} model with experimental compaction data for Ta (C) and WC (D). This model, which is separated into stress activated and non-stress activated components and was developed for granular ceramics, actually fits the Ta data

better than the WC data. At first, this result may seem surprising as the WC is more of the ideal system for which this model was developed. However, one of the key components of this model is the rearrangement of particles at low stresses, dominated by the non-stress activated component. As the WC has undergone vibratory processing to achieve higher densities prior to compression, much of the rearrangement has already taken place. On the other hand, no processing steps had been taken prior to compaction of the Ta powder, and significant rearrangement occurs in this system. Thus, it is seen that though the P-P_{Act} was originally developed for granular ceramics, it does an adequate job of describing the compaction behavior of ductile metallic powders as well. Furthermore, a primary component of this model is the rearrangement of particles, and it has been shown that when this phenomena does not occur in the powder under compression, the accuracy of predictions are reduced.

In contrast to the quasi-static models previously discussed, the P-α and P-λ models are not based on specific underlying physical phenomena like contact point deformation or rate activated processes. These models simply describe the irreversible process of compaction as a result of the application of an applied stress through their respective compaction parameters α and λ. As such, these models should serve to describe equally well distended systems with a wide range of material properties and configurations, with strength properties of the system being incorporated through the parameters Y (Eq. 97, P-α) and y_l (Eq. 104, P-λ). The main difference in these models lies in their ability to treat heterogeneous systems. As developed, the P-α model treats distended materials as a homogeneous continuous media, and has no means to incorporate individual material strength properties associated with heterogeneous systems. Therefore, one might expect the P-λ model, which

can explicitly incorporate individual material properties, to better predict the crush-up response of heterogeneous distended systems. To explore this effect, the crush-up response of two very different heterogeneous powder mixtures is examined.

The powder mixtures chosen are a nanoscale mixture of Ni-Al [92] and a micro scale mixture of Ti-Si [72]. These two systems are examined because of the availabity of experimental data in the crush-up region and because they represent two very different types of heterogeneous systems. In addition to particle size differences, the Ni-Al system is composed of relatively ductile fcc metals that have a nearly three fold difference in component density and a large difference in yield properties [93, 94], while the Ti-Si system has large variations in both density and soundspeed between constituents [72]. By examining these two particular systems one can test the applicability of the P-α and P-λ model over a wide range of initial configurations. The fits of these models with experimental data are shown in Fig. 4.7 for Ni-Al and in Fig. 4.8 for Ti-Si, note the solid Hugoniot is approximated as incompressible in this analysis.

Upon examining the Ni-Al P-α fit, it is evident that different formulations of α fit the data with varying degrees of accuracy, with the quasi-static approximation put forth by Carroll and Holt [10] being the least accurate. Both the standard relation for α (Eq. 100) and the more recent formulation (Eq. 101) do a much better job of approximating the compaction response; with the prediction from Eq. 101 falling consistently below but within the experimental error of all data points. A much better approximation is given by the P-λ model, where experimental results lie much closer to the predicted curve. In addition, the P-λ model does not require any information about the crush strength a-priori to yield a prediction.

Examination of Fig. 4.8 for the Ti-Si system shows similar results, with the P-λ fit

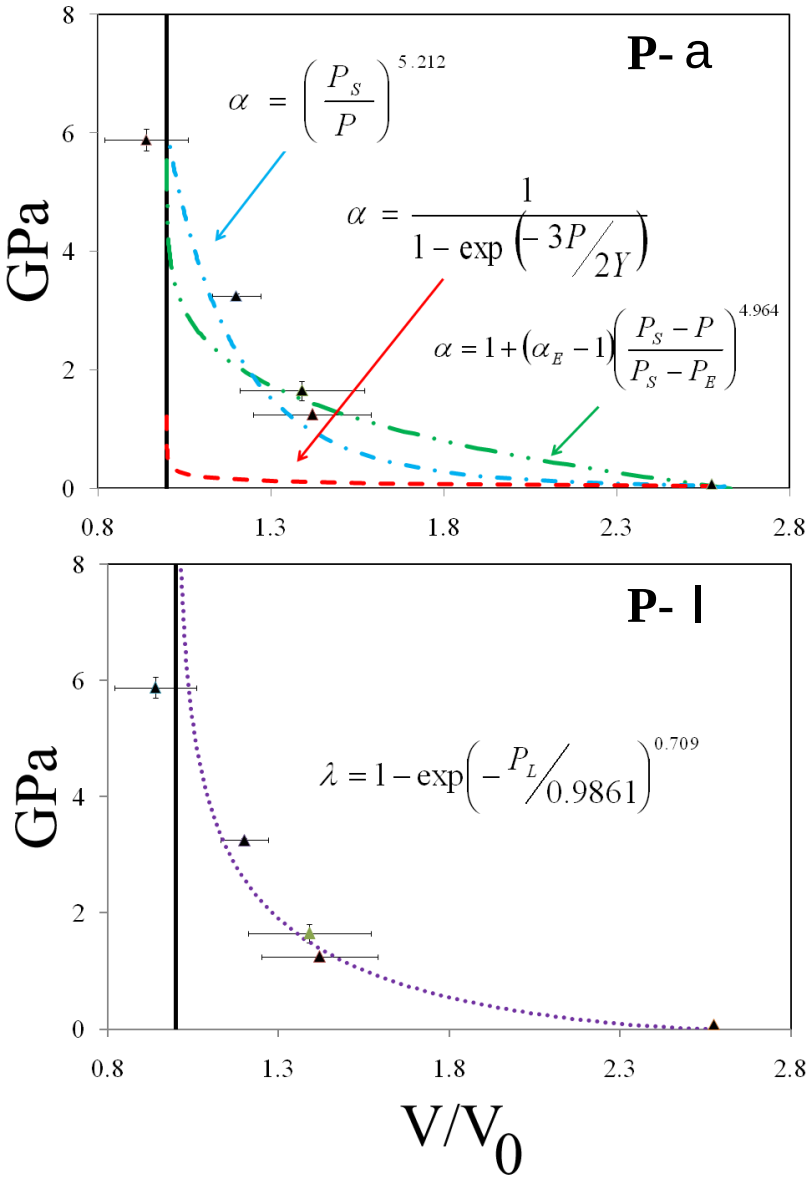

Figure 4.7: Crush-up response of nanoscale Ni-Al powder mixture showing P-α (top) and P-λ fits to the data. Numerical values shown in the equations are determined from best fit of experimental data, P_S set to 6 GPa, Y is volume fraction averaged, and P_E is determined through Eq. 98.

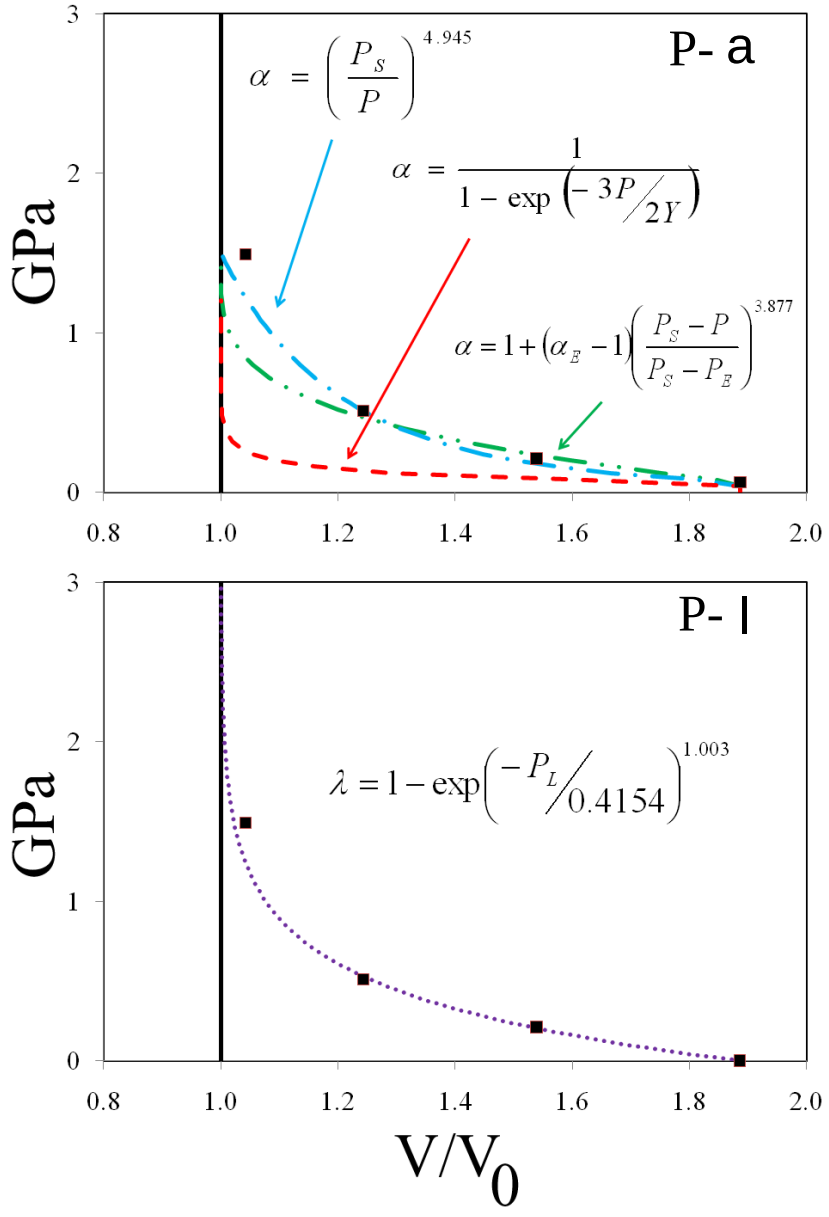

Figure 4.8: Crush-up response of micron sized Ti-Si powder mixture showing P-α (top) and P-λ fits to the data. Numerical values shown in the equations are determined from best fit of experimental data P_S set to 1.5 GPa, Y is volume fraction averaged, and P_E is determined through Eq. 98.

yielding the best fit overall and Eq. 101 yielding the best fit among the P-α predictions. This suggests that the P-α model, while proven to predict experimental results for homogeneous materials systems composed only of a single material and voids quite well, tends to decrease in accuracy as the system being modeled becomes more heterogeneous. Also, both models seem to work equally well for either system, indicating that compaction can be modeled with a moderate degree of accuracy with both models for systems spanning a wide range of material properties.

CHAPTER V

THERMITES AS ENERGETIC COMPONENTS

The materials investigated in this dissertation are in a class of materials collectively known as thermites. As a subset of pyrotechnics, thermites consist of a fuel which combines with oxygen through a combustion process to release heat, light, and smoke [95]. Traditionally, the term thermite had been used to describe the reaction of aluminum with iron oxide; however, this term has been expanded to represent any exothermic reaction involving a metal reacting with a metal oxide to form a more stable oxide.

Thermites mixtures are a unique class of energetic materials that are very different from traditional molecular based explosives, such as trinitrotoluene (TNT) and octogen (HMX). In molecular explosives, chemical kinetics controlls the energy release rate and as a result can yield extremely powerful explosions. While molecular explosives possess high energy release rates, they are composed of nominally low density materials, resulting in low overall energy densities [96]. Conversely, energy release rates in thermites are controlled by mass transport mechanisms, which can result in lower energy release rates. However, densities in thermite systems can be up to an order of magnitude greater than those in molecular based explosives and result in substantially increased energy densities, which make thermites an attractive class of materials for the transfer of both kinetic and chemical energy. One means of utilizing both the kinetic and chemical energetic components of thermites is through impact initiated reactions.

5.1 Impact Initiated Reactions

The impact initiation of thermite mixtures is, at present, an open and developing field of research. In comparison to initiation through conventional point sources, impact initiation has been studied to a much lesser extent, and several fundamental issues still remain unresolved for these systems. Of particular interest are the roles of particle morphology, packing density, constituent strength, and crush behavior on the initiation conditions of thermite mixtures. To date, very little time-resolved data exists on the crush-up and reactive response of these powder mixtures, and evidence of reactions have relied largely on the post-shock analysis of recovered specimens [24]. As interest in these types of energetic systems is growing, it would be beneficial to determine the role of initial configuration and crush behavior on the reaction initiation conditions. With little work published for thermite mixtures, one can look to other material systems, such as metal-metal reactive systems, for insight into initiation controlling mechanisms.

Generally, impact initiated reactions can be divided into two categories, shock-assisted and shock-induced reactions. Shock-assisted reactions are those which occur on the time scales of thermal equilibrium (several tens of microseconds), and are controlled by defect enhanced solid state diffusional processes [97]. In contrast, shock-induced reactions occur on the time scales of pressure equilibrium (tens to hundreds of nanoseconds), and the mechanisms which control these types of reactions are still being debated. To delineate between the two types of reactions in powder mixtures, time-resolved measurements capable of measuring material response at the sub-micro second level are required. As such, much of the early recovery work on metal-metal reactive systems such as Ni-Al [98], Nb-Si [99], and Ti- and Ta-based carbide and boride systems [100] offers only postulations as to the initiation mechanisms.

With regard to particle morphology, Strutt and co-workers [98] examined two different Ni-Al particle morphologies, flake-Ni + spherical-Al and spherical-Ni + spherical Al. They found that reacted zones were only visible in the mixture composed of flake-Ni + spherical-Al at the highest stresses, suggesting a morphology dependent initiation condition. Through examination and characterization of the post-shocked microstructures, it is suggested that the increased interfacial area between the constituents is responsible for the configurationally dependent reaction initiation. This claim is supported further by Eakins and Thadhani [79], who combined time-resolved measurements with particle level simulations of the shock front, and found that the presence of the flake-Ni leads to an increased rate of flattening for the spherical Al particles, thus increasing the surface area between reactive constituents.

To address the issue of particle size, Yu and co-workers examined stoichiometric mixtures of Nb + Si ($NbSi_2$) at shock stresses of 20, 46, and 70 GPa. With stoichiometry and initial density kept constant between experiments, analysis of recovered microstructures revealed regions of fully, partially, and non-reacted material. Microstructures from fully reacted regions, which illustrate the extent of reaction in mixtures with particle sizes of < 5 μm and 15-44 μm, are shown in Fig. 5.1. In this mixture it is supposed that solid Nb reacts with liquid Si to form the product phase $NbSi_2$. As such, the total amount of Nb-Si interfacial area influences the extent of reaction, where a more even distribution of reaction is observed for the smaller particles (Fig. 5.1(a)). For the larger particles shown in Fig. 5.1(b), the interior regions of Nb particles are shown to be unreacted, due to insufficient interaction with the surrounding Si.

The effect of constituent density on reaction threshold conditions in systems of Ti-

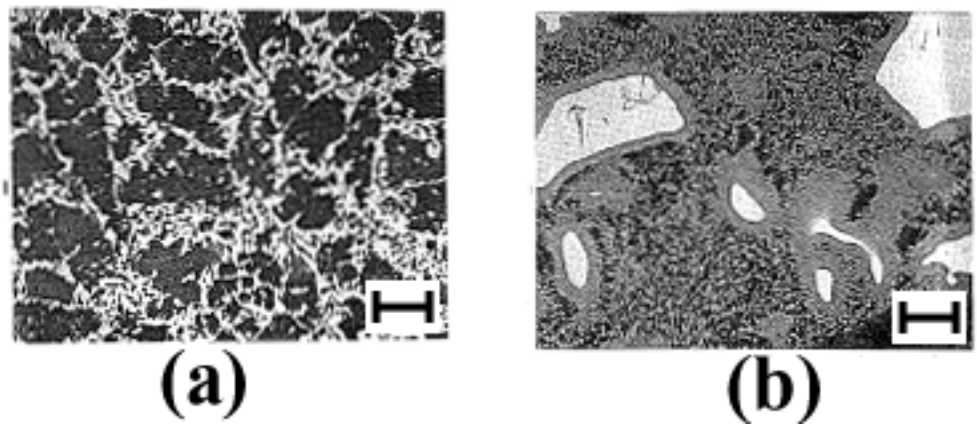

Figure 5.1: Fully reacted regions of Nb + Si mixtures for (a) fine (< 5μm) and (b) coarse (15-44 μm) particle sizes following impact at 1.96 km/s. Micron bars shown indicate length scales of (a) 5 μm and (b) 10 μm. Interior of Nb particles are observed in (b), surrounded by reacted $NbSi_2$.

and Ta-based carbide and boride systems was investigated by Joshi, Thadhani, and Graham [100]. In examining these systems, both large and small disparities in constituent densities were examined. The density ratios of Ta/C and Ta/B are 7.36 and 7.11, and those for Ti/C and Ti/B are 2.0 and 1.92. As such, it is hypothesized that if density were a contributing factor to reaction initiation, one would observe similar reaction responses in the Ta/C and Ta/B systems as well as in the Ti/C and Ti/B systems as their respective density ratios are similar. This behavior is not observed, and the investigators concluded that density difference between constituents in these systems is not a significant factor in reaction initiation. However, similar to the previous investigations on Ni-Al and Nb-Si, increased area of contact and dynamic deformability (and fracture) are found to contribute to reaction initiation and sustainability.

The duration of the shock pressure pulse has also been shown by Thadhani and co-workers [101] to affect reaction initiation in Ti-Si powder mixtures. In their work, specimens with initial densities ranging from 43 to 66 % TMD were impacted at 0.35 km/s and the recovered specimens were analyzed to determine if reaction had occurred. Copper flyer plates of different thickness were used, such that a thicker flyer is inferred to result in a longer pulse duration. The results of their work are shown in Fig. 5.2, and indictate that both pulse duration and initial density are factors that influence the initiation of reaction. At the lowest density, reaction is reported to occur for both short and long pulse durations, and is attributed to the better mixing and flow between constituents resulting from the increased amount of void collapse during compaction. As density increases, the effect of pulse duration becomes evident as longer pulse durations are found to increase the propensity for reaction for densities up to 61 % TMD. For the highest densities reaction is not observed, regradless of the pulse duration, and may result from an insufficient amount of particle movement and mixing during consolidation of the low porosity mixture.

From what has been discussed thus far, one can see that many different factors affect the impact initiated reactivity in metal-metal powder mixtures. It has been shown that surface area and initial mixture density are some of the more important parameters affecting reaction initiation, while pulse duration is found to influence initiation to a moderate extent. Furthermore, contrary to initial mixture density, the actual density of the constituents, or rather the density difference between the constituents, is found to not have a strong effect on initiation. With a lack of comparable studies performed on thermite systems, one can only assume that some of the same principles and observations found for metal-metal reactive systems also apply to thermite systems. There is still a considerable amount of work that is needed to determine the mechanisms operating and conditions necessary to initiate and

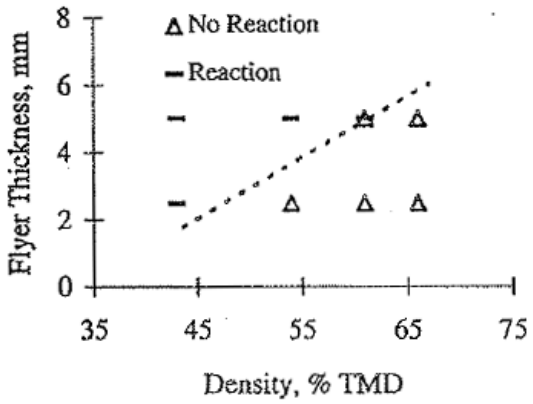

Figure 5.2: Reactivity plotted as a function of flyer thickness and initial density in stoichiometric (5:3) powder mixtures of Ti + Si. Initiation of reaction is shown to depend on both flyer thickness (pulse duration) and initial density.

propagate reactions in thermite powder mixtures.

One aspect of reactive powder mixtures that has yet to be explored, whether it be in metal-metal mixtures or thermite powder mixtures, is the influence of the crush strength on the initiation conditions. Recalling that the crush strength is the stress required for a powder or porous material to reach full density, is it possible that there is some corollary between this stress and the stress required for reaction initiation? To determine this, one would need to determine both the crush strength and the reaction initiation stress for a multitude of material systems, an endeavor that would be experimentally intensive. This is due in part to the current lack of models capable of predicting the crush strength and reaction thresholds in heterogeneous thermite powder mixtures. If there existed a means by which either of these values could be accurately predicted, one could significantly reduce the experimentation required to establish if such a connection exists. In an effort to develop such a predictive ability, the crush response of the thermite mixtures Ta + Fe_2O_3 and Ta + Bi_2O_3 are investigated.

CHAPTER VI

POWDER MIXTURES AND EXPERIMENTAL METHODS

The objective of this research is to determine how certain powder properties, both intrinsic and extrinsic, affect the dynamic consolidation of powder mixtures, leading to mechanically induced reaction. Of specific interest are highly heterogeneous thermite powder mixtures of Ta + Fe_2O_3 and Ta + Bi_2O_3. Bulk compressional response of the two types of thermite mixtures is obtained experimentally through a combination of uniaxial quasi-static compression and parallel plate impact shock densification tests, where the consolidation to full density is characterized using existing continuum level compaction models. In addition, the equilibrium equation of state response is modeled using several of the methods outlined in Section 3.4, where significant deviations from the inert equilibrium response can potentially be considered as evidence of a shock-induced reaction.

This chapter begins with a description of the powders investigated and their relevant material properties. Ample data exists in the literature for both Ta and Fe_2O_3; however, Bi_2O_3 is less well characterized and the appropriate material properties must be determined from a series of experiments. A brief overview of these experiments, and the resulting material data obtained for Bi_2O_3, in addition to the available literature data on Ta and Fe_2O_3, will be presented. This is followed by an outline of the experimental methods used to determine the compaction response of the mixtures, both quasi-static and dynamic. This chapter is concluded by a description of the impedance matching technique used to fully characterize the shocked state of the mixtures under compression and its associated error

analysis.

6.1 Starting Powders

The powders used throughout this investigation are Ta (TA-101) and Fe_2O_3 (FE-601) powders, obtained from Atlantic Equipment Engineers (Bergenfield, NJ), and Bi_2O_3 (B-1067) powders, obtained from CERAC Inc. (Milwaukee, WI). Particle size distributions for the Ta and Fe_2O_3 powders are listed as 1-5 μm, and purities are given at the 99.8% and 99.9% levels, respectively. The Bi_2O_3 powder is -325 mesh ($\leq$44 μm) with a purity of 99.9%. Microtrac particle analysis yielded a size distribution of 1-15 μm with an average particle size of 6 μm for the Bi_2O_3 particles. SEM images of each of the three starting powders are shown in Fig. 6.1.

Note the differences in morphology between the individual powders. The Ta particles have smooth edges and appear globular in morphology, in stark contrast to both the Fe_2O_3 and Bi_2O_3 powders. The Fe_2O_3 powder, as shown in Fig. 6.1, appears very open and porous with particle (aggregate) size on the order of tens of microns, where the Fe_2O_3 aggregates are actually agglomerates of 1-5 μm sized particles. Conversely, the morphology of the Bi_2O_3 particles is approximately equiaxed, with clearly resolved boundaries and surfaces. Considering morphology alone, it is expected that the extrinsic differences (size, shape, surface roughness, etc.) shown in Fig. 6.1 will result in significantly different mixing and compaction characteristics. Furthermore, if the intrinsic properties of the powders vary as well, as will be shown shortly, the mixing and compaction behavior of the mixtures are expected to diverge even further. The next section describes the methodology and results of the experimental work performed on Bi_2O_3 to ascertain the necessary material properties for further analysis.

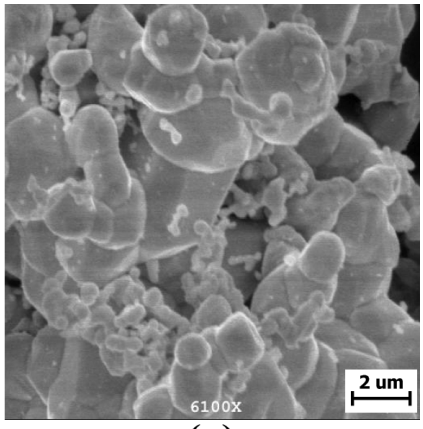

(a)

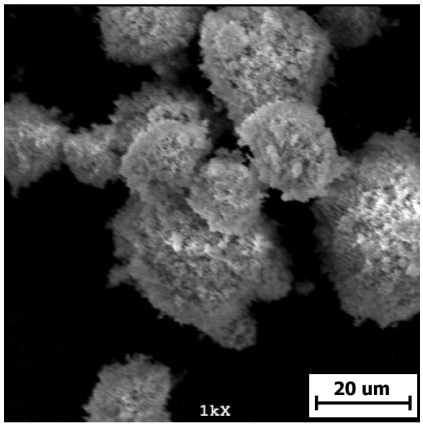

(b)

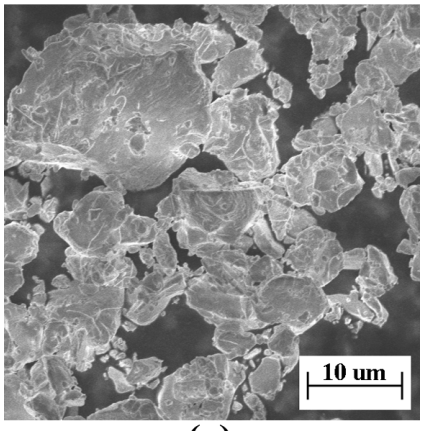

(c)

Figure 6.1: SEM micrographs of (a) Ta, (b) Fe_2O_3, and (c) Bi_2O_3 starting powders.

6.2 Characterization of Bismuth Oxide

To determine the properties of bulk Bi_2O_3, a series of experiments were performed on dense pellets formed from the starting powder (shown in Fig. 6.1(c)). The powder was hot pressed into dense compacts using a SATEC Systems, Inc. Uniframe TC-25 quasi-static compression machine fitted with a clamshell heater capable of reaching 1600 °C. The process of forming the pellets began by loading the powders into a 15.9 mm inner diameter steel punch and die and applying a compressional load of 1325 lbf for approximately two hours. During loading, the temperature was brought to 650 °C over the course of an hour and held at temperature for the remainder of the loading. Furthermore, the die was fitted with a thermocouple such that the temperature of the die could be continuously monitored. Following completion of the loading and heating cycle, the clamshell furnace was opened and allowed to cool to room temperature, at which point the dense pellet was retrieved and sanded parallel to within 5 μm or less. An photograph of the testing apparatus showing the test frame and clamshell furnace with a loaded die is shown in Fig. 6.2. A total of eight pellets were produced using this method, with dimensions of the pellets measuring 15.9 mm in diameter and heights ranging between 1-1.2 mm. The density of each pellet was determined from an average of four separate measurements of the Archimedes density [102], and the average density of all pellets was found to be 9.202 ± 0.036 g/cm^3, indicating the pellet has reached solid density.

Hot pressing was undertaken at 650 °C because at this temperature plasticity and diffusion are promoted. In addition, 650 °C is only slightly below the α-δ phase transition in Bi_2O_3. At temperatures above 730 °C, Bi_2O_3 has been shown to transform from its room temperature stable monoclinic phase (α-Bi_2O_3) to a high temperature superplastic cubic phase (δ-Bi_2O_3) [103]. To ensure that the hot pressed pellets remain in the α-Bi_2O_3 phase

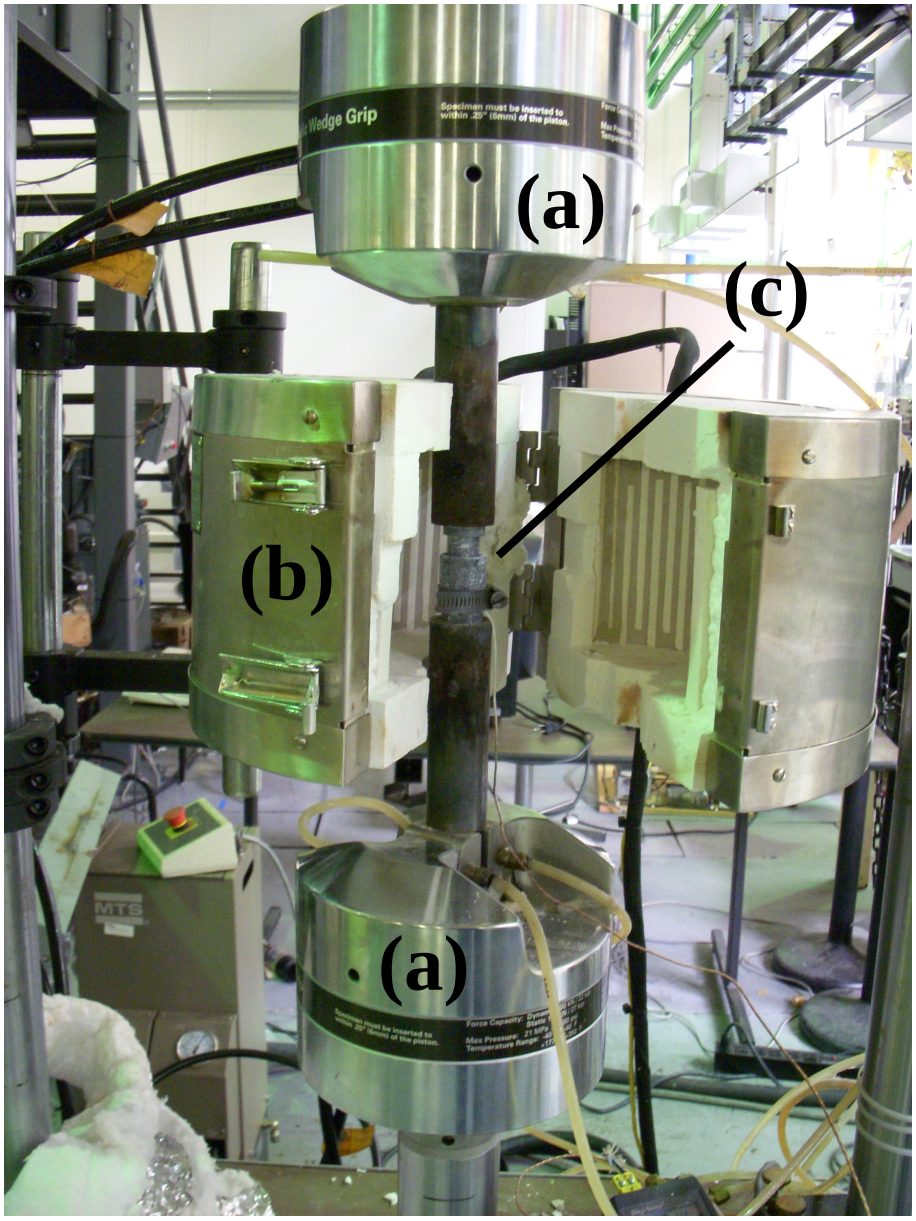

Figure 6.2: Hot pressing apparatus showing (a) water cooled grips on the uniaxial test frame, (b) clamshell furnace, and (c) die equipped with thermocouple.

following hot pressing, x-ray diffraction patterns of the starting powders and dense pellets were compared. The diffraction patterns and peak positions of ρ = 9.2 g/cm^3 monoclinic Bi_2O_3 (PDF: 04-003-2034) are shown in Fig. 6.3, which illustrate that the structure remains α-Bi_2O_3 following hot-pressing.

To determine the bulk elastic properties, both longitudinal and shear soundspeed measurements were made on five of the eight pellets. Waveforms were generated with an Agilent 33250 A 80 MHz function/arbitrary waveform generator with characteristic center frequencies of 5 MHz (longitudinal) and 2 MHz (shear). The signals were transmitted using Ultran WC50-2 and SWC50-5 transducers. Both the reference and transmitted waveforms were recorded on a Tektronix TDS 5034 B 350 MHz digitizing oscilloscope. To determine transit times through the pellets, the original time signal was subjected to a Hilbert transformation [104], which yielded a signal envelope that was used to determine the arrival time of the maximum frequency. A schematic showing the original time signal and its envelope is given in Fig. 6.4. The MATLAB [91] code used to determine the maximum time from the envelope signal is given in Appendix A.2. Time of travel between the connection lines and transducers was accounted for by subtracting the measured time for the signal to travel between the transducers with no sample between them.

Using the method outlined above, three separate measurements of longitudinal and shear wavespeeds in each of the pellets were taken from which average soundspeeds were determined. From these measurements, shear modulus μ and Lame's constant λ can be directly measured, with knowledge of the pellet density. Using a method put forth by Cousins et al. [105] which minimizes the error associated with determining the elastic properties of a material with an unknown Poisson's ratio, a Poisson's ratio of $1/2\sqrt{2}$ was assumed for

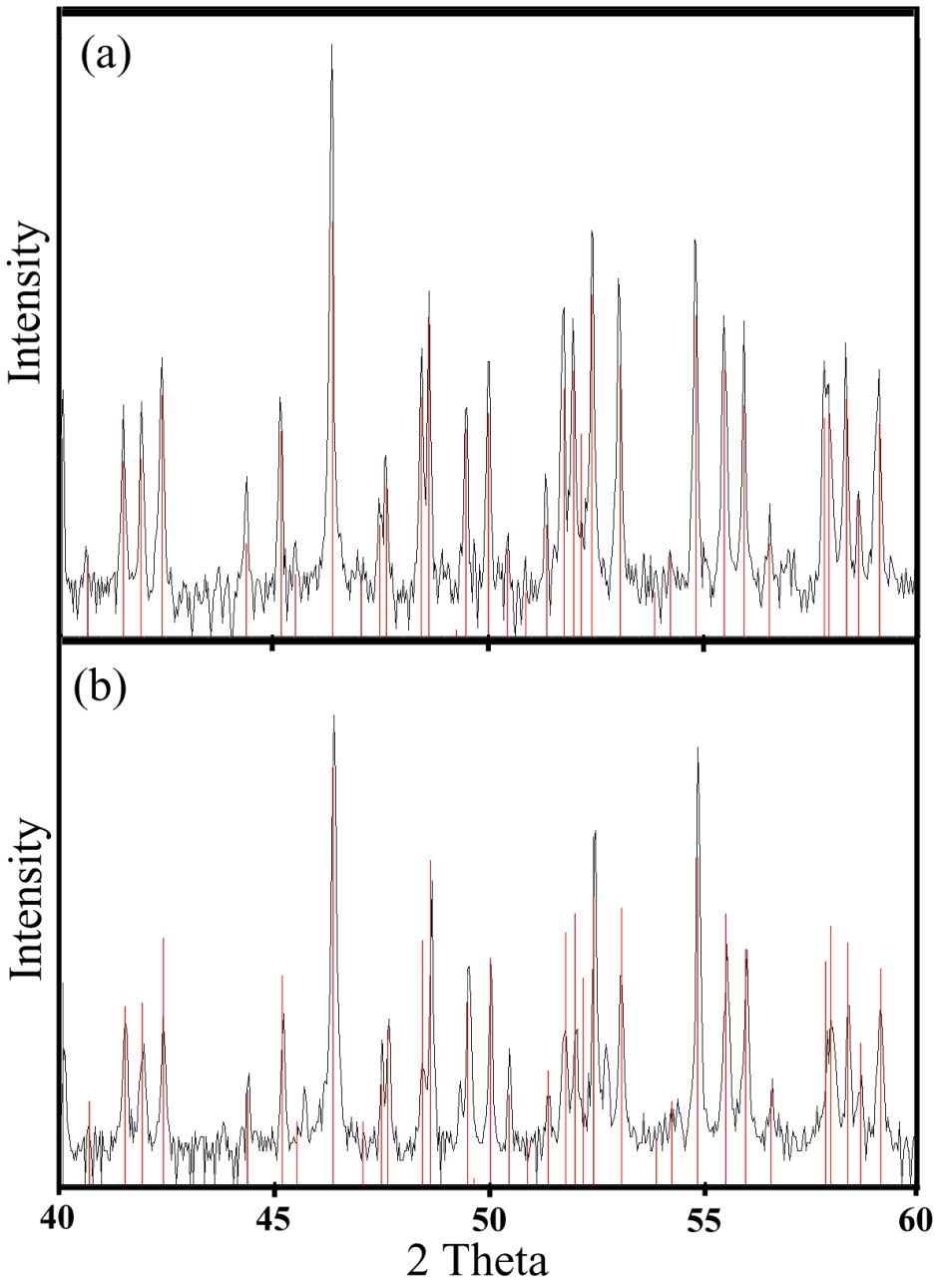

Figure 6.3: X-Ray patterns for (a) as-received Bi_2O_3 powder and (b) hot-pressed pellet over 2θ range 40-60. Peak lines shown (dotted lines) are for monoclinic Bi_2O_3, PDF: 04-003-2034.

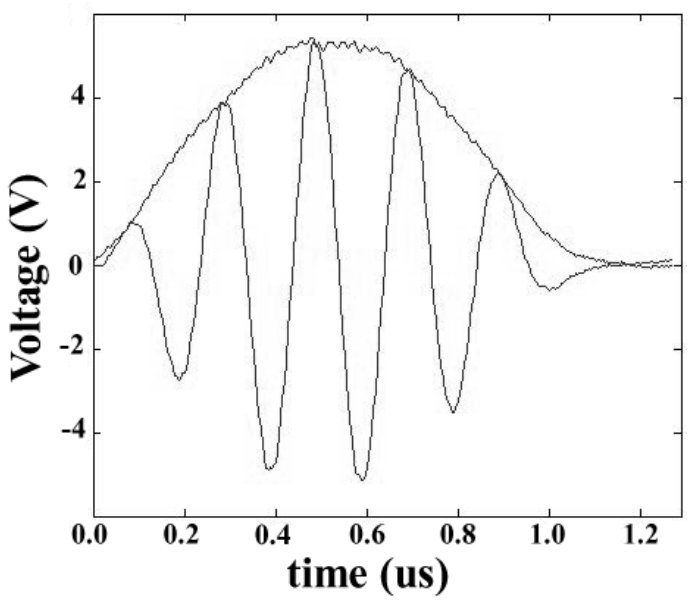

Figure 6.4: Voltage-time signal and Hilbert transformed data in time domain.

Bi_2O_3. Using this value, the elastic properties of Bi_2O_3 were determined through conventional elasticity analysis [106]. The results of these measurements, and their corresponding elastic properties are given in Table 6.1.

In addition to elastic properties, the equilibrium equation of state response for pure Bi_2O_3 is also needed for the current analysis. To accomplish this, a series of instrumented parallel plate impact experiments were performed. In these experiments, the target was composed of a Bi_2O_3 pellet mounted between a copper driver and a z-cut quartz backer window, as shown in Fig. 6.5. To determine shock velocity in the sample, polyvinlyidene fluoride (PVDF) gauges were sandwiched between two Teflon films and mounted on either side of the Bi_2O_3 pellet, where the purpose of the Teflon films was to electrically insulate the PVDF sensor. As the shock wave entered the gauge package, compression of the PVDF

Table 6.1: Measured values for longitudinal (C_L) and shear (C_S) soundspeeds, density (ρ), Lame's constant (λ), shear modulus (μ), Young's modulus (E), and bulk modulus (K) for Bi_2O_3.

Specimen	C_L (km/s)	C_S (km/s)	ρ (g/cm^3)	λ	μ (GPa)	E (GPa)	K (GPa)
A	2.195	1.140	9.191	20.393	11.945	22.867	26.025
B	2.078	1.137	9.165	15.879	11.848	17.805	20.264
D	2.510	1.181	9.157	32.146	12.772	36.046	41.023
F	2.904	1.043	9.264	57.970	10.078	65.003	73.978
G	2.941	1.503	9.177	37.914	20.731	42.514	48.384
Average	2.526	1.201	9.191	32.860	13.475	36.847	41.935

occurred and a charge was produced. The charge produced was then converted into a voltage through a current viewing resistor (CVR) and recorded in an oscilloscope. By recording the time between voltage signals, a measurement of the shock velocity in the sample under compression was determined. It should be noted that the current signal produced by the PVDF gauge can be converted into a measure of stress using a known calibration of current vs. stress [107]. However, inconsistencies in determining values for the equilibrated stress can lead to widely varying measures of stress. As such, the PVDF gauges were used strictly for measuring shock velocity.

Parallel plate impact experiments were performed on the Bi_2O_3 pellets over the velocity range 291-1000 m/s, with impact velocity (of the projectile) and shock velocity (in the sample) measured directly. With these two measurements, impedance matching (Sect. 6.8) was used to determine all other parameters of interest. Complete details of the gas-gun set-up, experimental configuration, and analysis techniques for similar experiments are given in greater detail in Sect. 6.7. The results from the parallel plate impact experiments are given in Table 6.2. Note the experiment performed at V_I = 291 m/s has been omitted due to an anomalous behavior of the propagated current trace that was observed.

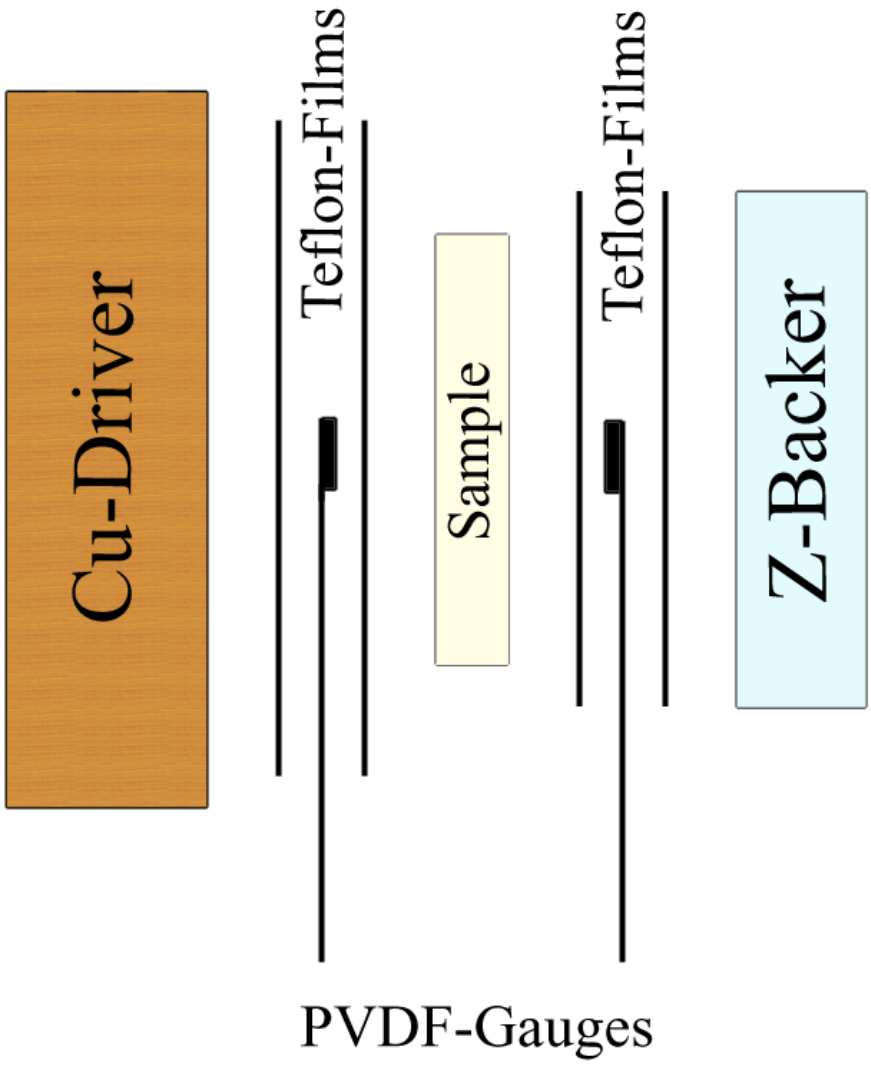

Figure 6.5: Schematic of components for a parallel plate impact experiment of Bi_2O_3.

Table 6.2: Parallel plate impact data for pure Bi_2O_3. Measured quantities are ρ_{00}, V_{Imp}, and U_S; all other quantities are calculated using impedance matching. Letter in parenthesis to the right of Shot() indicates sample corresponding to ultrasonic measurements.

Shot	ρ_{00} (g/cm^3)	V_{Imp} (km/s)	U_S (km/s)	u_P (km/s)	σ (GPa)	V (cm^3/g)	V/V_0
1015(A)	9.191	0.454	2.940	0.263	7.117	0.0991	0.914
1009	9.223	0.610	3.036	0.354	9.900	0.0958	0.884
1016(B)	9.165	0.828	3.194	0.480	14.06	0.0927	0.855
1010	9.217	1.000	3.319	0.577	17.66	0.0896	0.827

To determine the equation of state for Bi_2O_3, the U_S-u_P data in Table 6.2 is fit to Eq. 4 which yields values for the bulk soundspeed and linear fitting parameter S. Fitting the data set results in the dashed line shown Fig. 6.6 with C_0 = 2.611 km/s and S = 1.277. Using the C_0 and S values so reported, Eq. 4 can be used to estimate values for the isothermal bulk modulus K_0 and its stress derivative K_0' using the Murnaghan [108] equation of the form [109]

$$\sigma = \frac{3K_0}{2}\left[\left(\frac{\rho}{\rho_0}\right)^{7/3} - \left(\frac{\rho}{\rho_0}\right)^{5/3}\right]\left\{1 + 3\left(\frac{K_0'}{4} - 1\right)\left[\left(\frac{\rho}{\rho_0}\right)^{2/3} - 1\right]\right\} \tag{105}$$

Utilization of Eq. 105 requires the σ-V relationship along an isotherm to be known, which can be accomplished using the methodology given in Sect. 2.3. However, values for the Grüneisen coefficient γ_0, Debye theta θ_D, and zero-stress energy along the Hugoniot E_{0H} must first be determined. An approximation of the Grüneisen coefficient can be made using Eq. 10 with published values for the linear thermal expansion coefficient α = 14 x10^{-6} /° C [110] and specific heat C_V = 235.7 J/kg-° C [111], and the experimentally determined volume ($1/\rho$) and isothermal compressibility (β =1/K). Here, K assumes the value given in Table 6.1 such that the isothermal compressibility is taken to be equivalent to the standard compressibility. Inserting the appropriate values into Eq. 10 results in a

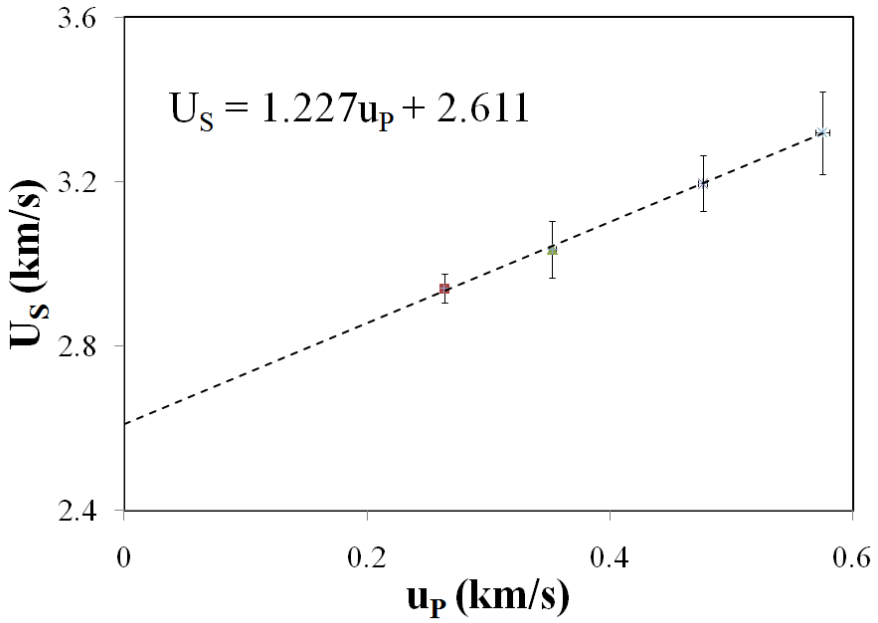

Figure 6.6: Plot showing fit of Eq. 4 using all the data points (solid line) and fit with lowest point omitted (dashed line).

value for the Grüneisen coefficient of $\gamma_0 = 0.812$.

The Debye theta was determined using Eq. 23 with $T_M = 825$ °C [103] and $\overline{A} = 464.96$ g/mol, resulting in $\theta_D = 43$ °C. The zero-stress Hugoniot energy was calculated through Eq. 22, giving $E_{0H} = 14826$ J/kg. Inserting the appropriate values into Eq. 105 the isothermal bulk modulus and its stress derivative, assuming σ, V, C_0, and S are related through Eq. 6, can now be determined. This procedure was carried out using the values of C_0 and S given in Fig. 6.6, resulting in $K_0 = 62.9$, $K_0' = 3.995$ with an R^2 =1. Note the isothermal bulk modulus determined from this method differs from the average bulk modulus obtained from soundspeed measurements in Table 6.1 by approximately 20 %; however, it still falls within the range of ultrasonic values. As this dissertation is largely concerned with material response under shock loading conditions, the equilibrium equation of state given in Fig. 6.6 is used to describe the shock response of Bi_2O_3 throughout this work and all subsequently derived quantities.

6.3 Powder Properties

As illustrated by the micrographs shown in Fig. 6.1, the extrinsic characteristics of the powders vary significantly with notable differences in size, shape, and surface roughness between the Ta, Fe_2O_3, and Bi_2O_3 powders. In addition, the intrinsic properties of the powders are also markedly different. A list of the relevant physical properties of each of the constituents is given in Table 6.3. Properties reported are for materials under standard conditions (ρ_0,T,σ) when available, with exceptions noted. All values for Fe_2O_3 from reference [112] were determined from soundspeed measurements on a bulk sample with a slightly reduced density $\rho_0 = 5.254$ g/cm^3, or 99.6 % theoretical. Yield strengths reported for Ta and Fe_2O_3 from references [113] and [114] were obtained from tests employing

quasi-static loading conditions, where the Fe_2O_3 tests were carried out at 600 °C. The elastic modulus, shear modulus, and poisson's ratio for Ta taken from reference [115] are averages determined from soundspeed measurements of a cold rolled specimen with measurements taken both parallel and perpendicular to the rolling direction. In this instance, Poisson's ratio has been corrected for anisotropy. The elastic modulus Fe_2O_3 (238* GPa) is calculated based on the relation $G = E/2(1 + \nu)$, using the G and ν values reported in the table. The bulk modulus for Bi_2O_3 (62.73* GPa) is also calculated from the density and zero stress soundspeed through $C_0 = (K/\rho)^{1/2}$. The origin of all other properties reported for Bi_2O_3 have been detailed in Sect. 6.2.

Table 6.3: Material properties of Ta, Fe_2O_3, and Bi_2O_3. Values denoted with * symbol indicate values are calculated using other parameters listed in the table.

Property	Units	Tantalum	Fe_2O_3	Bi_2O_3
Density, ρ_0	kg/m^3	16660 [116]	5274 [112]	9202
Bulk Modulus, K	GPa	194.1 [116]	206.6 [112]	62.73*
Shear Modulus, G	GPa	71.5 [117]	91.0 [112]	13.5
Elastic Modulus, E	GPa	184 [115]	238*	36.8
Yield Strength, σ_{YS}	MPa	250 [113]	20 [114]	-
Poisson's Ratio, ν		0.29 [115]	0.308 [112]	$1/2\sqrt{2}$
Thermal Expansion, α_V	(10^{-6})/°C	19.5 [117]	32.9 [112]	14.0 [110]
Specific Heat, C_P	kJ/kg-K	0.14 [117]	0.65 [112]	0.24 [111]
Melt Temperature, T_M	K	3293 [118]	1780 [119]	825 [103]

In addition to the elastic and physical properties given in Table 6.3, the equilibrium equation of state response of the constituents is also of primary importance. As such, the shock properties for these materials are given in Table 6.4 along with the references from which they were obtained. The bulk soundspeed value for Fe_2O_3 (6.258* km/s) was calculated from the bulk modulus given in Table 6.3 through the relation $C_0 = (K/\rho)^{1/2}$, which is in close agreement with that reported by Marsh [29]. All values reported for

Bi_2O_3 were derived in Sect. 6.2.

Table 6.4: .Shock properties of Ta, Fe_2O_3, and Bi_2O_3 used in this investigation. Value denoted with * is calculated.

Material	C_0 (km/s)	S	γ_0
Ta	3.293 [120]	1.307 [120]	1.689 [32]
Fe_2O_3	6.258*	1.371 [29]	1.99 [112]
Bi_2O_3	2.611	1.227	0.812

6.4 The Ta + Fe_2O_3 and Ta + Bi_2O_3 Powder Mixtures

The properties given in Tables 6.3 and 6.4 clearly show a large degree of heterogeneity between the different constituents. As many of the equations of state and compaction models covered previously are based on the consolidation of homogeneous materials, it is instructive to examine explicitly the differences in properties in both the Ta + Fe_2O_3 and Ta + Bi_2O_3 systems, and contemplate how these heterogeneities might effect the compaction response of the overall mixture. To get an idea of the degree of heterogeneity of each of these powder mixtures, one must examine the differences (Δ) in constituent material properties. These differences for the Ta + Fe_2O_3 and Ta + Bi_2O_3 systems are given in Table 6.5.

Notable differences in constituent properties listed in Table 6.5 are those of density, the various moduli, and bulk soundspeeds. Exacerbating the difference in density in the Ta + Fe_2O_3 mixture is the inherent porosity in the sponge like Fe_2O_3 particles resulting from agglomeration (Fig. 6.1(b)). Thus not only are the constituents themselves largely different in density, but also the location of porosity in the mixture is likely to be concentrated in and around the Fe_2O_3. Hence during compression, the removal of voids may be largely dominated by the mechanistic response of Fe_2O_3 through the breakup and consolidation of

Table 6.5: Differences in material properties for the Ta + Fe_2O_3 and Ta + Bi_2O_3 powder mixtures. Value in parenthesis is difference as a percentage of the value for tantalum.

Property	Units	Ta + Fe_2O_3	Ta + Bi_2O_3
Density, $\Delta\rho_0$	kg/m^3	11386 (68.3)	7458 (44.8)
Bulk Modulus, ΔK	GPa	12.5 (6.4)	131.4 (67.7)
Shear Modulus, ΔG	GPa	8.5 (27.3)	58 (81.1)
Elastic Modulus, ΔE	GPa	54 (29.3)	147.2 (80.0)
Yield Strength, $\Delta\sigma_{YS}$	MPa	230 (92.0)	-
Poisson, $\Delta\nu$		0.089 (6.2)	0.064 (22.0)
Thermal Expansion, $\Delta\alpha_V$	(10^{-6})/°C	13.9 (68.7)	5.5 (28.2)
Specific Heat, ΔC_P	kJ/kg-K	0.51 (364.2)	0.10 (71.4)
Melt Temperature, ΔT_M	K	1513 (45.9)	2468 (74.9)
Bulk Soundspeed, ΔC_0	km/s	2.965 (90.0)	0.682 (20.7)
Fitting Parameter, ΔS		.064 (4.9)	0.08 (6.1)
Gruneisen, $\Delta\gamma_0$		.301 (17.8)	0.877 (51.9)

the Fe_2O_3 agglomerates.

In contrast to the large difference in density observed for the Ta + Fe_2O_3 mixture, the differences in bulk and shear moduli are relatively minor, which may prove to homogenize the compaction process. Unlike Ta + Fe_2O_3, the Ta + Bi_2O_3 mixture contains large variations in all reported moduli, with Bi_2O_3 being the more compliant component. As a result, it could be postulated that a majority of the deformation during compaction will occur in the Bi_2O_3 rather than the Ta.

Also of great importance to the shock propagation process in these highly heterogeneous powder mixtures is the speed at which the shock can propagate through each constituent. If it is assumed that each powder particle behaves in a manner analogous to the bulk, whose U_S-u_P relationship can be described adequately by a linear equation of state (Eq. 4), the speed at which the shock can travel through each particle is largely influenced by the parameters C_0 and S. Noticing that the value of S differs little between constituents

for both mixtures, a postulation as to the heterogeneity in the shock front resulting from differences in shock velocity can be made based on differences in their bulk soundspeeds, $\Delta\ C_0$. As given in Table 6.5, the Ta + Fe_2O_3 mixture possesses the greatest difference in bulk soundspeed, a difference of nearly 3 km/s, and as a result may yield a shock front that is considerably more disperse than in the case of the Ta + Bi_2O_3 mixture.

Considering the differences in intrinsic properties listed in Table 6.5 and the extrinsic properties shown in Fig. 6.1, it is hypothesized that the degree of heterogeneity during compaction will be larger for the Ta + Fe_2O_3 mixture. As noted, the difference in heterogeneity between mixtures can manifest in different forms, including dispersion in the shock front, localized regions of void collapse, and material specific deformation. While many of these heterogeneities cannot be measured experimentally, the heterogeneous nature of compaction can be ascertained through scatter in the experimental data and conformity, or lack thereof, of the observed compaction behavior with homogeneous compaction models.

6.4.1 Energetic Considerations

The stoichiometric mixture of Ta + Fe_2O_3, which yields the highest heat of reaction of any combination of the constituents, is given by

$$6Ta + 5Fe_2O_3 \rightarrow 3Ta_2O_5 + 10Fe + \Delta H_R \tag{106}$$

where ΔH_R, the heat of reaction, is equal to -1.073 kJ/g of reactant, or -183.8 kJ/mol of reactant. Due to the large variation in constituent density, the stoichiometric mixture is approximately 30 % by volume tantalum and 70 % by volume Fe_2O_3. For solid state mechanically-driven reactions, where extent of reaction depends largely on intimate contact and mixing between constituents, the uneven volumetric distribution in the stoichiometric mixture results in a reduction in the amount of surface contacts between the heterogeneous

constituents. The lower overall amount of contact between the constituents has the potential to result in incomplete shock-induced reaction. In order to maximize the surface contacts between reactants, an equivolumetric mixture was considered. The equivolumetric reaction is

$$3Ta + Fe_2O_3 \rightarrow 0.6Ta_2O_5 + 1.8Ta + 2Fe + \Delta H_R \tag{107}$$

where ΔH_R is again the heat of reaction and is equal to -0.284 kJ/g of reactant, or -50 kJ/mol of reactant. By modifying the volumetric concentration to 50 % by volume Ta and 50 % by volume Fe_2O_3, the heat of reaction is reduced by nearly a factor of five. The reduced ΔH_R results from the excess tantalum in the mixture; however, its presence serves to increase the contacts between the reactive constituents for possible enhancement of the mechanically-driven (shock) initiated reaction.

In a similar fashion, the Ta + Bi_2O_3 powder system can also be combined stoichiometricly or equivolumetricly. The stoichiometric reaction corresponding to the highest overall heat of reaction is

$$6Ta + 5Bi_2O_3 \rightarrow 3Ta_2O_5 + 10Bi + \Delta H_R \tag{108}$$

where ΔH_R is equal to -298 kJ/mol, or -0.962 kJ/g of reactant. The equivolumetric reaction is:

$$33Ta + 7Bi_2O_3 \rightarrow 4Ta_2O_5 + 14Bi + 25Ta + \Delta H_R \tag{109}$$

where ΔH_R is equal to -104.7 kJ/mol, or -0.454 kJ/g of reactant. Similar to the previous system, the stoichiometric mixture of Ta + Bi_2O_3 is dominated by the oxide component on a volumetric basis, and by modifying the stoichiometry to the equivolumetric configuration the heat of reaction is lowered by nearly a factor of three. In the present investigation, only the equivolumetric mixtures of Ta + Fe_2O_3 and Ta + Bi_2O_3 are studied. It is also

noteworthy that the overall energy density in the Ta + Bi_2O_3 mixture is almost twice that of the Ta + Fe_2O_3 mixture.

6.5 Mixture Preparation

Equivolumetric powder mixtures of both thermite systems were prepared through a sequence of steps, beginning with determining the appropriate mass fraction of each component necessary to yield equal volumes of the constituents. Once this was determined, and the appropriate mass of each powder was weighed, the powders were vacuum degassed at 110 °C for 24 hours to remove any entrapped moisture. The powders were then transferred to an inert atmosphere where they were allowed to settle for 24 hours. Following that, the powders were combined and sealed in a PMMA bottle with a single 1/4 inch diameter ceramic ball. The sealed PMMA bottle was then transferred to a V-blender where the powders were mixed for 8 hours. The ceramic ball was added to aid in the breakup of agglomerates that might form during mixing. Furthermore, the PMMA bottle was surrounded with conducting tape and grounded to the V-blender to minimize electrostatic buildup during mixing. SEM images showing the loose powders of both mixtures are given in Fig. 6.7.

Note that as illustrated in Fig. 6.7(a) Ta is barely visible in the Ta + Fe_2O_3 mixture. It is believed that the porous Fe_2O_3 particles have nearly completely surrounded the Ta, forming large agglomerates. This is in distinct contrast to the Ta + Bi_2O_3 mixture where discrete particles of both Ta and Bi_2O_3 are easily observed. Also observed in the Ta + Bi_2O_3 mixture is the apparent tendency of the Ta particles to clump together, as shown in Fig. 6.7(b). From Fig. 6.7 one can formulate a few hypotheses about the consolidation behavior of these mixtures. Specifically, for the Ta + Fe_2O_3 mixture, compaction may be largely dominated by the crush up behavior of the Fe_2O_3, as it is the Fe_2O_3 that is likely

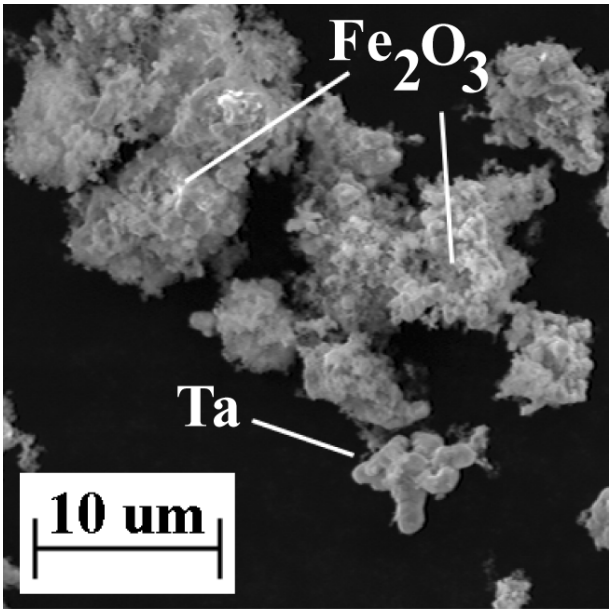

(a)

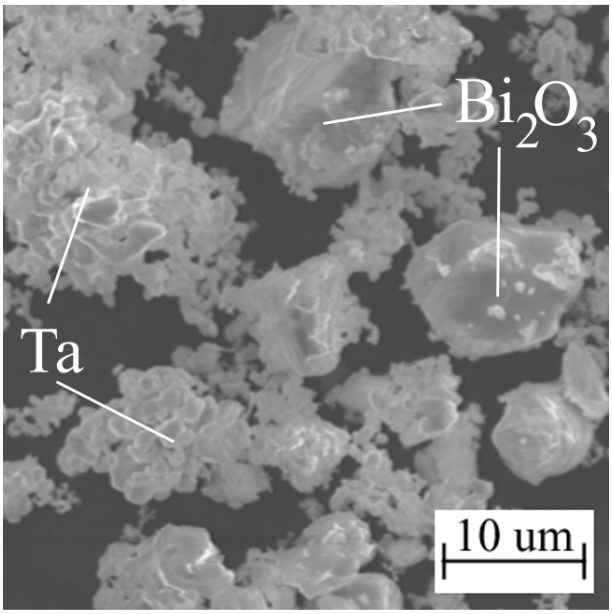

(b)

Figure 6.7: SEM images showing equivolumetric mixtures of (a) Ta + Fe_2O_3 and (b) Ta + Bi_2O_3.

to form the network of stress bridging material. In addition, it is anticipated that porosity is going to be largely located within the agglomerates of Fe_2O_3, and the removal of which will require deformation and crush up of the Fe_2O_3 particles. Conversely, in the Ta + Bi_2O_3 mixture, it is expected that tantalum will form the network of stress bridging material as these are the particles that are smaller and more numerous. As such, a large percentage of the void space in this mixture will likely be contained within localized regions of Ta, which may result in the deformation behavior of Ta dominating the compaction response of the mixture.

Having introduced the materials and mixtures, the remainder of this chapter focuses on the experimental methodology used to obtain information on the crush up and equation of state response of the Ta + Fe_2O_3 and Ta + Bi_2O_3 powder mixtures. Specifically, the method of quasi-static compaction is covered, highlighting the hardware used and compliance considerations. Following that, an outline of the parallel plate impact experiments, detailing target fabrication and data collection, is given. The remainder of the chapter focuses on the impedance matching method employed for obtaining the shocked state in the mixtures, and its associated error analysis.

6.6 Quasi-Static Compression Technique

Of primary importance to any porous material is the ability to characterize the system in terms of its 'crush strength', which is the stress at which the porous body consolidates to full density. In an effort to determine the crush strength as well as the characteristic shape of the compaction curve for the Ta + Fe_2O_3 and Ta + Bi_2O_3 material systems investigated, these systems were tested under quasi-static and dynamic loading conditions.

Quasi-static compaction of the mixtures was carried out on a SATEC Systems, Inc.

Unidrive TC-110 test frame, equipped with a load cell capable of measuring loads up to 445,000 N. The load-displacement data was recorded using MTS TestStar II hardware/software. The test frame was configured for single-action uniaxial displacement (see Sect. 3.2) such that displacement occurs from only one direction. As such, a single-action punch and die setup was used to determine the quasi-static σ-ρ relationship for the individual powders as well as the powder mixtures. A schematic showing the single-action punch and die setup, which was fabricated from an M2 tool steel and supplied by Porter Precision Products, Inc. (Alpharetta, GA), is shown in Fig. 6.8.

The die was filled such that the tap density results in a powder height of no more than 3-4 mm, so as to minimize die wall effects associated with variations in stress and density during compression. Following insertion of the punch into the filled die, the powder was loaded to between 45-90 N to bring the punch in direct contact with the powder. The apparatus was then unloaded and a measurement of the initial powder-loaded die height was recorded. With the unfilled punch and die height known a priori, the reduction in powder height as a function of load can be determined using the load-displacement data recorded from the MTS TestStar II software. In this analysis, the inner diameter of the die wall is assumed to remain rigid such that the load applied to the powder can be converted directly to an applied stress using the initial diameter of the die. From this, the instantaneous volume at load can be determined from measurements of displacement relative to the initial powder height. Compliance of the machine and the punch/die in the direction of the applied compression was accounted for by measuring the force and resulting displacement of an empty die and subtracting this compliance from the measurement of the die filled with powder.

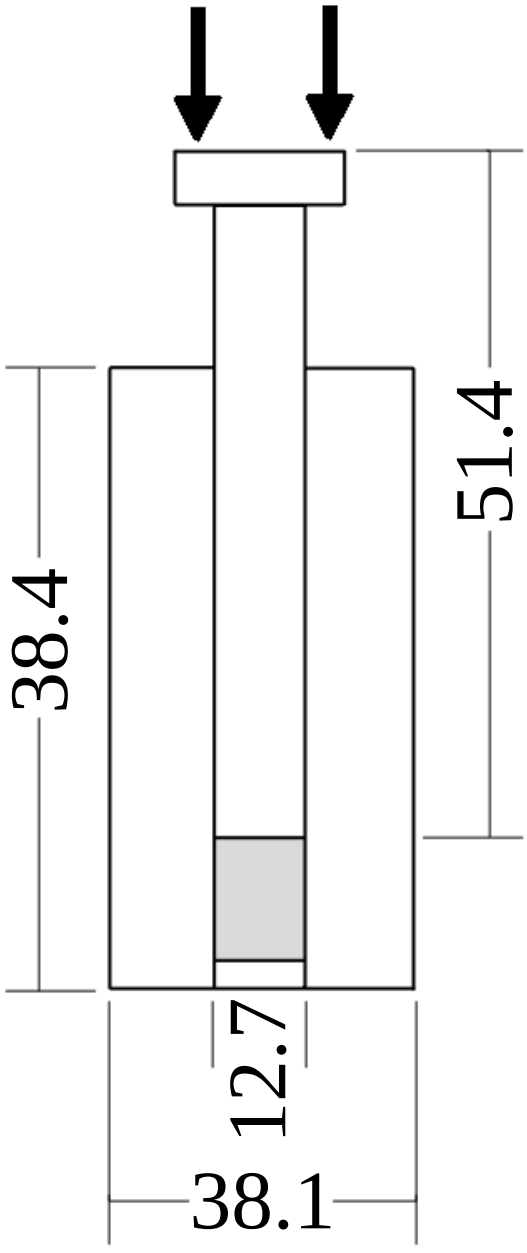

Figure 6.8: Schematic showing punch and die setup for quasi-static compression experiments. All dimensions are in mm.

6.7 Parallel Plate Impact Experiments

In contrast to the quasi-static compression process which yields stress-density information along a continuous loading path, the parallel plate impact experiment used to characterize the dynamic compressional response of the powder mixtures yields only a single data point. In the parallel plate impact experiments, compression occurs in a state of one dimensional strain such that the conservation equations of mass, momentum, and energy can be applied to obtain a complete description of the powder under dynamic loading using the impedance matching technique. The impedance matching technique, which is covered in greater detail in Sect. 6.8, requires the measurement of two quantities, the velocity of the projectile when it impacts the target (impact velocity), and the shock velocity in the powder.

6.7.1 Polyvinlyidene Fluoride Stress Guages

Shock velocity in the powder is measured using a pair of piezoelectric polyvinlyidene fluoride (PVDF) gauges developed by Piezotech S.A.S. (Hesingue, France), which, similar to conventional piezoelectric materials, produce an electrical charge when subjected to a mechanical stress. The active gauge area of 3 mm by 3 mm is biaxially stretched, poled by the patented ISL-Bauer process, and sputtered with gold over the platinum electrodes. Figure 6.9 shows the PVDF gauge electrodes as well an enlarged view of the active gauge area. The gauge thickness is nominally 25 μm. As a mechanical stress is applied to the gauge, a charge is produced in the active gauge area and is conducted through the electrodes to a current viewing resistor (CVR) which converts the current to a voltage.

With the active gauge area known, a charge density is determined which can, if desired, be converted into a measure of stress. These particular gauges were chosen because they provide nanosecond response times to applied loads. In the current work, only the

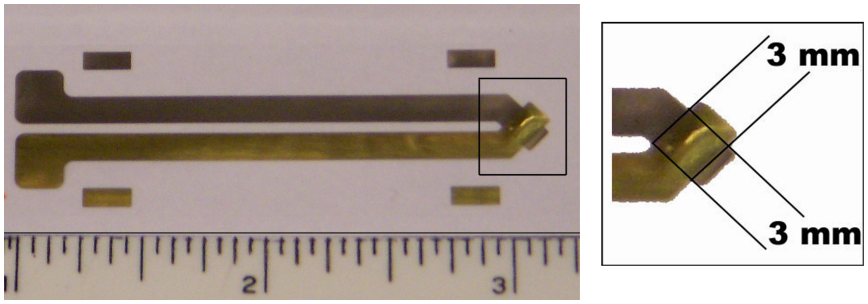

Figure 6.9: Polyvinlyidene fluoride (PVDF) gauge showing size of entire gauge and active area 3x3 mm.

charge/current output of the gauges were used to measure the arrival times of the compaction waves.

6.7.2 Target assembly

6.7.2.1 Ta + Fe_2O_3 Compaction Fixture

Measuring the shock velocity in the powder requires the target fixtures to be instrumented with two PVDF gauges, one on either side of the powder. For the Ta + Fe_2O_3 mixture, the target fixtures were composed of a solid copper driver plate with dimensions thickness T=6.35 mm, diameter D=57.15 mm, and a hollow copper ring into which the powder was pressed. The ring had dimensions T=17.65 mm and outer and inner diameters of O.D.=57.15 mm and I.D.=50.8 mm. In addition, a fused silica (FS) backer with dimensions T=12.75 mm, D=50.8mm was attached to the rear surface of the powder to restrict powder movement during loading and facilitate placement of the second gauge. With this configuration, gauges were mounted on the rear of the copper driver and the front of the FS backer, to effectively measure the arrival time of the compaction (shock) wave front on both surfaces of the powder mixture. Images of an unfilled PVDF target fixture and a completed target assembly are shown in Fig. 6.10.

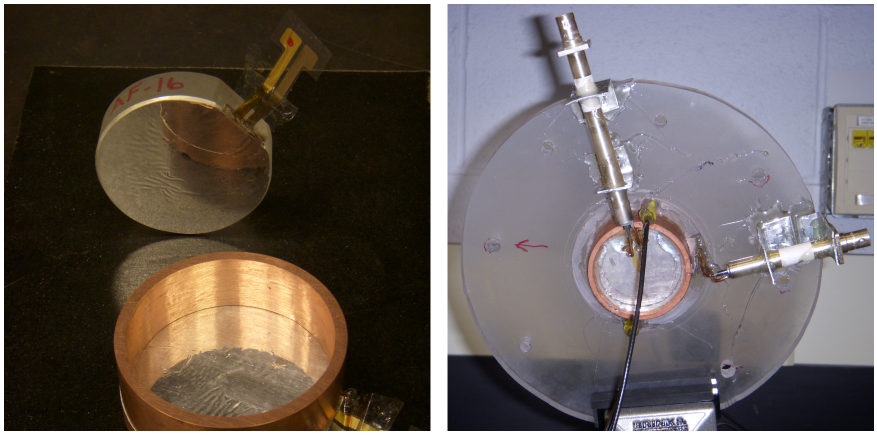

Figure 6.10: Unfilled PVDF target (left) and rear surface view of filled PVDF target mounted inside target assembly. Current viewing resistors (CVRs) are shown attached to the gauges and mounted to the target.

The PVDF gauges were affixed to the Cu driver and FS backer with a series of low viscosity epoxy and Teflon® thin films. The epoxy used to assemble the gauge package was a low viscosity Loc-Tite®Hysol resin RE2038 and hardener HD3475 mixed 4:1 by mass resin to hardener. Following mixing, the epoxy was vacuum degassed for approximately 10 minutes to remove entrapped gas. To assemble the gauge packages, a small amount of epoxy was placed on the surfaces of the driver and backer and covered with a 25 μm thick Teflon® film. After the epoxy was spread evenly over the surfaces, the epoxy was allowed to dry for 24 hours under a load of approximately 10 kilograms. Next, the PVDF gauge was placed on top of the first film, and an additional Teflon® film was epoxied on top on top of the gauge. Following attachment of the second film, an 150 angstrom thick layer of aluminum was vapor deposited onto the exposed film (as shown in Fig. 6.10), completing the gauge package. Measurements of the bare driver/backer, the driver/backer + epoxy + 1 film, and the driver/backer + epoxy + gauge + 2 films ware made to determine the location of the active gauge surface within the gauge package. The total gauge package

thickness was nominally 75 μm, and when determining the shock velocity in the powder, the transit time through the gauge package was subtracted from the total measured transit time between the gauge locations.

With the gauge packages mounted, the Cu surrounding ring was attached to the driver (as shown in Fig. 6.10), and a known mass of Ta + Fe_2O_3 powder was pressed to a height of 2 mm at a density of approximately 49 % theoretical mass density (TMD). Subsequent to loading the powder to its preshot density, ρ_{00}, the FS backer was pressed into the ring such that the gauge package on the FS surface was in direct contact with the rear surface of the powder mixture. The FS backer was then held under a 10 kg load and epoxied into place using five minute Hardman® 8173 two-part epoxy. With the FS backer in place, the fixture was mounted into an acrylic target plate. The target and target plate were then lapped flat such that the driver impact surface and the target plate were flush. A current viewing resistor (CVR), from T & M Research Products (Albuquerque, NM), was then soldered to each of the gauges which served to convert the current produced by the gauges into a voltage and could be monitored by an oscilloscope. The assembled target fixture showing the location of the completed Cu target and mounted CVRs is shown in Fig. 6.10.

6.7.2.2 Ta + Bi_2O_3 Compaction Fixture

For the Ta + Bi_2O_3 experiments, the driver was also composed of copper, but had dimensions T=6.35 mm and D=70.0 mm, where the diameter is increased to accommodate the two powder rings. In this configuration, two steel rings (T=10 mm, I.D.=27 mm, O.D.=33 mm) were attached to the driver, into which the powder was pressed and two different sets of instrumentation were attached. One ring employed PVDF gauges in the same fashion as those used to measure the shock velocity in the Ta + Fe_3O_3 mixtures, while the other was

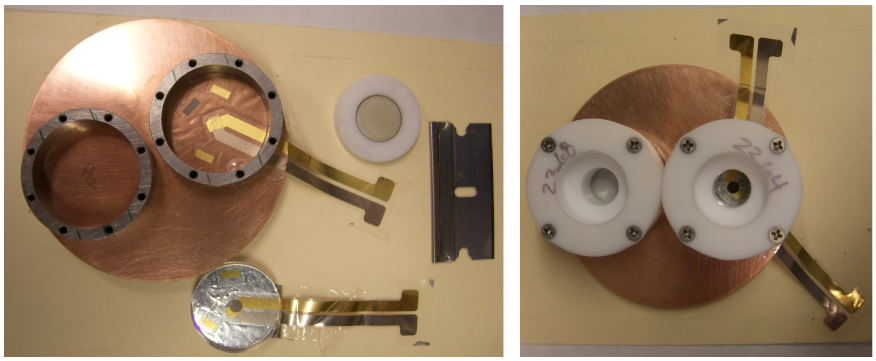

Figure 6.11: Target assembly used in Ta + Bi_2O_3 parallel plate compaction experiments. The image on the left shows all components in the unassembled condition with a razor blade shown for perspective, while image on the right shows target assembly loaded with powders and assembled, prior to insertion into acrylic target ring.

equipped for obtaining a measurement of the material velocity using velocity interferometry. Images of the dual ring compaction fixture in both the unassembled and assembled condition are shown in Fig. 6.11.

Also shown in Fig. 6.11 are the backer windows used in these experiments, both of which were z-cut quartz. This particular material was chosen for the backer because its deformation remains elastic over much of the stress range investigated [121]. The window equipped with the PVDF gauge had dimensions T=5 mm, D=24 mm which, when attached, contained the powder completely. A smaller window (T=3.0 mm, D=12.7 mm) was used to obtain velocity interferometry measurements. To create a surface onto which the interferometry measurements could be obtained, one side of the window was lightly bead blasted and coated in evaporated aluminum with a nominal thickness of a few hundred angstroms. The purpose of the bead blast was to yield a diffuse aluminum coating. Due to the smaller diameter of the window, a PMMA ring was machined which fit securely around the window with an O.D.=24 mm to secure the powder in place, as shown in Fig. 6.11.

The two windows were held securely against the rear surface of the powder by the PMMA plugs shown in Fig. 6.11. The completed assembly was then inserted into a larger acrylic plate, similar to that shown in Fig. 6.10, onto which CVR's and interferometry probes were attached prior to performing the experiment.

With the exception of shot SAND-140, all parallel plate impact experiments for the Ta + Bi_2O_3 system were performed in the manner outlined above. For shot SAND-140, the experiment was performed on a similar gas-gun at the DICE facility at Sandia National Laboratories. In contrast to the previous experiments, where the transit time through the powders was measured by a series of PVDF gauges, the transit time in SAND-140 was measured using laser interferometry. In this configuration, the two powder capsules were filled to different measured heights, and the difference in arrival times of the stress pulse at the buffer/window interface was used to calculate the transit time throught the powder. This measurement, in conjunction with the known difference in height of the powder thickness allowed for the shock velocity in the specimen to be calculated.

6.7.3 Performing the Measurements

Experiments were performed on the 80 mm bore diameter single-stage light gas-gun at the Georgia Institute of Technology (Atlanta,GA). A schematic of the gas-gun setup is shown in Fig. 6.12. In this configuration, an aluminum projectile with a copper or W-6Ni-4Cu flyer plate at initial location (B) was accelerated down the barrel of the gun (C) using compressed helium as the driving gas (A). The target assembly was attached to a set of parallel stand-off blocks directly on the muzzle face, and impact between the target and the projectile occurred in the experiment tank (D). Following impact, the target assembly and projectile were brought to rest in the soft-catch recovery tank (E).

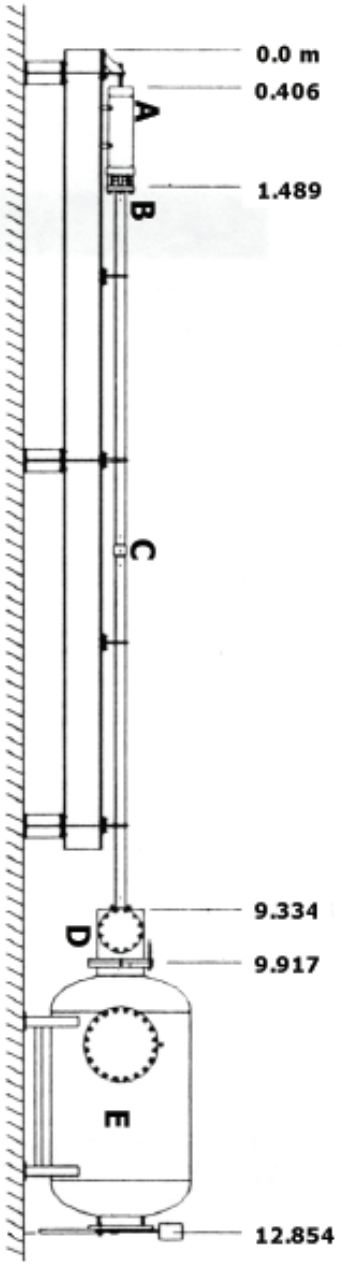

Figure 6.12: The 80 mm gas-gun at Georgia Tech, where numbers in the figure give approximate dimensions, in meters. Shown schematically are the (A) high pressure gas chamber, (B) initial location of the projectile, (C) barrel, (D) experiment chamber, and (E) soft-catch recovery tank (from [122]).

As the projectile and flyer plate exit the barrel, they immediately strike a series of pins whose distances relative to one another have been previously measured. Upon striking these pins, an electrical signal is sent to an oscilloscope which records the time at which the shorting of each pin occurs. Using the time between successive shortings and the known distance between each pin, the incoming projectile velocity was measured. Recall this quantity is one of the required measurements used in the impedance matching technique to determine the shocked state in the powder.

Immediately prior to the impact of the flyer plate with the target driver, a second series of shorting pins were activated which triggered a second series of oscilloscopes to measure the PVDF gauge and velocity interferometry responses. When impact of the projectile and the target occurs, a compressive stress wave travels through the driver and into the gauge packages and powder. The voltage signals from both the PVDF gauges and the velocity interferometry system were recorded on TDS 784 A digitizing oscilloscopes. For the PVDF gauge setup, both signals were recorded on the same oscilloscope. Similar cable lengths for each gauge allowed for a direct measurement of the time of flight between the active areas of the input and propagated gauge packages (inclusive of the powder thickness). The time of flight so measured is used to calculate shock velocity in the powder. A schematic showing approximate locations of the projectile, target fixture, and shorting pins prior to impact is given in Fig. 6.13 for the Ta + Fe_2O_3 experiments.

The impact experiment for the Ta + Bi_2O_3 mixtures looks nearly identical to that shown in Fig. 6.13, with the exception that instead of having only one ring filled with powder there are two rings, with one ring used to measure the shock velocity and the other to measure the material velocity in the powder. Unfortunately, due to internal inconsistencies in the velocity interferometer setup, material velocity measurements in these experiments were

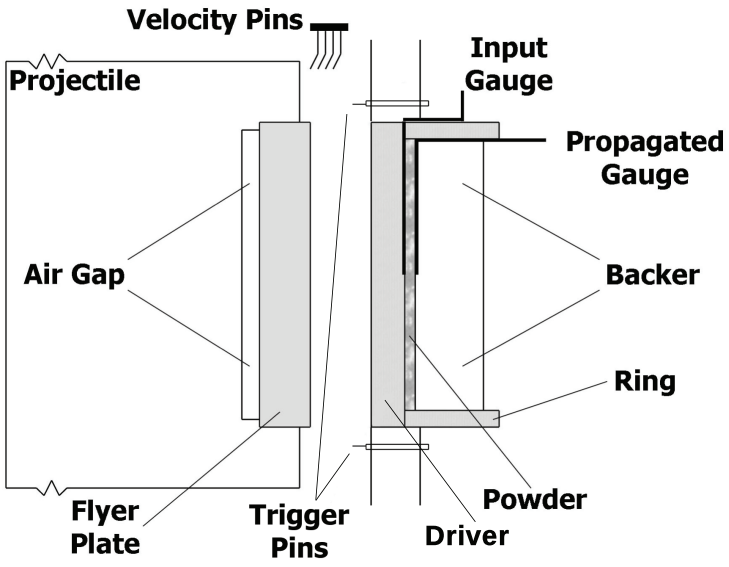

Figure 6.13: Schematic showing location of powder and gauge packages in a typical PVDF instrumented fixture as it is loaded experimentally for a dynamic compaction experiment.

not considered reliable and were not used in this analysis. In both sets of experiments impact was assumed planar and no direct measurements of tilt were made. In a separate series of experiments performed explicitly to characterize tilt in the system, the average tilt was measured to be < 2 mrad, which can result in deviations in measured shock velocities at the sub-nanosecond level.

6.8 Impedance Matching - Interpreting Measured Quantities

As instrumented, the parallel plate impact experiment measures two quantities directly; the impact velocity of the projectile (V_I), and the time of propagation of the compaction wave through the powder thickness, from which one determines the shock velocity (U_S). From measurements of only V_I and U_S, the impedance matching technique is used to fully determine the equilibrium shocked state in the powder. This technique assumes, through

the conservation equations of mass, momentum, and energy, that the stress and material velocity at the interface between the flyer and driver and driver and powder are continuous. Imposing these continuity constraints along the flyer/driver and driver/powder interfaces results in a convenient means of determining the shock state of an unknown material, provided the Hugoniots of both the flyer and driver materials are known. It should be noted that the experimental configuration is designed such that the diameter to thickness ratio of the powder mixture is large, thus ensuring one-dimensional wave propagation throughout the powder thickness, justifying use of this technique.

In this investigation, the driver and flyer materials for all experiments were composed of OHFC copper, with the exception of two experiments where the flyer was a W-6Ni-4Cu alloy obtained from Mi-Tech Metals, Inc (Indianapolis, IN). For the impedance matching technique to yield accurate results, one must know the equations of state of the flyer and driver materials with some degree of accuracy. To this end, the shock properties (ρ,C_0,S) of the flyers and drivers are obtained from references [3, 29, 120, 123, 124], where only data with material velocities less than 2 km/s are taken into account. For the Cu data taken from [29], every fifth data point is considered. Unfortunately, Hugoniot data for the W-6Ni-4Cu alloy is not readily available in the literature, and its shock properties must be determined using an isothermal mixture routine [125] similar to that presented in Sect. 2.5.2. The Cu and W-6Ni-4Cu alloy material parameters used for impedance matching calculations are given in Table 6.6, where the methodology used to obtain the parameters C_0 and S, with associated error bounds, is presented in Sect. 6.9

For a flyer impacting directly onto a driver, where Hugoniots of both materials are known, the continuity of stress and material velocity at the interface between the two is used to compute the shocked state at the flyer/driver interface in the method outlined below.

Table 6.6: Cu and W-6Ni-4Cu alloy shock parameters used in impedance matching calculations

Material	ρ (g/m^3)	C_0 (km/s)	S
Cu	8.925	3.905 ± 0.0316	1.512 ± 0.0299
W-6Ni-4Cu	17.194	3.874 ± 0.0304	1.50 ± 0.0364

In the following equations, the subscripts $'FL'$ and $'DR'$ indicate properties of the flyer and driver materials, respectively. At the flyer/driver interface stress and material velocity are constant such that

$$\sigma_{FL} = \sigma_{DR} \quad and \quad u_{P,FL} = u_{P,DR} = u_{P,1}. \tag{110}$$

where the subscript $'1'$ in $u_{P,1}$ indicates the material velocity is at the first interface. Using the linear equation of state given by Eq. 4, the stress in the flyer plate initially traveling at velocity V_I and impacting a stationary driver is

$$\sigma_{FL} = \rho_{0,FL}(C_{FL} + S_{FL}(V_I - u_{P,1}))(V_I - u_{P,1}) \tag{111}$$

where the stress in the initially stationary driver is

$$\sigma_{DR} = \rho_{0,DR}(C_{DR} + S_{DR}u_{P,1})u_{P,1}. \tag{112}$$

Substituting Eqns. 111 and 112 into the left hand side of Eq. 110 results in a quadratic equation which can be solved in terms of $u_{P,1}$. Inserting the resultant value of $u_{P,1}$ into either Eqn. 111 or 112 yields the stress at the flyer/driver interface $\sigma_{FL,DR}$. To determine the shocked state at the driver/powder interface, in the case for which the Hugoniot of the powder is unknown, the measured shock velocity is used in conjunction with the predetermined values of $u_{P,1}$ and $\sigma_{FL,DR}$. In this instance the stress in the powder is given as

$$\sigma = \rho_{00}U_S u_P \tag{113}$$

which is simply Eq. 2 with $\sigma_0 = 0$. This relationship can be represented as a straight line in σ-u_P space with a slope of $\rho_{00}U_S$ (see Fig. 6.14). Accurately determining the shocked state at the driver/powder interface requires knowledge of the either the isentropic unloading path or the reflected shock Hugoniot of the driver material. If the shock velocity in the target material is such that $\sigma > \sigma_{FL,DR}$ (see 'Target - 1' in Fig. 6.14), the shocked state in the powder falls along the reflected Hugoniot of the driver. McQueen and co-workers [1] have shown that a reflected Hugoniot centered about the point $\sigma_{FL,DR}$, $V_{FL,DR}$ can be represented by the following relation

$$\sigma_2(V) = \frac{\sigma_H - (\gamma/V)_2[(\sigma_H - \sigma_{FL,DR})(V_0 - V_2)/2]}{1 - (\gamma/V)_2(V_{FL,DR} - V_2)/2} \tag{114}$$

where σ_H is the stress on the original driver Hugoniot at volume V_2, and the original Hugoniot is centered at zero stress and $V = V_0$. Solving for the intersection of the reflected shock Hugoniot given by Eq. 114 with Eq. 113 results in the shocked state for a powder with a higher shock impedance than the driver.

For powders with lower shock impedances than the driver, the shocked state in the powder falls along the release isentrope, or reflection adiabat, of the driver. This scenario is shown in Fig. 6.14 as the line 'Target - 2'. In this instance, one must determine the intersection of Eq. 113 with an equation that describes the release isentrope in terms of material velocity. To find this intersection, one must first determine the σ-V relationship for the isentrope as it releases from the point ($\sigma_{FL,DR}$,$u_{P,1}$). This procedure can be accomplished using the relations put forth in Sect. 2.4. Once the σ-V behavior of the isentrope is known, the material velocity along this curve is determined from [41]

$$u_P = \int_{\sigma_0}^{\sigma_{FL,DR}} (-\frac{\partial V}{\partial \sigma})_S^{1/2} d\sigma. \tag{115}$$

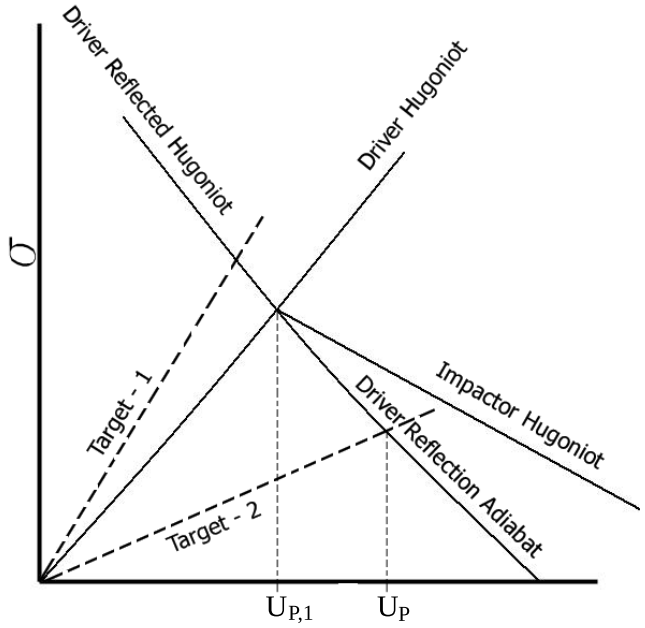

Figure 6.14: Schematic illustrating the impedance matching technique for the case of a flyer impacting a stationary driver backed by the target material.

and the results of Eq. 115 can be combined with Eq. 113 to solve for the stress and material velocity in the powder. With σ and u_P of the powder known, Eqns. 1-3 are used to determine the specific volume and internal energy of the shocked state.

6.9 Error Analysis

Quantification of error in impedance matched quantities was carried out in a manner similar to the analysis of Mitchell and Nellis [120], who examined the sources of error when an impactor (flyer) directly impacts a target material. In this section, their analysis is extended to the case where the material of interest is not impacted directly; rather the flyer impacts a driver backed by the material of interest. As such, the total error in the sample must incorporate both the error at the flyer/driver interface as well as that at the driver/powder interface. The two sources of error dealt with directly in this section are experimental (random) errors and systematic (non-random) errors. Random errors are those which result from errors in experimentally determined quantities, which in this investigation are the impact velocity V_I, initial density of the powder sample ρ_{00}, and shock velocity in the sample U_S. Systematic errors arise due to uncertainties in the predicted Hugoniots of the flyer and driver materials which are calculated based on the linear U_S-u_P relationship.

6.9.1 Systematic Uncertainties in Impedance Matching for Three Materials

To determine the systematic uncertainty in the flyer and driver Hugoniots, one must first determine the experimental uncertainty in the parameters C_0 and S used to calculate the Hugoniot through the linear equation of state, Eq. 4. This was accomplished by obtaining U_S-u_P pairs from published impedance matched data for the material of interest, e.g. [29, 120], and fitting the data using a linear least squares method. This analysis requires knowledge

of the uncertainty in U_S, $\delta\ U_S$, for each U_S-u_P pair, which in some instances may be published. However, if the uncertainty in U_S is not given, a value of 1% of the measured shock velocity is assigned, where this value is in line with the uncertainties measured by Michell and Nellis [120]. For a non-weighted linear least squares fit, the coefficients C_0 and S are found through [126]

$$C_0 = \frac{[u_P^2][U_S] - [u_P][u_P U_S]}{n[u_P^2] - [u_P]^2} \tag{116}$$

$$S = \frac{n[u_P U_S] - [u_P][U_S]}{n[u_P^2] - [u_P]^2} \tag{117}$$

where n is the number of U_S-u_P data pairs and the brackets denote summation of all a pairs, e.g. $[u_P U_S]$ is equal to $\sum_{a=1}^{n} u_{P,a} U_{S,a}$. To determine the uncertainty in each of these coefficients it is first necessary to calculate the standard deviation in shock velocity σ_{U_S} about the line defined by C_0 and S. Assuming the coefficients were determined from all possible U_S-u_P pairs, this is defined as [126]

$$\sigma_{U_S} = \sqrt{\frac{[\delta\ U_S^2]}{n-2}} \tag{118}$$

where the $\delta\ U_S^2$ for each U_S-u_P pair is either given or assumed as 1 % of the measured value of U_S. The standard deviation in each coefficient is determined from the root of the sum of the squares of the standard deviation in shock velocity (given by Eq. 118) multiplied by the derivative of the coefficient with respect to $U_{S,a}$. This results in the standard deviations [127]

$$\sigma_{C_0} = \sigma_{U_S} \sqrt{\frac{[u_P^2]}{n[u_P^2] - [u_P]^2}} \tag{119}$$

$$\sigma_S = \sigma_{U_S} \sqrt{\frac{[n]}{n[u_P^2] - [u_P]^2}} \tag{120}$$

These equations are applied directly to the Cu flyer and driver materials; however, the analysis is complicated somewhat for the W-6Ni-4Cu alloy. For this alloy, the C_0 and S values of its constituents are first determined using the method outlined above, and a mixing routine (similar to that outlined in Sect. 2.5.2) is applied to determine the corresponding properties of the alloy. The uncertainties in C_0 and S reported in Table 6.6 for the alloy are simply the quadrature addition of the individual errors in C_0 and S for its constituents, taking into account the correct mass fraction of each material.

Having computed the coefficients C_0 and S, whose values inherently possess some degree of uncertainty, it is not unexpected that a predicted value of U_S using the relation $U_S = C_0 + S\,u_P$ will also contain some level of uncertainty. Determining the uncertainty in the predicted shock velocity $U_{S,0}$ for a given $u_{P,0}$ is carried out through [127]

$$\sigma_0 = \sigma_{U_S} \sqrt{\frac{[u_P^2] - 2u_{P,0}[u_P] + nu_{P,0}^2}{n[u_P^2] - [u_P]^2}} \tag{121}$$

which can be used to estimate the uncertainty in U_S at any given u_P. A value of twice the standard deviation so determined, $2\sigma_0$, is fit to a third order polynomial of the form

$$2\sigma_0 = A_0 + A_1 u_P + A_2 u_P^2 + A_3 u_P^3 \tag{122}$$

where the coefficients A_0, A_1, A_2, and A_3 are fitting parameters. The systematic uncertainty in Cu is obtained directly from the method outlined above. For the W-6Ni-4Cu alloy, the $2\sigma_0$ relation as a function of u_P is determined using Eq. 122 for each of its constituents. The resultant $2\sigma_0$ for each constituent is then multiplied by its respective mass fraction, and the errors in each constituent are added together in quadrature to yield $2\sigma_0$ for the alloy. The values for the coefficients A_0, A_1, A_2, and A_3 used in this investigation are given in Table 6.7. From Eq. 122 the systematic error in the flyer and driver can be represented by a band of uncertainty in the stress-material velocity plane, as shown in Fig. 6.15.

Table 6.7: Parameters used to calculate systematic uncertainties in Cu and W-6Ni-4Cu. Coefficients are determined from U_S-u_P data in km/s.

Material	A_0	A_1	A_2	A_3
Cu	3.5234 x10^{-2}	-2.6175 x10^{-2}	2.7992 x10^{-2}	-2.3090 x10^{-3}
W-6Ni-4Cu	4.1757 x10^{-2}	-1.2611 x10^{-3}	1.6614 x10^{-5}	-2.7835 x10^{-8}

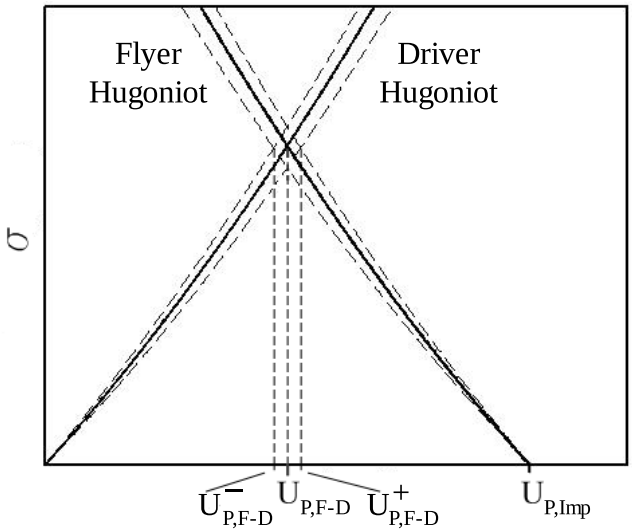

Figure 6.15: Bands of uncertainty in flyer and driver calculated using the relation U_S =$(C_0 + 2\sigma_0) + S$ and $U_S = (C_0 - 2\sigma_0) + S$.

Examining Fig. 6.15, it is evident that some finite amount uncertainty in the equilibrium material velocity predicted at the interface between the flyer and driver exists. To determine this systematic uncertainty, $\delta u^S_{P,F-D}$, the value of $2\sigma_0$ at $u_{P,F-D}$ is determined using Eq. 122 and C_0 is replaced with some combination of $C_0 \pm 2\sigma_0$ in the linear equation of state for the flyer and driver materials. The value of $u^-_{P,F-D}$ (Fig. 6.15) is obtained using C_0 - $2\sigma_0$ for the flyer and C_0 + $2\sigma_0$ for the driver, and $u^+_{P,F-D}$ is obtained using C_0 + $2\sigma_0$ for the flyer and C_0 - $2\sigma_0$ for the driver.

The uncertainty in the driver Hugoniot must also be imposed upon its release isentrope,

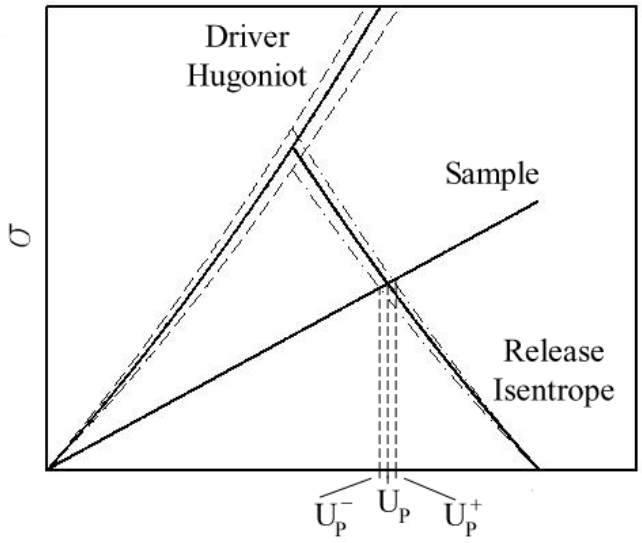

Figure 6.16: Schematic illustrating uncertainty bands in the release isentrope calculated by replacing C_0 with $C_0 + 2\sigma_0$ and $C_0 - 2\sigma_0$.

which results in a finite amount of systematic uncertainty in the powder material velocity. The uncertainty already determined at $u_{P,F-D}$ through Eq. 122 is applied directly to the release isentrope, resulting in a band of uncertainty around the isentrope, as shown in Fig. 6.16. The upper and lower uncertainty bounds along the isentrope are calculated by setting $C_0 = C_0 + 2\sigma_0$ and $C_0 = C_0$ - $2\sigma_0$ into the $\sigma - V$ isentrope relation, where the value of $2\sigma_0$ is that calculated at $u_{P,F-D}$. The terms u_P^+ and u_P^- are determined from the intersection of the line defined by the slope $\rho_{00}U_S$ with their respective bounding curve. The systematic uncertainty in the powder sample resulting from uncertainty in the release isentrope is thus $\delta\, u_P^S = 1/2\ |u_P^+ - u_P^-|$. Combining the two systematic uncertainties in quadrature, the total systematic uncertainty in material velocity for the powder sample resulting from systematic uncertainties at the flyer/driver and driver/sample interfaces is

$$\delta\, u_P^S = [(\delta\, u_{P,F-D}^S)^2 + (\delta\, u_P^S)^2]^{1/2} \tag{123}$$

where Eq. 123 is used throughout the remainder of the calculations to determine systematic uncertainties in all other properties of interest.

6.9.2 Remaining Uncertainties

With systematic uncertainties in the flyer and driver materials accounted for in their respective Hugoniots and isentropes, the additional complexity introduced by performing impedance matching calculations on three materials (instead of two as in Mitchell and Nellis [120]) has been accounted for. As such, the remainder of this analysis follows directly from Mitchell and Nellis [120] as all other uncertainties are either determined directly from measured quantities in the powder or can be inferred from the value of $\delta\, u_P$ given by Eq. 125.

The experimental error in material velocity results from uncertainties in measured quantities and is defined through quadrature as

$$\delta\, u_P^E = [\ (\delta\, u_P(U_S))^2\ +\ (\delta\, u_P(V_I))^2\ +\ (\delta\, u_P(\rho_{00}))^2\ ]^{1/2} \tag{124}$$

To determine each of the $\delta\, u_P$ terms in Eq. 124, the maximum and minimum measured values for each quantity is individually inserted into the impedance matching calculation and a corresponding value of u_P is determined. The maximum and minimum values are then combined to yield $\delta\, u_P(X) = 1/2\ |u_P^+(X) - u_P^-(X)|$ for the measured quantity X, and the individual uncertainties are combined through Eq. 124. The total uncertainty in powder/sample material velocity is given by the addition of both the systematic and experimental uncertainties

$$\delta\, u_P = \delta\, u_P^E + \delta\, u_P^S. \tag{125}$$

The total fractional uncertainty in stress $\delta\,\sigma/\sigma$ is again a combination of its experimental and systematic uncertainties through [120]

$$\frac{\delta\,\sigma}{\sigma} = \left(\frac{\delta\,\sigma}{\sigma}\right)_E + \left(\frac{\delta\,\sigma}{\sigma}\right)_S \tag{126}$$

where the experimental uncertainty is given by

$$\left(\frac{\delta\,\sigma}{\sigma}\right)_E = \left[\left(1+\frac{U_S}{u_P}\frac{\partial\,u_P}{\partial\,U_S}\right)^2\left(\frac{\delta\,U_S}{U_S}\right)^2 + \left(1+\frac{\rho_{00}}{u_P}\frac{\partial\,u_P}{\partial\,\rho_{00}}\right)^2\left(\frac{\delta\,\rho_{00}}{\rho_{00}}\right)^2 + \left(\frac{\delta\,u_P(V_I)}{u_P}\right)^2\right]^{1/2}$$

and the systematic uncertainty is

$$\left(\frac{\delta\,\sigma}{\sigma}\right)_S = \frac{|\delta\,u_P|}{u_P} \tag{127}$$

In a similar fashion, the fractional uncertainty in specific volume is the sum of its experimental and systematic uncertainties where experimental uncertainty is given by [120]

$$\left(\frac{\delta\,V}{V}\right)_E = \left[(\eta-1)^2\left(1-\frac{U_S}{u_P}\frac{\partial\,u_P}{\partial\,U_S}\right)^2\left(\frac{\delta\,U_S}{U_S}\right)^2 + \left(1+(\eta-1)\frac{\rho_{00}}{u_P}\frac{\partial\,u_P}{\partial\,\rho_{00}}\right)^2\left(\frac{\delta\,\rho_{00}}{\rho_{00}}\right)^2 + (\eta-1)^2\left(\frac{\delta\,u_P(V_I)}{u_P}\right)^2\right]^{1/2}$$

and the systematic uncertainty is [120]

$$\left(\frac{\delta\,V}{V}\right)_S = (\eta-1)\frac{|\delta\,u_P^S|}{u_P} \tag{128}$$

where η is a measure of powder compression $\eta = \rho/\rho_{00}$. The total fractional uncertainty in specific internal energy is defined using Eq. 125 as [120]

$$\frac{\delta\,E}{E} = 2\frac{\delta\,u_P}{u_P} \tag{129}$$

The final source of error is that resulting from the uncertainty in shock velocity. In the experiments performed in the present work the shock velocity is obtained from the relation

$U_S = \Delta\ x/\Delta\ t$, where $\Delta\ x$ is the thickness of the powder sample and $\Delta\ t$ is the time it takes for the compaction wave to traverse the powder thickness. The uncertainty in powder thickness $\delta(\Delta\ x)$ is taken as twice the standard deviation in powder thickness if multiple measurements of the thickness are obtained, or as twice the value of the finest increment of the measuring device, which is 50.8 μm, if only one measurement of the thickness is recorded. The uncertainty in transit time $\delta(\Delta\ t)$ is determined from the measurements $\Delta\ t_R$ and $\Delta\ t_F$, where the subscripts R and F indicate that the respective transit time is determined from the the rise (R) and fall (F) of the current trace, as detailed in Sect. 7.2.3. Here, the total uncertainty in transit time is defined as twice the standard deviation through

$$\delta(\Delta\ t) = |\Delta\ t_F - \Delta\ t_F| \tag{130}$$

Therefore, the fractional standard deviation in shock velocity is given as

$$\frac{\delta\ U_S}{U_S} = \left[\left(\frac{\delta(\Delta\ x)}{\Delta\ x} \right)^2 + \left(\frac{\delta(\Delta\ t)}{\Delta\ t} \right)^2 \right]^{1/2} \tag{131}$$

where U_S is determined from $\Delta\ t_P$, the transit time at the peak of the current trace. With regard to the different sources of error, those due to variations in measured impact velocity and transit time through the powder tend to cause to the largest uncertainties.

CHAPTER VII

COMPRESSION OF THERMITE POWDER MIXTURES

The experimental procedures outlined in the previous chapter have been carried out on the Ta + Fe_2O_3 and Ta + Bi_2O_3 powder mixtures. The focus of this chapter is to present the results of these experiments and evaluate the applicability of existing equations of state and compaction models, both quasi-static and dynamic, to describe the compaction behavior of the highly heterogeneous thermite powder mixtures. As such, this chapter begins by presenting results from the quasi-static and dynamic compaction experiments in various forms; looking first at the raw data, and then at model fits to the experimental data. Of specific interest will be the ability of the equations of state (EOS) and compaction models to adequately describe the experimentally observed compaction behavior, specifically the crush strength.

7.1 Results of Quasi-Static Compaction of Reactant Powders

Quasi-static compaction yields information about the consolidation behavior of materials in the absence of rate effects. Prior to examining the crush up response of the powder mixtures, it is instructive to first examine that same response for the individual constituents. Thus, by examining the compaction response of the constituents, one can gain insight into some of the compaction mechanisms occurring in the mixtures and determine if any one of the components is dominating the compaction process. The stress versus density (defined as percent theoretical density, % TMD) compaction curves for each of the three powder constituents are shown in Figs. 7.1-7.3. Also shown are fits of the compaction data to the

P-σ_Y [20], P-P_{Act} [58], and the modified Kawikata [13] models. Fitting parameters to the respective models/relations are given in Table 7.1

In examining Fig. 7.1 it is evident that the P-σ_Y model fits each of the constituents to varying degrees. The compaction behavior of Ta is well characterized by the P-σ_Y model, while the oxide powders are less well characterized; a trait attributed to the minimal amount of plastic deformation that occurs during the compaction of brittle oxide powders. Of the two oxides, the P-σ_Y model has the poorest fit to the Fe_2O_3 data.

Comparatively, the P-P_{Act} model fits shown in Fig. 7.2 appear to follow the compaction data much closer for all materials. For the fit shown, the P-P_{Act} model is that for a single pressure (stress) barrier. The goodness of fit shown in Fig. 7.2 suggests that all the powders can be described fairly well by a stress activated and a non-stress activated component in the range of applied stress. It should be noted that inspection of the model parameters for Fe_2O_3 indicates the best fit for the activation stress (P_a = 1150 MPa) occurs above of the stress range investigated. Though Kenkre and co-workers [58] find similar results in some of the powders they investigated initially, the fact that the stress activated value lies outside of the range of experimentally collected values brings the physical basis of the single stress activated value into question. The fact that compaction of Fe_2O_3 may not be well described by a single activation stress is not too surprising when one considers the initial morphology of the particles, which are large agglomerates (>10 μm) of much smaller particles. In this instance, consolidation is likely to be dominated by the breakup of agglomerates at low stresses followed by the fracture and rearrangement of the actual particles at greater stresses.

The modified Kawikata fits to the experimental data are given in Fig. 7.3. For this fitting procedure, the initial density of the starting powder, ρ_{00}, is allowed to vary to achieve

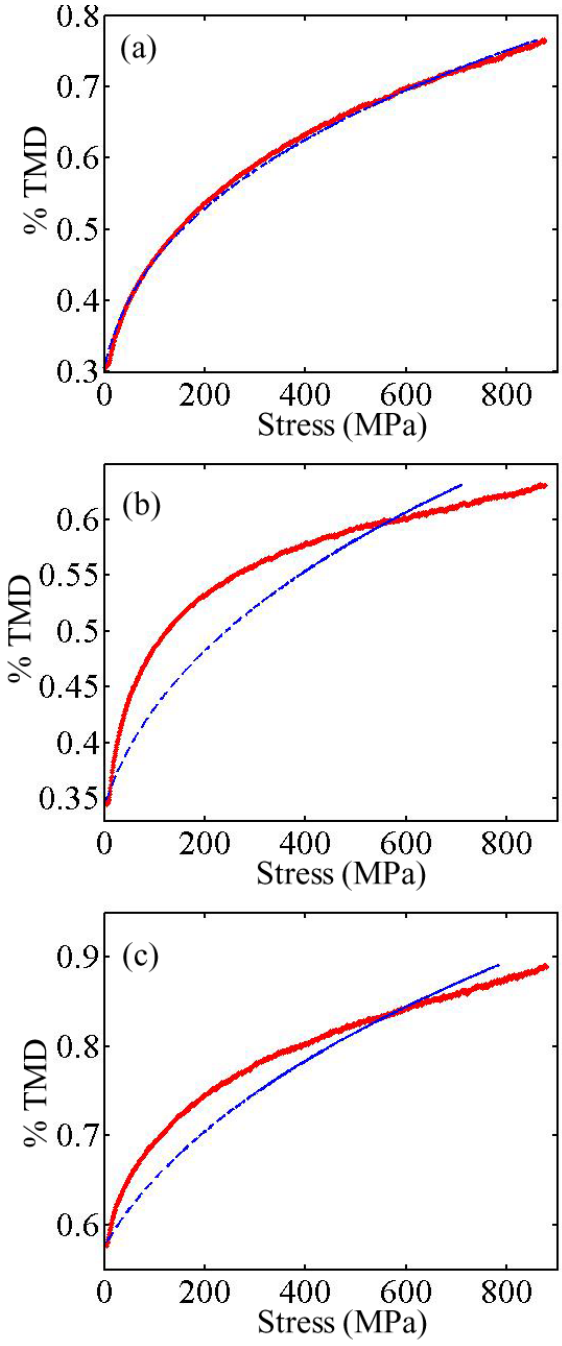

Figure 7.1: Quasi-static compaction curves for (a) Ta, (b) Fe_2O_3, and (c) Bi_2O_3 shown by broad (red) line. Fits of the data to the P-σ_Y model are illustrated by the dashed (blue) line.

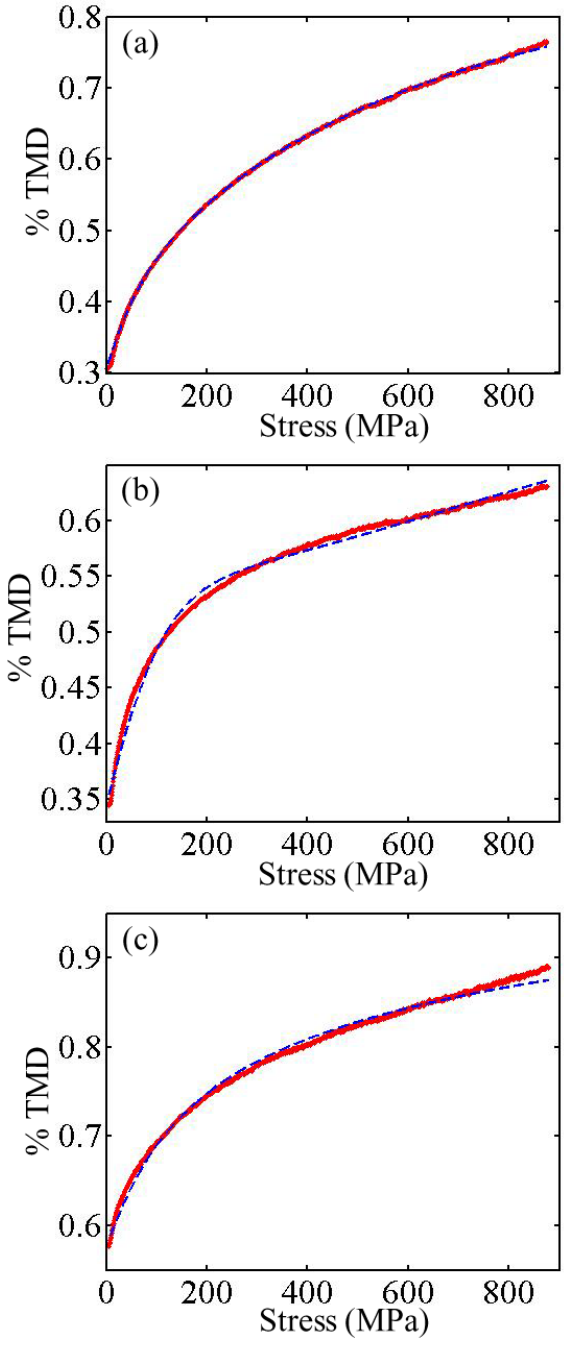

Figure 7.2: Quasi-static compaction curves for (a) Ta, (b) Fe_2O_3, and (c) Bi_2O_3 shown by broad (red) line. Fits of the data to the P-P_{Act} model are illustrated by the dashed (blue) line.

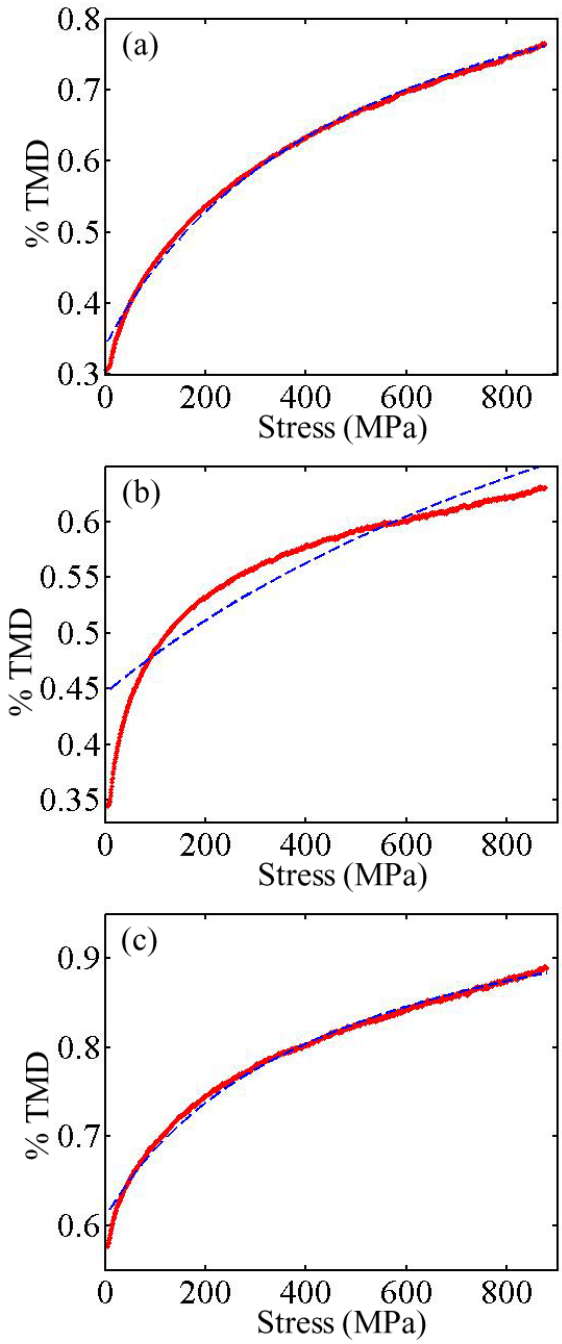

Figure 7.3: Quasi-static compaction curves for (a) Ta, (b) Fe_2O_3, and (c) Bi_2O_3 shown by broad (red) line. Fits of the data to the modified Kawikata equation [13] are illustrated by the dashed (blue) line.

Table 7.1: Fitting parameters for experimental data of Ta, Fe_2O_3, and Bi_2O_3 to the P-σ_Y, P-P_{Act}, and modified Kawikata models.

Material	Measured	P-σ_Y	P-P_{Act}			Mod. Kawikata		
	ρ_{00} (% TMD)	σ_{YS} (MPa)	C	P_a (MPa)	P_l (MPa)	K (MPa)	ρ_{00} (% TMD)	b (MPa^{-1})
Ta	30.5	744.5	0.5276	308	48.2	194100	34.0	5.865 x10^{-3}
Fe_2O_3	34.4	1369	0.5893	1150	72.5	206600	44.6	1.497 x10^{-3}
Bi_2O_3	57.6	446.6	0.5760	537	90.4	62730	60.8	4.009 x10^{-3}

the best fit with the data under the stipulation that the parameter $'a'$ follows the behavior $a = \rho_{00}/\rho_{s0}$ set forth by Petrie and Page [13]. One can see that by slightly adjusting ρ_{00} from its actual value allows for a good fit to the Ta and Bi_2O_3 compaction data over almost the entire stress range investigated. This is not so for Fe_2O_3, whose compaction behavior is less well represented by the modified Kawikata relationship. Again, the presence of agglomerates is thought to significantly effect the consolidation response and result in a poor fit with the model.

Having examined the compression response of the individual powders in light of the aforementioned compaction models, attention now shifts to the quasi-static compression behavior of the powder mixtures. Compaction curves for the Ta + Fe_2O_3 and Ta + Bi_2O_3 mixtures as well as fits of the data to the P-σ_Y, P-P_{Act}, and modified Kawikata models are shown in Figs. 7.4-7.5. Model parameters resulting in a best fit to the experimental data are given in Table 7.2.

Experimental quasi-static compaction data for the Ta + Fe_2O_3 mixture is shown in Fig. 7.4 and is marked by two nearly linear regions separated by a region of steadily increasing stiffness. At stresses below approximately 100 MPa density increases quasi-linearly, at which point further increases in stress result in continuously reduced increases in density. Furthermore, at stresses above approximately 400 MPa ($\rho \approx 65\%$ TMD) linearity resumes, although in this stress range the slope has decreased. If one recalls the SEM image of the Ta + Fe_2O_3 mixture shown in Fig. 6.7(a), postulations on the physical basis of the curvature shown in Fig. 7.4 can be made.

The initial linear region in the Ta + Fe_2O_3 mixture is likely attributed to the breakup of Fe_2O_3 agglomerates. Figure 6.7(a) clearly shows Fe_2O_3 agglomerating and completely surrounding the Ta particles. These agglomerates, formed as a result of van Der Waals

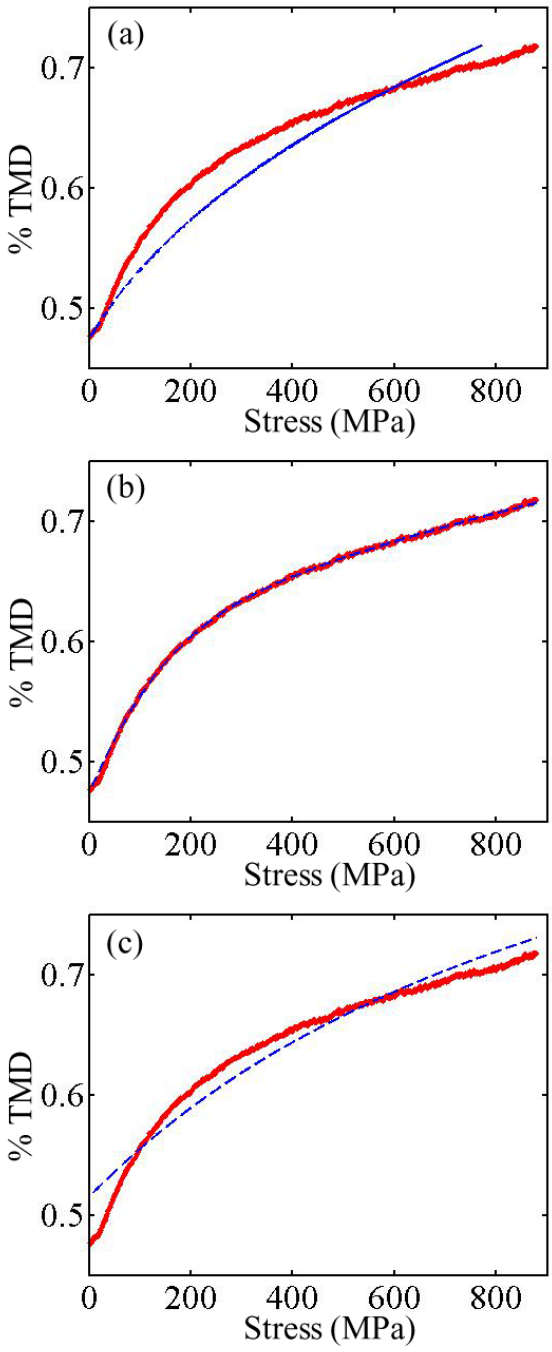

Figure 7.4: Quasi-static compaction of Ta + Fe_2O_3 fit to the (a) P-σ_Y, (b) P-P_{Act}, and (c) modified Kawikata models. Experimental data is represented by the broad (red) line, and fits to the models are shown by the dashed (blue) line.

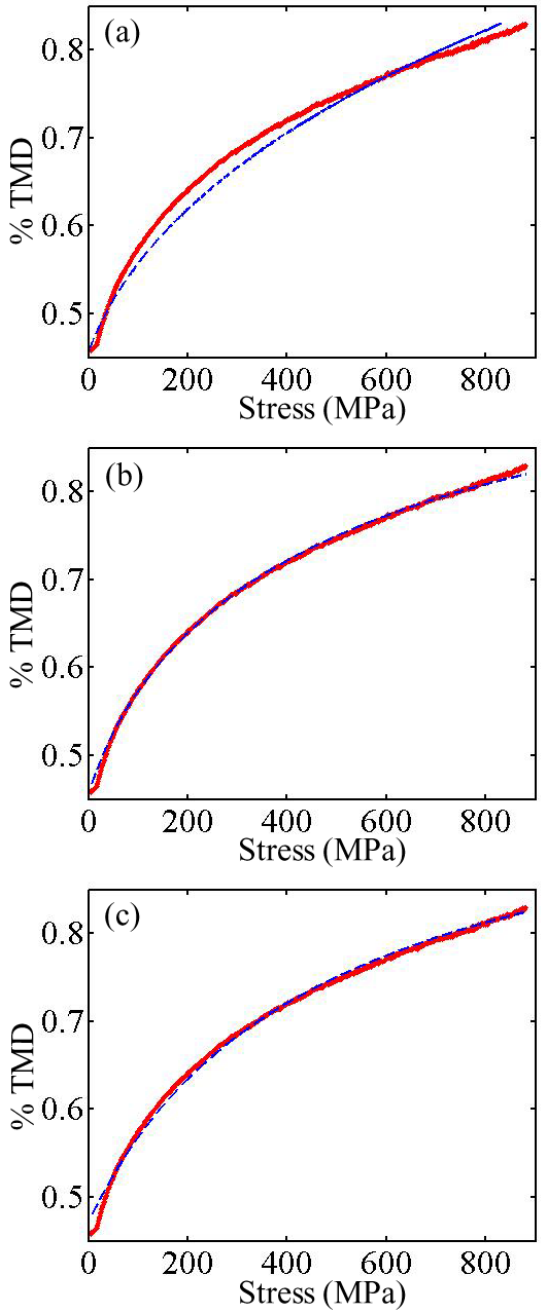

Figure 7.5: Quasi-static compaction of Ta + Bi_2O_3 fit to the (a) P-σ_Y, (b) P-P_{Act}, and (c) modified Kawikata models. Experimental data is represented by the broad (red) line, and fits to the models are shown by the dashed (blue) line.

Table 7.2: Fitting parameters for experimental data of Ta + Fe_2O_3 and Ta + Bi_2O_3 to the P-σ_Y, P-P_{Act}, and modified Kawikata models.

Material	Solid	Measured	P-σ_Y	P-P_{Act}			Mod. Kawikata		
	ρ (g/cm^3)	ρ_{00} (% TMD)	σ_{YS} (MPa)	C	P_a (MPa)	P_l (MPa)	K (MPa)	ρ_{00} (% TMD)	b (MPa^{-1})
Ta + Fe_2O_3	10.967	.474	1084	0.5337	1283	138.4	200350	51.5	1.748 x10^{-3}
Ta + Bi_2O_3	12.931	0.457	590.5	0.4746	381.3	70.4	128415	47.2	4.692 x10^{-3}

and electrostatic forces, are easily broken under low applied stresses and are most likely responsible for the initial linear region of compression. Following breakup of the initial agglomerates, the region of increasing stiffness observed in Fig. 7.4 is a likely result of the competing processes of rearrangement, fracture and deformation as the compact forms a continuous network of stress bridging particles. As stress increases further, it becomes distributed quasi-homogeneously throughout the compact, and consolidation of the bulk occurs by deformation and fracture of the primary particles. In this region, densification proceeds linearly with increasing stress.

Keeping the aforementioned compaction mechanisms in mind, a look is now given at how well the P-σ_Y, P-P_{Act}, and modified Kawikata models capture these trends. One can see that both the P-σ_Y (Fig. 7.4(a)) and the modified Kawikata (Fig. 7.4(c)) fits to the experimental data are rather poor. In both instances, the model over predicts the density which can be achieved at a given stress level for $\sigma > 600$ MPa, where over prediction is greater for the P-σ_Y model. One reason for the greater over prediction of the P-σ_Y model is that the P-σ_Y model only has one adjustable fitting parameter, the yield strength σ_{YS}. If the initial density ρ_{00} is allowed to vary in the P-σ_Y model as it is in the modified Kawikata model, the two fits closely resemble one another and predict a nearly identical compaction response (not shown in Fig.7.4).

The P-P_{Act} fit shown in Fig. 7.4(b) more closely resembles actual compaction data for the Ta + Fe_2O_3 powder mixture. The question naturally arises, does this model predict well the physical phenomena that occurs during compaction, or is this merely a case of having an adequate number of fitting parameters such that model prediction can align with experiment without substantial physical meaning? Answering this question requires one to examine values of the fitting parameters given in Table 7.2. Assuming a single stress

activated process of compaction, the P-P_{Act} model predicts a rearrangement threshold of P_l = 138.4 MPa and stress activated process at P_a = 1283 MPa. Inserting these values into the P-P_{Act} equation, results in these processes becoming dominant at relative densities of 0.576 and 0.753, respectively. This suggests that rearrangement is the dominant mechanism by which compaction proceeds near densities of 0.58 % TMD, and that a single stress activated process would not become dominant until approximately 0.75 % TMD. While rearrangement may likely be the dominant mechanism near 0.58 % TMD, it is unlikely that no stress activated processes occur until stress and density reach 1283 MPa and 0.75 % TMD. Thus, while the P-P_{Act} model follows the experimental compaction behavior of Ta + Fe_2O_3 quite well, and may well yield good predictions for particle rearrangement, it is believed that the single stress activated form of the P-P_{Act} model does not reflect the underlying physical mechanism responsible for compaction as stress increases.

Turning now to the Ta + Bi_2O_3 powder mixture, one can see distinct differences in the compaction behavior of this mixture, as shown in Fig. 7.5. One of the major differences between the two systems is the absence of a linear densification region in the low stress regime. For the Ta + Bi_2O_3 mixture, the rate of change in density with applied stress continuously decreases up to approximately 500 MPa, at which point further increases in stress result in a linear increase in density.

One of the major distinctions between the two physical mixtures is the absence of a large agglomerate structure of oxide particles in the Ta + Bi_2O_3 mixture. The micrograph in Fig. 6.7(b) clearly shows discrete particles of both Ta and Bi_2O_3, with Ta shown to slightly clump together and form an agglomerate structure. Moreover, as the density of Ta is almost three times that of Fe_2O_3 it is supposed that the Ta agglomerates will breakup at much lower applied stresses than the oxide agglomerates in the previous mixture. As

a result, one does not see the linear compaction region at low stresses in this mixture as the breakup of agglomerates is not believed to be the primary mode of compaction at these stresses. Rather, the continuously increasing stiffness which is observed at stresses below 500 MPa is likely a result of rearrangement and a minimal amount of primary particle deformation as the compact increasingly becomes a complete network of stress bridging particles. After the formation of this network, densification proceeds linearly with increases in stress through the deformation and fracture of primary particles.

With the breakup of agglomerates not being the primary densification mode at low stresses for the Ta + Bi_2O_3 mixture, it is expected that the P-σ_Y, P-P_{Act}, and modified Kawikata models will perform better on the Ta + Bi_2O_3 system than they did on the Ta + Fe_2O_3 system. This hypothesis is clearly proven in the case of both the P-σ_Y and modified Kawikata models as model fits are much closer to actual experimental data. However, similar to the previous case, the P-σ_Y model still offers the poorest fit to the data. This model under predicts the compacted density at stresses below approximately 600 MPa, and over predicts as stress increases beyond this point. Again, this results from the constraint imposed by the initial density, and a much better fit results if ρ_{00} is allowed to vary.

Both the P-P_{Act} and the modified Kawikata models offer exceptionally good fits to the experimental data for the Ta + Bi_2O_3 system. With the bulk modulus K of the powder set (determined through a volume fraction averaged rule of mixtures), adjustable parameters in the modified Kawikata model are the initial density ρ_{00} and stiffness parameter b. By increasing ρ_{00} only slightly, the modified Kawikata model is able to predict closely the experimental densification behavior at all but only the lowest values of stress, as shown in Fig. 7.5(c). With the fit value of ρ_{00} not having a true physical basis, one looks to the

stiffness parameter, which has units equivalent to the inverse of stress, to reflect some aspect of the mechanical behavior of the mixture. Unfortunately, no substantive correlations between the parameter b and the mechanical properties of the compacts it describes have been found [64,128]. However, it is observed that the value of b for the Ta + Bi_2O_3 mixture (see Table 7.2) does lie close to the midpoint of the values of b reported for its constituents (see Table 7.1).

Of the equations examined, the P-P_{Act} model allows for the best fit with experimental data. Again, if only rearrangement and a single stress activated process are considered, these processes are determined to be the dominant compaction mechanisms at σ = 70.4, ρ = 0.55 and σ = 381.3 MPa, ρ = 0.72 % TMD, respectively. This implies that both rearrangement and the stress activated process occur within the stress range investigated. Just what is the stress activated process? The P-P_{Act} model does not give specifics as to what this process is; it just notes that the process exists. For the case of the Ta + Bi_2O_3 mixture, shown in Fig. 7.5(b), this process is likely the initial bridging of particles as a continuous network of particles begins to form. As stresses proceed beyond this point, a minor amount of rearrangement will occur, but it is predominantly the deformation and fracture of particles which result in increases in density.

If one considers all the compaction models with regard to their ability to describe the densification behavior of the individual constituents, Ta is by far the best fit material by all the models. After Ta, Bi_2O_3 shows the next best fit, and the poorest fit material is Fe_2O_3. Accordingly, one might expect that mixtures containing Fe_2O_3 would also be poorly fit by these models. This is certainly true for the P-σ_Y and modified Kawikata models, whose fits poorly reflect the curvature observed experimentally during quasi-static compaction of Ta + Fe_2O_3 mixtures. Conversely, the P-P_{Act} model fits the Ta + Fe_2O_3 mixture quite

well, where the goodness of fit for this mixture is attributed to the similar goodness of fit to its constituents. It is important to note that this model, while predicting a stress activated process well out of the range of experimental data, does give an estimate as to the stress range where particle rearrangement is presumed to be the dominant compaction mechanism.

With the consolidation behavior of both Ta and Bi_2O_3 being fairly well characterized by all the compaction models investigated, it is not surprising that the mixtures of these components are also fairly well characterized by these same models. The model suffering the greatest as a result of the two components being mixed is the P-σ_Y model. The lack of agreement found with this model is due in part to the brittle nature of the Bi_2O_3 particles, which causes the contact point deformation assumption underlining the P-σ_Y model to break down. Better fits are offered by the P-P_{Act} and modified Kawikata models. Of these models, the modified Kawikata model is largely empirical in nature and offers no quantitative information about the mechanical and/or yield properties of the compact. The main use of this model is as a component of the equation of state for the mixture put forth by Petrie and Page [13]. The P-P_{Act} model does, however, yield information about the dominant stress range for rearrangement, which will be useful in further analysis.

Ideally, in describing the quasi-static compaction behavior of powder mixtures, one would like to be able to determine two things. One, at what point of stress(σ) and/or density (ρ) the bulk of rearrangement has occurred and the compact has formed a quasi-continuous network of stress bridging particles. Two, what are the yield properties of the mixture once this continuous network of particles has formed. From these two pieces of information, one might be able to use the data collected quasi-statically to aid in predicting the consolidation behavior of the mixture in the dynamic regime. Unfortunately, none of

the models covered thus far can provide both of the desired quantities. The P-P_{Act} model, while yielding information regarding particle rearrangement, does not offer any insight into the yield properties of the mixture once it has formed a continuous network. Conversely, the P-σ_Y model gives information regarding the yield behavior of the mixture; however, significant particle rearrangement occurs within this predicted yield behavior, and correspondingly the model tends to over predict the density achievable at higher stresses. The question then arises, can these models be combined to form a hybrid model or analysis technique that will allow for both of the aforementioned quantities to be determined? This question will be dealt with specifically in the next chapter.

7.2 Dynamic Compaction Results

In examining the results of dynamic compaction experiments, it is first necessary to have a general idea as to what the equilibrium equation of state response of the thermite powder mixture will be as predicted through the various compaction models outlined in the previous chapters. As such, this section begins with a discussion of the relevant porous equations of state as they pertain to each of the thermite mixtures. Following that, results and analysis techniques for the parallel plate impact experiments performed in this work are presented, and comparisons are made between experimental data and the equilibrium predicted response. Finally, data in the crush-up region will be fit using existing compaction models and correlations will be described in light of the ability of these models to adequately describe the dynamic compaction response of heterogeneous thermite powder mixtures.

7.2.1 Equilibrium Equation of State Response

When porous mixtures of Ta + Fe_2O_3 and Ta + Bi_2O_3 are subjected to steady-state shock loading, it is assumed that material behind the shock front is in a state of equilibrium. This implies that both materials in the mixture experience similar stresses, material velocities, etc., and that the response of the mixture can be described by a single equilibrium equation of state (EOS). Several different methods of determining the equilibrium EOS have been covered, and their applicability to each of the mixtures is now investigated. However, prior to this analysis one must first define certain initial and averaged properties for the mixtures.

As reported in Section 6.4, the Ta + Fe_2O_3 and Ta + Bi_2O_3 mixtures investigated were prepared using equal volumes of each constituent. With knowledge of constituent density, mass fractions for each component are computed and used to determine other averaged mixture quantities. The first averaged quantity to be discussed is the zero stress density of the mixture. Following the rule of mixtures used by McQueen and co-workers [1], the standard density of the mixture ρ_0 is determined by the summation of the mass fractions of the volumes of the individual components i through [1]

$$1/\rho_0 = V_0 = \sum X_i V_{0,i} \tag{132}$$

where the subscripts 0 and i indicate the standard (zero stress) condition and properties of the individual component, respectively, and X is the mass fraction. Similarly, the Grüneisen coefficient of the mixture γ_0 is given by [1]

$$V_0/\gamma_0 = \sum X_i (V_{0,i}/\gamma_i) \tag{133}$$

The average bulk modulus K (given in Table 7.2) is determined using a volume fraction average

$$K = \sum Y_i K_i \tag{134}$$

where Y_i is the volume fraction of each component, which in all cases is equivalent to 0.5. Also of great importance in determining the equilibrium equations of state for the mixtures is the initial porous density ρ_{00}. For the Ta + Fe_2O_3 mixture the targeted initial density was approximately 49 % TMD, and for the Ta + Bi_2O_3 mixture it was 62 % TMD. The initial and averaged quantities used throughout the different equilibrium EOS calculations are given in Table 7.3. Note that only the mass fraction of Ta is given in Table 7.3, as the mass fraction of the oxide component is determined by the summation of both being equavalent to one.

Table 7.3: Initial and averaged properties for Ta + Fe_2O_3 and Ta + Bi_2O_3 shock compacted mixtures.

	X_{Ta}	ρ_0 (g/cm^3)	ρ_{00} (g/cm^3)	γ_0
Ta + Fe_2O_3	0.7569	10.968	5.367	1.827
Ta + Bi_2O_3	0.6442	12.931	7.945	1.097

7.2.1.1 Solid Mixture EOS

Prior to the additional complexity of incorporating porosity, equations of state for the solid mixtures are presented. To this end, only the isothermal mixing method of McQueen and co-workers [1] and the energy partitioning method of Krueger and Vreeland [44] are developed, as these methods are considered to be more accurate than the other approximate relations. The isothermal mixing method used to predict the equilibrium EOS response for the solid mixtures is performed at zero Kelvin, where the methodology used for these calculations can be found in Sects. 2.3.1 and 2.5.2. Similarly, the method for determining the energy partitioned EOS can be found in Sect. 2.5.4.

A list of the relevant material parameters for these models is given in Table 7.4. Note

that certain values in Table 7.4 have been defined previously, yet are given again at this juncture for the sake of completeness. All parameters listed in Table 7.4 have been previously derived in their respective sections, with the exception of the isothermal bulk modulus K_0 and its stress derivative K_0'. These two quantities are determined using the Murhaghan [108] EOS given by Eq. 105, which was presented in Sect.6.2. Calculations of the solid mixture Hugoniot are performed using MATLAB [91] with scripts similar to those given in Appendix A.1.

Table 7.4: Model parameters used to calculate the solid mixture EOS from the isothermal mass mixing [1] and energy partitioning [44] relations.

Property	Units	Ta	Fe_2O_3	Bi_2O_3
ρ_0	kg/m^3	16660	5274	9202
C_0	m/s	3293	6258	2611
S		1.307	1.371	1.227
γ_0		1.689	1.990	0.812
$3NK$	at-J/kg-K	137.8	156.2	53.5
C_V	J/kg-K	140	650	236
θ_D	K	231.1	128.5	43.2
E_{0H}	J/kg	29677	38677	14827
E_{0K}	J/kg	0	0	0
V_{0K}	m^3/kg	5.97488 x10^{-5}	1.89238 x10^{-4}	1.08481 x10^{-4}
σ_0	kg-m^2/s^2	0	0	0
T_0	K	293	293	293
K_0	kg-m^2/s^2	183.6 x10^9	208.4 x10^9	62.9 x10^9
K_0'		4.036	4.324	3.955

Results from the two mixing routines are shown in Fig. 7.6, which gives the mixture response in both the (a) σ-V and (b) U_S-u_P planes. For the curves shown in Fig. 7.6, the energy partitioning ratio is set to 1, resulting in equally partitioned energy between the components. It is observed in Fig. 7.6 that both methods of mixing result in nearly identical Hugoniots for the Ta + Fe_2O_3 mixture. However, agreement between the two

mixing routines is not quite as good for the Ta + Bi_2O_3 mixture, and predictions tend to diverge as stress and material (particle) velocity increases.

The exact cause the observed divergence is unknown; yet, it is hypothesized that it may result from the largely different values of bulk moduli of Ta and Bi_2O_3. In the energy partitioning model, energy and stress in each component are determined from the Murhaghan relations given by Eqns. 57 and 58. These relations rely solely on K_0 and K_0' to determine energy and stress as a function of volume. Examining the K_0 values for the two mixtures, one can see that these values vary by nearly 65 % in the Ta + Bi_2O_3 mixture, compared to a difference of only 12 % in the Ta + Fe_2O_3 mixture. With such a large difference in moduli values, it might be expected that energy is more preferrentially distributed in one component rather than equally as has been assumed in the current analysis. In fact, if one modifies the energy partitioning ratio such that more energy is deposited in Bi_2O_3, the slope S in the linear equation of state is reduced, bringing the energy partitioning prediction closer to that given by the isothermal mixing method. Furthermore, differences in the predicted responses over the stress and material velocity range considered in this investigation are relatively minor. As such, the equation of state determined from the isothermal mixing method is used to describe the Hugoniot response of the solid mixtures. The parameters so determined are given in Table 7.5.

Table 7.5: Solid equation of state parameters as determined from the isothermal mixing method [1].

	C_0 (km/s)	S
Ta + Fe_2O_3	4.186	1.338
Ta + Bi_2O_3	2.686	1.415

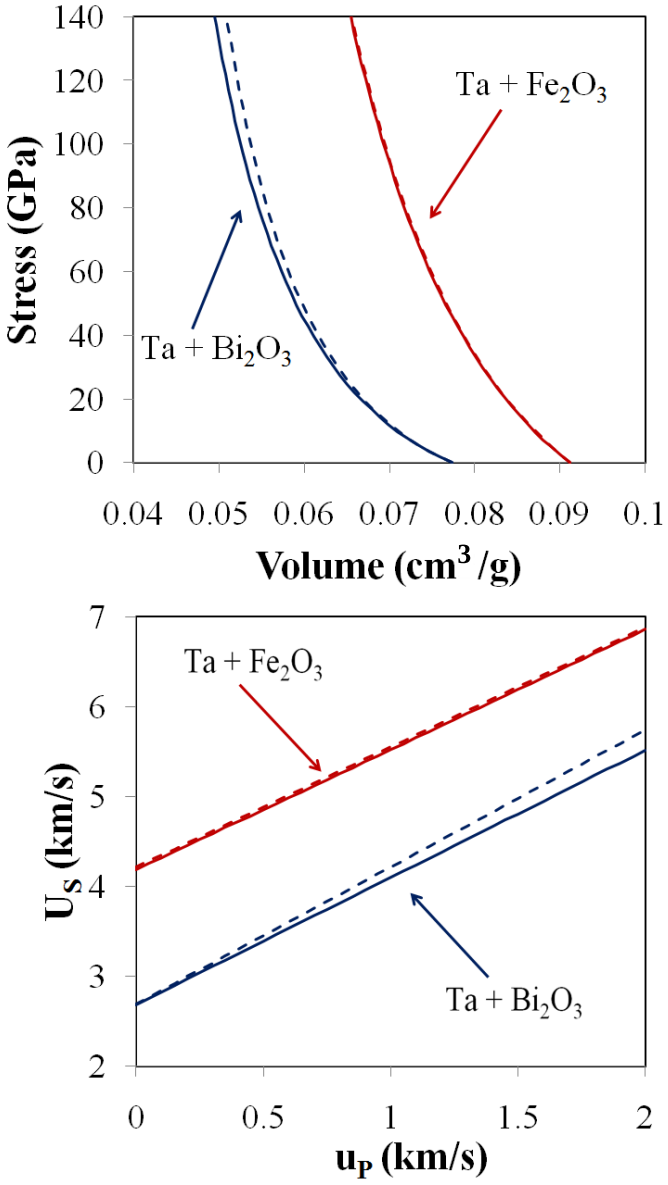

Figure 7.6: Mixture Hugoniots for Ta + Fe_2O_3 and Ta + Bi_2O_3 mixtures as predicted from the isothermal mass mixing (solid line) and energy partitioning (dashed line) methods.

7.2.1.2 Porous Mixture EOS

With the compressional response of the solid mixture defined by the isothermal mixing method, there now exists a solid curve from which a porous EOS can be extrapolated. Generally, porous equations of state are divided into two categories; as extrapolations from the solid Hugoniot are made in either an isochoric (equal volume) or isobaric (equal pressure) manner. Of the isochoric models, this dissertation has specifically discussed the Mie-Gr*ü*neisen extrapolation [15], the energy partitioning method [44], and the two term porous/powder EOS of Petrie and Page [13]. The isobaric models that have been covered are the high-pressure EOS of Oh and Persson [82] and the thermodynamic EOS of Wu and Jing [83].

In examining the foundations on which each of these models are built, it becomes apparent that certain equations of state are better suited to describe each mixture. Recalling Eq. 67, it is found that the initial density of the Ta + Fe_2O_3 mixture is below that which predicts an anomalous Hugoniot behavior in equations that use the Mie-Gr*ü*neisen relation explicitly. As such, the isochoric Mie-Gr*ü*neisen extrapolation and the energy partitioning method of predicting the porous Hugoniot are considered the least favorable options for the Ta + Fe_2O_3 mixture. Furthermore, while the Hugoniot predicted by Petrie and Page [13] incorporates the cold (quasi-static) compaction behavior to remove the anomalous curvature, the authors [13] also note that the model may not be able to predict complete densification for low initial density materials. In addition, Oh and Persson's [82] high-pressure EOS is not well suited for the present analysis as this dissertation focuses on the relatively low stress (< 15 GPa) Hugoniot response of the mixtures. As such, for the highly porous mixture of Ta + Fe_2O_3 the thermodynamic EOS of Wu and Jing [83] is likely to most accurately describe the porous EOS.

For the mixture of Ta + Bi_2O_3, the initial porous density is high enough such that a Gr*ü*neisen extrapolation will not result in an anomalous Hugoniot curve. As a result, the Mie-Gr*ü*neisen extrapolation [15] and the energy partitioning EOS [44] can be applied directly. Inherent in both models is the assumption that the mixture crushes to full density at essentially zero stress. Thus, while these models yield approximations of the Hugoniot response for a solid mixture that was initially porous, they yield no information about the crush-up response to full density. In contrast, both the Wu and Jing [83] and the Petrie and Page [13] models incorporate the crush-up response of the powder mixtures in their equations of state. The model of Oh and Persson [82] is also deemed unfit for the analysis of the Ta + Bi_2O_3 system as, similar to the previous system, the stress range investigated is below that for which the model was originally developed.

Of all the models available, that of Wu and Jing [83] seems to offer the most flexibility in describing the stress range of interest in the current investigation. This model has the capability to describe the crush-up response of the material in the incomplete compaction region, as well as the response of the fully dense material at high stresses. This is not to say that the other models do not have their strengths as well. Specifically, the Mie-Gr*ü*neisen extrapolation [15] and the energy partitioning models [44] will be very useful as reference curves when employing the P-α and P-λ compaction models to describe the densification process.

7.2.2 Initial Powder Configuration

Powders are pressed to initial densities of approximately 49 % and 62 % TMD for the Ta + Fe_2O_3 and Ta + Bi_2O_3 mixtures, respectively. SEM images of the initial powder configurations in the precompacted state are shown in Figs. 7.7 and 7.8. To obtain these

images, loose powders were mixed with a small amount of epoxy prior to compacting such that particle pullout is inhibited during sectioning and polishing.

From Fig. 7.7(a) distinct particles of Ta surrounded by a nearly continuous matrix of Fe_2O_3 are observed; this is consistent with SEM images of the loose powders (Fig. 6.7(a)). Though isolated regions of voids are observed within and around clusters of Ta, as shown in Fig. 7.7(b), the primary location of porosity and voids in this mixture is located within the porous agglomerate regions of Fe_2O_3. In stark contrast to the pre-compacted Ta + Fe_2O_3 mixture, the Ta + Bi_2O_3 mixture (Fig. 7.8) clearly shows distinct particles of both Ta and Bi_2O_3. Furthermore, instead of having a continuous matrix of oxide surrounding the metal component as in the previous mixture, it is the metal component that surrounds the oxide in the Ta + Bi_2O_3 mixture. Another differentiating factor between the mixtures is the composition of the continuous particle network. In the Ta + Fe_2O_3 mixture, it is Fe_3O_3 that makes up the continuous network of particles, and as shown in Fig. 7.7(a), this is also where the majority of the void space to be removed during compaction is located. As such, with passage of a shock wave it may be the mechanisms by which the continuous network of porous Fe_2O_3 breaks down and densifies that may dominate the compaction characteristics of the mixture. For the mixture of Ta + Bi_2O_3 the exact opposite is true, as it is the Ta particles which form the continuous network. However, the continuous network in this mixture is significantly different in that it is supported by discrete contact points between particles (Ta-Ta, Ta-Bi_2O_3, and Bi_2O_3-Bi_2O_3 contacts). From these observations it is speculated that densification of the Ta + Bi_2O_3 mixture will be controlled by the growth and coalescence of contact points as the shock front passes through the mixture.

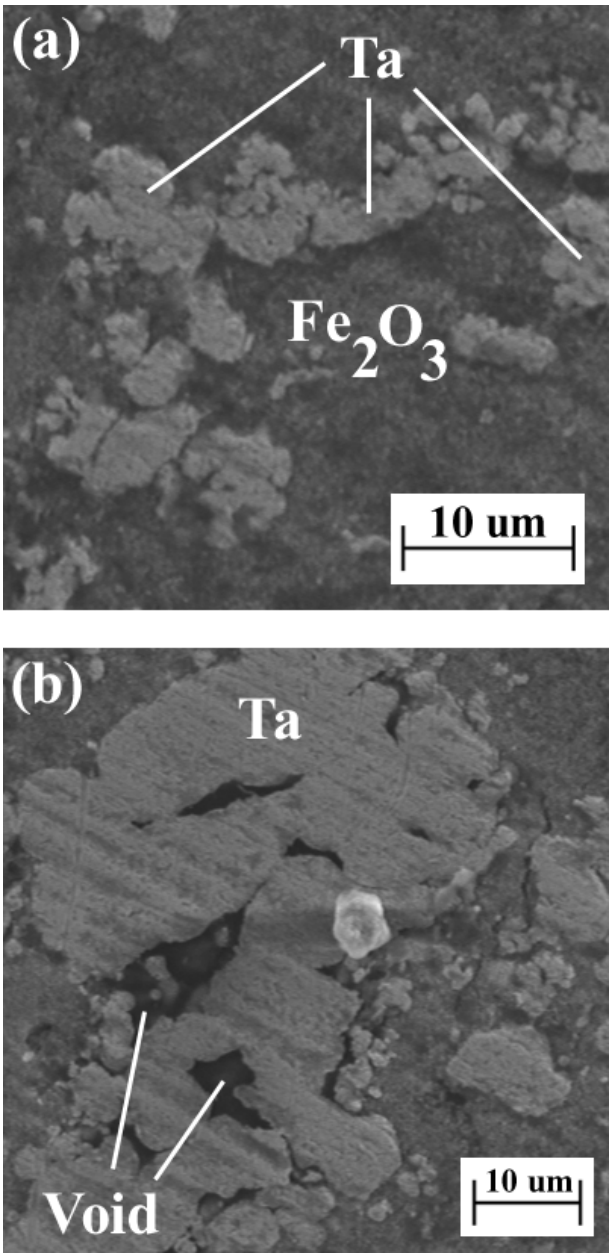

Figure 7.7: Initial powder configuration for Ta + Fe_2O_3 pressed to 49 % TMD, showing (a) location of Ta and Fe_2O_3 and (b) locations of voids localized within regions of Ta.

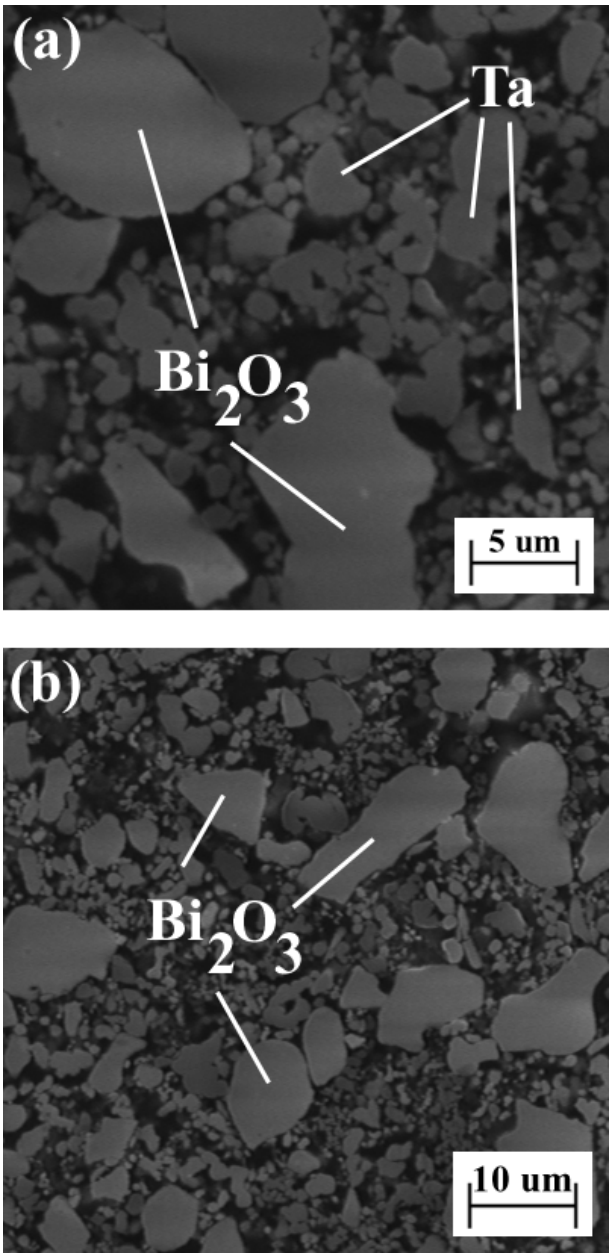

Figure 7.8: Initial powder configuration for Ta + Bi_2O_3 pressed to 62 % TMD, showing (a) location of Ta, Bi_2O_3, and voids with the mixture and (b) the predominantly larger Bi_2O_3 particles.

7.2.3 Experimental Data

A series of parallel plate impact experiments were conducted on the Ta + Fe_2O_3 and Ta + Bi_2O_3 powder mixtures which were precompacted to result in mixtures whose microstructures are similar to those shown in Figs. 7.7 and 7.8. The manner in which the experiments were performed was consistent with that outlined in Sect. 6.7. The results of which are presented here. With details of the initial powder configuration presented, this section examines the analysis techniques used to interpret the parallel plate impact data. Following this, results of the experiments are presented in conjunction with the predicted Hugoniot response from applicable equations of state and compaction models.

With initial density of the powder mixtures measured prior to conducting the experiments, two parameter are measured during shock loading which can, through the impedance matching technique, be used to fully determine the shocked state in the powder. These two parameters are the impact velocity V_I and the shock velocity in the sample U_S. Details of how these two values are determined are presented next.

Prior to performing the parallel plate impact experiment, measurements of the velocity pin locations are made such that the relative distance between each pin is known. Upon launching the projectile, the flyer plate strikes the pins and a voltage signal is produced and recorded on an oscilloscope. With the voltage signals from each pin recorded on a single oscilloscope there is a common time axis from which the relative time difference ($\Delta\, t$) between impact of each pin is determined. An example voltage signal from a single pin is shown in Fig. 7.9 where the x-axis is time and the y-axis is voltage. The enlarged image in Fig. 7.9 shows the voltage response at the moment of impact, T_i. With the distance between pins and the time between impact of each pin known, a measurement of the incoming projectile velocity can be calculated. The average impact velocity reported for

each experiment is calculated from six separate measurements of the impact velocity determined between pins 1-2, 2-3, 3-4, 1-3, 2-4, and 1-4. Minimum and maximum values of the impact velocity are also recorded for use in uncertainty analysis. With average value of the impact velocity known, one of the two variables needed to calculate the shocked state in the powder mixture is determined.

The second required measurement is the shock velocity in the powder. This quantity is determined from the arrival time of the stress wave as it passes through a series of PVDF gauges mounted on either side of the powder compact. For each of the powder mixtures, the input and propagated PVDF gauges are located as shown schematically in Fig. 6.13. The voltage signal from each gauge is split prior to arrival at the oscilloscope, such that two separate measurements of each gauge signal are recorded in high resolution and low resolution. This process is undertaken in an effort to enhance the accuracy of the measured voltages. The high resolution recording is set such that the maximum range on the oscilloscope is approximately 10-15 times less than the maximum expected voltage signal. This allows for accurate measurements of the signal at low voltages and reduces the 'noise' in the signal. The low resolution is set so that the maximum voltage range on the oscilloscope is approximately 1.5 to 2 times greater than the maximum voltage expected. Maximum expected voltages are based on estimates of stress the gauges are likely to experience from calibrations of charge density versus measured stress [107].

The high and low voltage signals are then combined into a single signal using PlotData 2.3 [129], a software package designed by Sandia National Laboratories for the explicit purpose of analyzing various forms of experimental shock data. After the voltage signals are combined, the combined signal is multiplied by a factor of two to return it to its original amplitude (recall the original signal was split into two). From this voltage signal, both a

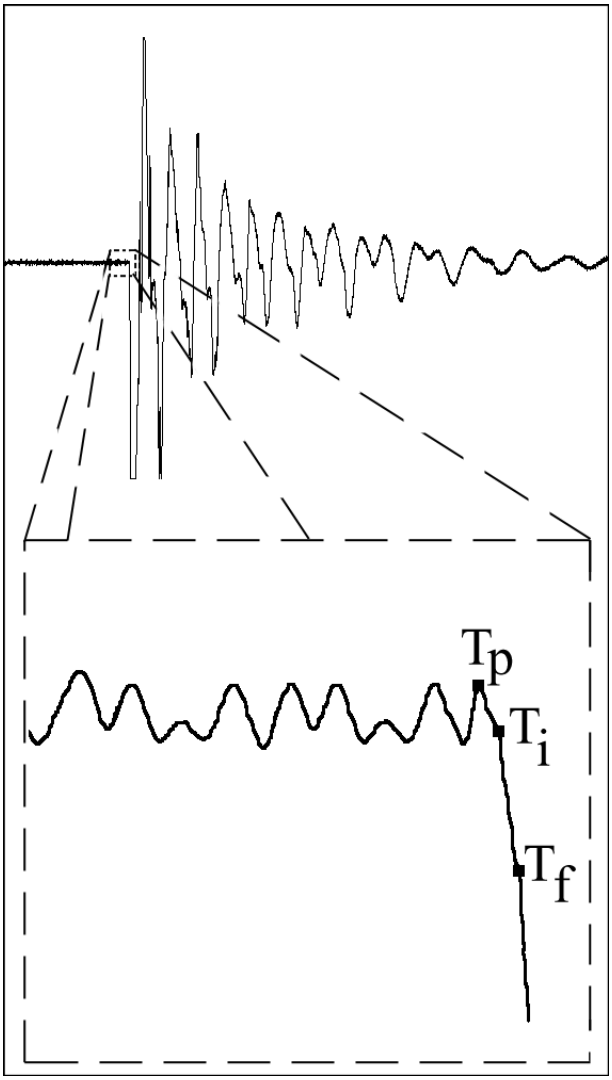

Figure 7.9: Voltage signal produced as a result of incoming flyer plate striking a velocity pin. Image contained within the dashed box is an enlarged view of the signal behavior at impact, where the times T_p, T_i, and T_f indicate times prior to impact, at impact, and following impact. Time is plotted on the x-axis and voltage is on the y-axis.

current trace and a stress trace can be determined using the known resistance of the current viewing resistor (CVR). In this analysis, only the current trace is used to calculate shock velocity.

Representative current traces for the input and propagated gauges are shown in Fig. 7.10. Note the variation in behavior, especially as the signal decreases from its peak value. In the typical input gauge trace, a sharp rise to peak current is observed, followed by significant reverberations before equilibrating at a steady state value, as shown in the leftmost trace in Fig. 7.10. The majority of the propagated traces look similar to that shown by the rightmost trace in Fig. 7.10, whose rise to peak current is slightly more broad and whose reduction from the peak value is characterized by rapid equilibration.

The time of flight (TOF) between the gauge packages, inclusive of the powder, is determined at three different locations on the gauge current traces. The first being taken from the peak values of current, shown as $\Delta\ t$ in Fig. 7.10. Another TOF is based on the $\Delta\ t$ between the points labeled 10-R, which are taken at a current value 10 % of the maximum value on the initial rise of the trace. The final TOF is the $\Delta\ t$ between the points 10-F, which is determined differently for different characteristic trace shapes. For traces similar to the input, where the current reverberates about its steady state value a number of times before equilibrating, the value of 10-F is taken at the midpoint between the first two peaks whose total difference in current is less than 10 % of the maximum value. For traces similar to the propagated trace, which do not exhibit significant reverberations prior to equilibrating, the value of 10-F is taken at the time when the current trace first falls below 10 % of its maximum value. The TOF taken at the maximum point in the current trace is used to determine the reported shock velocity in the powder, while those from the 10-R and 10-F locations are used to calculate uncertainty in the shock velocity (see Sect. 6.9).

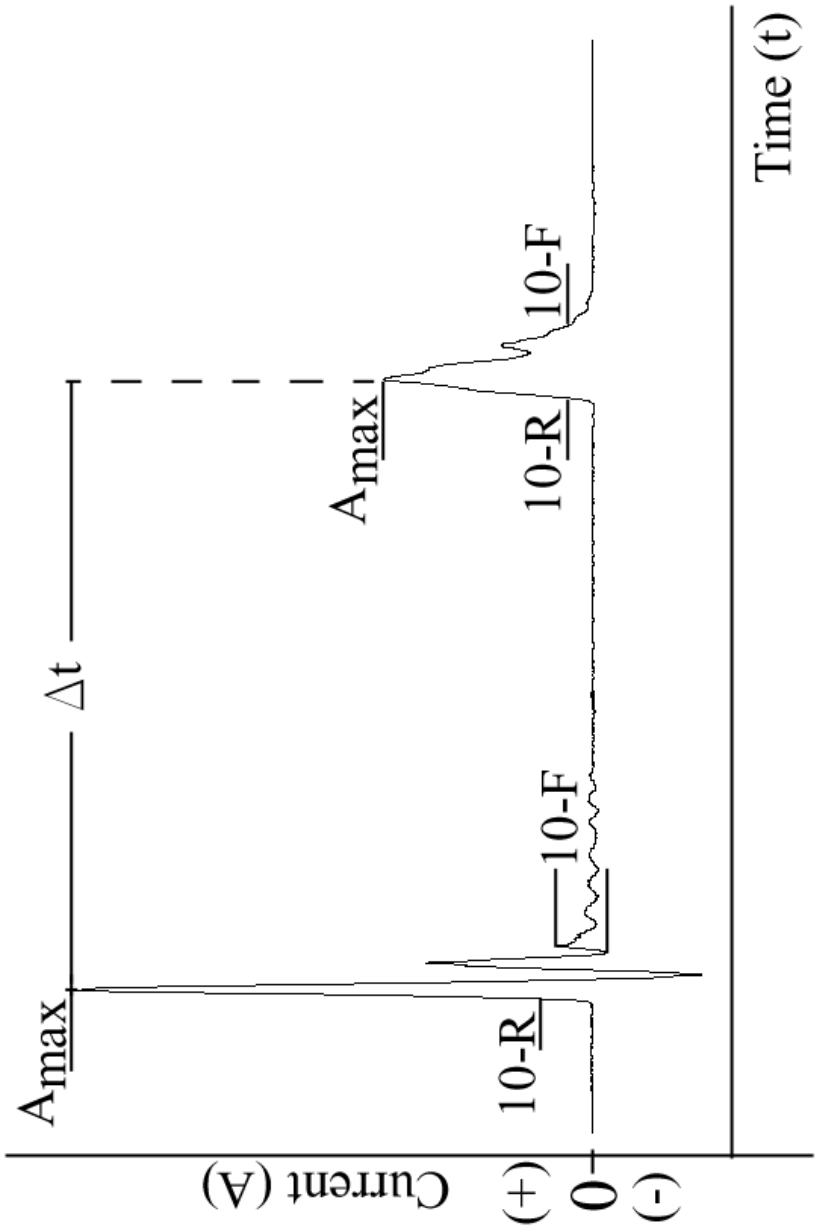

Figure 7.10: Typical input (left) and propagated (right) current traces output from PVDF gauge experiments on powder mixtures. Max current times (A_{max}) are used to compute the time of flight through the powder and gauge packages.

To determine the actual time of flight in the powder, from which the shock velocity can be calculated, one must subtract the time which the wave spends in the gauge packages. To accomplish this, one uses the measured values for the gauge package thickness at various stages of completion shown by locations M_i in Fig. 7.11, where i is the measurement number. It is assumed that the time of flight previously measured spans the distance ΔX in Fig. 7.11, and as such the package thickness between the powder and the line indicated by ΔX must be determined. It can be seen in Fig. 7.11 that there are essentially four layers of epoxy, film, and gauge between locations M_2-M_3 and M_4-M_5. Near the impacting surface the wave travels through three of these layers prior to reaching the powder, and upon exiting travels through two layers prior to reaching the propagated gauge. Therefore, the distance the wave travels through the gauge packages is three quarters the distance measured between M_2-M_3 for the input gauge, and half the distance measured between M_4-M_5 for the propagated gauge.

To determine the time it takes for the wave to travel through these distances in the gauge packages, the stress in each gauge package must be known such that the shock velocity in the package can be obtained. To this end, the impedance matching technique outlined in Sect. 6.8 is first applied using the measured impact velocity and the initial TOF and known powder thickness to determine an estimate of the shock velocity in the powder. From this, an initial value of stress in the copper driver and the powder mixture is established. It should be noted that in the impedance matching analysis, the gauge material is neglected and the calculations are performed as if the driver were directly impacting the powder mixture. The stress in the first gauge package is assigned that of the copper driver, while the stress in the propagated gauge package is assigned the stress in the powder. With these stresses, shock velocities in the gauge packages are obtained using the known equation of state of the film

(Teflon). This value of shock velocity is then used to compute the time of travel through the two gauge packages, and these values are subtracted from the initial TOF. The new TOF is then used to calculate the shock velocity and subsequent stress in the powder mixture. This process is iterated several times until convergence of less than 1 m/s in shock velocity is achieved.

Having determined the impacting projectile velocity and the shock velocity in the powder, the impedance matching technique is used to determine the remainder of the shocked state properties in the powder (σ, u_P, V). The MATLAB [91] script used to carry out these calculations is given in Appendix A.3. From this program, the equilibrium values of σ and u_P are determined, and by modifying certain input parameters in the manner outlined in Sect. 6.9 uncertainties in material velocity as a function of the impact velocity, initial density, and shock velocity are determined. In addition, this program also yields information regarding the stress and material velocity, and its associated uncertainties, at the flyer-driver interface. Recall these uncertainties are combined with those in the sample to determine the total systematic uncertainty in material velocity in the sample, see Sect. 6.9.

The calculated parameters σ and u_P are then combined with the measured initial specific volume ($1/\rho_{00}$) to determine the volume at the shocked state through [15]

$$V = V_{00} - \frac{u_P^2}{\sigma} \tag{135}$$

At this point all of the Hugoniot values of interest (σ, U_S, u_P, V) are known. The next two sections present dynamic compaction results for the Ta + Fe_2O_3 and Ta + Bi_2O_3 systems, where results are given in tabular and graphical forms.

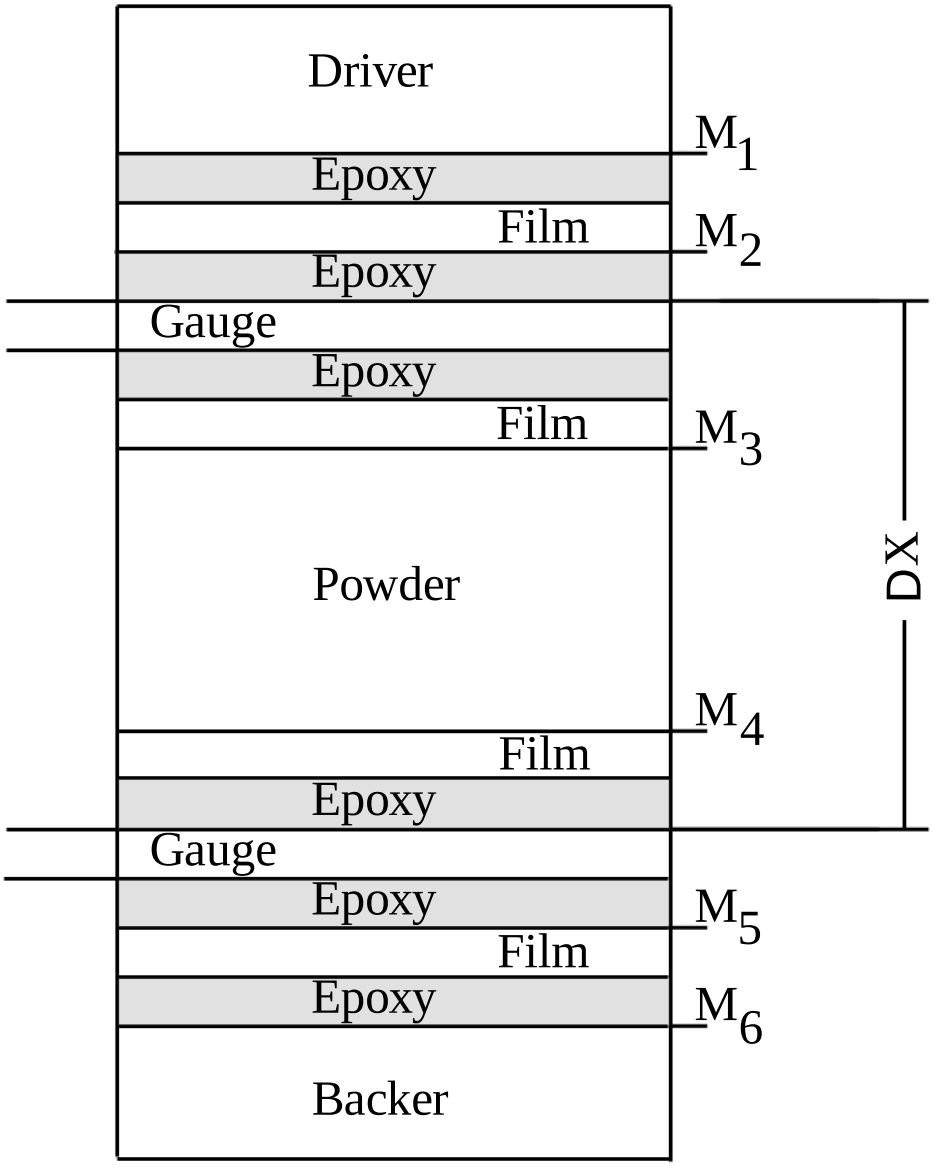

Figure 7.11: Schematic showing location of films, epoxy, and gauges within gauge package and powder fixture, where ΔX is the distance traveled by the wave during the TOF measured by the gauges. Points marked M_i show where height measurements are taken during target assembly.

7.3 Hugoniot Response of Ta + Fe_2O_3

Results of measured and calculated parameters from the parallel plate impact experiments on the Ta + Fe_2O_3 powder mixture are given in Table 7.6. For the experiments listed in Table 7.6, all shots were performed with a Cu flyer mounted on an Al sabot, with the exception of shots 805* and 1002*, whose flyers were composed of the W-6Ni-4Cu alloy. Values of uncertainty following the ± sign in the table are one half the values calculated using the error analysis techniques described in Section 6.9. These results, are shown in the U_S-u_P and σ-V (relative volume) planes in Figs. 7.13 and 7.14. Also shown in the σ-V plane is the Hugoniot for a solid mixture of Ta + Fe_2O_3, where all points along the porous Hugoniot are expected to fall to the right of this solid curve.

7.3.1 Equations of State

The experimentally determined results, along with predictions of the densification and Hugoniot responses from the models of Petrie and Page [13] and Wu and Jing [83] are shown in the U_S-u_P plane in Fig. 7.13 and in the σ-V plane in Fig. 7.14. In relation to the experimentally obtained data, predictions from the model of Petrie and Page's [13] fall predominantly above the data on the U_S-u_P plane and to the right of the data in the σ-V plane. The location of the data points in relation to the prediction of Petrie and Page [13] indicates that the model is consistently under predicting the level of compaction for a given applied stress, with only two data points (shots 901 and 823) falling near to or on the opposite side of the prediction. This result is not surprising as the initial density of the Ta + Fe_2O_3 system is relatively low (less than the anomalous Hugoniot limit), and Petrie and Page [13] have noted that the model may not predict full compaction for materials with similar initial

Table 7.6: Results of the parallel plate impact experiments on the Ta + Fe_2O_3 powder mixture. Quantities listed to the right of ± are one half of the uncertainties obtained using the methodology from Sect. 6.9. Relative volumes are based on a solid density of 10.968 g/cm^3.

Shot	V_{Imp} (km/s)	ρ_{00} (g/cm^3)	U_S (km/s)	u_P (km/s)	σ (GPa)	V (cm^3/g)	V/V_0
901	0.261	5.4767	0.914 ± 0.020	0.229 ± 0.002	1.144 ± 0.013	0.14068 ± 0.00360	1.543 ± 0.026
756	0.263	5.6477	0.671 ± 0.014	0.237 ± 0.003	0.899 ± 0.022	0.12369 ± 0.00375	1.357 ± 0.030
807	0.454	5.1950	0.953 ± 0.013	0.399 ± 0.067	1.976 ± 0.651	0.10576 ± 0.02880	1.160 ± 0.272
812	0.513	5.2563	1.043 ± 0.015	0.445 ± 0.014	2.437 ± 0.147	0.10518 ± 0.00621	1.154 ± 0.059
814	0.583	5.3028	1.114 ± 0.023	0.501 ± 0.004	2.961 ± 0.025	0.10145 ± 0.00432	1.113 ± 0.043
704	0.716	5.2126	1.257 ± 0.020	0.607 ± 0.010	3.976 ± 0.116	0.09375 ± 0.00500	1.028 ± 0.053
823	0.711	5.5169	1.384 ± 0.044	0.588 ± 0.009	4.493 ± 0.100	0.10935 ± 0.00619	1.199 ± 0.057
751	0.877	5.5390	1.425 ± 0.025	0.724 ± 0.007	5.710 ± 0.068	0.09465 ± 0.00381	1.038 ± 0.040
805*	0.977	5.1118	1.990 ± 0.027	0.984 ± 0.012	10.013 ± 0.212	0.08955 ± 0.00437	0.982 ± 0.049
1001	1.036	5.3825	1.599 ± 0.035	0.843 ± 0.009	7.257 ± 0.082	0.08837 ± 0.00527	0.969 ± 0.060
1002*	1.080	5.3573	2.148 ± 0.035	1.062 ± 0.009	12.221 ± 0.132	0.09404 ± 0.00385	1.031 ± 0.041

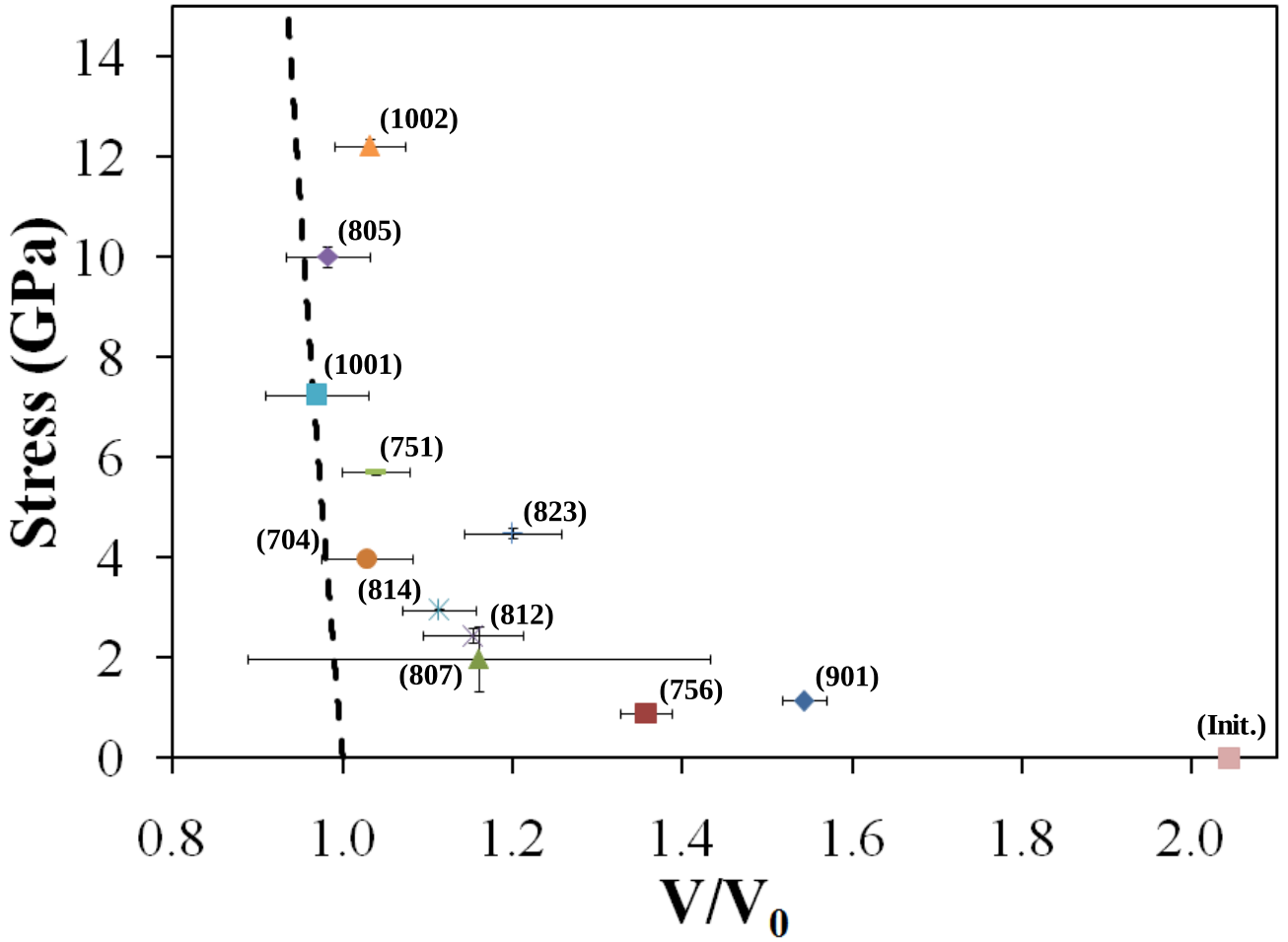

Figure 7.12: Results of parallel plate impact experiments on equivolumetric mixture of Ta + Fe_2O_3. Solid mixture Hugoniot calculated from isothermal mixing routine [1] shown as dotted line.

conditions. Therefore, model predictions of Petrie and Page [13], which are based on extrapolations of compaction in the quasi-static regime, are not considered representative of actual material response to dynamic loading for this mixture.

The other porous model applicable to the low density Ta + Fe_2O_3 system is that of Wu and Jing [83]. As implemented, the model uses a 'P-α' type relationship to describe material response in the incomplete compaction region as given by Eq. 84. Inherent in this description is a definition of the yield strength of the matrix (solid) material. For Ta and Fe_2O_3, whose yield properties are given in Table 6.3, the yield strength of the mixture is determined using a volume fraction (f) average of the individual yield strengths (Y) of the materials through the iso-strain mixture modulus $Y = f_1 Y_1 + f_2 Y_2$. Following the definition of critical stress σ_{crit} outlined bu Wu and Jing [83], results of the model predictions are shown in Figs. 7.13 and 7.14.

Comparing experimental data to the U_S-u_P Wu-Jing [83] prediction, the data is observed to fall consistently above model predictions at lower shock and material velocities, seemingly approaching the predicted curve as velocities increase. This type of behavior is often observed for models which under predict the crush strength of a material, as illustrated by the work of Thadhani and co-workers [72] in the case of Ti + Si powder mixtures. Shots 751 and 1001 appear to fall directly on top of the model prediction, indicating close agreement between model predictions and experimental results. For models with zero crush strengths (e.g. the Mie-Grüneisen extrapolation [15]) this behavior indicates that full consolidation of the porous material has occurred. However, as the Wu-Jing [83] model incorporates material strength effects through the P-α [5, 10] relation, overlap between experimental and model predictions does not necessarily indicate full compaction of the material.

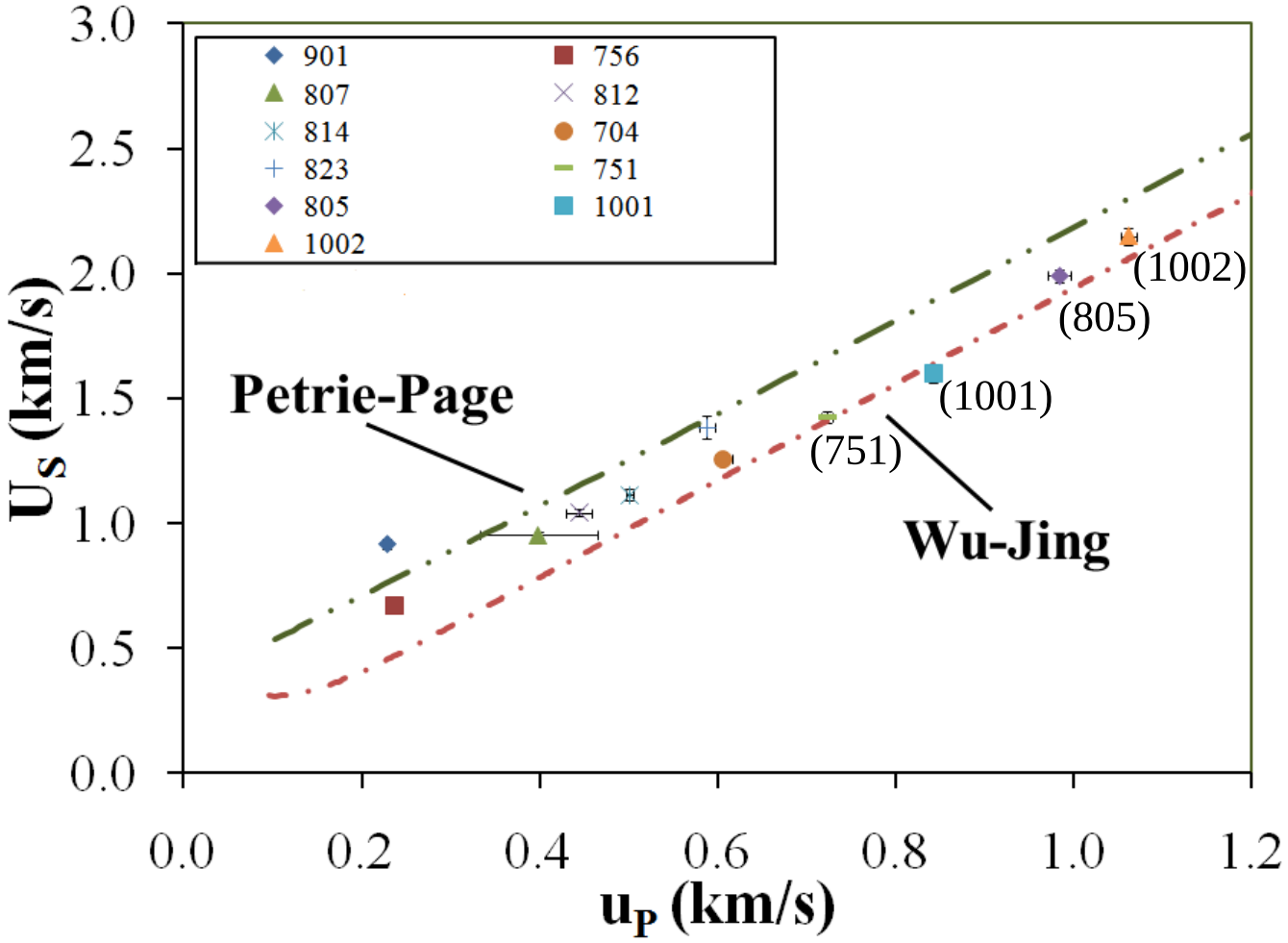

Figure 7.13: Results of parallel plate impact experiments on equivolumetric mixture of Ta + Fe_2O_3. Preliminary fits of the Wu-Jing [83] and Petrie-Page [13] models shown.

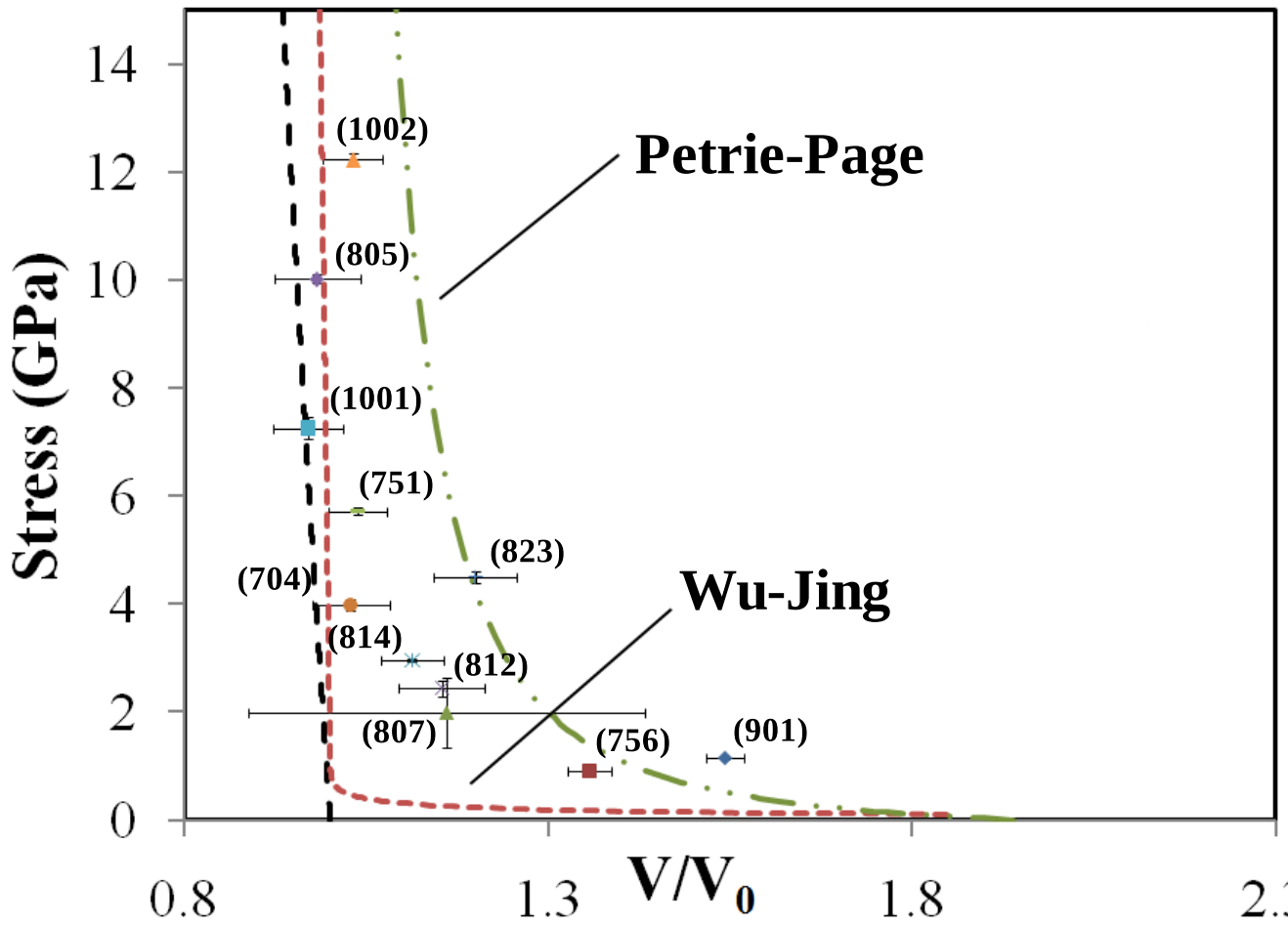

Figure 7.14: Results of parallel plate impact experiments on equivolumetric mixture of Ta + Fe_2O_3. Preliminary fits of the Wu-Jing [83] and Petrie-Page [13] models also shown.

Shown at the lower portion of the Wu-Jing [83] U_S-u_P prediction is a finite amount of curvature. The observed curvature represents the portion of the model where incomplete compaction is predicted and the P-α behavior is dominating. Therefore, with the current model implementation, the agreement between shots 751 and 1001 with the predicted curve indicate that full compaction of the material has occurred under these experimental conditions.

At higher velocities still, results from shots 805 and 1002 are shown to fall slightly above the model prediction. Recalling that positive deviations (increased U_S at a given u_P) from the inert curve are indicative of reaction initiation, one might be inclined to postulate that a reaction has occurred in the two highest velocity shots. However, it has been shown for similar mechanochemical based reactions by Eakins and Thadhani [130] and Batsanov and co-workers [131] that increases in stress above that required for reaction initiation result in increases in the measured deviations in shock velocity from the inert behavior. Thus if a reaction were taking place in this system, the deviation in U_S for shot 1002 is expected to be observably larger than the deviation from the inert curve for shot 805. With deviations in U_S from the inert curve similar in magnitude for both shots 805 and 1002, results are inconclusive as to whether reaction is initiating in the highest velocity shots.

Examining the σ-V plot in Fig. 7.14, it is shown that as formulated the Wu-Jing [83] model predicts a considerably lower crush strength than is experimentally observed. Though not aligning well with the Wu-Jing [83] prediction, most all of the data points in the incomplete compaction regime seem to follow the general trend of increasing compaction with increasing stress, and it is postulated that with the correct modification to the yield behavior employed, better agreement may be achieved. Comparing the data points with predictions

of both the solid Hugoniot and the porous Wu-Jing [83] model, it is observed that full compaction for the Ta + Fe_2O_3 mixture is occurring somewhere between 6-7 GPa. As stress increases, the experimentally measured points tend to follow along the inert prediction up to approximately 10 GPa. Shot 1002 is shown to fall slightly to the right of the inert curve; however its band of uncertainty lies within the range of the inert behavior, and one cannot say with certainty if a reaction is occurring.

7.3.2 Compaction Model Fits

In addition to the Wu-Jing [83] model which describes both the complete and incomplete compaction regimes, the P-α and P-λ models, which deal explicitly with the incomplete compaction regime, are also applied to this mixture. Application of both models require a fully compacted porous equation of state for use as a reference curve. With mixture model options limited for the Ta + Fe_2O_3 system due to its low initial density, one might choose to use the solid EOS predicted from McQueen's isothermal mixing method [1] as the reference curve (shown in Fig. 7.14). However, this reference curve does not include any of the extra energy associated with the compaction of the porous material (see Fig. 3.13). To incorporate the effects of porosity into the reference equation of state, the Wu-Jing [83] model is modified from its original implementation, setting the yield strength of the matrix to an extremely low value (10 MPa), thus simulating a material with a crush strength of approximately zero.

The P-α and P-λ models are fit to the experimental data. The three P-α fits are shown alongside experimental data in Fig. 7.15. Notice the varying degrees to which the different models fit the data. As observed in Fig. 7.15, the rate-independent form of α given by

Carroll and Holt [10]

$$\alpha = \frac{1}{1 - exp(-3P/2YS)} \tag{136}$$

is by far the worst at fitting the experimental data. In the fit shown, the yield strength YS is taken as the volume fraction average of the yield strengths of the components ($Y = f_1 Y_1 + f_2 Y_2$) resulting in $YS = .135$ GPa. Clearly this fit in not representative at all of the actual compaction observed for Ta + Fe_2O_3.

Slightly more representative of the experimental data is the α formulation proposed by Butcher and Karnes [6] and Herrmann [5]

$$\frac{\alpha - 1}{\alpha_E - 1} = \left(\frac{(P_s - P)}{(P_s - P_e)} \right)^n \tag{137}$$

In this formulation, α_E and P_e are the porosity and stress at the elastic limit, which is defined using Carroll and Holt's [10] critical stress relation (Eq. 98 by setting $\alpha_E = \alpha_0$ at $P_e = P_{crit}$). For this system, these terms take the values $\alpha_E = 2.0408$ and $P_e = 0.0606$. Also defined in this equation is the experimentally observed crush strength P_s which has been set to 6 GPa (recall near full compaction is observed for shot 751 with $\sigma = 5.71$ GPa). With these values set, the experimental points in the incomplete compaction regime are fit with Eq. 137 to determine the fitting parameter n, which is determined to be $n = 4.446$. This fit does a moderate job of fitting the experimentally observed compaction trend in the lower stress regime, but tends to over predict the level of compaction as stress increases.

The α formulation that best fits the compaction data is that given by Grady [88] represented by the relation

$$\alpha = \left(\frac{P_s}{P} \right)^{1/n} \tag{138}$$

Similar to the previous relation given by Eq. 137, this formulation also requires knowledge of the materials crush strength prior to implementation. However, no assumptions are made

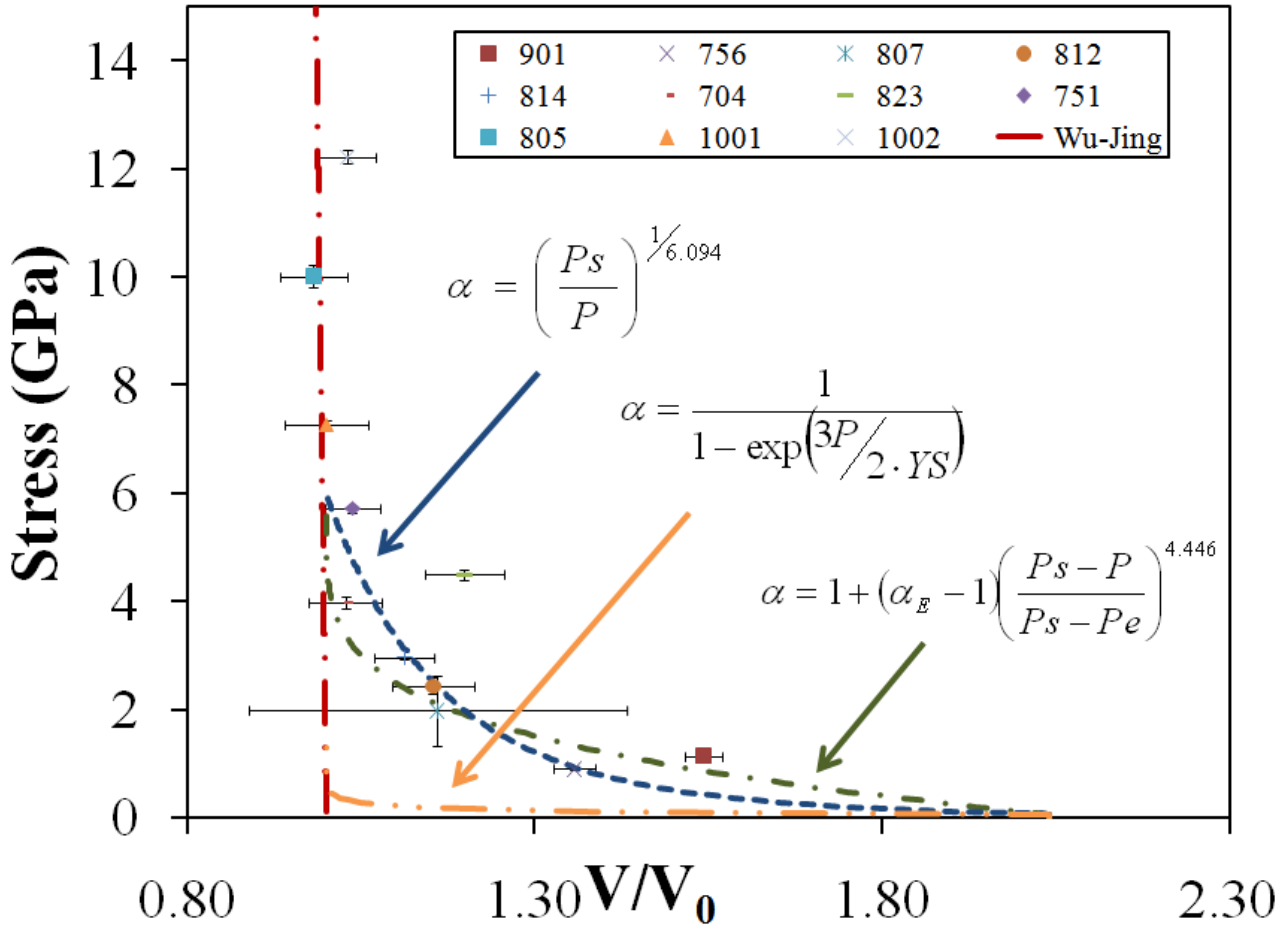

Figure 7.15: Experimental compaction data for Ta + Fe_2O_3 fit to various forms of the P-α compaction model. Porous equation of state is derived from the Wu-Jing [83] model with the yield strength arbitrarily set to 10 MPa to simulate material with zero crush strength.

in this model regarding the elastic stress or porosity at the elastic limit of the powder. With few constraints, this model follows the experimental data points quite well with the fitting parameter $(1/n)$ set to $n = 6.094$.

In order of increasing effectiveness, the P-α model given by Eq. 136 shows a weaker fit than Eq. 137 which is in turn weaker than Eq. 138. While the P-α relation given by Eq. 136 is not considered a satisfactory means of describing the experimentally observed compaction trend for mixtures of Ta + Fe_2O_3, the other two relations offer moderately good fits to the experimental data. Unfortunately, both fits also require knowledge of the crush strength P_s and contain a non-physical fitting parameter n. While a value of the crush strength could be determined from a few well designed experiments, the parameter n, which dictates the shape of the compaction curve, requires multiple experiments to be performed in the incomplete compaction region. As such, without sufficient experimental data points one would be hard-pressed to predict the compaction behavior of these mixtures.

Compaction data for the Ta + Fe_2O_3 powder mixture is also fit to the P-λ compaction model, where results of this fit are shown in Fig. 7.16. For the fit shown in Fig. 7.16 the yield strength is set to the volume fraction averaged value of 0.135 GPa. One can see that overall, the P-λ model does an adequate job of describing the consolidation behavior of this mixture, with the exception of the data point for shot 823. What is interesting to note about this model is that the same fit can be achieved with any number of combinations of YS and n. While the yield strength YS defined in the current implementation assumes a value equal to the volume fraction averaged YS of the components resulting in $n = 0.1049$, the exact same fit can be achieved with any number of different values of the yield strength. As the predefined value of yield strength increases, so too does the value of the fitting parameter n, and for values of $0.2 < YS < 2.0$ GPa the same fit as that shown in Fig. 7.16 with R^2

= 0.9115 can be obtained with any value of yield strength through the linear relation n = $0.777YS$ + 6.667 x10^{-}5.

Thus with regard to the P-α and P-λ models, overall the P-λ model does a slightly better job of fitting the experimentally observed compaction data. However, both models lack true predictive ability as a number of experiments must be performed to obtain the model fitting parameters. The P-α model relies on an accurate estimate of the crush strength as well as the empirical fitting parameter n to predict the compaction behavior, while the P-λ model fit can be obtained with nearly any combination of values for YS and n. Unfortunately, for the case of both models the parameter n is not assigned any physical basis. In the P-α model n is purely empirical, while the P-λ model of Grady [12] defines n as a measure of the homogeneity of the compaction transition, an unmeasurable quantity.

7.3.3 Concluding Remarks

From these results it is observed that while the compaction models (P-α and P-λ) do offer adequate fits to the data once a number of experiments have been performed, they lack in predictive ability based on known material properties. Conversely, the model of Wu and Jing [83], while not performing very well in the incomplete compaction region in its current implementation, does offer significant advantages over the compaction models. In the EOS of Wu and Jing [83], the incomplete compaction region is largely defined by the relationships between the parameters α, P_{crit}, and YS, which if the definitions for α and P_{crit} are kept in their original formulation then they all depend on the assigned value of YS. Thus if one can formulate a better way to define the YS of a powder mixture, it is likely that much better agreement between experimental data and model predictions could result.

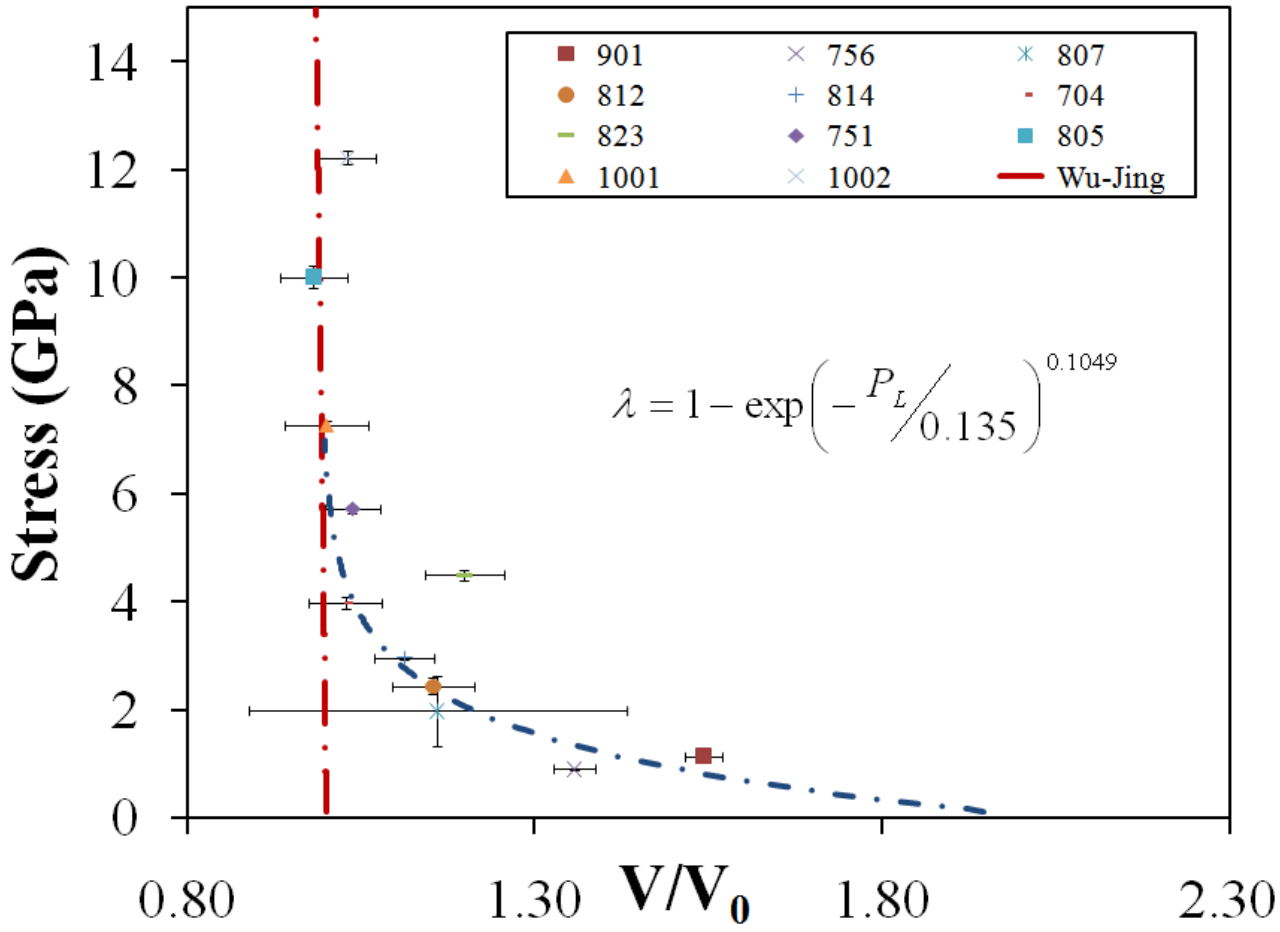

Figure 7.16: Experimental compaction data for Ta + Fe_2O_3 system fit to P-λ compaction model. Porous equation of state derived from Wu-Jing [83] with yield strength arbitrarily set to 10 MPa to simulate material with zero crush strength.

7.4 Hugoniot Response of Ta + Bi_2O_3

Results from the parallel plate impact experiments on the Ta + Bi_2O_3 powder mixture are given in Table 7.7 and shown schematically in the σ-V plane in Fig. 7.17, where all the experiments listed in the table were performed with Cu flyers. Measured values are V_{Imp} and U_S, with all other values calculated using the impedance matching technique. Numerical values to the right of the ± sign are one half of the uncertainty values calculated using the technique outlined in Sect. 6.9.

7.4.1 Equations of State

The data listed in Table 7.7 along with fits to the isothermal mass mixing [1], Petrie and Page [13], Wu and Jing [83], and Krueger and Vreeland [44] models are shown in Figs. 7.18 and 7.19. Also shown in Fig. 7.19, in the σ-V plane, is the predicted solid Hugoniot from McQueen's [1] isothermal mixing method. Upon first examination of the model predictions shown in Fig. 7.19 it is evident that the isothermal mixing [1], Wu-Jing [83], and Krueger-Vreeland [44] models all predict similar behaviors over the majority of the range investigated, while that of Petrie-Page [13] diverges significantly from the other models, especially at lower stresses and lower and material velocities. These results are not surprising when one considers the origin of each compaction model.

Both the isothermal mass mixing [1] and Krueger-Vreeland [44] are isochoric models which assume the material compresses to solid density at zero stress. As such, one would expect at the very least to see close agreement between these two models in the low stress range as both models contain the same origin. Indeed, this is what is observed in Figs. 7.18 and 7.19, as the two predictions are nearly indistinguishable at low material velocities and stress. However, as stress and material velocity increase, the Krueger-Vreeland [44] model

Table 7.7: Results of the parallel plate impact experiments on the Ta + Bi_2O_3 powder mixture. Quantities listed to the right of ± are one half of the uncertainties obtained using the methodology from Sect. 6.9. Relative volumes are based on a solid density of 12.931 g/cm^3.

Shot	V_{Imp} (km/s)	ρ_{00} (g/cm^3)	U_S (km/s)	u_P (km/s)	σ (GPa)	V (cm^3/g)	V/V_0
1021	0.235	7.8963	1.012 ± 0.012	0.192 ± 0.002	1.534 ± 0.015	0.10186 ± 0.00208	1.317 ± 0.020
1017	0.408	7.8275	0.897 ± 0.024	0.342 ± 0.004	2.352 ± 0.039	0.07619 ± 0.00353	0.985 ± 0.046
1018	0.736	8.084	1.410 ± 0.021	0.564 ± 0.074	6.424 ± 0.150	0.07644 ± 0.00232	0.988 ± 0.030
1020	0.974	7.9771	1.759 ± 0.044	0.714 ± 0.074	10.016 ± 0.190	0.07500 ± 0.00354	0.970 ± 0.047
SAND-140	0.220	7.8934	0.929 ± 0.011	0.182 ± 0.102	1.333 ± 0.148	0.10107 ± 0.00392	1.307 ± 0.039

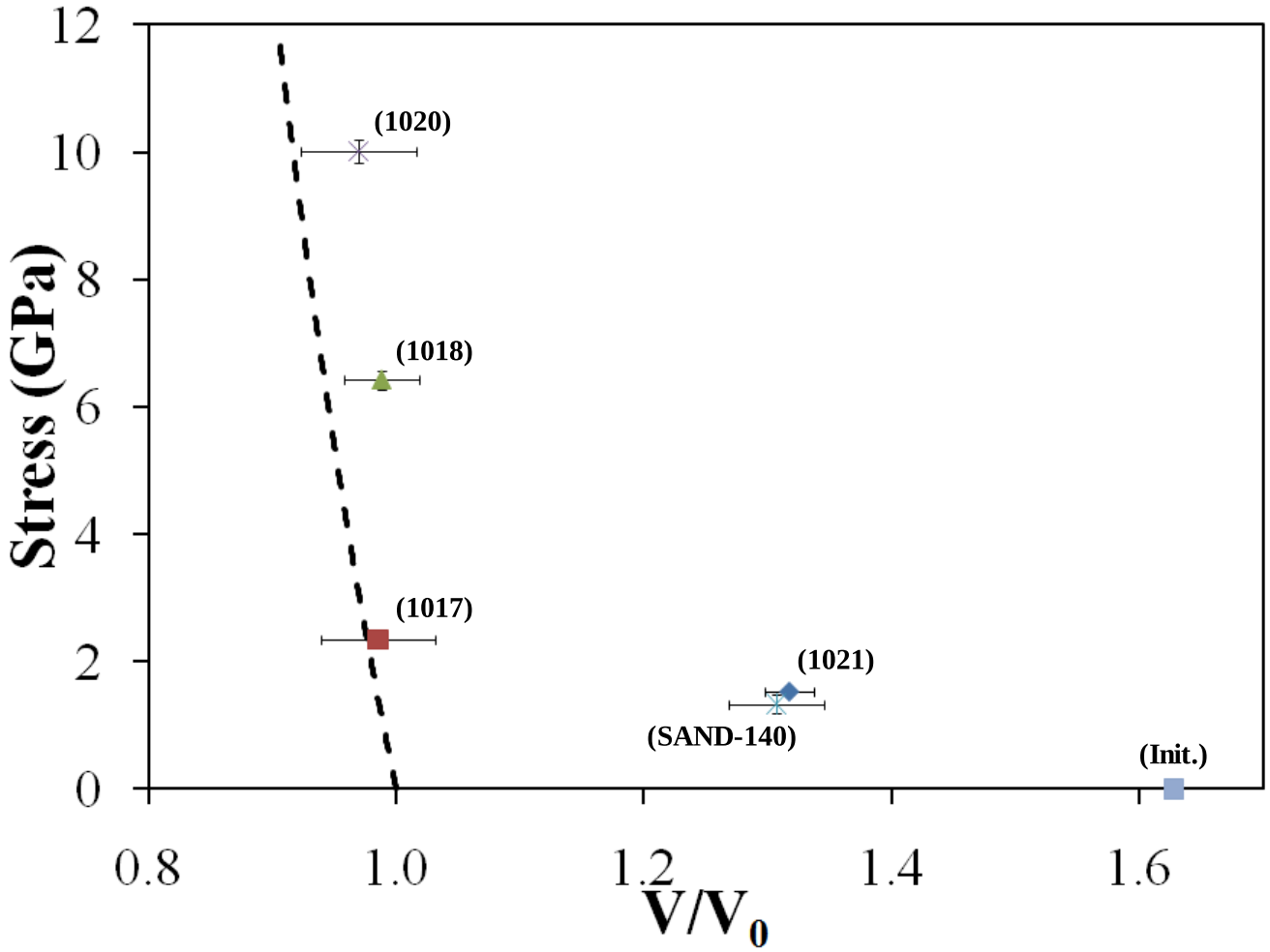

Figure 7.17: Results of parallel plate impact experiments on equivolumetric mixture of Ta + Bi_2O_3. Solid mixture Hugoniot calculated from isothermal mixing routine [1] shown as dotted line.

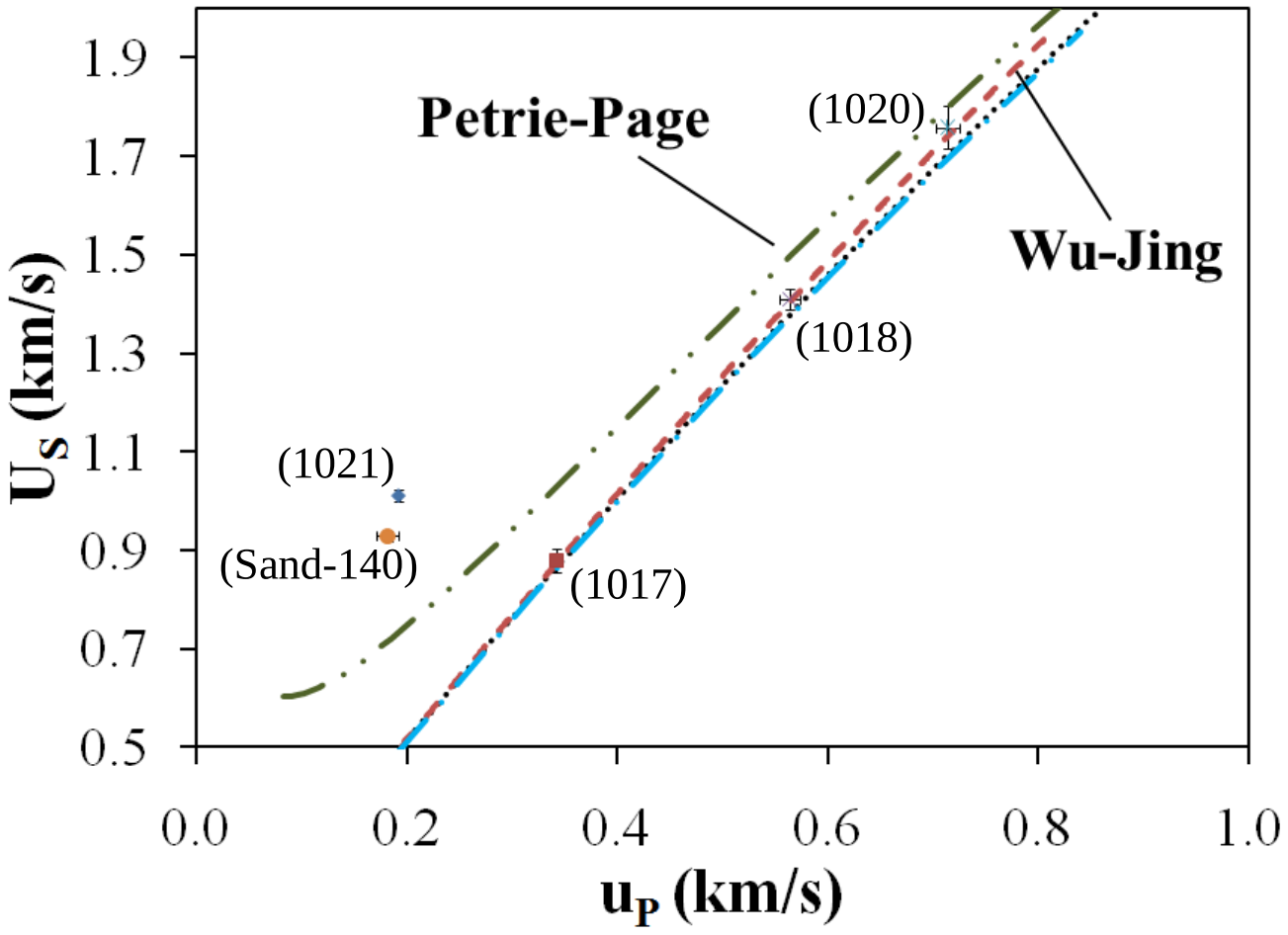

Figure 7.18: Results of parallel plate impact experiments on equivolumetric mixture of Ta + Bi_2O_3 in the U_S-u_P plane shown with preliminary fits of the isothermal mass mixing [1], Petrie and Page [13], Wu and Jing [83], and Krueger and Vreeland [44] models.

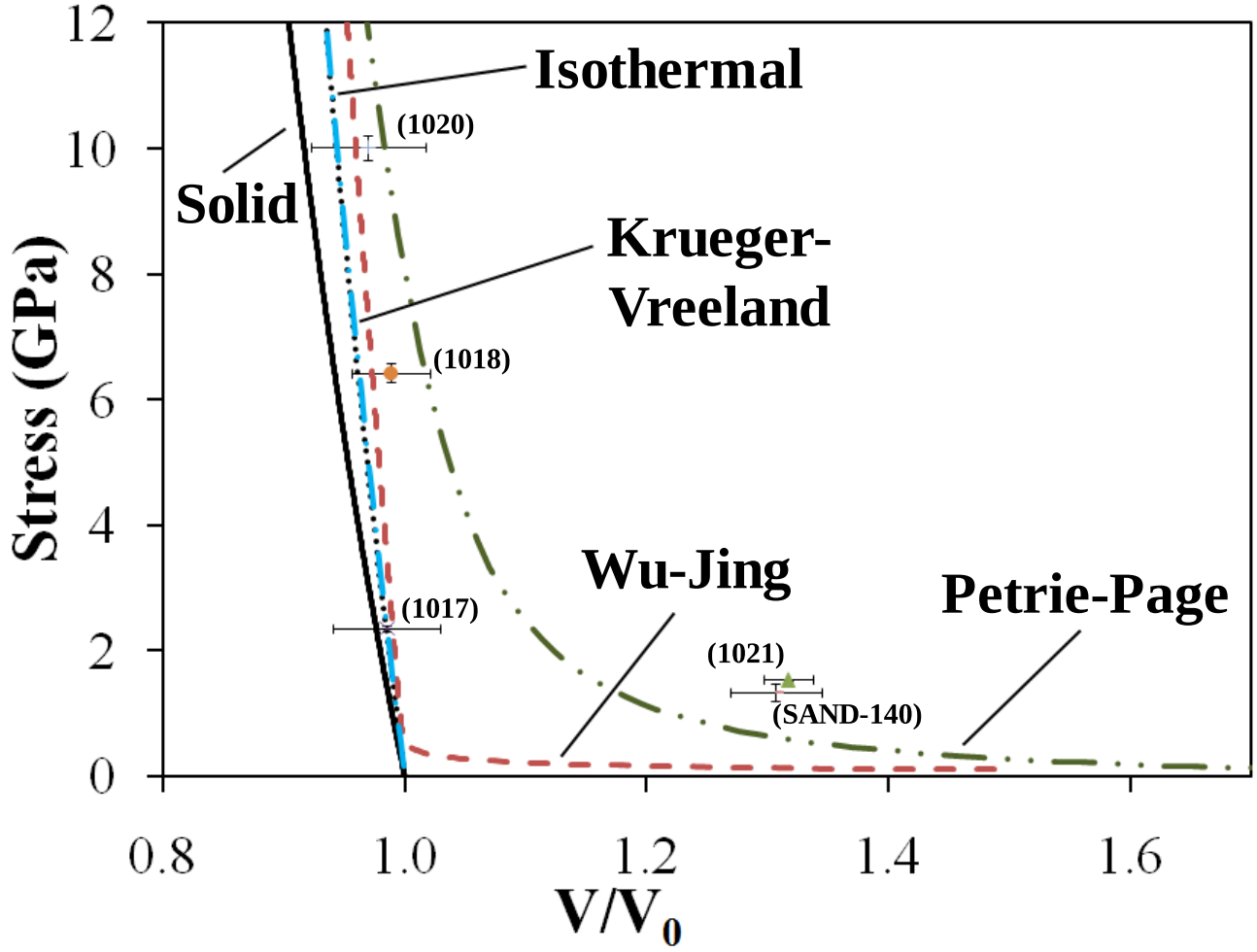

Figure 7.19: Results of parallel plate impact experiments on equivolumetric mixture of Ta + Bi_2O_3 in the σ-V plane shown with preliminary fits of the isothermal mass mixing [1], Petrie and Page [13], Wu and Jing [83], and Krueger and Vreeland [44] models. The predicted solid curve from McQueen's [1] isothermal mixing method is also shown.

falls slightly below the isothermal mass mixing [1] model in the U_S-u_P plane; the two predictions are nearly indistinguishable in the σ-V plane. Interestingly, this behavior differs from what was observed earlier when the two models were applied to a system with zero initial porosity. This indicates that with the incorporation of porosity, the Krueger-Vreeland [44] model predicts that a slightly greater amount of energy will be deposited with the passage of a shock wave of amplitude σ with respect to the isothermal mixing model [1]. This is in opposition to the case of the solid material where it is the isothermal mixing model that predicts the greater amount of energy deposited.

Also predicting a similar response to the aforementioned isochoric models is the isobaric model of Wu and Jing [83]. In the model implementation shown in Figs. 7.18 and 7.19 the yield strength of Fe_2O_3 is assumed for Bi_2O_3, as the yield strength of α-Bi_2O_3 is not known. This results in the same averaged yield strength for the mixture of Ta + Bi_2O_3 as was reported for the mixture of Ta + Fe_2O_3, $YS = 0.135$ GPa. Agreement between the isochoric and isobaric models is especially good at low stresses and material velocities due to the relatively low value of the yield strength chosen for the Wu-Jing [83] model. As stress and material velocity increase, the Wu-Jing [83] model tends to slightly under predict the stress at a given volume and over predict the shock velocity at a given material velocity in comparison with the two isochoric models. This type of behavior can be linked to the energy deposited during shock compaction, with the isobaric model predicting that a slightly lesser amount of energy will be deposited for a shock wave of a given amplitude.

A distinctly different compaction response is observed for the model of Petrie and Page [13]. As stress increases, this model initially over predicts and then under predicts the level of compaction achievable for a given applied stress. With the low stress portion

of this model based solely on the cold (quasi-static) compaction behavior, this observation is in line with the work of Sethi and co-workers [67] who found that quasi-static compaction is more efficient (higher density achievable for a given applied stress) than dynamic compaction at low stresses. It should also be noted that for the Ta + Bi_2O_3 system, the model of Petrie and Page [13] does predict compaction to full density at elevated stresses, which is in contrast to the same model prediction for the Ta + Fe_2O_3 system. This is observed in Fig. 7.19 as the Petrie-Page [13] prediction approaches the other fully dense compaction curves (isothermal mixing [1] and Krueger-Vreeland [44]) at elevated stresses, and is due to the higher initial density in this system. However, agreement of Petrie and Page's model [13] is relatively poor over the entire stress range investigated.

From a comparison of the experimentally obtained data with model predictions for the Ta + Bi_2O_3 system, it is observed that compaction to full density for this material occurs at approximately 2.5 to 3 GPa. As stress increases above this, the material follows along the inert curves for stresses up to the highest obtained experimentally, i.e. at 10 GPa. This behavior indicates that a shock-induced reaction, measurable on the time scale of the experiment, may not be occurring during parallel plate impact of the Ta + Bi_2O_3 system for stresses up to 10 GPa.

7.4.2 Compaction Model Fits

In applying the P-α and P-λ compaction models, a reference porous Hugoniot that assumes a zero crush strength is required, and the isothermal mixing model of McQueen [1] is chosen as this reference. This choice is a matter of personal preference as the Krueger-Vreeland [44] model could similarly be employed for the reference curve with little effect on the P-α and P-λ model predictions. Fits of the experimental data with the P-α predictions

are shown in Fig. 7.20.

Similar to the mixture of Ta + Fe_2O_3, the rate independent α fit of Carroll and Holt [10] (shown as the double dot-dashed line in Fig. 7.20) does a poor job of describing the experimental compaction behavior observed for the Ta + Bi_2O_3 mixture. Though this model incorporates the yield strength, an experimentally measurable quantity, either the form of this equation or the method of determining the yield strength is unsuitable for describing this mixture.

The exponential form of α proposed by Grady [88] (shown by the dashed line in Fig. 7.20) does only a slightly better better job than the previous rate independent model. The best fit with this relation is found with $n = 6.854$. With experimental data points in the lower stress region lying well above the curve predicted by this formulation, the model is shown to significantly over predict the level of densification achievable at low stresses. Furthermore, with the crush strength P_s set to 3 GPa, convergence of the model is forced at this point, and results in an under prediction of the actual density during compaction. Taking into account the forced convergence at 3 GPa and the relatively poor fit with experimental data points, this formulation is not deemed as a satisfactory method of describing the compaction behavior of Ta + Be_2O_3.

The standard α formulation of Butcher and Karnes [6] and Herrmann [5] (shown by the single dot-dashed line in Fig. 7.20) is by far the best at following the experimentally observed densification trend. Shots 1021 and SAND-140 fall very close to the model prediction, while shot 1017 falls only slightly below the predicted trend. In this formulation, P_e and α_E are determined using Carroll and Holt's [10] critical stress relation in a similar manner as presented for the Ta + Fe_2O_3 mixture. Using this approximation, inputs in the model include $P_e = 0.0858$ GPa, $\alpha_E = 1.6276$, and $P_S = 3.0$ GPa, where the value of n

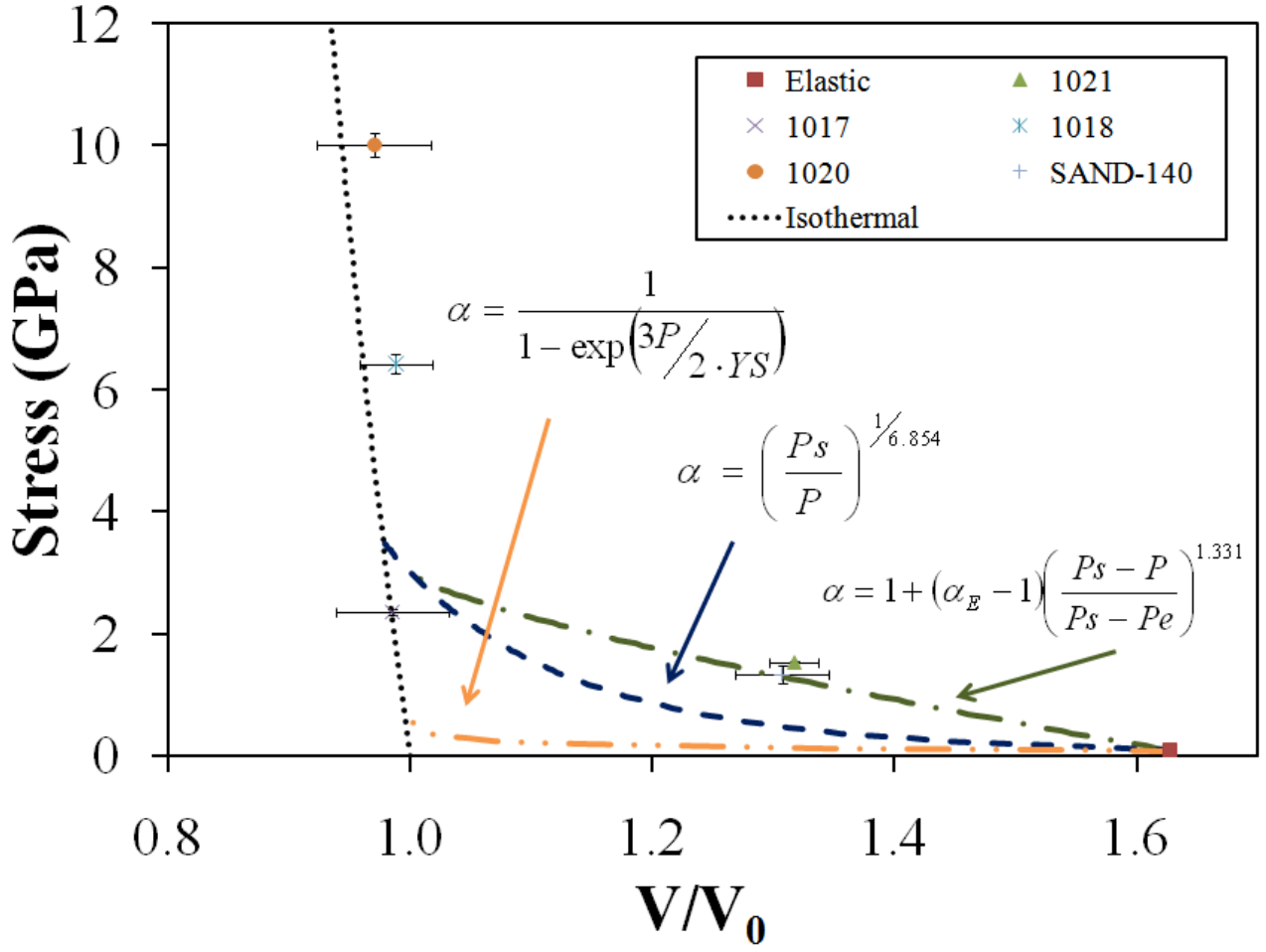

Figure 7.20: Experimental compaction data for Ta + Bi_2O_3 fit to various forms of the P-α compaction model. The porous equation of state shown is from the isothermal mixing method of McQueen [1].

determined from a best fit to the experimental data is n = 1.331. Agreement between experimental results and the model prediction is moderately good for this formulation of α; however, this may be due more to the entire stress range over which compaction occurs being relatively small, and the forcing of P_s = 3.0 GPa.

The P-λ fit to the experimental data is shown in Fig. 7.16, where results from shots 1021, 1017, and SAND-140 are used, together with the initial conditions. For this fit, the yield strength (densification strength) is set to 0.135 GPa and n is allowed to vary to achieve the best agreement between model prediction and experimental results. With YS = 0.135 GPa, a best fit of the experimental data is achieved with n = 0.08358. However, similar to the previous mixture studied, n is found to vary linearly with YS, where the linear relationship for this mixture is found to be $n = 0.619YS + 4.739 \text{ x}10^{-5}$. Thus the same fit could be achieved with any combination of YS and n that obey this linear relationship.

Immediately observable in Fig. 7.21 is the significantly higher crush strength predicted by this formulation than is experimentally observed. From the model, it appears that this material compacts to near full density around 7 to 8 GPa. However, it is shown experimentally (shot 1017) that near full compaction is observed closer to 2.5 to 3 GPa. Discrepancy between experimental points and the model fit are attributed to the functional form of the model and the location of the two lowest stress data points (shots 1021 and SAND-140). By fitting the model to the initial conditions (σ=0, λ=0) and the results from shots 1021, 1017, and SAND-140, the prediction is going to be weighted heavily toward the data points corresponding to shots 1021 and SAND-140 as they fall near the same location in the σ-λ plane. Furthermore, with the fit weighted toward these data points, the exponential nature of the fit forces the prediction to yield a higher than experimentally observed value for the crush strength.

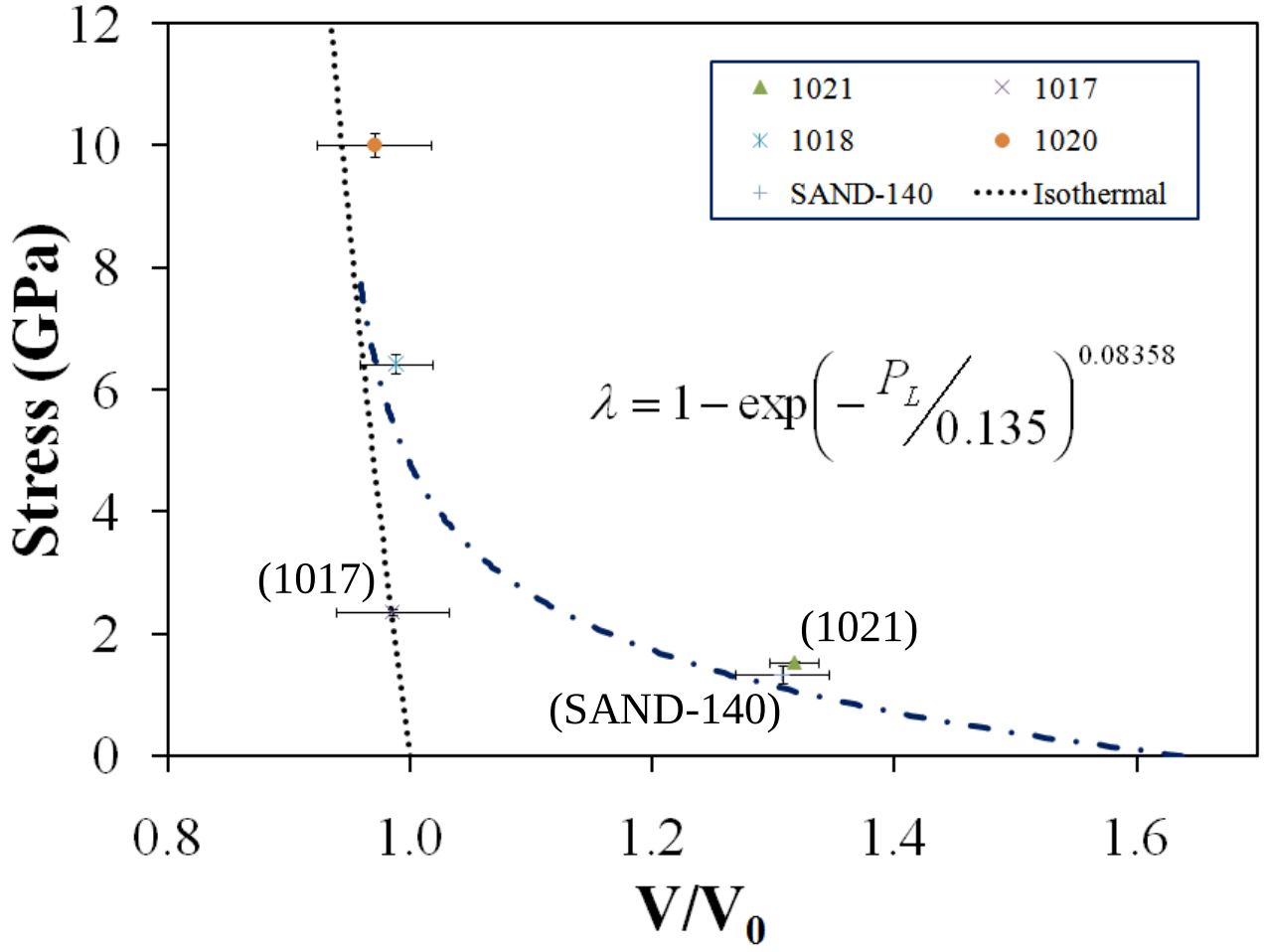

Figure 7.21: Experimental compaction data for Ta + Bi_2O_3 system fit to P-λ compaction model. Porous equation of state shown is that which is determined using the isothermal mixing method of McQueen [1].

7.4.3 Concluding Remarks

From the analysis of the Ta + Bi_2O_3 material system it is shown that the isochoric equations of state of McQueen [1] and Krueger and Vreeland [44] as well as the isobaric EOS of Wu and Jing [83] largely predict the same Hugoniot response for the porous mixture. From these curves compaction to full density for this mixture is determined to occur somewhere in the neighborhood of 2.5 to 3 GPa, where the value of 3 GPa has been used in implementing the P-α compaction model. Over the stress range investigated, it is determined that the model of Petrie and Page [13] is not suited well to describe either the compaction response or the fully compacted equation of state response of the mixture. With regard to compaction models, neither the P-α or the P-λ models do an exceptionally good job of describing the experimentally observed compaction behavior. However, it should be noted that the lack of a good fit between the models and the experimental data may be due in part to the limited number of data points in the incomplete compaction region.

7.5 Summation of Results and Trends

Though both mixtures studied in this investigation are thermites comprised of Ta and an oxide component (Fe_2O_3 or Bi_3O_3), large variations in the consolidation behavior of these systems exist. To begin with, the initial density of the mixtures are such that one is below the anomalous limit of the Hugoniot response while the other is not. This difference alone limits direct comparison of certain mixture models between the two systems, as some models are not applicable to lower initial density systems. Furthermore, while the plenitude of data for the Ta + Fe_2O_3 system warrants greater confidence in a model's ability to adequately describe the observed compaction phenomena, the exact opposite is true for the Ta + Bi_2O_3 system. Add to this the extremely different morphology for each of the two

oxides, and similarities in compaction characteristics between the two systems decreases even further.

However, certain characteristics of the mixtures and underlying phenomena occurring during the compaction process are shared between both mixtures. For instance, the location and method by which porosity is removed heavily influences the characteristic shape of the compaction curves for both mixtures. Although the primary location of voids differs between the mixtures, the mechanisms by which their removal occurs is of great importance to the observed compaction characteristics. Also, both powder mixtures possess an inherent yield strength, and though this property may not be directly determined from the yielding behavior of the individual solid constituents, as has been shown by the relatively poor fit for models employing volume fraction averaged yield strengths (Wu-Jing [83] and Carrol and Holt rate independent P-α [10] models), it may be a property which can be directly measured from the yielding behavior of the powder mixture.

Keeping these similarities and differences in mind, it is desired that a framework be found which can bridge the compaction behaviors of these markedly different, yet also markedly similar, thermite powder mixtures. Of great importance will be finding a common physical framework within which the compaction of these powder mixtures can be defined.

CHAPTER VIII

ANALYSIS AND DISCUSSION OF RESULTS

Considering results from the previous chapter, it is observed that the equations of state and compaction models discussed, in their current forms, vary significantly in their ability to describe and/or predict the dynamic (shock) compression response of the heterogeneous powder mixtures. With regard to the equations of state (EOS), their strength lies in the ability to predict the high stress shock response, after complete consolidation of the mixture has occurred. For those equations of state that do incorporate a crush-up response (Wu-Jing [83], Petrie-Page [13]), the densification response predicted lies either well above or well below the experimentally observed compaction curve. In contrast to the EOS predictions, the compaction models describe specifically the lower stress crush-up response of the mixtures, and rely on an appropriately chosen equation of state to characterize the fully consolidated shock response. In addition, while the dynamic compaction models do incorporate certain physically measurable properties, P-$\alpha(YS,\ P_e,\ \alpha_E,\ P_S)$ and P-$\lambda(YS)$, they also employ a completely empirical fitting parameter n.

As a result, the compaction models' strength lies in their ability to describe a densification trend that has been pre-determined through a number of dynamic experiments; they lack in true predictive ability. Furthermore, a comparison of model predictions between the two thermite systems illustrates the inability of these models to consistently predict the compaction response across multiple heterogeneous systems. What is desired is a common framework within which one can predict the consolidation behavior of different thermite

powder systems, specifically the crush strength. Moreover, it would be of even greater benefit if this predicted response could be formulated based on some combination of measurable constituent/mixture properties and observations of initial microstructures. The focus of this chapter is to examine the possibility of developing such a framework.

In developing this framework, the author seeks to answer a few fundamental questions. First and foremost, is it possible to predict the dynamic consolidation response and crush strength of a heterogeneous powder mixture without performing a single dynamic experiment? Naturally, the question then arises, can this prediction be validated through experimental results? This chapter seeks to address these questions within the context of the two heterogeneous thermite powder mixtures investigated. To this end, a systematic, continuum level approach for predicting the crush-up response of highly heterogeneous thermite powder mixtures will be presented. Within this analysis the quasi-static yielding behavior, initial morphology (configuration), and volumetric distribution of both the individual constituents and the powder mixture are of primary importance.

8.1 Analysis Framework

In developing a framework to predict the shock consolidation response of thermite powder mixtures, one needs to first identify the key features of compaction that are to be contained within this framework. Although it would be most desirable to capture the entire densification trend, from small initial compactions incrementally up to full densification (crush), past work has shown that continuum level approaches to this type of problem often result in models that are well suited for describing only specific regions of compaction. Considering the enumerable intricacies associated with the densification of powders in the incomplete compaction regime, where not only strength, but also rate dependencies, and

powder morphology can strongly influence the observed response, the continuum level approach developed here will seek only to predict the stress at which full compaction occurs. However, in formulating this approach it is prudent to examine both the initial configuration of the powder mixture as well as the yield properties thereof.

8.1.1 Configurational Considerations

It has been shown that initial powder configuration is a parameter that must be considered when describing both the densification [16, 92] and reaction [72, 130] responses in energetic powder mixtures. Thus, if an attempt to predict the crush strength in heterogeneous powder mixtures is to be made, it is necessary to examine the initial powder configuration and determine if there are any features which would suggest a particular component or characteristic may dominate the compaction response. At minimum, one could examine micrographs of the loose powder mixtures to obtain the necessary configurational information, and at best, micrographs of the initial (pre-compressed) powder configuration. For the mixtures investigated, both types of micrographs are available, and are shown in Fig. 8.1.

One of the key features of any mixture is the composition of the 'matrix' material. To be defined as a matrix, one component of the mixture must be clearly shown to surround the alternate component, such that discrete and isolated particles of the non-matrix material are observed. For the Ta + Fe_2O_3 mixture, Fig. 8.1(b) clearly shows discrete particles of Ta that are nearly completely surrounded by Fe_2O_3. Thus in this mixture, the matrix is the Fe_3O_3 component. Aside from the occasional isolated void pockets found within localized region of Ta (shown in Fig. 7.7(b)), the majority of the voids in the Ta + Fe_2O_3 mixture are contained within the matrix of porous and/or agglomerated Fe_2O_3. Thus, upon first inspection, the configuration of this mixture would lead one to suppose that the removal of

voids may be heavily influenced by the consolidation behavior of Fe_2O_3.

Figure 8.1(d) shows the pre-compacted mixture on which impact experiments were performed for the Ta + Bi_2O_3 powder system. Immediately apparent from Fig. 8.1(d) is that the two components in this mixture are more evenly distributed than the previous mixture, and that it is the metal (Ta) component rather than the oxide that seems to form the matrix. As such, the bulk of porosity in this mixture is located within localized regions of Ta. Again, one may suppose that the deformation and yielding properties of Ta will dominate the consolidation behavior of the mixture.

The presence of distinct particle contacts is also observed in the Ta + Bi_2O_3 mixture. It has been shown by Kumar and co-workers [61] and others [71, 132] that during the process of shock consolidation, particle contacts are the primary locations where stress is transfered. Thereby, densification is initiated at and around these contacts through particle deformation and fracture. As such, the localized stresses and strains at these points of contact can be significantly larger than those of the bulk. This phenomena may in turn have a pronounced effect on the strength properties of rate dependent materials, such as Ta. In the Ta + Bi_2O_3 system, the majority of contacts within the mixture are Ta-Ta contacts. Therefore, the rate dependence of Ta [133], and its effect on yielding behavior would need to be accounted for explicitly, if an accurate response is to be predicted over the entire compaction region.

Key aspects of the initial configuration that need be considered in developing a framework to predict the densification response in thermite powder mixtures are:

1. *Identify the matrix material.* Are there any features of the matrix that would lead one to believe it would dominate the compaction process?

2. *Determine the location of voids.* Are these voids discrete, or are they contained

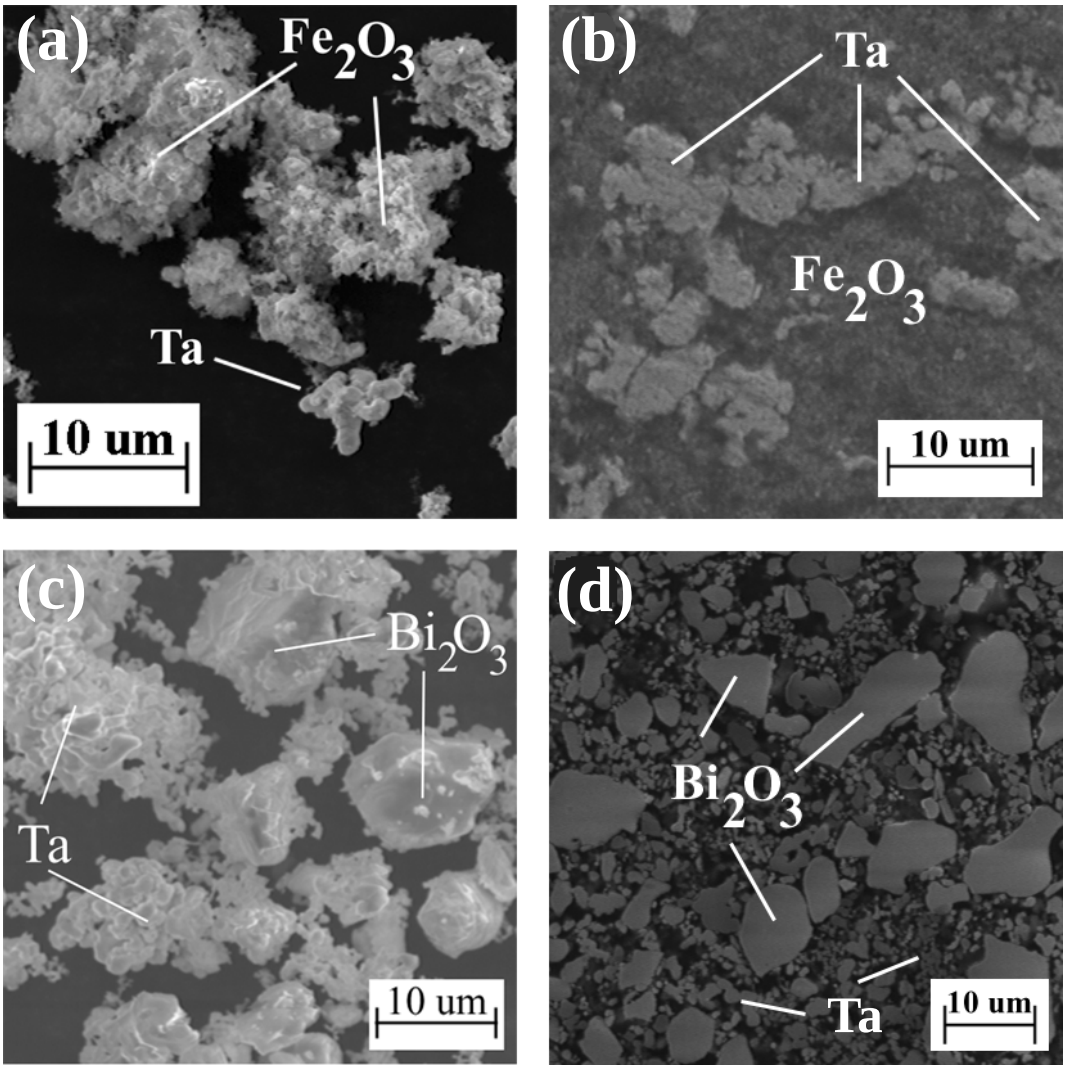

Figure 8.1: SEM images showing Ta + Fe_2O_3 mixture in (a) loose and (b) 49 % TMD precompacted state, and Ta + Bi_2O_3 mixture in (c) loose and (d) 62 % TMD precompacted state.

within a porous structure?

3. *Establish the primary mode of stress transfer.* Is this through the growth and deformation of particle contacts or through the crushing up of porous aggregates?

4. *Identify the differences in yield properties between the components.* Are any of these materials, especially the matrix material, rate sensitive?

For the Ta + Fe_2O_3 system, Fe_2O_3 is identified as the matrix material, and *its yield properties are found not to be rate sensitive*. In addition, with Fe_2O_3 composing the matrix, the primary mode of stress transfer in this system is through the aggregates of porous Fe_2O_3, where the passage of stress results in the crushing up of Fe_2O_3. For the Ta + Bi_2O_3 system, Ta is the matrix material, and *its yield properties are rate dependent*. In this mixture, stress is transferred primarily through discrete Ta-Ta particle contact points, and the majority of void space is located in the volume surrounding these contacts.

With yield properties of the matrix materials differing between systems, it is expected that the path of densification in the incomplete compaction regime, where strength effects dominate will be significantly different between the two systems. As the matrix is composed of a rate insensitive material in the Ta + Fe_2O_3 mixture, it is expected that a rate independent compaction model may well describe the consolidation behavior of the mixture over the entire stress range up to crush. On the other hand, in the Ta + Bi_2O_3 mixture where the matrix (Ta) is rate sensitive, the consolidation behavior may not be well represented by a rate independent model. However, as stress is increased to levels above the yield strength and beyond, the densification responses of the two mixtures will tend to converge toward their respective crush strengths, a value which will soon be shown to depend on measurable quasi-static densification strength properties.

It should be noted that at present, the postulations as to the yielding behavior of the mixtures have been made based on observations of microstructures in the pre-compressed (initial) configuration, shown by Figs. 8.1(b) and (d). However, similar predictions could be made from the loose powder configurations, as shown in Figs. 8.1(a) and (c).

8.1.2 Densification Strength Properties

Determining the rate independent densification strength properties of the constituents and/or mixtures is the primary component in the current approach used to predict the dynamic crush strength. In determining these properties, what is actually desired is a measure of the resistance the powders and mixtures offer to densification. As illustrated in the previous chapter, certain equations of state and compaction models, e.g. the Wu-Jing [83] and P-α [10] models, go as far as to require certain yield properties as input parameters into their models. However, the poor fit of these models with experimental data, shown in Figs. 7.14, 7.15, 7.19, and 7.20, clearly indicates that the current methodology used to extend yield properties to describe the compaction behavior of the mixtures is flawed. Recall, the yield strength in both relations was determined from volume fraction averages using the rule of mixtures for the individual yield strengths of the solid materials ($YS = f_1 YS_1 + f_2 YS_2$). Furthermore, the actual yield strength of Bi_2O_3 is at present unknown, and the yield properties of Bi_2O_3 were assigned to those of Fe_2O_3. This further exacerbates the ineffectiveness of any model which incorporates this yield.

For these powder systems, and specifically for the mixture involving Bi_2O_3 (whose yield properties are unknown), it is desired that a *densification strength parameter* be determined. This densification strength parameter should capture the powders resistive effect to densification, and can considered as a corrolary to the flow strength for solids. It should

also describe the stress necessary to further densify the powder, regardless of compaction mechanism. This is important because thermite system are composed of metal and oxide components, two classes of materials that typically have very different deformation mechanisms. However, at high stresses and small particle sizes (comparable to the conditions in this work), even extremely brittle materials like diamond and silicon [134] have been found to undergo plastic deformation during consolidation, serving to unify the compaction mechanisms occurring during dynamic loading between different material systems.

Recall from the discussion on compaction models, that the P-σ_Y model provides a means by which one can determine an effective yield strength for homogeneous monosized powders. In this model the yield strength of the powder is determined through a functional relationship that assumes the initial powder configuration is such that rearrangement has already taken place. This model, with slight modifications, will be used for determining the densification strength parameter of the powders and powder mixtures because of the limited assumptions in its derivation. Recalling the practical extension of the P-σ_Y model put forth by Meyers and co-workers [85] from Sect. 4.1, it is found that there are two main assumptions. The first is that particles are spherical, and the second is that plastic yielding at the particle level occurs at stresses greater than 2.97 times the yield strength of the powders.

With regard to the first assumption, Fischmeister and Artz [20] have shown that differences in particle shape (and size) become less important as the compaction stress is increased. Thus if the model is applied to densification at higher stresses, the effects of particle shape effect can be minimized. Application of the plastic yield criterion to the constituents and mixtures requires further discussion. If it is assumed that the model is to be applied only to the densification response at higher stresses, it is likely that at these

higher stresses the material has already transitioned (at least to some degree) from elastic to plastic yielding. As such, in the higher stress regime, one is not measuring a yield strength in the strict sense of the term, but rather a resistance to densification that takes into account both elastic and plastic yielding, with the majority being plastic at higher stresses. For brittle particles, some finite amount of plastic deformation does take place, even in extremely brittle particles, prior to the onset of fracture [135] such that the plastic yield criteria is not thought to limit the applicability of the P-σ_Y model to exclude thermite powder systems.

Yield properties of the constituents and mixtures reported previously using the P-σ_Y model (see Tables 7.1 and 7.2), were determined over the entire densification range, inclusive of particle rearrangement. Though rearrangement is shown to have only a minor effect on the P-σ_Y models ability to describe the compaction behavior of Ta, its accuracy is significantly reduced in the case of both the oxide constituents (Fig. 7.1) and the mixtures which contain them (Fig. 7.4(a) and Fig. 7.5(a)). As such, if the density at which rearrangement has ceased can be determined, and the P-σ_Y model can be applied to only the compressional response of the powder at stresses where rearrangement no longer occurs (at higher stresses), it is expected that agreement between the P-σ_Y model and the experimentally observed quasi-static compaction data should improve significantly. Recall determining the effective yield, or densification strength parameter, at higher stresses also minimizes the particle size effect, thus allowing added confidence in the computationally fit apparent yield strength of the powder.

To determine the point at which rearrangement has completed in the constituents and mixtures, one could simply choose 64 % TMD similar to Fischmeister and Artz [20] in thier original development of the P-σ_Y model [20], as this is the density at which rearrangement

ceases in a random dense packing of monosized spheres. As powders in the current investigation are not monosized, nor perfectly spherical, this option presents a worst case scenario for determining the termination point of rearrangement. To arrive at a more accurate range of stress, the P-P_{Act} model is used to systematically predict this value.

Recall the P-P_{Act} model outlined in Sect. 4.2 predicts both a stress activated and a non-stress activated process, where the non-stress activated process is defined as corresponding to particle rearrangement. From the model parameter P_l in Tables 7.1 and 7.2, which is determined from a best fit of the quasi-static data, a measure of the stress at which rearrangement is the dominant mechanism can be found. However, it is not the stress at which rearrangement is dominant that is required, but rather the stress (and density) at which rearrangement has ceased. From the exponential nature of the P-P_{Act} equation (Eqn. 94), a value of stress four times that of P_l results in a contribution to compaction of less than 2 % based on rearrangement. This effectively supposes that rearrangement has completed at stresses four times greater than the stress P_l. As such, in this analysis a value of four times that of the P_l reported in Tables 7.1 and 7.2 is taken as the stress at which rearrangement has terminated. Inserting this value of stress into Eqn. 94 yields the corresponding density at which rearrangement has ceased.

Using the values of stress and density so determined, the form of the P-σ_Y model given by Eqn. 91 is modified slightly to reflect the fact that the data over which the model is now being applied no longer occurs at an initial stress equal to zero, but rather at some elevated stress P_0. The modified form of the P-σ_Y model is given by

$$P_Y = P_0 + 2.97\rho^2\left(\frac{\rho-\rho_0}{1-\rho_0}\right)\sigma_D \tag{139}$$

where P_0 and ρ_0 are the values of stress and percentage theoretical maximum density determined from the P-P_{Act} model for the point at which rearrangement has terminated and

σ_D describes the resistance of the powder to densification, hereafter referred to as the densification modulus. Using this equation, the densification modulus is determined for the constituents and the thermite powder mixtures for the stress range above which rearrangement has ceased. Fits of Eqn. 139 to the experimentally obtained quasi-static compaction data are shown in Figs. 8.2 and 8.3, and model parameters for the fits shown are given in Table 8.1.

Table 8.1: Fitting parameters for experimental data to the modified P-σ_Y model in the region of compaction where rearrangement no longer occurs for constituents and mixtures. Values of ρ_0 and P_0 are determined from P-P$_{Act}$ model at a value of four times P_l for the respective component/mixture.

	ρ_0 (% TMD)	P_0 (MPa)	σ_D (MPa)	R^2
Ta	0.532	193	802	0.999
Fe_2O_3	0.556	290	2863	0.984
Bi_2O_3	0.795	362	487	0.998
Ta + Fe_2O_3	0.675	553	1683	0.984
Ta + Bi_2O_3	0.679	281	634	0.999

Without rearrangement, the modified P-σ_Y model is shown to predict the experimentally observed compaction curve much closer. This behavior is observed for the starting components (Fig. 8.2) as well as the thermite powder mixtures (Fig. 8.3). Though still following the densification trend quite well, the poorest fit of the modified P-σ_Y model is shown for fits of Fe_2O_3 and the Ta + Fe_2O_3 mixture. The poorer fit is thought to result from the variation in both morphology and yield behavior of Fe_2O_3 from that of the ideal model assumptions. However, with model predictions still yielding fits with an R^2 value greater than 0.98, the densification moduli so obtained are taken to represent those of the

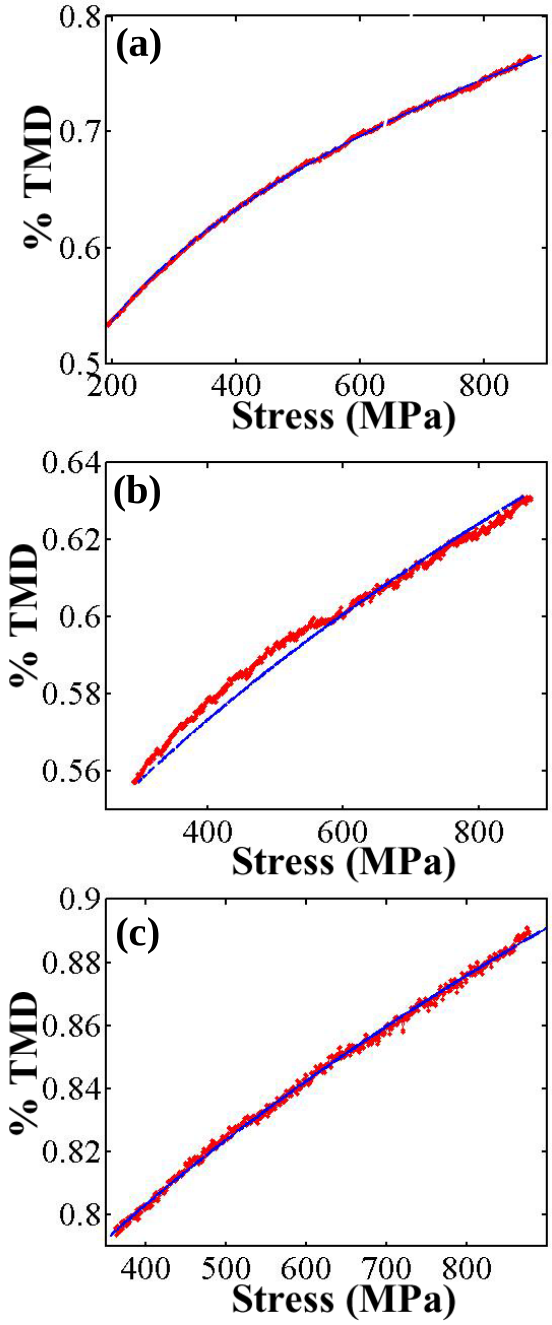

Figure 8.2: Quasi-static compaction curves in the range where rearrangement has ceased for (a) Ta, (b) Fe_2O_3, and (c) Bi_2O_3 shown by broad (red) line. Fits of the data to the modified P-σ_Y model in this range are illustrated by the dashed (blue) line.

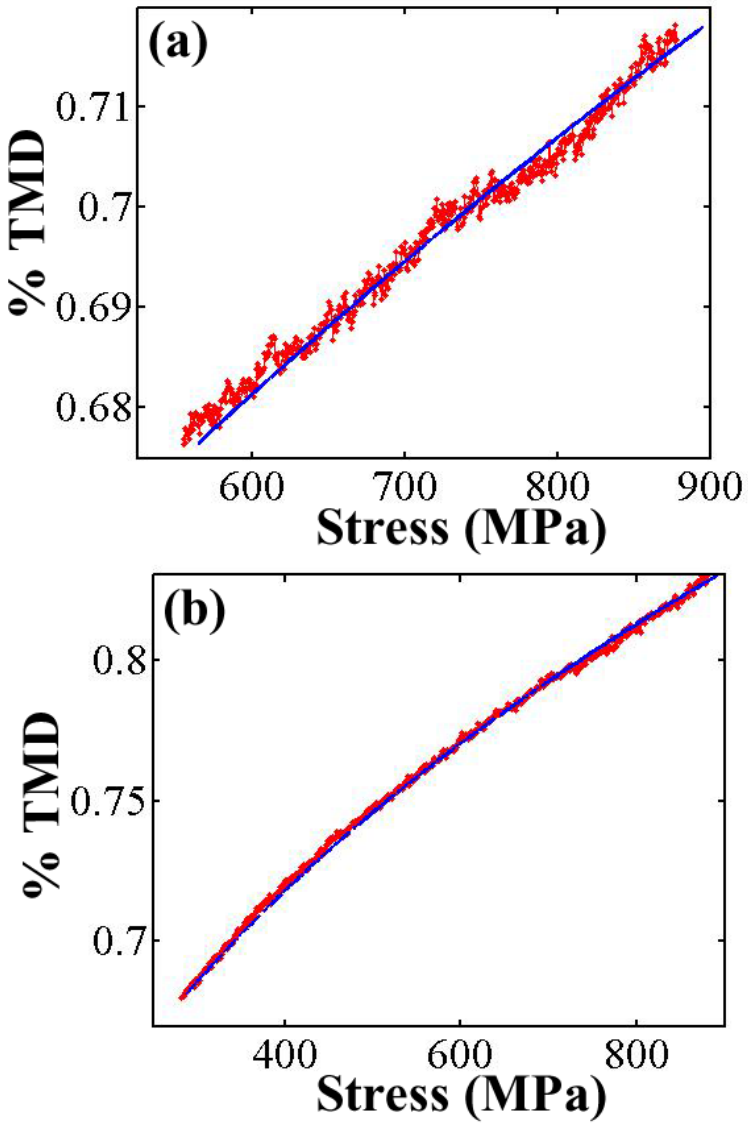

Figure 8.3: Quasi-static compaction curves in the range where rearrangement has ceased for (a) Ta + Fe_2O_3 and (b) Ta + Bi_2O_3 shown by broad (red) line. Fits of the data to the modified P-σ_Y model in this range are illustrated by the dashed (blue) line.

systems investigated. At this point, densification moduli for all powders and powder mixtures have been determined, and can now be used to predict the crush strengths for the powder mixtures.

8.1.3 Application to Dynamic Compaction Data

With the densification moduli for the powder constituents and their mixtures determined, a look at how these values can be used to predict the dynamic crush strength of the thermite powder mixtures is now presented. In applying the quasi-statically determined densification moduli, a method is desired that will encompass not only both of the heterogeneous systems currently under investigation, but also one that could be extended to many other heterogeneous systems. Of the models investigated, it is observed that only two are applicable for initial powder configurations both above and below the anomalous Hugoniot limit. These two models are the Wu-Jing [83] model, and the model of Petrie and Page [13]. Both models, in their current implementation, have been shown to not match well with experimentally obtained compaction data. The Petrie and Page [13] model is shown to under predict the density achievable at a given stress, while the model of Wu and Jing [83] is shown to over predict the same trend. Can either of these models be modified to reflect the densificaiton moduli of the powder previously determined? The answer is yes, the model of Wu and Jing [83] is well suited to this purpose.

Recall that in its previous implementation, the Wu-Jing [83] model had used the volume fraction averaged yield strength of the solid constituents to determine the critical stress at which plastic deformation begins. With the extremely low yield strength reported in Table 6.3 for Fe_2O_3 it is not surprising that incorporation of this value into the Wu-Jing [83]

model results in a significantly lower crush strength than is observed experimentally. Moreover, with the yield properties of Bi_2O_3 unknown, and taken to be equivalent to those of Fe_2O_3, uncertainties in the predicted properties of the mixture containing Bi_2O_3 are amplified further. It is obvious from the fits previously shown, Figs. 7.14 and 7.19, that using the yield properties of the solid for predicting the powder response can lead to highly non-representative fits. The effective yield properties of the powders, specifically, the densification moduli calculated previously, will be incorporated into the Wu-Jing [83] model in an attempt to obtain better agreement between model predictions and an experimentally determined crush strength.

The densification moduli determined for the powders and their mixtures given in Table 8.1 are incorporated into the Wu-Jing [83] model to replace volume fraction averaged yield properties of the solid, and the predicted compaction responses are obtained for both mixtures. The model prediction based on the measured densification modulus, combined with the experimentally obtained dynamic compaction data and plotted for the Ta + Fe_2O_3 system in Fig. 8.8.

What is immediately noticed in Fig. 8.4 is the remarkably good agreement between experimental data and model predictions for not only the crush strength, but also the majority of the experimental data in the incomplete compaction region. With the exception of shots 756 and 823, the prediction follows along the experimentally obtained data through the incomplete compaction region and approaches the crush-up to full densification at approximately 6-7 GPa. To determine whether one constituent or another is dominating the compaction response of the mixture, the crush-up response predicted from the densification moduli of the constituents as well as a volumetric average of the two densification moduli are shown in Fig. 8.5. The two predictions that follow closely to the majority of

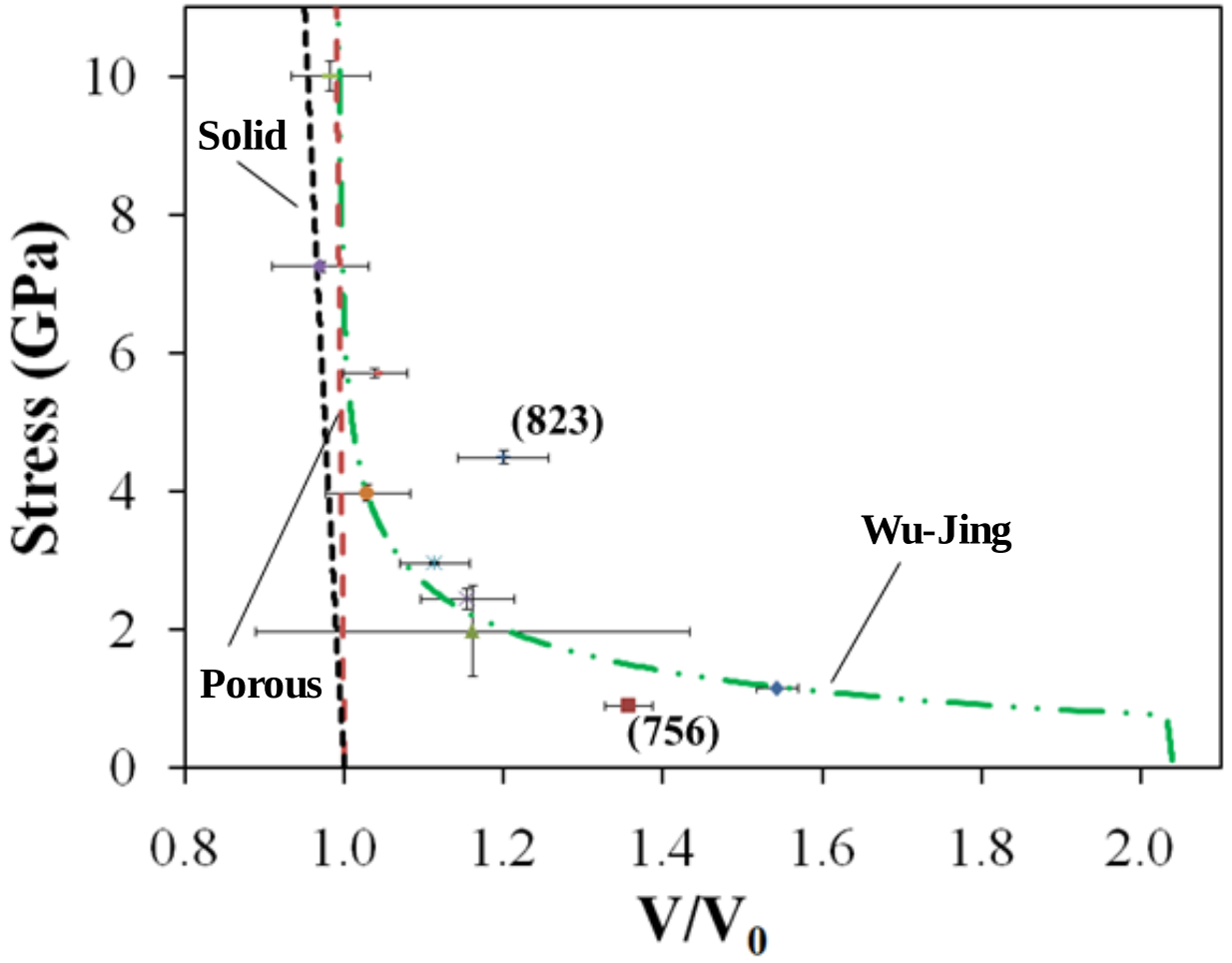

Figure 8.4: Experimental data and Wu-Jing model fit inclusive of the densification moduli for the Ta + Fe_2O_3 powder mixture. Shown in the plot are the Hugoniots of the solid and porous mixtures, and Wu-Jing [83] prediction based on the densification modulus obtained from quasi-static data. Porous Hugoniot is predicted by setting yield strength in original Wu-Jing [83] model to 10 MPa, which allows for complete crush up at nearly zero applied stress.

the data are those based on the densification modulus obtained directly for the mixture given in Table 8.1 (double dot-dashed line in Fig. 8.5) and that calculated by averaging the densification moduli of the individual constituents (dashed line in Fig. 8.5).

Also shown in Fig 8.5 are the densification responses obtained from the Wu-Jing [83] model if the moduli of Ta (dotted line) and Fe_2O_3 (dot-dashed line) are assumed. These curves illustrate what the crush and compaction response would look like if either Fe_2O_3 or Ta were dominating the densification response. One can see that the Ta prediction falls well below the experimental data, while the Fe_2O_3 prediction lies well above. The crush strengths predicted by these curves are approximately 3 and 10 GPa, respectively. The actual crush strength of the mixture is found to be between 6 and 7 GPa, and it is shown in Fig. 8.5 that both the measured densification moduli and the calculated 50 % mixture moduli predict crush strengths within this range.

For this mixture, it is shown that neither Ta nor Fe_2O_3 dominates the densification response of the heterogeneous mixture. Rather, the response appears to be controlled by the densification moduli of the mixture as a whole. Thus, for the system of Ta + Fe_2O_3, whose matrix is composed of a non-rate sensitive material (Fe_2O_3), the rate independent quasi-statically determined densification moduli of the mixture combined with the rate independent P-α formulation in the Wu-Jing [83] model are shown to not only describe the crush strength of the mixture well, but also the material response in the incomplete compaction regime. Agreement between experimental data and the model prediction in the incomplete compaction region is attributed to the matrix material being composed of a rate insensitive material.

In a similar manner, model predictions are plotted with experimental data for the Ta + Bi_2O_3 material system in Fig. 8.6. It is observed that the crush strength for the mixture

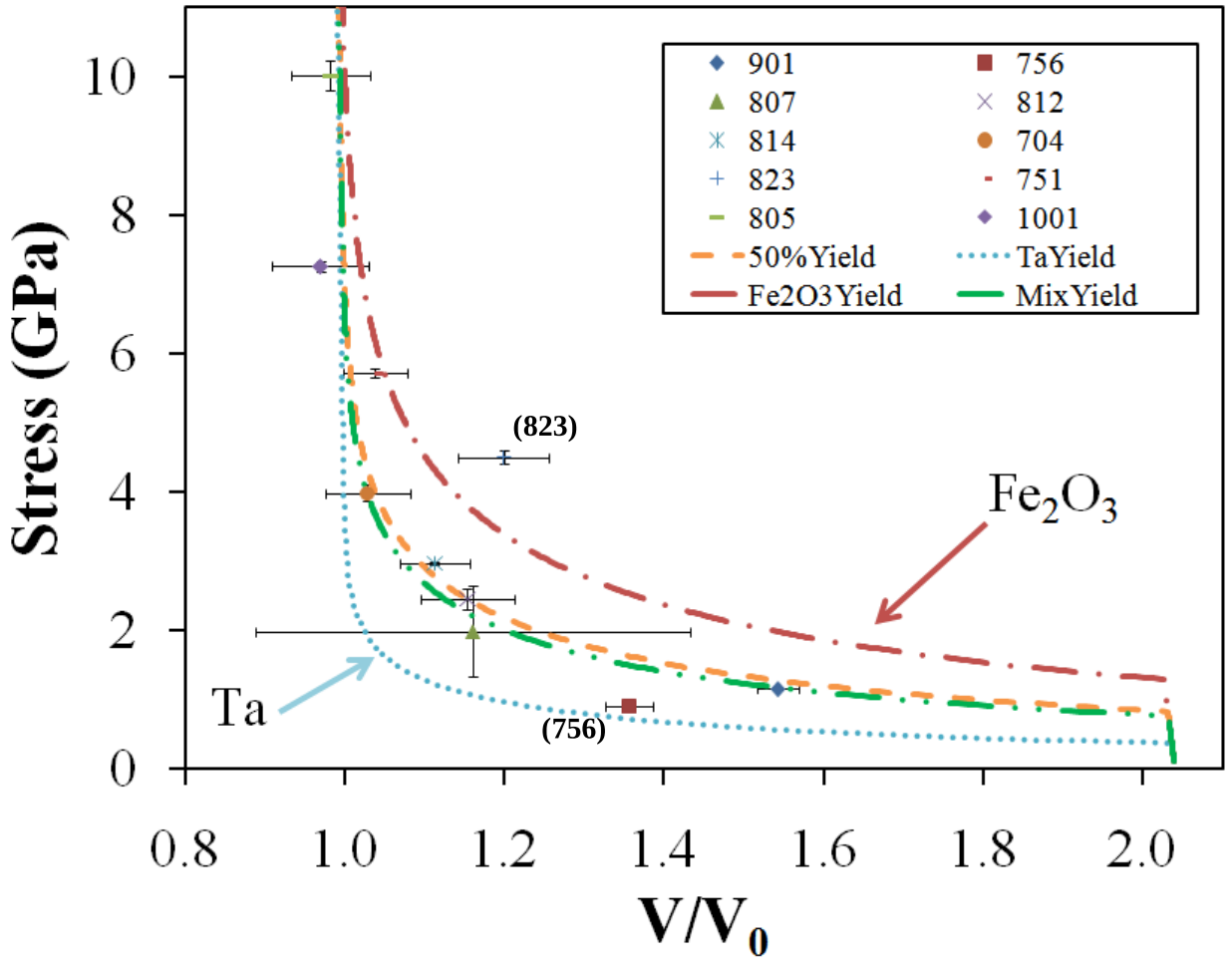

Figure 8.5: Experimental data and Wu-Jing model fits for the Ta + Fe_2O_3 material system. Shown in the plot are predictions based on the densification moduli of Ta (dotted), Fe_2O_3 (dot-dash), Ta + Fe_2O_3 mixture (double dot-dash), and moduli determined from a 50 % mixture of the moduli of Ta and Fe_2O_3 (dashed).

is predicted well with similar approximations and model implementation. However, upon further inspection of Fig. 8.6 it is observed that experimental data in the incomplete compaction region does not match well with any of the predicted densification paths. Though the approached developed in this dissertation is not formulated to describe the compaction response in this region, it is useful to examine the origins of this deviation to better understand the compaction processes occurring in these mixtures.

In formulating a hypothesis as to why the experimental data in the incomplete compaction region is so far removed from the model predictions in the Ta + Bi_2O_3 mixture, one looks for insights from the initial powder configuration and material properties. Recalling the initial powder configuration shown in Fig. 8.1(d), it is observed that Ta comprises the matrix material. One explanation for the deviation in predicted and measured responses in the incomplete compaction regions is due to the rate sensitive yield properties of Ta. To examine the effect of rate sensitivity on the densification moduli of the mixture, the constitutive behavior of Ta from Chen and Gray [133] is applied within the Johnson-Cook [136, 137] strength model. For shots 1021 and SAND-140, the total strain experienced by the compact is defined through $\epsilon = (V - V_{00})/V_{00}$ where V is the shock compressed volume and V_{00} is the initial volume of the powder. From this a strain of $\epsilon \approx 0.19$ is obtained. Using the rise time of the propagated stress pulse from the PVDF gauge, $t_{rise} \approx 170$ ns, and dividing the total strain by the rise time, the strain rate in the mixture is found to be on the order of 10^6/s. Neglecting temperature effects, the yield strength for Ta predicted from the Johnson-Cook [136] model is slightly over 1 GPa at 10^6/s. Increases in temperature result in decreased predicted yields.

The strain rate so determined is based on the total strain in the compact, and it is expected that strains and their corresponding strain rates at particle interfaces are going to be

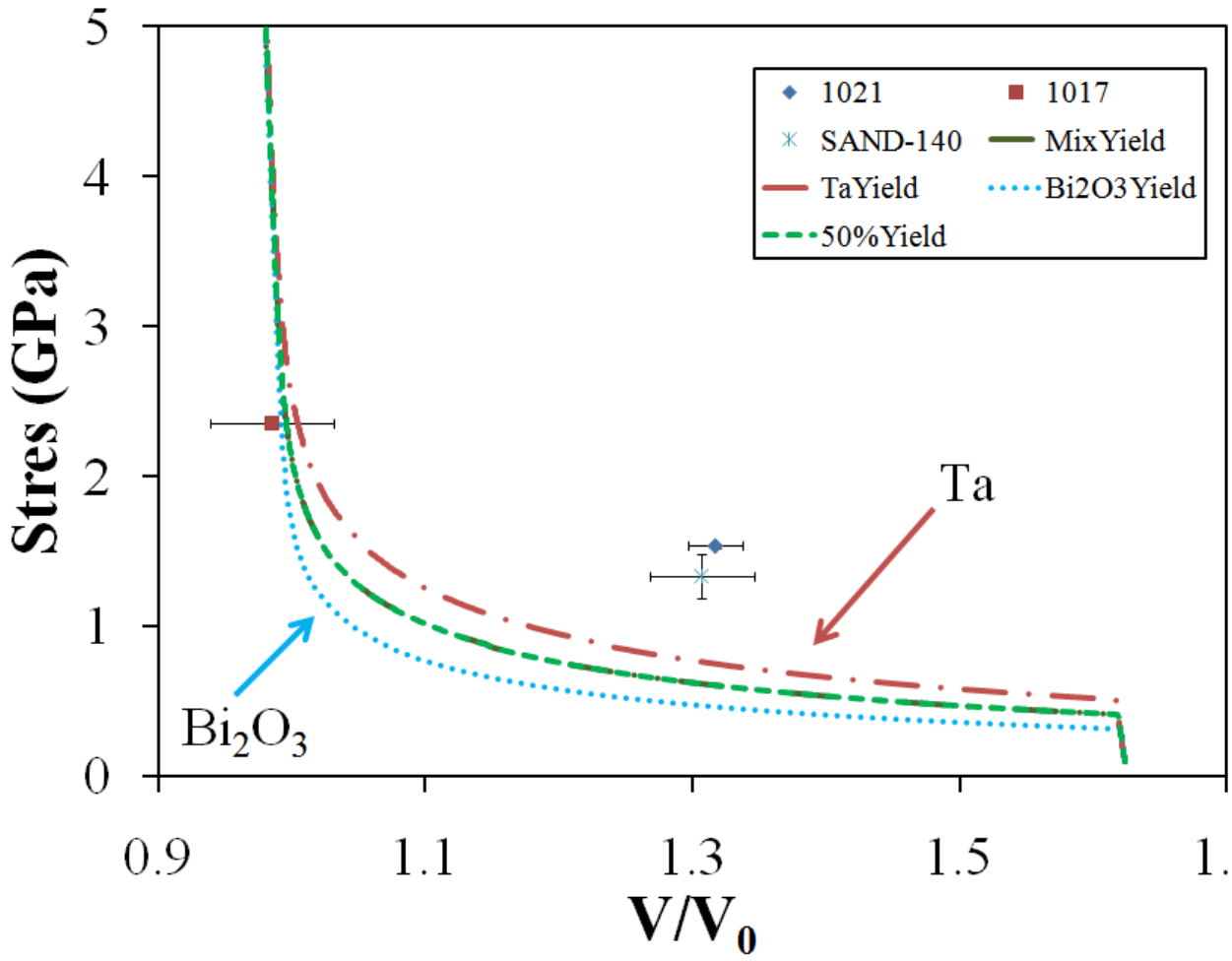

Figure 8.6: Experimental data and Wu-Jing model fits for the Ta + Bi_2O_3 material system. Shown in the plot are predictions based on the densification moduli of Ta (dot-dashed), Bi_2O_3 (doted), Ta + Bi_2O_3 mixture (double dot-dash), and the moduli determined from a 50 % mixture of the densification moduli of Ta and Bi_2O_3 (dashed), wher the last two predictions are on top of one another.

much higher than those of the bulk, thus further increasing the rate sensitive yield properties of Ta. To examine how this rate sensitivity might effect the consolidation response of the mixtures, results of the Wu-Jing model based on the densification modulus of the mixture, as well as a moduli of pure Ta assuming a rate insensitive yield strength, and those of Ta with rate sensitive yield properties predicted at 10^6/s and 10^9/s are shown in Fig. 8.7. Shown in this figure is that increasing the mixture moduli value to reflect the increase in strength due to the rate sensitive yield behavior of Ta results in the predicted densification curves in the incomplete compaction region lying much closer to the experimentally observed data. However, increasing the moduli as such also increases the predicted crush strength to a value well above that which is observed experimentally. Thus it is shown that incorporating rate sensitive strengths into a rate insensitive compaction model to reflect the densification response in the incomplete compaction region results in unrealistic values for the crush strength.

From Figs. 8.5 and 8.6 it is shown that the Wu-Jing [83] prediction based on the rate independent densification moduli of the powder mixtures determined using the current approach, is able to predict the experimental crush strength in both mixtures. Furthermore, this formulation also predicts well the densification behavior of the Ta + Fe_2O_3 mixture in the incomplete compaction region. This trend is not observed for the Ta + Bi_2O_3 mixture as predictions fall well below the experimentally determined data in the incomplete compaction region. One explanation for the variation in model prediction between the two incomplete compaction regions can be formulated if one considers the stress levels active in each of these regions.

In defining a crush strength, one is effectively defining a level of stress that is well above the yield strengths of either of the components, such that at this stress materials can

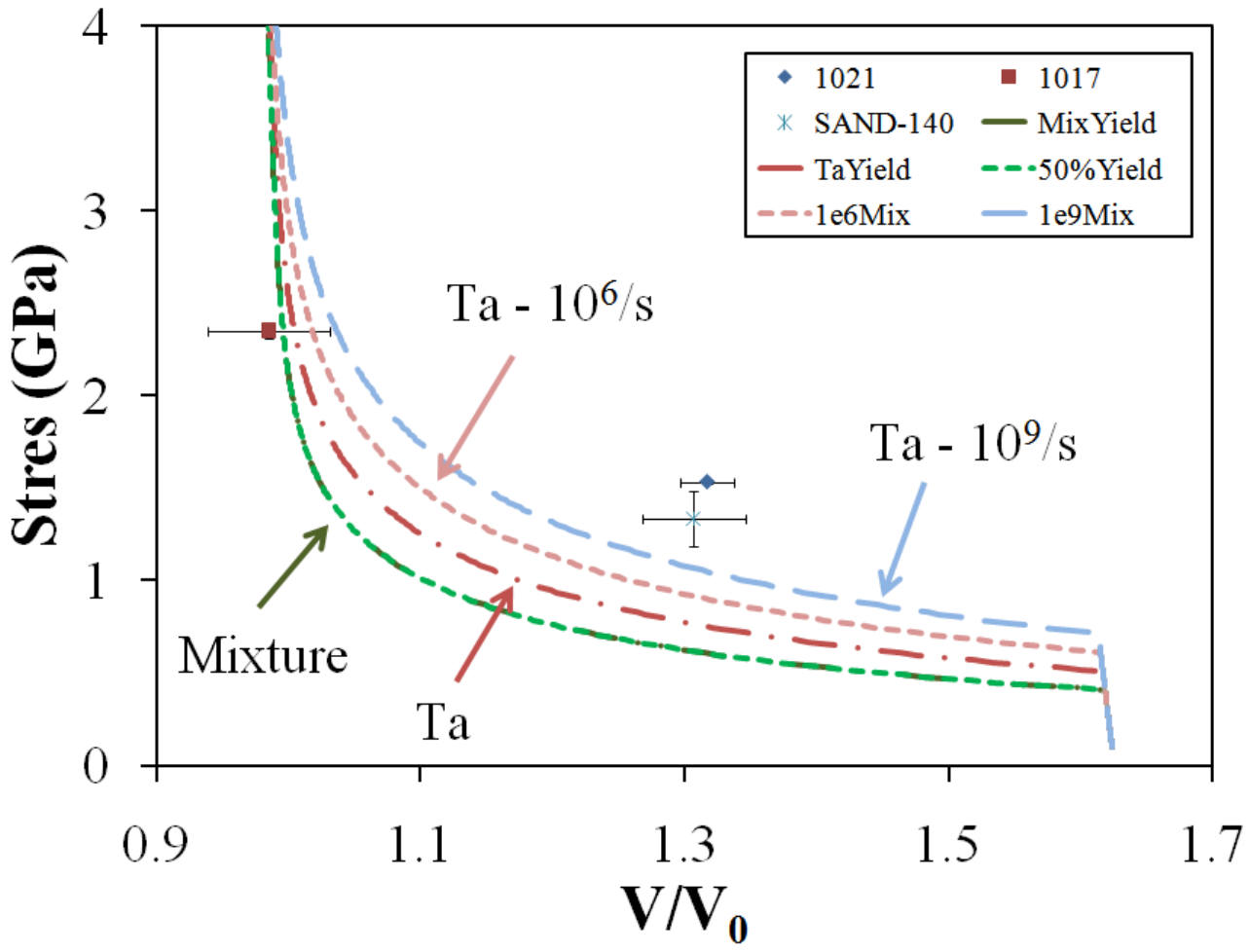

Figure 8.7: Wu-Jing model predictions based on quasi-static densification moduli of the mixture and Ta, and a moduli that reflects the increased strength of Ta due to its rate sensitivity. Note that model predictions based on the rate sensitive yield properties of Ta (10^6/s and 10^9/s) bring curve closer to experimental points in incomplete compaction region at the cost of over predicting the crush strength.

flow freely and fill the surrounding voids. Therefore, the influence of dynamic strength effects would be greatly reduced at values of stress greater than and equal to those of the crush. This is why models that do not specifically incorporate strength effects, such as the isochoric Mie-Gr*ü*neisen extrapolation [15] and the energy partitioning Krueger and Vreeland [44] model, can predict the high-stress Hugoniot response with significant accuracy.

For stresses below the crush, dynamic strength properties of the components influence the Hugoniot response of the mixtures, and can result in deviations between model predictions and experimental data in the incomplete compaction region. As such, any model which seeks to predict the entire crush-up response of a material (or mixture) must be able to include a means to incorporate strength effects that may dominate in the low stress range. In addition, at these low stresses other effects such as those due to particle morphology, size, shape, roughness, etc. are expected to also influence the compaction response. Thus, a continuum level approach to describe these types of phenomena is not practical. A more realistic approach to solving these types of problems is through meso-scale (particle level) simulations, especially those employing imported experimental microstructures [79]. In summation, while lacking agreement between predicted and experimental results in the incomplete compaction region, the continuum level approach developed in this dissertation does, as desired, predict the crush strength in both of the thermite powder mixtures investigated. A look is now given to how this approach might be used to predict the compaction response in other thermite mixtures.

8.2 Model Extension

With a continuum level approach taken, a methodology has been developed to predict the crush strength in thermite powder mixtures based solely on the quasi-static loading behavior of the materials and/or mixture. Furthermore, this methodology has been shown to work quite well for two separate mixtures whose matrix materials are composed of rate sensitive and non-rate sensitive materials. The approach has been successfully applied to equivolumetric mixtures of Ta + Fe_2O_3 and Ta + Bi_2O_3, for which experimental data were obtained. The approach is now extended to other configurations. First, a look is given to the effect of volumetric distribution on the compaction behavior, e.g. equivolumetric versus stoichiometric. Next, mixtures of Al + Fe_2O_3 are examined.

In the case of the thermite mixtures investigated thus far, the constituents have been combined in an equivolumetric ratio; that is, there are equal volumes of the metal and oxide components. Recall, the equivolumetric ratio was chosen because the large density difference between constituents in the stoichiometric configuration reduces the amount of contacts between the reactive components. By adjusting the volumetric ratio to unity, the components become more evenly distributed, which should increase the propensity for mechanically initiated reactions. At the same time, the overall heat of reaction is reduced as one goes away from the stoichiometric ratio. Thus, one can see that there is a trade-off between initiating a reaction to completion and the performance based on the total energetic yield of the components. What then, is the effect of varying stoichiometry on the observed densification trends in these mixtures, and how might this be related to reaction initiation conditions?

The predicted σ-V densification responses of the Ta + Fe_2O_3 and Ta + Bi_2O_3 mixtures in the equivolumetric and stoichiometric ratios, are shown in Figs. 8.8 and 8.9. It should

be noted that all mixtures are for an initial porous density of 50 % TMD, and that the densification moduli used in the Wu-Jing [83] model are volume fraction averages of the constituent densification moduli based on the equivolumetric or stoichiometric ratios of the constituents. Also shown in the figures are the densification responses of the mixtures assuming they are controlled by one of the constituents, e.g. either the metal or the oxide.

In examining the different densification curves for the Ta + Fe_2O_3 mixtures, shown in Fig. 8.8, one can see that varying the ratios of the constituents influences the densification response and results in a wide range of predicted crush strengths. Altering the ratio of constituents from equal volumes to the stoichiometric configuration increases the predicted crush strength from approximately 7 to 9 GPa. Furthermore, if the response were controlled solely by the crush response of Fe_2O_3, the crush strength would raise to nearly 11 GPa. Thus, for the Ta + Fe_2O_3 system, increasing the volume percentage of Fe_2O_3 to that of the stoichiometric ratio ($\approx 70\%$), results in an increased crush strength. On the other hand, for the Ta + Bi_2O_3 mixture, where the oxide is now the more compliant component, altering the ratio of constituents from equivolumetric to stoichiometric results in a decrease in the predicted crush strength, as shown in Fig. 8.9. The total range of predicted crush strengths resulting from a Ta dominated or a Bi_2O_3 dominated mixture is just slightly over 1 GPa. As such, the relatively similar compliance between Ta and Bi_2O_3 results in a crush strength difference between the equivolumetric and stoichiometric configurations of only ≈ 0.25 GPa.

From the predictions shown for the different volumetric configurations in Figs. 8.8 and 8.9, information regarding the reaction initiation conditions for different volumetric ratios of thermite mixtures can be obtained. Consider the schematic shown in Fig. 8.10, which illustrates the amount of PdV work that must be done to consolidate mixtures of varying

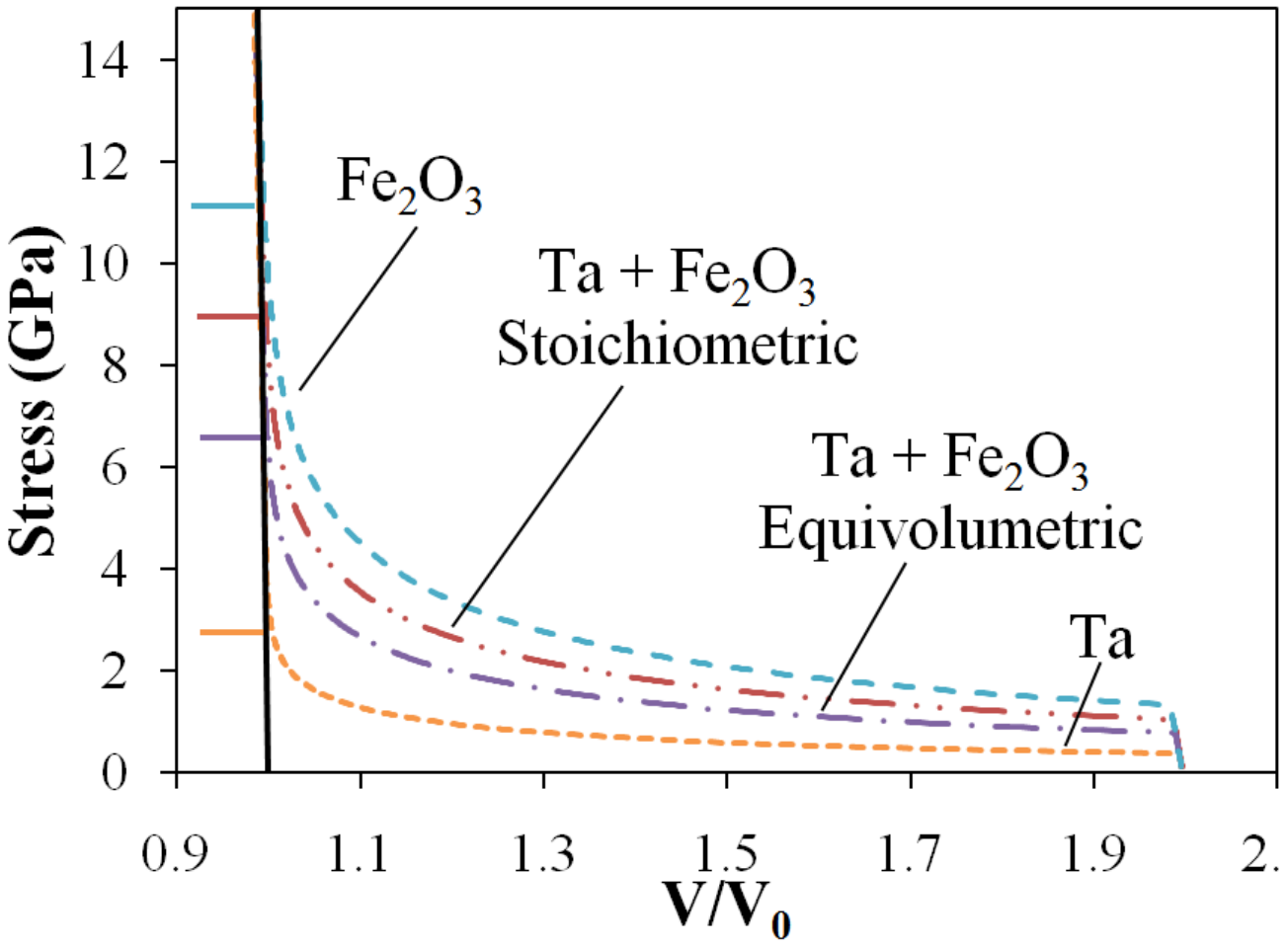

Figure 8.8: Wu-Jing model predictions based on quasi-static densification moduli of the Ta + Fe_2O_3 mixture in the equivolumetric and stoichiometric ratios. Also shown is the densification response of the mixture if it were controlled by the densification moduli of each of the constituents. Indicated along the solid Hugoniot are approximate values of the crush strength predicted by the various densification responses.

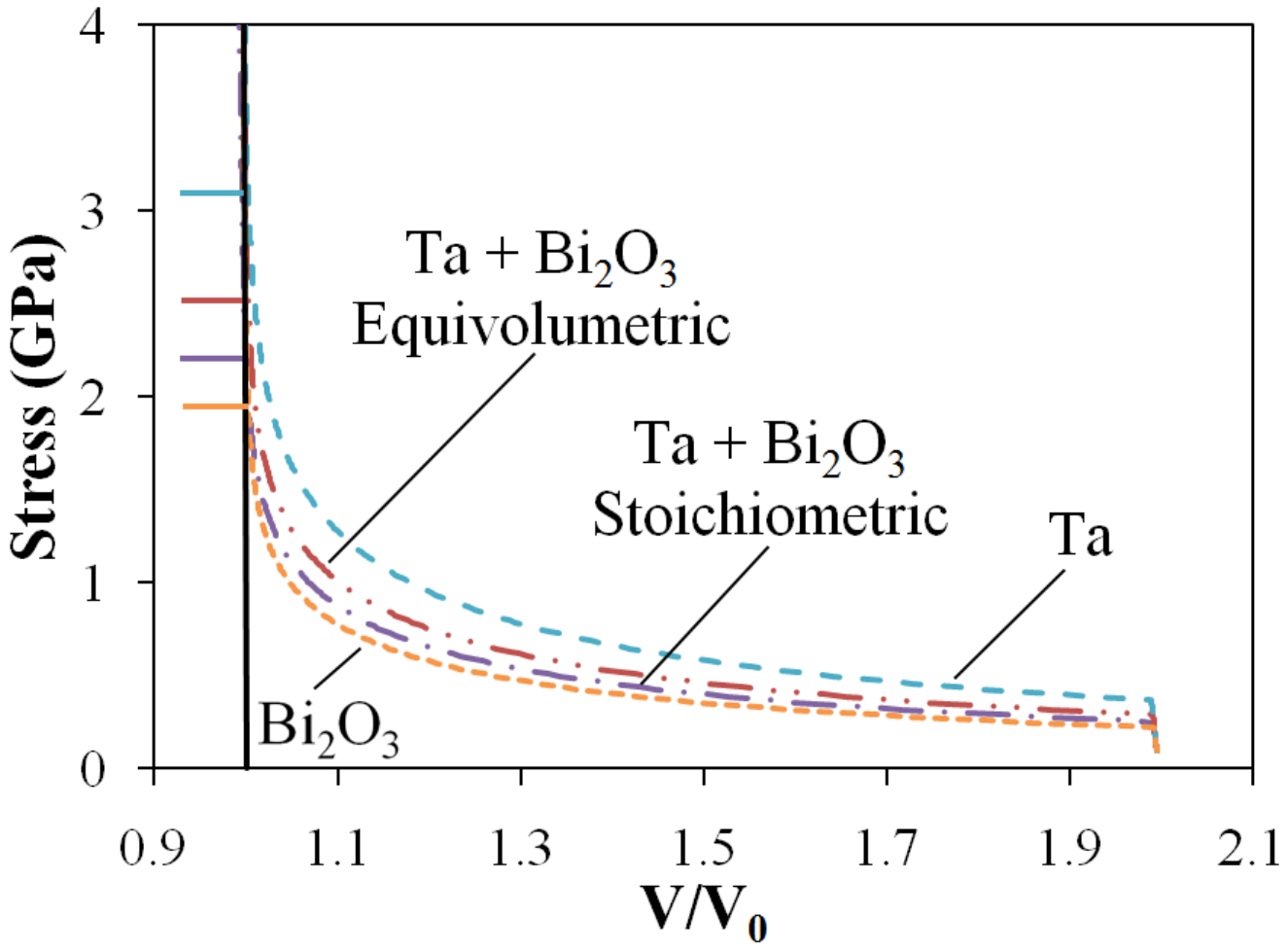

Figure 8.9: Wu-Jing model predictions based on quasi-static densification moduli of the Ta + Bi_2O_3 mixture in the equivolumetric and stoichiometric ratios. Also shown is the densification response of the mixture if it were controlled by the densification moduli of each of the constituents. Indicated along the solid Hugoniot are approximate values of the crush strength predicted by the various densification responses.

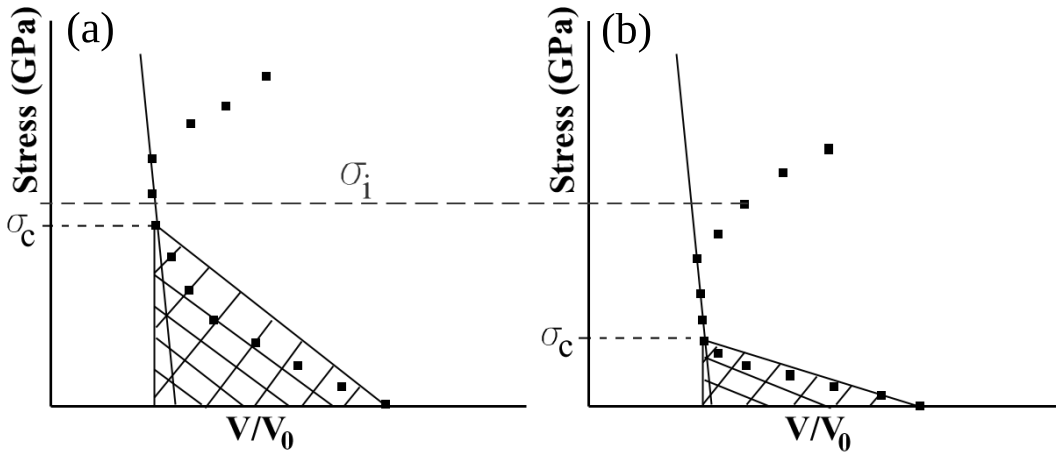

Figure 8.10: Schematic illustrating the vastly different *PdV* energies (hatched regions) associated with fully densifying two materials whose crush strengths differ. Note the energy consumed during consolidation may not be available for initiation of reaction.

crush strength. If the two crush curves represent a single mixture (say the Ta + Fe_2O_3 mixture) in different volumetric configurations, it is evident that a significantly greater amount of energy (hatched region in Fig. 8.10) goes into densifying the mixture having the higher crush strength. Hence for a given applied stress, σ_i, a significant portion of the energy is consumed during consolidation and so may not be available for initiation of reaction. Such that a material with a higher crush strength may thus have a higher reaction initiation threshold.

For the Ta + Fe_2O_3 mixture, where the stoichiometric configuration results in a higher crush strength, this result is intuitive as the stoichiometric mixture has less inter particle contacts between the reactive constituents and may require a higher energy to initiate. However, the exact opposite is true for the Ta + Bi_2O_3 mixture, where the stoichiometric mixture now has the lower crush strength. Thus, attempting to infer a relative magnitude

for the reaction threshold based simply on which mixture has the more even volumetric distribution may not be justified. Rather, it is the crush strength, dominated by configurational effects, that influences the threshold condition for reaction initiation.

To further investigate the effectiveness of the approach developed, mixtures of Al + Fe_2O_3 are examined in conjunction with the crush strength predictions from the two equivolumetric mixtures previously covered. Of particular interest is how the variation in densification moduli of the constituents and mixtures effects the predicted crush strength. Aluminum is chosen because its shock properties are well characterized, its strength is much lower than Ta, and being fcc, its strength properties are not rate sensitive; thus allowing for the approach to be applied to a wide variety of thermite systems.

The densification moduli of an equiaxed Al 6061 powder are determined using the approach previously outlined in Sections 8.1.2 and 8.1.3. The initial powder morphology and modified P-σ_Y fit to the non-rearrangement portion of the quasi-static compaction data is shown in Fig. 8.11. The stress at which rearrangement has ceased, as determined through the P-P_{Act} model, is P_0 = 13 MPa. Fitting the modified P-σ_Y model given by Eqn. 139 to the quasi-static data results in densification moduli for the aluminum powder of σ_D = 224 MPa.

Using the densification moduli for aluminum, the dynamic crush strength for a mixture of Al + Fe_2O_3 is determined for an initial density of 50 % TMD. It should be noted that this mixture is combined in an equivolumetric ratio. For the Al mixture, the predicted crush behavior is based on a calculated 50 % mixture moduli of the components. This is thought to be a sufficiently accurate approach as the calculated 50 % moduli and the measured densification moduli for the Ta containing mixtures were found to predict similar responses. The results of the predicted Al mixture response, together with similar predicted

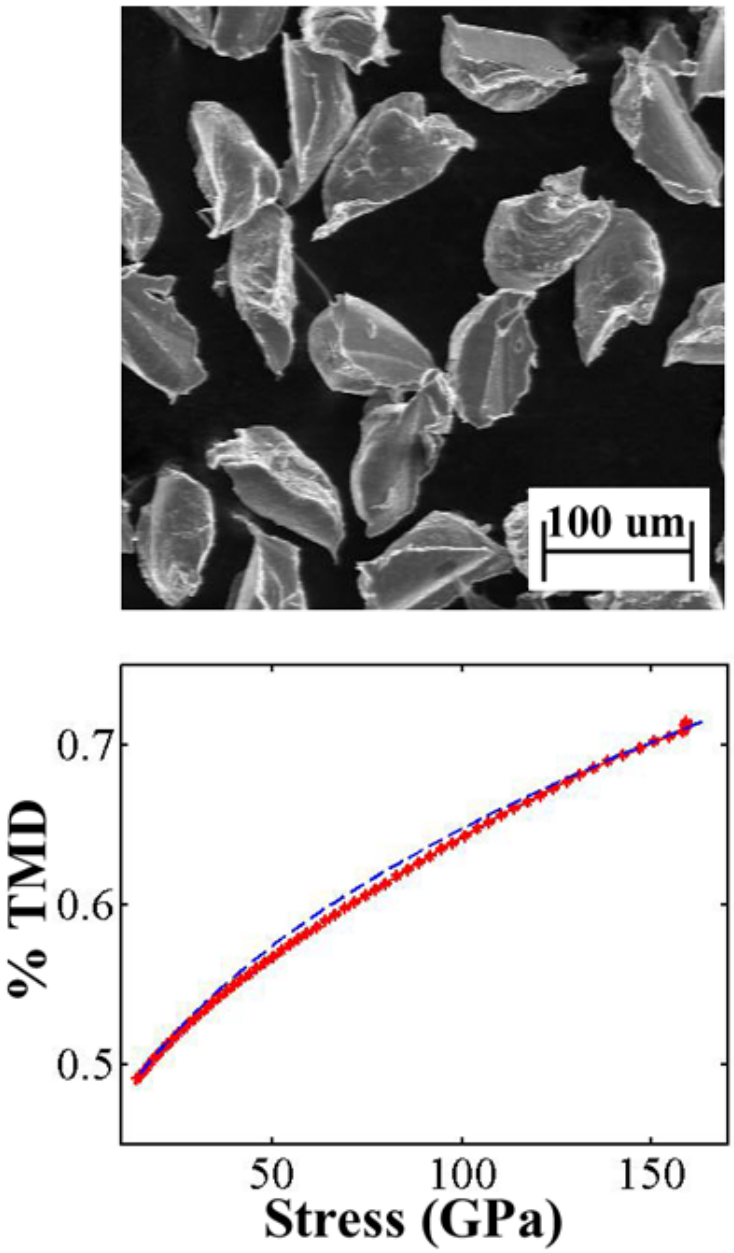

Figure 8.11: Initial powder configuration of aluminum powder, with approximately equiaxed dimensions of 50x50x75 μm, and fit of experimental quasi-static compaction data without rearrangement to the modified P-σ_Y model.

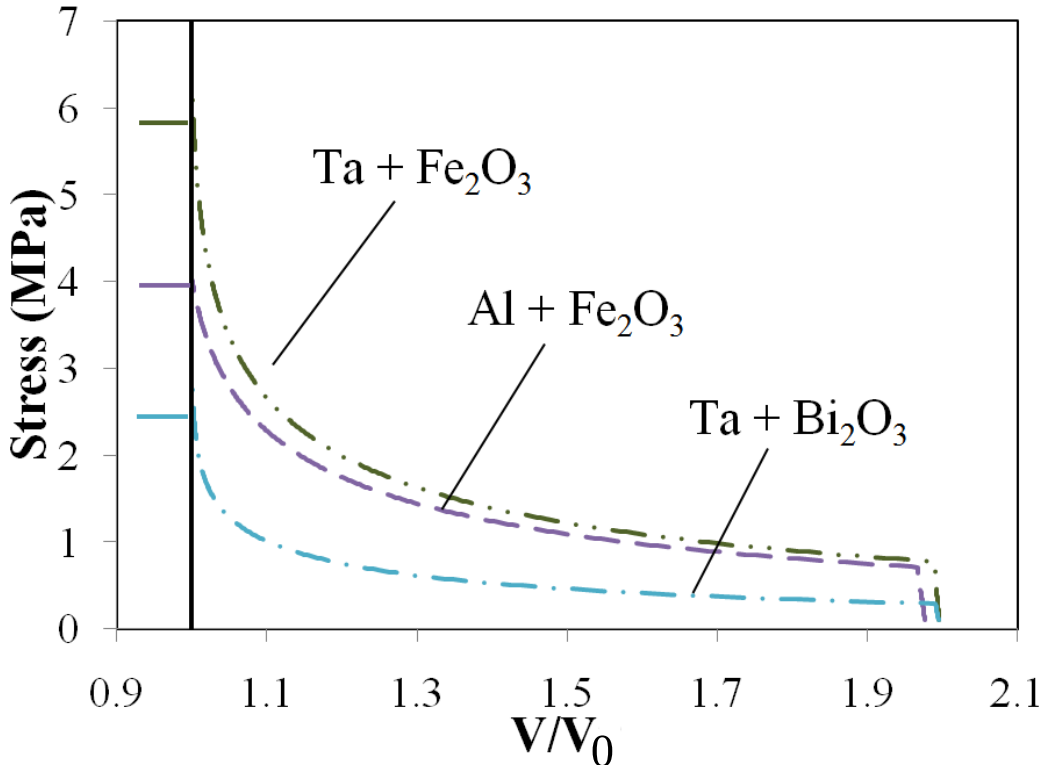

Figure 8.12: Plot showing the predicted crush strengths of various thermite powder mixtures based on densification moduli determined quasi-statically. The densification moduli of the mixtures containing Al are determined from calculated 50 % mixture moduli of the constituent moduli, and mixtures containing Ta are measured.

results for Ta + Fe_2O_3 and Ta + Bi_2O_3 mixtures, also at an initial density of 50 % TMD, are shown in Fig. 8.12. For the Ta mixtures, the densification moduli given in Table 8.1 are used.

One can see from Fig. 8.12 that by varying the components in the mixtures, the approach clearly predicts a wide range of crush strengths, a span of greater than 3 GPa for the systems investigated. Looking first at the Al + Fe_2O_3 mixture, the calculated densification moduli of 1.54 GPa results in a predicted crush strength of approximately 4 GPa. This is almost 2 GPa less than the crush strength for the Ta + Fe_2O_3 mixture which has

a densification moduli of only 1.68 GPa. From this observation alone, one can see that only minor changes in the densification moduli can result in significant differences in the predicted crush strength. Interestingly, reducing the densification moduli by slightly more than half, to that of the Ta + Bi_2O_3 mixture (σ_D = 634 MPa), results in a reduction in crush strength of only 1.5 GPa. Thus a direct multiplication of crush strengths based on the ratio of densification moduli is not appropriate, and full implementation of the model approach is needed for describing the densification response of heterogeneous powder mixtures.

In comparing the Ta + Fe_2O_3 mixture with the Ta + Bi_2O_3 mixture, it is observed that the densification modulus of the oxide component significantly effects the predicted crush strength for the mixture. This is due to the widely different moduli values reported for the oxides, see Table 8.1. Recall from Fig. 8.5 that if the predicted crush strength for the Ta + Fe_2O_3 mixture were based on the densification modulus of only Fe_2O_3, the crush would be approximately 11 GPa, as opposed to a crush strength of < 2 GPa if it were controlled by Bi_2O_3. Thus any mixture containing Fe_2O_3 of the same morphology as that in the current investigation is expected to have a significantly higher crush strength than those containing Bi_2O_3.

It is also of interest to note how the magnitude of the metal components densification modulus compares with that of the oxide. In the Al mixtures, it is found that Al is always the more compliant component. For the Ta + Fe_2O_3 mixture, Ta is the more compliant component, while in the Ta + Bi_2O_3 mixture, Bi_2O_3 is more compliant. If one considers only the yield properties, a more compliant component would indicate a greater amount of deformation during compaction. However, with regard to describing the deformation characteristics that occur during consolidation one must also consider particle morphology. To fully determine the effect of morphology in the densification response of the mixtures,

careful analysis of either post-shocked microstructures, or meso-scale simulations, or both would be required. Thus, while the current approach does capture an important aspect of the compaction process, namely the crush strength, it still leaves certain questions unanswered.

As a further extension and validation of this approach, the Al + Fe_2O_3 system is re-examined along with time resolved data for a 50%-50% volume mixture found in the literature [138]. The experiments were carried out in a similar fashion as those in the current investigation, using PVDF gauges to measure the shock response in the powder mixture. Unfortunately, no images of the starting powders are available; however, the reported particle size for both the Al and Fe_2O_3 is approximately 15 μm. Powders are pre-compressed to 53 %TMD, and the quasi-static σ-ρ relationship for densities of 53 and 72 % TMD is known. The stresses corresponding to these densities are found to be 22 and 135 MPa, respectively. From this limited information, an estimate of the densification modulus of the mixture can be obtained.

Using the modified P-σ_Y model with P_0 = 22 MPa and ρ_0 = 53 % TMD, Eq. 139 is fit to the two data points available and the densification modulus for the mixture is determined as σ_D = 181 MPa. Recalling that for the Ta + oxide mixtures the approximate density at which rearrangement was determined to no longer occur was 68 % TMD, it is hypothesized that rearrangement may not be complete for the Al + Fe_2O_3 mixture at 53 % TMD. If this is the case, the densification modulus of σ_D = 181 MPa is expected to be lower than that which would be determined if the measurement were taken using compressional data in the non-rearrangement region. To get an estimate as to what the modulus might be in the Al + Fe_2O_3 system, if the calculated σ_D did not incorporate rearrangement, the value of σ_D is recalculated for the Ta + oxide mixtures using quasi-static compaction data beginning

at 53 % TMD. The densification moduli of the mixtures obtained using non-rearrangement data only and with the data beginning at 53 % TMD is shown in Table 8.2.

Table 8.2: Fitting parameters for experimental data to the modified P-σ_Y model in the region of compaction where rearrangement no longer occurs and beginning at 53 % TMD. Values of ρ_0 and P_0 are determined from P-P_{Act} model at a value of four times P_l for the respective component/mixture.

	σ_D (MPa) Non-Rearrangement	σ_D (MPa) 53 % TMD
Ta + Fe_2O_3	1683	1197
Ta + Bi_2O_3	634	607

The largest difference in the two sets of calculated values for σ_D are found in the Ta + Fe_2O_3 mixture. The densification moduli calculated using only non-rearrangement compaction data is determined to be 1.4 times that using data starting at an initial density of 53 % TMD. With Fe_2O_3 also being a constituent in the Al mixture (albeit of a different particle size), this multiplication factor is applied to the previously measured σ_D value in an attempt to account for the inclusion of rearrangement in the previously determined densification modulus; the adjusted σ_D is calculated to be 253 MPa. Results of model predictions using both values of the densification moduli, σ_D = 181 MPa and σ_D = 253, are shown in Fig. 8.13.

In an effort to keep the analysis technique similar across all time resolved systems, the impedance matching method was used to determine the stress and relative volumes shown in Fig. 8.13 from the measured values of shock velocity (toe-to-toe) given in reference [138]. From the densification curves shown in Fig. 8.13, it is apparent that the two crush strengths predicted using the the different σ_D values differ only slightly. As such, both predictions are shown to fall within close proximity to the experimental point 9713-B,

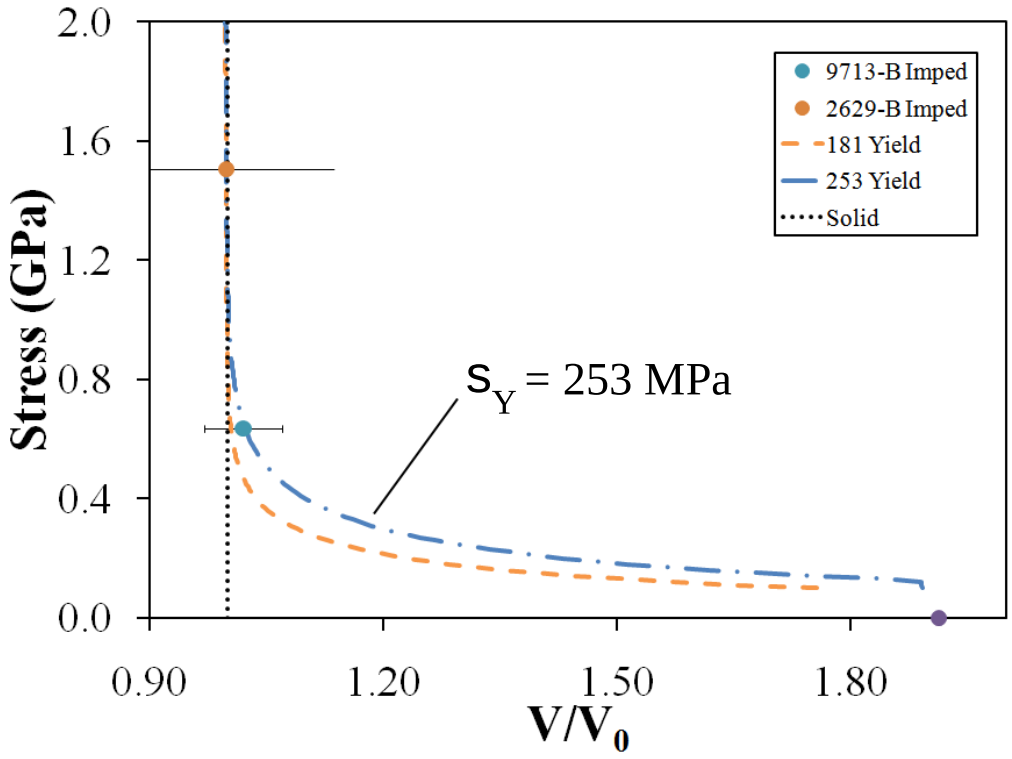

Figure 8.13: Plot showing the predicted crush strengths of an equivolumetric Al + Fe_2O_3 mixture based on densification moduli of 181 and 253 MPa. Experimental data points are taken from [138].

which is near the crush. With only two experimental points it is difficult to draw a definitive conclusion as to the true value of the crush strength. However, agreement between model predictions and the single experimental result near the crush strength suggest that the approach put forth in this dissertation is also valid for the Al + Fe_2O_3 system. For further validation of the approach developed here, additional systems should be investigated.

This work uses a continuum level approach to solve for the dynamic crush strength in thermite powder mixtures. What is experimentally measured is the stress-density relationship for the powders and powder mixtures; from which a densification modulus is determined using a modified form of the P-σ_Y model. The densification modulus is subsequently inserted into the Wu-Jing [83] model, where the compaction to full density is controlled by the rate independent form of the P-α [10] model, and a predicted value for the crush strength results. From this, one can see that the predicted crush strength relies heavily on the measured value of the densification modulus and the P-α formulation chosen in the Wu-Jing [83] model. With the P-α formulation consistent across the multiple systems investigated, the variations observed in the predicted values of the crush are dependent on the measured densification modulus. As such, it is important to discuss what a particular measured value for the densification modulus means in terms of powder and mixture properties.

In attempting to achieve a better understanding of the meaning of σ_D, recall the form of the modified P-σ_Y model used in this investigation given by Eqn. 139 and re-written below, where density is reported in percentage theoretical maximum density:

$$P_Y = P_0 + 2.97\rho^2 \left(\frac{\rho - \rho_0}{1 - \rho_0} \right) \sigma_D$$

Having addressed the assumptions within this model in Sections 4.1 and 8.1.2, the resulting functional form is now discussed, addressing each term. The term P_0 gives the initial stress at which the model is applied, corresponding to the density ρ_0 as determined from the P-P_{Act} model. The next two terms, $2.97\rho^2$, are a result of particle level yielding [59] and geometric considerations [85], respectively. The fractional term involving densities is of particular significance because it provides a quantifiable measure of the compaction process. The denominator (1 - ρ_0) can be thought of as the total amount of compaction available to the system, while the numerator (ρ - ρ_0) represents the instantaneous amount of compaction that has occurred as a result of the stress P_Y. Thus, this term is essentially the ratio of the instantaneous compaction resulting from a given applied stress, relative to the total compaction available. Furthermore, controlling this ratio (the measured compaction behavior) is the densification modulus of the powder mixture σ_D. Thus, σ_D is a measure of the stress required to further densify a powder mixture from initial density ρ_0 to some final density ρ due to applied stress P_Y.

Considering first a single component material, σ_D is the stress required to further densify the powder as a result of either deformation of the particle, fracture of the particle, or both. In the case of ductile materials, like Ta and Al, densification of the powders is dominated by the process of plastic deformation and flow. For the oxide particles, Fe_2O_3 and Bi_2O_3, the measured densification modulus captures the simultaneous processes of deformation, fracture, and rearrangement. This indicates that the densification modulus measured through the modified P-σ_Y method is mechanism independent, in that the value itself does not reflect any one particular deformation mode. This is extremely beneficial when one is attempting to describe the densification behavior of a mixture, as components can have widely different yield responses, as is the case for the thermite powder mixtures.

Thus, the σ_D determined from the quasi-static densification curves is effectively capturing the multitude of interactions and process that occur as the mixture densifies.

How then, does a measured value for the densification modulus lead to an accurate prediction of the dynamic crush strength? In fact, σ_D is exactly the term which is required by the Wu-Jing [83] model in its simplified description of the compaction process. Therefore, the value for σ_D as determined using the current approach is substituted directly for the yield strength of the solid Y in Eqns. (24) and (25) found in reference [83]. The densification modulus so determined then allows for an accurate prediction of the critical stress at which plastic deformation begins, P_{crit}, as well as the shape of the densification curve, α. By determining the correct value of the critical stress necessary to initiate plastic deformation, the measured densification modulus allows for the appropriate offset of the compaction curve from which the crush strength is determined. Thus, through the systematic approach presented in this dissertation, an accurate method for determining the densification moduli of powders and powder mixtures has been developed, which in turn allows for a direct prediction of the crush strength of the mixtures through the model of Wu and Jing [83].

8.3 Significance of the Crush Strength

What has been developed in this dissertation is a continuum level approach to estimate the crush strength in thermite powder mixtures. Its strength lies in its ability to use quasi-static compaction data in combination with existing compaction models and equations of state to predict a dynamic mixture property, the crush strength. While this approach does address the issue of determining the stress necessary to reach full compaction in the powder mixtures, still open are issues regarding the processes which occur as the mixtures approach

the crush.

What then, is the significance of the crush strength, and why should one be interested in its accurate prediction? In reactive mixtures, such as the thermite mixtures investigated, it is important to determine the conditions necessary to initiate reactions relative to the work of densification. In systems where compaction precedes reaction [139], quantification of the total energy and work of compaction is an integral component in determining the reaction initiation conditions.

Recall Fig. 8.10, which illustrates the PdV work that goes into crushing two powder mixtures with very different crush strengths. For the mixture with the higher crush strength (Fig. 8.10(a)), a greater amount of work is expended during the crushing of this material to full density. Consider the scenario where the total amount of energy needed to initiate reaction is equivalent between the two mixtures, and a shock stress σ_i is applied to both mixtures (see Fig. 8.10). In this instance, the mixture with the higher crush strength will consume more energy during compaction, such that it may have less energy remaining to initiate reaction. Thus one might expect the mixture with the lower crush strength to have a greater chance of reacting at the applied stress σ_i, as shown schematically in Fig. 8.10.

Is this a situation that is consistent across all reactive systems? Will all mixtures with higher crush strengths react at higher threshold stresses than mixtures with lower crush strengths? In systems that may react during compaction, does the magnitude of crush strength determine the reaction initiation conditions? With regard to the last question posed, one would expect that the crush strength would still influence the reaction initiation threshold condition. This is due to the fact that the crush strength not only dictates the ability of the reactant powders to reach full density, but also the ability to mix and generate a configuration amenable for reaction initiation. Hence, a higher crush strength would also

lead to higher stresses needed for generating an intimately mixed configuration and thus a higher reaction initiation threshold.

The approach considered herein does not explicitly address the particle level phenomena that control the densification response in the incomplete compaction region. In this region, not only strength, but also particle size, shape, configuration, and rate dependencies play a major role in influencing the compaction response. These issues require the implementation of particle level (meso-scale) simulations. Describing the process of shock compaction of powders and mixtures through meso-scale simulation has been a continued area of research for a number of years, and has typically involved the use of simulated beds of particles [132, 140]. Through simulations of this type, Benson and co-workers [60] and Benson [141] have been able to describe both qualitatively and quantitatively the characteristics associated with the transition from quasi-static to dynamic loading behavior as well as the shock velocity - particle velocity relationship. However, using simulated particle beds simplifies the particle shapes and limits the types of interactions one can observe.

Recently, Eakins and Thadhani [79] have incorporated the use of experimentally obtained microstructures in shock wave simulations in reactive Ni + Al powder mixtures. Specifically, they examine the effects of initial density (80%, 60%, 52%, and 45% TMD) and initial configuration (spherical and flake morphologies) on not only the bulk response, but also on the rise characteristics, stress distribution, and deformation behavior of the constituents. They found that particle morphology significantly influences these traits, illustrating the power of experimentally based computational shock compaction simulations. Thus, while the continuum level approach oulined in this thesis is appropriate for predicting the crush strength, and thus a correlation with the reaction initiation threshold, a complete description of the powder compaction process, inclusive of the phenomena occurring in the

incomplete compaction region, requires the implementation of meso-scale simulations.

CHAPTER IX

SUMMARY OF RESULTS, CONCLUSIONS, AND FUTURE WORK

9.1 Summary of Results

This work set out to determine the densification and reaction response of two configurationally and mechanically dissimilar thermite powder mixtures of Ta + Fe_2O_3 and Ta + Bi_2O_3. In doing so, the quasi-static compaction response of the constituent powders and equivolumetric ratios of the thermite mixtures were investigated first. The quasi-static compaction data was fit to the P-σ_Y [20] and P-P_{Act} [58] models and the modified Kawikata [13] equation with varying degrees of success. Goodness of fit was found to be influenced by initial configuration, particle rearrangement, preferential deformation modes, and the number of fitting parameters inherent in the models. Through direct analysis of the model fits over the entire densification range, the most relevant parameters obtained were the stress and density range over which rearrangement of the mixtures dominated the compaction response.

To determine the dynamic compaction response, a series of instrumented parallel plate impact experiments were performed. The stress range investigated was 0.9 to 12.2 GPa for the Ta + Fe_2O_3 mixture, and 1.3 to 10.0 GPa for the Ta + Bi_2O_3 mixture, and the initial densities for the mixtures were 49 % and 62 % theoretical maximum density. In order to evaluate the levels of stress necessary to reach full compaction and reaction in each of these mixtures, knowledge of the inert equation of state (EOS) of the solid mixtures was

required. For the Ta + Fe_2O_3 mixture, the isothermal mixing method of McQueen and co-workers [1] was applied directly to EOS data available in the literature for the constituents to obtain the solid mixture EOS. For the Ta + Bi_2O_3 mixture, EOS information was not available for Bi_2O_3, and a series of ultrasonic and dynamic impact tests were performed on solid pellets of Bi_2O_3 to obtain its elastic and EOS properties.

With the inert solid equation of state of the mixtures defined, porosity was incorporated into the EOS response through the Mie-Grüneisen extrapolation [15], Krueger and Vreeland's [44] energy partitioning method, and the models of Wu and Jing [83] and Petrie and Page [13] for the mixtures, as applicable. Using the inert porous curves, the crush strengths for the Ta + Fe_2O_3 mixture was found to be between 6-7 GPa, and for the Ta Bi_2O_3 mixture it was approximately 2.5 GPa. Evidence of shock induced reaction was inconclusive in both systems up to the maximum stresses investigated.

The dynamic compaction response for each of the mixtures was analyzed in the framework of the P-α [5,6] and P-λ [12] models, as well as those of Wu and Jing [83] and Petrie and Page [13]. The various forms of the P-α model and the P-λ model were found to fit the data with moderate success; however, each of these models contained an empirically determined fitting parameter. In their original formulations, the Wu-Jing [83] and Petrie-Page [13] models did not fit the compaction data well. As the Wu-Jing [83] model does not contain any empirically fit parameters, it was chosen for further analysis to determine if a more accurate fit with the data could be obtained.

In examining the formulation of the Wu-Jing [83] model, it was found that the value of the yield strength used heavily influenced the predicted compaction response, where yield properties of the solid materials was used to predict the compaction response of the porous mixtures. Defining the yield properties as such led to highly unrepresentative fits

of the model response to experimentally obtained compaction data. To obtain better fits of the compaction data with the Wu-Jing [83] prediction, the P-P_{Act} model was implemented to determine the compaction range in the quasi-static data over which rearrangement had ceased, and further densification of the mixture could only proceed by deformation and fracture of the primary particles. This densification range was then fit with a modified form of the P-σ_Y model to determine the densification modulus of the powder mixture, which was subsequently substituted back into the Wu-Jing [83] model, replacing the yield strength of the solid. In substituting the densification modulus for the yield strength of the solid, compaction responses from the Wu-Jing [83] model were able to accurately predict the crush strengths of both powder mixtures investigated. Furthermore, for the Ta + Fe_2O_3 mixture, this model predicted well the entire densification response.

This analysis was extended to published time-resolved compaction data for an equivolumetric mixture of the Al + Fe_2O_3 [138], and was found to agree well with the experimentally determined crush strength in this system. As such, a systematic approach to predicting the crush strength in thermite powder mixtures has been proposed, and verified on equivolumetric mixtures of Ta + Fe_2O_3, Ta + Bi_2O_3, and Al + Fe_2O_3. Further experimental analysis will be required to determine if this approach is valid across other thermite systems.

9.2 Conclusions

An approach that allows for accurate predictions of the crush strength in thermite powder mixtures of varying constituents and configurations would serve to significantly advance experimental capability in the field of reactive powder mixtures. This dissertation has presented one such approach.

In analyzing the quasi-static and dynamic compaction response of two thermite powder mixtures, a method for predicting the dynamic crush strength, based solely on the quasi-statically obtained densification modulus of the mixtures, has been developed. This method is unique in that it details a systematic approach to solving for a complex dynamic property using existing continuum level approaches to powder compaction, e.g. the P-σ_Y [20], P-P_{Act} [58], and Wu-Jing [83] models.

In their original formulations, each of these models describes well a certain aspect of compaction. Assuming the powder mixture investigated is initially composed of mono-sized spheres at a density of 64 % TMD where rearrangement no longer occurs, the P-σ_Y model will allow for determination of the appropriate densification modulus of the powder. Assuming rearrangement is the dominant densification mechanism at low stresses, application of the P-P_{Act} model will give the stress and density range over which rearrangement and some other stress activated process dominate. Assuming the rate independent strength properties of the powder can be determined from its corresponding solid properties, the Wu-Jing [83] model will predict the entire densification and Hugoniot response of the powder and/or mixture. However, in the case of many real world powder systems and mixtures these assumptions do not hold, and direct application of these models can lead to poor predictions and fits with experimental data.

To increase model functionality and advance the predictive ability of determining the crush strength in thermite powder mixtures, these models were applied collaboratively. Knowing that the Wu-Jing [83] model requires a strength parameter for the powder mixture, one could use the P-σ_Y model to determine this quantity. However, to obtain an accurate value for the densification modulus with the P-σ_Y model, it is necessary that rearrangement not occur in the data being analyzed. To this end, the P-P_{Act} model was used to determine

the range of stress and densities over which the P-σ_Y model needs to be applied to obtain an accurate measure of the densification modulus. Thus, by seeking out the strengths in each of these models, and applying them systematically to solve a common problem, the strengths of the individual models combine to form a sound framework within which the densification response, specifically the crush strength, in highly heterogeneous thermite powder mixtures can be predicted.

With regard to crush strength, it was found that properties of the mixture prevailed, while the densification response in the incomplete compaction region appears to be configurationally dependent. For the Ta + Fe_2O_3 mixture, where rate insensitive Fe_2O_3 comprises the matrix, the rate independent model of Wu and Jing [83], inclusive of the measured densification modulus of the mixture, is able to predict both the crush strength and the densification response in the incomplete compaction region. For the Ta + Bi_2O_3 mixture, where rate sensitive Ta is the matrix material, the rate independent form of the Wu-Jing [83] model is found to not agree well with experimental results in the incomplete compaction region. However, regardless of matrix rate sensitivity, the experimentally observed crush strength, and that which is predicted using the Wu-Jing [83] model, inclusive of the appropriately determined densification modulus, are found to coincide.

Accurate determination of the crush strength for different reactive powder mixtures is important because of its influence on the threshold reaction initiation conditions. Current methods of establishing the crush strength for heterogeneous thermite powder mixtures are often experimentally intensive due to the lack of consistency and applicability of predictive models over the wide range of material properties found in thermite mixtures. As such, the approach set forth in this dissertation has sought to eliminate some of the guesswork in determining the crush strength for thermite mixtures. In doing so, it is hoped that this

approach can be extended to a multitude of different reactive mixtures, and be used as a predictive tool to reduce the experimental costs associated with determining the crush strengths in thermite systems; thus aiding in establishing the link between the crush strength and the reaction initiation stress.

9.3 Future Work

As shown, this approach does well to predict the experimentally determined crush strength for the thermite mixtures investigated; however, its ability to predict the entire densification response depends on the matrix configuration and whether or not its strength properties are rate sensitive. Determining the exact cause of the observed agreement and disagreement between the predicted response in the various regions of compaction requires further research and extension of the approach to additional thermite systems. Future work in this area would benefit greatly if answers to a few fundamental questions could be obtained. Is it possible that a continuum level approach could ever accurately capture the entire densification response, and if so what would be the appropriate form of α (or any other parameter) that is best suited to do so? Furthermore, what other experimental, theoretical, or computational techniques are available that may be better suited to describe the consolidation process?

Within this dissertation, two separate thermite systems were investigated explicitly. Both of these systems contained the same metal component and varied in the composition of the oxide. Thus, it was the configuration and properties of the oxide component which resulted in the observed differences in crush response of the mixtures. In this investigation, the dynamic response of Ta combined with a relatively soft Bi_2O_3, and Ta combined with a significantly stiffer Fe_2O_3 was investigated. However, the morphology of the oxide

particles were such that when combined with Ta the configurations of the resulting mixtures were extremely different. The porous and agglomerated Fe_2O_3 powder resulted in a mixture where Ta was found in isolated regions surrounded by a matrix of the oxide. Conversely, the larger particle size and discrete morphology of the Bi_2O_3 particles led to a mixture whose matrix was composed of Ta. What if the stiffer porous Fe_2O_3 particles were replaced with another high strength oxide that was composed of discrete particles. With this configuration, the mode of stress transfer between the Ta + stiff oxide and the Ta + Bi_2O_3 would both be through direct particle contacts and a better comparison of the influence of oxide strength on the compaction behavior of the mixtures could be obtained.

By examining mixtures where the oxides are of similar (discrete particle) morphology, one could eliminate the uncertainties associated with the crushing behavior of the porous particles and focus on the deformation mechanism inherent for each of the materials and how these mechanisms effect the observed compaction response of the mixture. The size and/or volume fraction of each constituent could also be modified. This would result in mixtures whose matrices are composed of either the metal or oxide component; thus allowing one to determine explicitly the effect of the matrix material on the compaction response of the mixture.

Through examination of the compaction response of these 'designer' mixtures, one would be able to gain insight into the applicability of the current form of α chosen to represent the consolidation response. If agreement between the predicted and actual responses in certain mixtures varies, one would have a clearer framework within which to analyze the observed differences. Furthermore, alternate forms of α could be examined to see if there exists some other functional form which could better represent the entire densification response, while still having a foundation in experimentally determinable material properties,

e.g. σ_D.

If it is found that no single continuum level approach is able to accurately describe the compaction behavior in these heterogeneous thermite mixtures, then other options should be explored. One promising area of research that has been gaining momentum in the past few years is the implementation of particle level simulations that employ experimentally obtained microstructures. This approach offers significant benefits over the continuum level approach in that this technique allows the researcher to visualize and quantify interactions at the particle level. Ultimately, it is the interactions at the particle interfaces that lead to the bulk responses observed, and without a detailed understanding of these interactions the continuum level approach can only offer postulations as to the origins of the the observed responses. Thus the insights gained from meso-scale modeling could be used to develop better continuum level models, or could replace the need for continuum level models altogether. It is not too hard to envision a day when computational power has grown to a level such that larger scale modeling, where materials that are traditionally assigned continuum level properties, could be replaced with materials whose compositions contain information at the micro-scale.

APPENDIX A

MATLAB SCRIPTS FOR DATA CALCULATIONS

A.1 Scripts for comparison of mixture models with Elkonite 10W3

The following MATLAB scripts use the properties given in Table 2.1 to plot fits of the basic mass average, material velocity average, isothermal mass average, and energy partitioning mixture routines against experimental data for Elkonite 10W3 from Marsh [29]. The text located between 'BEGIN PROGRAM'and 'END PROGRAM' is direct script from separate matlab files, and will be briefly described.

In all files, lines beginning with an % symbol indicate commented lines. Similarly, commented sections of the code are located between the symbols

% and %

which are on lines by themselves. Section 'Front Matter' simply closes any figures that may be open and clears any variables in MATLAB, in addition to declaring the necessary global variables which are needed to pass between function files. All initial material properties for the copper and tungsten are found in section 'Initial Material Properties', with standard SI units given. The basic mass averaging routine described in Sect. 2.5.1 is described in the section 'Basic Mass Averaging'. In this section, average values for the bulk soundspeed, 'S' fitting parameter in the linear EOS, and initial volume are found through mass averaging. Next, a compressional range is defined and the Hugoniot stress corresponding to a given volume is determined. Following that, a range of material velocities is defined and the mass averaged values of 'C0' and 'S' are used to determine the shock

velocity.

For the 'Material Velocity Mass Averaging' routine, a range of stress points if first defined. Then, the particle velocity at every stress point is determined for each component using its individual EOS. Next, the individual particle velocities are combined using the mass averaged technique given by Eq. 47. From there, the volume and shock velocity are also determined for each value of stress.

The '0K Isothermal Mass Averaging' routine begins by defining a range of volumes for each material over which the compressional response will be determined. Following that, the stress at each value of compression is determined for each component. Next, the 0K isotherm is detemined for each component by calling the function 'IsoFun' (a separate file which will be described later) and fit to a fifth order polynomial. The 0K volumes are then averaged by mass at a given stress stress value to result in an averaged $\sigma - V$ relationship for the mixture at 0K. Finally, the 0K isotherm is heated up yield the Hugoniot by calling the function 'HugFun' (described later) and values for the shock and material velocities along the Hugoniot are determined from the conservation relations.

The 'Results from Energy Partition' are values for the shock velocity as a function of the particle velocity, where the $U_S - u_P$ relationship has been fit to a second order polynomial. The results shown in this section are those for an energy partitioning ratio $\xi = 1$, and are produced from a separate program which will be discussed in a following section. The remainder of the code in this section plots the resultant mixture program results against the experimental data of Marsh [29] for Elkonite 10W3.

'BEGIN PROGRAM'

```
% This program is to calculate the Hugoniot of a mixture of
```

```
% two components, based on different Mixing Routines
% The mixing routines are:
% 1) Basic mass averaging
% 2) Material Velocity Mass Averaging
% 3) 0 K Isothermal Mass Averaging
% 4) Energy Partitioning

% ---------------------------------------- %
%           Front Matter                   %
% ---------------------------------------- %
close all hidden;
clear all;
format long;
global C0 S V0H Grun0H i
global PKV5 PKV4 PKV3 PKV2 PKV1 PKV0 V0HMix3 Grun0HMix3
global V0KMixInit3
NumMats =2;

% ---------------------------------------- %
%        Initial Material Properties       %
% ---------------------------------------- %
% ----- Copper ----- %
Rho0H(1) = 8930;          %kg/m3
V0H(1) = 1./Rho0H(1);         %m3/kg
```

```
C0(1) = 3940;              %m/s
S(1) = 1.489;                %unitless
Grun0H(1) = 1.99;           %unitless
ThreeNK(1) = 392.5;          %atoms-J/kg-K
Cv(1) = 371.8;             %J/kg-K
ThetD(1) = 306;            %K
E0H(1) = 77000;            %J/kg
E0K(1) = 0;                %J/kg
V0K(1) = .000110902;    %m3/kg
P0H(1) = 0;
T0(1) = 293;
G0HovV0H(1) = Grun0H(1)/V0H(1);
VFin(1) = V0H(1)./1.25;
MFrac(1) = 0.24;

% ----- Tungsten ----- %
Rho0H(2) = 19224;          %kg/m3
V0H(2) = 1./Rho0H(2);         %m3/kg
C0(2) = 4029;              %m/s
S(2) = 1.237;                %unitless
Grun0H(2) = 1.540;           %unitless
ThreeNK(2) = 135.7;          %atoms-J/kg-K
Cv(2) = 131;             %J/kg-K
ThetD(2) = 247;            %K
```

```
E0H(2) = 29000;            %J/kg
E0K(2) = 0;                %J/kg
V0K(2) = .0000518779;    %m3/kg
P0H(2) = 0;
T0(2) = 293;
G0HovV0H(2) = Grun0H(2)/V0H(2);
VFin(2) = V0H(2)./1.8;
MFrac(2) = 0.76;

% ---------------------------------------- %
%        Marsh Elkonite 10W3 Data          %
% ---------------------------------------- %
UsMarsh=[3.535 3.616 3.783 3.733 4.393 4.791 4.723 4.812 4.878];
UpMarsh=[0.189 0.208 0.265 0.288 0.581 0.818 0.824 0.837 0.875];
PHMarsh = [0 10 11 15 16 24 38 58 58 60 63];
VHMarsh = 1./[14.88 15.73 15.74 15.96 16.07 16.5 17.07 17.97 18.0...
              18.01 18.08];

% ---------------------------------------- %
%        Basic Mass Averaging              %
% ---------------------------------------- %
C01 = 0;
S1 = 0;
V0H1 = 0;
```

```
for i=1:NumMats
    C01 = C01 + C0(i).*MFrac(i);
    S1 = S1 + S(i).*MFrac(i);
    V0H1 = V0H1 + V0H(i).*MFrac(i);
end
% ----- Determine P,Us,Up,V ----- %
VPoints1 = 500;
VFin1 = V0H1/1.2;
VRange1(:,1) = linspace(V0H1,VFin1,VPoints1);
PH1(:,1) = ((C01.^2).*(V0H1-VRange1(:,1)))./((V0H1-S1.*...
            (V0H1-VRange1(:,1))).^2);
UpPoints1 = 500;
UpFin1 = 1000;
UpRange1(:,1) = linspace(0,UpFin1,UpPoints1);
Us1 = zeros(UpPoints1,1);
Us1(:,1) = C01 + S1.*UpRange1(:,1);

% ---------------------------------------- %
%    Material Velocity Mass Averaging      %
% ---------------------------------------- %
PHPoints2 = 500;
PHFin2 = 75.*10^9;
PHRange2(:,1) = linspace(0,PHFin2,PHPoints2);
for i=1:NumMats
```

```
    UpI2(:,i) = (C0(i)./(2.*S(i))).*(sqrt(1+(4.*S(i).*V0H(i).*...
                PHRange2(:,1))./((C0(i)).^2))-1);
end
UpM2(:,1) = sqrt(MFrac(1).*(UpI2(:,1).^2) +...
            MFrac(2).*(UpI2(:,2).^2));
VH2(:,1) = V0H1 - (UpM2(:,1).^2)./PHRange2(:,1);
Us2(:,1) = V0H1.*sqrt((PHRange2(:,1))./(V0H1-(VH2(:,1))));

% ---------------------------------------- %
%       0K Isothermal Mass Averaging       %
% ---------------------------------------- %
VPoints3 = 500;
for i=1:NumMats
    VRange3(:,i) = linspace(V0H(i),VFin(i),VPoints3);
end
% ----- Stress of Individual Component ----- %
PH3 = zeros(VPoints3,NumMats);
for i = 1:NumMats
 PH3(:,i) = (C0(i).^2.*(V0H(i)-VRange3(:,i))./((V0H(i)-S(i).*...
            (V0H(i)-VRange3(:,i))).^2);
end
% ----- 0 K Isotherm of Individual Component ----- %
VInc3 = 1000;
for i = 1:NumMats
```

```
    VSpan3 = linspace(V0K(i),VFin(i),VInc3);
    Po(1,i) = 0;
    [A,B] = ode45(@IsoFun,VSpan3,Po(1,i));
    V0KCalc3(:,i) = A;
    P0KCalc3(:,i) = B;
end
% ----- Mix 0 K Isotherms ----- %
StrFin3 = 75.*10^9;
StrPoints3 = 500;
P0KRange3(:,1) = linspace(0,StrFin3,StrPoints3);
V0KMix3 = zeros(StrPoints3,1);
for i=1:NumMats
    VatP3(:,i) = interp1(P0KCalc3(:,i),V0KCalc3(:,i),...
                         P0KRange3(:,1),'spline');
    V0KMix3 = V0KMix3 + VatP3(:,i).*MFrac(i);
end
PK = polyfit(V0KMix3,P0KRange3(:,1),5);
PKV5 = PK(1,1);
PKV4 = PK(1,2);
PKV3 = PK(1,3);
PKV2 = PK(1,4);
PKV1 = PK(1,5);
PKV0 = PK(1,6);
% ----- Heat Up Isotherm to Hugoniot ----- %
```

```
Grun0HMix3 = 0;
V0HMix3 = 0;
V0KMixInit3 = V0KMix3(1,1);
for i = 1:NumMats
    Grun0HMix3 = Grun0HMix3 + Grun0H(i).*MFrac(i);
    V0HMix3 = V0HMix3 + V0H(i).*MFrac(i);
end
Span3 = linspace(V0HMix3(1,1),V0KMix3(end,1),VInc3);
Qo = 0;
[K,Q] = ode45(@HugFun,Span3,Qo);
VHMix3 = K;
PHMix3 = Q;
VHMix3(1,1) = V0HMix3;
Us3 = V0HMix3.*(PHMix3(:)./(V0HMix3-VHMix3(:))).^(0.5);
Up3 = (PHMix3(:).*(V0HMix3-VHMix3(:))).^(0.5);
Us3(1,1) = Us3(2,1);

% ---------------------------------------- %
%     Results from Energy Partition        %
% ---------------------------------------- %

for i = 1:10
    UsKV(i,1) = -.051901.*UpMarsh(1,i).^2 + 1.6343.*...
                  UpMarsh(1,i) + 3.7127;
```

```
end
UsKV;
% ---------------------------------------- %
%        Plotting of Data                  %
% ---------------------------------------- %
%{
    hold on
    %title('Stress-Volume of Mixture')
    plot(VHMarsh(1,:),PHMarsh(1,:),'squareb')
    plot(VRange1(:,1).*1000,PH1(:,1)./10^9,'-r')
    plot(VH2(:,1).*1000,PHRange2(:,1)./10^9,'-g')
    plot(VHMix3(:,1).*1000,PHMix3(:,1)./10^9,'-m')
    ylabel('Stress (GPa)')
    xlabel('Volume (cm3/g)')
    %}

    hold on
    %title('Comparison of Mixture Models')
    plot(UpMarsh(1,:).*1000,UsMarsh(1,:).*1000,'squareb')
    plot(UpRange1(:,1),Us1(:,1),'-r','LineWidth',2)
    plot(UpM2(:,1),Us2(:,1),'--k')
    plot(Up3(:,1),Us3(:,1),'-.m')
    plot(UpMarsh(1,:).*1000,UsKV(:,1).*1000,':b','LineWidth',2)
    legend('Experimental','Basic','Material Velocity',...
```

```
        'Isothermal','Partitioning')
    ylabel('Us (m/s)','LineWidth',2)
    xlabel('Up (m/s)')
    axis([0, 950, 3400, 5200])
    set(gca,'YTick',[3400, 3800, 4200, 4600, 5000])
    set(gca,'XTick',[0, 200, 400, 600, 800])
    grid off
```

'END PROGRAM'

A.1.1 Code for Function 'IsoFun'

The function 'IsoFun' is called in the previous code to determine the 0K isotherm of each component in McQueen's mixture model [1]. The equation 'dpdvK' is Eq. 28 which results in the stress along the 0K isotherm as a function of volume.

'BEGIN PROGRAM'

```
function dpdvK = IsoFun(A,B)
global C0 S V0H Grun0H i

C0L = C0(i);
SL = S(i);
V0HL = V0H(i);
Grun0HL = Grun0H(i);
```

```
PH = ((C0L.^2.*(V0HL-A))./(V0HL-SL.*(V0HL-A)).^2);
dPHdV = ((C0L.^2).*(V0HL+SL.*V0HL-SL.*A))./...
        ((-V0HL+SL.*V0HL-SL.*A).^3);
GovV = Grun0HL./V0HL;

dpdvK =  -GovV.*B+(1-0.5.*GovV.*(V0HL-A)).*dPHdV+0.5.*GovV.*PH;
```

'END PROGRAM'

A.1.2 Code for Function 'HugFun'

The function 'HugFun' is called in the previous code to heat up the 0K isotherm of the mixture to yield the Hugoniot. The equation 'dpdvH' is Eq. 17 which results in the $\sigma - V$ Hugoniot from the known isotherm.

'BEGIN PROGRAM'

```
function dpdvH = HugFun(K,Q)
global V0HMix3 Grun0HMix3 PKV5 PKV4 PKV3 PKV2 PKV1 PKV0
global V0KMixInit3

% K is V, Q is P

P0KMix = PKV5.*K.^5 + PKV4.*K.^4 + PKV3.*K.^3 + PKV2.*K.^2 +...
         PKV1.*K + PKV0;
dP0KdV = 5.*PKV5.*K.^4 + 4.*PKV4.*K.^3 + 3.*PKV3.*K.^2 +...
         2.*PKV2.*K + PKV1;
```

```
GovV = Grun0HMix3./V0HMix3;
dpdvH =  (-0.5.*GovV.*Q + dP0KdV + GovV.*P0KMix)./...
         (1-0.5.*GovV.*(V0KMixInit3-K));
```

'END PROGRAM'

A.1.3 Energy Partition Mixture Program

The following code performs the calculations given in Krueger and Vreeland's energy partitioning model [44]. The code begins by first defining the necessary component material parameters in the section 'Initial Material Properties', and listing the experimental data from Marsh [29] in 'Marsh Elkonite 10W3 Data'. The section 'Avg. Behavior for Homogeneous Mixture' pridicts the mixture response if the material properties are averaged and the stress and energy are those produced from a single phase homogenous mixture. The average mixture response is needed to supply initial guesses for the simultaneous equations that must be solved in successive steps. In 'Initial Guesses of P,Us,VA,VB', the average mixture response is used to predict initial guesses as to the values for the stress, shock velocity, and volumes of components A and B. Within this section, the initial guesses are used to solve the set of simultaneous equations for a given assigned material velocity through the function 'simuleq'. The simultaneous equations are solved for each discreet value of material velocity assigned, which in this case is ten separate values. Data is plotted within section 'Plotting of Data'. The meat of the calculations are performed in the section 'Simultaneous Equations to solve'. Here, the relations developed in [44], Eqns. 53 and 60, together with the conservation relations, Eqns. 1, and 2, are solved simultaneously at a given material velocity.

'BEGIN PROGRAM'

```
function [KVOut, AvgOut] = EnergyPartition(NrgRatio)
% Script for Energy Partitioning Mixture EOS
% B.R. Krueger, T. Vreeland, J. Appl. Phys. 69
% (1991) 710-716.

close all hidden;
clear all;
format long;

% ---------------------------------------- %
%        Initial Material Properties       %
% ---------------------------------------- %
% ----- Copper ----- %
Rho0H1 = 8.930;          %kg/m3
V0H1 = 1./Rho0H1;         %m3/kg
Grun0H1 = 1.99;           %unitless
BT1 = 139.76;
BTP1 = 4.994;
MFrac1 = 0.24;

% ----- Tungsten ----- %
Rho0H2 = 19.224;          %kg/m3
V0H2 = 1./Rho0H2;         %m3/kg
```

```
Grun0H2 = 1.540;           %unitless
BT2 = 308.1;
BTP2 = 3.996;
MFrac2 = 0.76;

Distention = 1.;
% ---------------------------------------- %
%        Marsh Elkonite 10W3 Data          %
% ---------------------------------------- %
UsMarsh=[3.535 3.616 3.783 3.733 4.393 4.791 4.723 4.812 4.878];
UpMarsh=[0.189 0.208 0.265 0.288 0.581 0.818 0.824 0.837 0.875];
PHMarsh = [0 10 11 15 16 24 38 58 58 60 63];
VHMarsh = 1./[14.88 15.73 15.74 15.96 16.07 16.5 17.07 17.97 18.0...
              18.01 18.08];

% ---------------------------------------- %
%  Avg. Behavior for Homogeneous Mixture   %
% ---------------------------------------- %
V0Avg = V0H1.*MFrac1 + V0H2.*MFrac2;
V00Avg = Distention.*V0Avg;
V0ovG0 = MFrac1.*(V0H1./Grun0H1) + MFrac2.*(V0H2./Grun0H2);
BTAvg = V0Avg./(MFrac1.*V0H1./BT1 + MFrac2.*V0H2./BT2);
BTPAvg =((BTAvg.^2)./V0Avg).*(MFrac1.*V0H1.*((1+BTP1)./BT1.^2)+...
           MFrac2.*V0H2.*((1+BTP2)./BT2.^2)) -1;
```

```
NumPts = 100;
VRange = linspace(0.96.*V0Avg, 0.835.*V0Avg,NumPts);
PEAvg = (BTAvg./BTPAvg).*(((V0Avg./VRange).^BTPAvg)-1);
EEAvg = ((BTAvg.*VRange)./BTPAvg).*(((V0Avg./VRange).^BTPAvg)./...
        (BTPAvg-1) + 1) - (BTAvg.*V0Avg)./(BTPAvg-1);
PAvg = (V0ovG0.*PEAvg - EEAvg)./(V0ovG0-0.5.*(V00Avg-VRange));
UsAvg = V00Avg.*sqrt(PAvg./(V00Avg-VRange));
UpAvg = sqrt(PAvg.*(V00Avg-VRange));

AvgOut = [PAvg; UsAvg; UpAvg; VRange];
% ----- Coefficients of Quadratic Us-Up Relation ----- %
AvgCoeff = polyfit(UpAvg,UsAvg,2);
disp(sprintf('Avg. Function,C,S,andQ,are%0.5g,%0.5g,and%0.5g',...
             AvgCoeff(1), AvgCoeff(2), AvgCoeff(3)));

% --------------------------------------- %
%      Initial Guesses of P,Us,VA,VB      %
% --------------------------------------- %
% ----- Uses Average data for 1st Guess ----- %
%NrgLimit = 1e5;
%if NrgRatio > NrgLimit
%    NrgRatio = NrgLimit;
%end
NrgRatio = 1;
```

```
UpGMin = UpAvg(1);
UpGMax = UpAvg(end);
NumPoints = 10;
Up = linspace(UpGMin,UpGMax,NumPoints);
% ----- Iteration Scheme for Initial Guesses ----- %
for i = 1:NumPoints
    if i == 1;
        UsG1 = AvgCoeff(3) + Up(i).*AvgCoeff(2)+...
              (Up(i).^2).*AvgCoeff(1);
        PHG1 = (1./V00Avg).*UsG1.*Up(i);
        VovV0G1 = (UsG1-Up(i))./UsG1;
        xG = [PHG1, UsG1, VovV0G1.*V0H1, VovV0G1.*V0H2];
    elseif i == 2;
        UsG2 = AvgCoeff(3)+Up(i).*AvgCoeff(2)+...
               (Up(i).^2).*AvgCoeff(1);
        PHG2 = (1./V00Avg).*UsG2.*Up(i);
        VovV0G2 = (UsG2-Up(i))./UsG2;
        CorrectionFactor = 1-(VovV0G1-VovV0G2);
        xG = [PHG2, UsG2, CorrectionFactor.*VA(i-1),...
             CorrectionFactor.*VB(i-1)];
    elseif i >= 3;
        UsG3 = interp1(Up(1:i-1),Us,Up(i),'spline','extrap');
        PHG3 = interp1(Up(1:i-1),P,Up(i),'spline','extrap');
        VAG3 = interp1(Up(1:i-1),VA,Up(i),'spline','extrap');
```

```
        VBG3 = interp1(Up(1:i-1),VB,Up(i),'spline','extrap');
        xG = [PHG3, UsG3, VAG3, VBG3];
    end

 options = optimset('Display','off','MaxFunEvals',5e4,'TolX',...
           1e-6, 'TolFun', 1e-6) ;
    fhandle = @(x)simuleq(x,MFrac1,MFrac2,Distention,V0H1,V0H2,...
              Grun0H1,Grun0H2,BT1,BT2,BTP1,BTP2,NrgRatio, Up(i));
    [x,fval] = fsolve(fhandle, xG, options);
    fval;
    P(i) = x(1,1);
    Us(i) = x(1,2);
    VA(i) = x(1,3);
    VB(i) = x(1,4);
    VAB(i) = VA(i).*MFrac1 + VB(i).*MFrac2;
end
KVOut = [P; Us; Up; VAB].';
KVFit = polyfit(Up,Us,2);
disp(sprintf('Full Solution,C,S,andQ,are%0.5g,%0.5g,and%0.5g',...
             KVFit(1), KVFit(2), KVFit(3)));

% ---------------------------------------- %
%        Plotting of Data                  %
% ---------------------------------------- %
```

```
    hold on
    title('Us-Up of Mixture')
    plot(UpMarsh,UsMarsh,':squareb')
    plot(UpAvg,UsAvg,'-r')
    plot(Up, Us,'xm')
    ylabel('Us (m/s)')
    xlabel('Up (m/s)')
    grid off

% ---------------------------------------- %
%    Simultaneous Equataions to Solve      %
% ---------------------------------------- %

function G = simuleq(x,MFrac1,MFrac2,Distention,V0H1,V0H2,...
         Grun0H1, Grun0H2, BT1, BT2, BTP1, BTP2, NrgRatio, Up);
P = x(1,1);
Us = x(1,2);
VA = x(1,3);
VB = x(1,4);

% ----- Supporting Relations ----- %
VAB = VA.*MFrac1 + VB.*MFrac2;
V00AB = Distention.*(V0H1.*MFrac1 + V0H2.*MFrac2);
SigmaA = MFrac1./(Grun0H1.*V0H2);
```

```
SigmaB = MFrac2./(Grun0H2.*V0H1);
EtaA = MFrac1./V0H2;
EtaB = MFrac2./V0H1;
LambdaA = VA./V0H1;
LambdaB = VB./V0H2;
Phi = V00AB./(V0H1.*V0H2);
Epsilon = (V0H2.*Grun0H1)./(V0H1.*Grun0H2);
% ----- Murnaghan Equations given in Krueger-Vreeland ----- %
PEA = (BT1./BTP1).*((V0H1./VA).^BTP1 -1);
PEB = (BT2./BTP2).*((V0H2./VB).^BTP2 -1);
% ----- Kit's Integral Equation of PE ----- %
EEA = (BT1.*VA./BTP1).*(((V0H1./VA).^BTP1)./(BTP1-1) + 1) -...
      (BT1.*V0H1./(BTP1-1));
EEB = (BT2.*VB./BTP2).*(((V0H2./VB).^BTP2)./(BTP2-1) + 1) -...
      (BT2.*V0H2./(BTP2-1));
% ----- Equations in Paper to Solve ----- %
Eqn1 = -(1./V00AB).*Us + (1./VAB).*(Us-Up);
Eqn2 = -P + (1./V00AB).*Us.*Up;
Trm1 = SigmaA.*PEA;
Trm2 = SigmaB.*PEB;
Trm3 = (MFrac1.*EEA)./(V0H1.*V0H2);
Trm4 = (MFrac2.*EEB)./(V0H1.*V0H2);
Trm5 = SigmaA + SigmaB - 0.5.*(Phi-EtaA.*LambdaA-EtaB.*LambdaB);
Eqn8 = -P + (Trm1 + Trm2 - Trm3 - Trm4)./Trm5;
```

```
Eqn12 = -P.*(1-NrgRatio./Epsilon)+PEB-(NrgRatio./Epsilon).*PEA;
G = [Eqn1; Eqn2; Eqn8; Eqn12];
```

'END PROGRAM'

A.2 Script for Hilbert Transformation of Soundspeed Data

The following program opens the file 'LongG1.txt', which is a voltage-time (V-T) signal of a longitudinal waveform. After reading the V-T data into the matrix Data, it performs a Hilbert transformation on the V-T data, and finds the maximum values of both the original V-T data as well as the transformed data. Next, the time at which the maximum value of the envelope occurs is determined, and output. Also output are plots showing the transformed data as well as the original V-T signal.

'BEGIN PROGRAM'

```
clear('all');
close('all');
fid = 'LongG1.txt';
Data = dlmread(fid);
SZ = size(Data);
SE = abs(hilbert(Data));

SEM = max(SE);
DataM = max(Data);
DataMaxA = DataM(1,2)
for i = 1:SZ(1,1)
    if Data(i,2) == DataMaxA
```

```
        DataMaxT = Data(i,1);
    end
end
DataMaxT
MaxHilb = SEM(1,2)
SE(:,1) = Data(:,1);
for i = 1:SZ(1,1)
    if SE(i,2) == MaxHilb
        MaxHilbT = SE(i,1);
    end
end
MaxHilbT
SESm(:,1) = smooth(SE(:,2),3);
plot(Data(:,1),Data(:,2));
hold on
plot(Data(:,1),SE(:,2));
```

'END PROGRAM'

A.3 Impedance Matching Technique

The following program calculates the shocked state in a material using the impedance matching technique. In this configuration in is assumed that a flyer impacts a driver material which in turn impacts the material of interest. This is a general program that has been

used for all the material systems investigated in this dissertation. The only shot-specific parameters are the impact velocity of the projectile and flyer and the measured initial density and shock velocity of the specimen.

The program begins by defining the known properties of the impactor (flyer) and driver materials, where the parameters A0Fl, A1Fl, etc. are the $2\sigma_0$ uncertainties in the shock velocity resulting from the uncertainties in the parameters C_0 and S as oulined in Sect. 6.9. Note there is the option to choose either the copper driver or the W-6Ni-4Cu alloy driver. The shocked state in the flyer and driver materials is calculated at the point of impact first, along with the uncertainty in each as a function of $2\sigma_0$. Stress and material velocity error bounds are then calculated at the using the value of $2\sigma_0$ at the point of intersection in the $\sigma - u_P$ plane. With the shocked state at the flyer-driver characterized, the unloading Hugoniot of the primary driver and its uncertaity bounds are calculated. Following this step, the unloading Hugoniots are used to calculate the release isentropes of the primary driver and its bands of uncertaintly. This is accomplished by calling the separate files 'IsentFun', 'IsentUncer1', and 'IsentUncer2' to calculate the release isentropes in $\sigma - V$ space. Within this calculation the $2\sigma_0$ value calculated at the flyer-driver interface is used for uncertainty in the release isentrope. Next, the isentrope is transformed from $\sigma - V$ space into $\sigma - u_P$ space for each of the aforementioned release curves. Finally, the intersection of the line defined by $\rho_{00}U_S$ for the powder with the release isentrope and its uncertainty bands is found.

'BEGIN PROGRAM'

```
%This Program is to use impedance matching techniques to
%determine the stress and material velocity in a sample
%using the measured value of shock velocity in the sample
```

```
%
% This Program Works!
close all hidden;
clear all;
format long;
global C02 S2 V0H2 Grun0H2 C0UD1 C0UD2

%%% ---------------- INPUT PARAMETERS ---------------- %%%
% Impact Velocity
VImp = .5455;        %m/s   974.1

% - Sample Properties
Rho0H3 = 8.0982;          %kg/m3  7979
V0H3 = 1./Rho0H3;         %m3/kg
USsample = .928;        %Value 1759 in m/s
%%% ------------------------------------------------- %%%

%%% --- Known Impactor/Driver Material Parameters --- %%%
%
% - Impactor
    % Copper
Rho0H1 = 8.925;          %g/m3
V0H1 = 1./Rho0H1;         %cm3/g
C01 = 3.905;              %km/s
```

```
S1 = 1.512;                %unitless
Grun0H1 = 2;           %unitless
A0Fl=.035234; A1Fl=-.026175; A2Fl=.027992; A3Fl=-.002309;
%{
% - Impactor
    % W-6Ni-4Cu
Rho0H1 = 17.194;          %g/m3
V0H1 = 1./Rho0H1;         %cm3/kg
C01 = 3.874;              %km/s
S1 = 1.50;                %unitless
Grun0H1 = 1.828;           %unitless
A0Fl = .041757; A1Fl = -.0012611;
A2Fl = 1.6614*10^-5; A3Fl = -2.7835*10^-8;
%}
% - Driver
 % Copper
Rho0H2 = 8.925;          %g/m3
V0H2 = 1./Rho0H2;         %cm3/kg+
C02 = 3.905;              %km/s
S2 = 1.512;                %unitless
Grun0H2 = 2;           %unitless
A0Dr=.035234; A1Dr=-.026175; A2Dr=.027992; A3Dr=-.002309;

%%% ------------------------------------------------ %%%
```

```
%%% ------------ Begin Calculations -------------------- %%%
% - Create evenly spaced pts. in Up to evaluate Hugoniot
UpPoints = 1000;
UpRange = zeros(UpPoints,1);
UpRange(:,1) = linspace(VImp,0,UpPoints);


% - Pressure Along Flyer as function of C,S,Up - %
PHFlyr(:,1) = Rho0H1.*(C01+S1.*(VImp-UpRange(:,1))).*...
              (VImp-UpRange(:,1));
TwoSigFlyr(:,1) = A0Fl+A1Fl.*UpRange(:,1)+A2Fl.*UpRange(:,1).^2+...
                  A3Fl.*UpRange(:,1).^3;
PFlyUncer1(:,1) = Rho0H1.*((C01+TwoSigFlyr(:,1))+...
                  S1.*(VImp-UpRange(:,1))).*(VImp-UpRange(:,1));
PFlyUncer2(:,1) = Rho0H1.*((C01-TwoSigFlyr(:,1))+...
                  S1.*(VImp-UpRange(:,1))).*(VImp-UpRange(:,1));

% - Pressure along Driver - %
PHTarget1(:,1) = Rho0H2.*(C02+S2.*UpRange(:,1)).*UpRange(:,1);
TwoSigDriv(:,1) = A0Dr+A1Dr.*UpRange(:,1)+A2Dr.*UpRange(:,1).^2 +...
                  A3Dr.*UpRange(:,1).^3;
PTarUncer1(:,1) = Rho0H2.*((C02+TwoSigDriv(:,1))+...
                  S2.*UpRange(:,1)).*UpRange(:,1);
```

```
PTarUncer2(:,1) = Rho0H2.*((C02-TwoSigDriv(:,1))+...
                  S2.*UpRange(:,1)).*UpRange(:,1);

% - Properties at Intersection Point
UpCuInterFit = @(Z) Rho0H2.*(C02+S2.*Z).*Z -...
                    Rho0H1.*(C01+S1.*(VImp-Z)).*(VImp-Z);
UpCuImpact1 = fsolve(UpCuInterFit,VImp/2);
PCuImpact1 = Rho0H2*(C02+S2*UpCuImpact1)*UpCuImpact1;
VCuImpact1 = 1/Rho0H2 - (UpCuImpact1^2)/PCuImpact1;
ECuImpact1 = 0.5*PCuImpact1*(V0H2-VCuImpact1);

  % - Uncertainty Properties at Intersection UpF-D(-)
  C0UI1 = C01-A0Fl+A1Fl.*UpCuImpact1+A2Fl.*UpCuImpact1.^2 +...
          A3Fl.*UpCuImpact1.^3;  %Impactor
  C0UD1 = C02+A0Dr+A1Dr.*UpCuImpact1+A2Dr.*UpCuImpact1.^2+...
          A3Dr.*UpCuImpact1.^3;  %Driver
  UpInterUncer = @(U) Rho0H2.*(C0UD1+S2.*U).*U -...
                 Rho0H1.*(C0UI1+S1.*(VImp-U)).*(VImp-U);
  UpInterUncer1 = fsolve(UpInterUncer,VImp/2);
  PInterUncer1 = Rho0H2*(C0UD1+S2*UpInterUncer1)*UpInterUncer1;
  VInterUncer1 = 1/Rho0H2 - (UpInterUncer1^2)/PInterUncer1;

  % - Uncertainty Properties at Intersection UpF-D(+)
  C0UI2 = C01+A0Fl+A1Fl.*UpCuImpact1+A2Fl.*UpCuImpact1.^2+...
```

```
          A3Fl.*UpCuImpact1.^3;  %Impactor
  C0UD2 = C02-A0Dr + A1Dr.*UpCuImpact1+A2Dr.*UpCuImpact1.^2+...
          A3Dr.*UpCuImpact1.^3;  %Driver
  UpInterUn = @(V) Rho0H2.*(C0UD2+S2.*V).*V -...
              Rho0H1.*(C0UI2+S1.*(VImp-V)).*(VImp-V);
  UpInterUncer2 = fsolve(UpInterUn,VImp/2);
  PInterUncer2 = Rho0H2*(C0UD2+S2*UpInterUncer2)*UpInterUncer2;
  VInterUncer2 = 1/Rho0H2 - (UpInterUncer2^2)/PInterUncer2;


% - Calculate Hugoniot of Material to do Isentrope Calculation - %
VolPoints = 1000;
VolRange(:,1) = linspace(V0H2,VCuImpact1,VolPoints);
PCuLoad(:,1) = ((C02.^2).*(V0H2-VolRange(:,1))./...
               ((V0H2-S2.*(V0H2-VolRange(:,1))).^2);
UpCuLoad(:,1) = (PCuLoad(:,1).*(V0H2-VolRange(:,1))).^(0.5);
  % - Uncertainty Hugoniot for Isentrope Calcualtions
  VRangeUncer1(:,1) = linspace(V0H2,VInterUncer1,VolPoints);
  PHugUncer1(:,1) = ((C0UD1.^2).*(V0H2-VRangeUncer1(:,1))./...
                    ((V0H2-S2.*(V0H2-VRangeUncer1(:,1))).^2);
  UpHugUncer1(:,1) = (PHugUncer1(:,1).*...
                     (V0H2-VRangeUncer1(:,1))).^(0.5);
  VRangeUncer2(:,1) = linspace(V0H2,VInterUncer2,VolPoints);
  PHugUncer2(:,1) = ((C0UD2.^2).*(V0H2-VRangeUncer2(:,1))./...
```

```
                    ((V0H2-S2.*(V0H2-VRangeUncer2(:,1))).^2);
  UpHugUncer2(:,1) = (PHugUncer2(:,1).*...
                     (V0H2-VRangeUncer2(:,1))).^(0.5);

% - Calcualte Isentrope from known P*,V* - %
VIsenCalc = zeros(VolPoints,1);
PIsenCalc = zeros(VolPoints,1);
Po = PCuImpact1;
    VSpan = linspace(VCuImpact1,(V0H2+0.1*V0H2),VolPoints);
    [A,B] = ode45(@IsentFun,VSpan,Po);
    VIsenCalc(:,1) = A;
    PIsenCalc(:,1) = B;

% Fit of Isentrope in P-V Space to a 5th order polynomial
% Fits V(P)
PI = polyfit(PIsenCalc(:,1),VIsenCalc(:,1),5);
PIV5 = PI(1,1); PIV4 = PI(1,2); PIV3 = PI(1,3);
PIV2 = PI(1,4); PIV1 = PI(1,5); PIV0 = PI(1,6);

      % Isentrope for Uncertainty 1
      VIsenUncer1 = zeros(VolPoints,1);
      PIsenUncer1 = zeros(VolPoints,1);
      Po1 = PInterUncer1;
          VSpan1 = linspace(VInterUncer1,(V0H2+0.1*V0H2),VolPoints);
```

```
        [C,D] = ode45(@IsentUncer1,VSpan1,Po1);
    VIsenUncer1(:,1) = C;
    PIsenUncer1(:,1) = D;
    % Fits V(P)
    PU1 = polyfit(PIsenUncer1(:,1),VIsenUncer1(:,1),5);
    PU1V5 = PU1(1,1); PU1V4 = PU1(1,2); PU1V3 = PU1(1,3);
    PU1V2 = PU1(1,4); PU1V1 = PU1(1,5); PU1V0 = PU1(1,6);

    % Isentrope for Uncertainty 2
    VIsenUncer2 = zeros(VolPoints,1);
    PIsenUncer2 = zeros(VolPoints,1);
    Po2 = PInterUncer2;
        VSpan2 = linspace(VInterUncer2,(V0H2+0.1*V0H2),VolPoints);
        [E,F] = ode45(@IsentUncer2,VSpan2,Po2);
    VIsenUncer2(:,1) = E;
    PIsenUncer2(:,1) = F;
    % Fits V(P)
    PU2 = polyfit(PIsenUncer2(:,1),VIsenUncer2(:,1),5);
    PU2V5 = PU2(1,1); PU2V4 = PU2(1,2); PU2V3 = PU2(1,3);
    PU2V2 = PU2(1,4); PU2V1 = PU2(1,5); PU2V0 = PU2(1,6);

% - Uses Term 2 in Eqn 5.116 in Zharkov 'Eqns of State for Solids
    % at High Pressures and Temperatures' p. 143
PRange(:,1) = linspace(PCuImpact1,0,1000);
```

```
dVdPEqn = @(P) sqrt(-(5.*PIV5.*P.^4+4.*PIV4.*P.^3+3.*PIV3.*P.^2+...
               2.*PIV2.*P + PIV1));
for i=1:1000
    URF(i,1) = quadl(dVdPEqn,PRange(i,1),PCuImpact1);
end
URF = URF + UpCuImpact1;
% - Fit stress along rarefaction as f(URF)
PIURF = polyfit(URF(:,1),PRange(:,1),5);
PRF5 = PIURF(1,1); PRF4 = PIURF(1,2); PRF3 = PIURF(1,3);
PRF2 = PIURF(1,4); PRF1 = PIURF(1,5); PRF0 = PIURF(1,6);
% - Plotted data fit and it overlays actual data

  % Isentrope Uncertainty 1 Up(P)
  PRangeU1(:,1) = linspace(PInterUncer1,0,1000);
  dVdPUncer1 = @(Q) sqrt(-(5.*PU1V5.*Q.^4+4.*PU1V4.*Q.^3+...
                   3.*PU1V3.*Q.^2 + 2.*PU1V2.*Q + PU1V1));
  for i = 1:1000
      URFUnc1(i,1) = quadl(dVdPUncer1,PRangeU1(i,1),PInterUncer1);
  end
  URFUnc1 = URFUnc1 + UpInterUncer1;

  % Fit P(Up)
  PUPRFU1 = polyfit(URFUnc1(:,1),PRangeU1(:,1),5);
  PRF1U5 = PUPRFU1(1,1); PRF1U4 = PUPRFU1(1,2);
```

```
  PRF1U3 = PUPRFU1(1,3); PRF1U2 = PUPRFU1(1,4);
  PRF1U1 = PUPRFU1(1,5); PRF1U0 = PUPRFU1(1,6);

  % Isentrope Uncertainty 2 Up(P)
  PRangeU2(:,1) = linspace(PInterUncer2,0,1000);
  dVdPUncer2 = @(R) sqrt(-(5.*PU2V5.*R.^4+4.*PU2V4.*R.^3 +...
                   3.*PU2V3.*R.^2 + 2.*PU2V2.*R + PU2V1));
  for i = 1:1000
      URFUnc2(i,1) = quadl(dVdPUncer2,PRangeU2(i,1),PInterUncer2);
  end
  URFUnc2 = URFUnc2 + UpInterUncer2;

  % Fit P(Up)
  PUPRFU2 = polyfit(URFUnc2(:,1),PRangeU2(:,1),5);
  PRF2U5 = PUPRFU2(1,1); PRF2U4 = PUPRFU2(1,2);
  PRF2U3 = PUPRFU2(1,3); PRF2U2 = PUPRFU2(1,4);
  PRF2U1 = PUPRFU2(1,5); PRF2U0 = PUPRFU2(1,6);

%- Determination of Material velocity and stress in Sample - %
StartUp = VImp./4;
UpSampRange(:,1) = linspace(0,(VImp+VImp*.5),1000);
PHSample(:,1) = Rho0H3.*USsample.*UpSampRange(:,1);

% - Fit for Standard Hugoniot
```

```
PFit = @(Y) Rho0H3.*USsample.*Y - (PRF5.*Y.^5+PRF4.*Y.^4+...
            PRF3.*Y.^3 + PRF2.*Y.^2 + PRF1.*Y + PRF0);
UpCuImpact2 = fsolve(PFit,StartUp);
PCuImpact2 = PRF5.*UpCuImpact2.^5 + PRF4.*UpCuImpact2.^4+...
             PRF3.*UpCuImpact2.^3 + PRF2.*UpCuImpact2.^2+...
             PRF1.*UpCuImpact2 + PRF0;

% - Fit for Uncertainty 1
PFitU1 = @(S) Rho0H3.*USsample.*S-(PRF1U5.*S.^5+PRF1U4.*S.^4+...
              PRF1U3.*S.^3 + PRF1U2.*S.^2 + PRF1U1.*S + PRF1U0);
UpUncer1 = fsolve(PFitU1,StartUp);
PUncer1 = PRF1U5.*UpUncer1.^5 + PRF1U4.*UpUncer1.^4 + ...
          PRF1U3.*UpUncer1.^3 + PRF1U2.*UpUncer1.^2 + ...
          PRF1U1.*UpUncer1 + PRF1U0;
% - Fit for Uncertainty 2
PFitU2 = @(T) Rho0H3.*USsample.*T-(PRF2U5.*T.^5 + PRF2U4.*T.^4+...
              PRF2U3.*T.^3 + PRF2U2.*T.^2 + PRF2U1.*T + PRF2U0);
UpUncer2 = fsolve(PFitU2,StartUp);
PUncer2 = PRF2U5.*UpUncer2.^5 + PRF2U4.*UpUncer2.^4 + ...
          PRF2U3.*UpUncer2.^3 + PRF2U2.*UpUncer2.^2 + ...
          PRF2U1.*UpUncer2 + PRF2U0;

fprintf('Impactor/Driver Stress');
PCuImpact1
```

```
fprintf('Impactor/Driver Material Velocity');
UpCuImpact1
fprintf('Impactor/Driver Mat. Vel. Uncertainty (+)');
UpInterUncer2
fprintf('Impactor/Driver Mat. Vel. Uncertainty (-)');
UpInterUncer1
fprintf('Driver/Sample Stress');
PCuImpact2
fprintf('Driver/Sample Material Velocity');
UpCuImpact2
fprintf('Driver/Powder Mat. Vel. Uncertainty (+)')
UpUncer2
fprintf('Driver/Powder Mat. Vel. Uncertainty (-)')
UpUncer1

% - Plotting of Data - %

hold on
  %plot(UpRange(:,1)./1000,PHFlyr(:,1)./10^9,'-k')
  %plot(UpRange(:,1)./1000,PFlyUncer1(:,1)./10^9,':k')
  %plot(UpRange(:,1)./1000,PFlyUncer2(:,1)./10^9,':k')
  plot(UpRange(:,1),PHTarget1(:,1),'-k')
  plot(UpRange(:,1),PTarUncer1(:,1),':k')
  plot(UpRange(:,1),PTarUncer2(:,1),':k')
```

```
  plot(URF(:,1),PRange(:,1),'-k')
  plot(URFUnc1(:,1),PRangeU1(:,1),':k')
  plot(URFUnc2(:,1),PRangeU2(:,1),':k')
  plot(UpSampRange(:,1),PHSample(:,1),'-k')
  %title('Isentrope Impedance Match')
  %xlim([0 1.2])
  %ylim([0 30])
  ylabel('Stress (GPa)')
  xlabel('Up (km/s)')
  grid off
%}
```

'END PROGRAM'

A.3.1 Release Isentrope, 'IsentFun'

'BEGIN PROGRAM'

```
function dpdvS = IsentFun(A,B)
global C02 S2 V0H2 Grun0H2
% A = Volume
% B = Stress along Isentrope
C0L = C02;
SL = S2;
V0HL = V0H2;
Grun0HL = Grun0H2;
```

```
PH = ((C0L.^2.*(V0HL-A))./(V0HL-SL.*(V0HL-A)).^2);
dPHdV = ((C0L.^2).*(V0HL+SL.*V0HL-SL.*A))./...
        ((-V0HL+SL.*V0HL-SL.*A).^3);
GovV = Grun0HL./V0HL;
dpdvS =  -GovV.*B + 0.5.*GovV.*PH +...
          dPHdV.*(1-0.5.*GovV.*(V0HL-A));
```

'END PROGRAM'

A.3.2 Uncertainty in Release Isentrope, 'IsentUncer1'

'BEGIN PROGRAM'

```
function dpdvS = IsentUncer1(C,D)
global C0UD1 S2 V0H2 Grun0H2
% C = Volume
% D = Stress along Isentrope
C0L = C0UD1;
SL = S2;
V0HL = V0H2;
Grun0HL = Grun0H2;


PH = ((C0L.^2.*(V0HL-C))./(V0HL-SL.*(V0HL-C)).^2);
dPHdV = ((C0L.^2).*(V0HL+SL.*V0HL-SL.*C))./...
        ((-V0HL+SL.*V0HL-SL.*C).^3);
GovV = Grun0HL./V0HL;
```

```
dpdvS =  -GovV.*D + 0.5.*GovV.*PH +...
         dPHdV.*(1-0.5.*GovV.*(V0HL-C));
```

'END PROGRAM'

A.3.3 Uncertainty in Release Isentrope, 'IsentUncer2'

'BEGIN PROGRAM'

```
function dpdvS = IsentUncer2(E,F)
global C0UD2 S2 V0H2 Grun0H2
% E = Volume
% F = Stress along Isentrope
C0L = C0UD2;
SL = S2;
V0HL = V0H2;
Grun0HL = Grun0H2;

PH = ((C0L.^2.*(V0HL-E))./(V0HL-SL.*(V0HL-E)).^2);
dPHdV = ((C0L.^2).*(V0HL+SL.*V0HL-SL.*E))./...
        ((-V0HL+SL.*V0HL-SL.*E).^3);
GovV = Grun0HL./V0HL;
dpdvS =  -GovV.*F + 0.5.*GovV.*PH +...
         dPHdV.*(1-0.5.*GovV.*(V0HL-E));
```

'END PROGRAM'

REFERENCES

[1] R. McQueen, S. Marsh, J. Taylor, J. Fritz, and W. Carter, The Equation of State of Solids from Shock Wave Studies, in *High Velocity Impact Phenomena*. New York: Academic Press, 1970. 1, 2.1, 2.2, 2.3, 2.3.1, 2.5.1, 2.5.2, 2.5.2, 2.1, 3.4.1, 3.4.3, 6.8, 7.2.1, 7.2.1, 7.2.1.1, 7.4, 7.5, 7.12, 7.3.2, 7.4.1, 7.4.1, 7.17, 7.18, 7.19, 7.4.2, 7.20, 7.21, 7.4.3, 9.1, A.1.1

[2] L. Al'tshuler, K. Kurpnikov, B. Ledenev, V. Zhuchikhin, and M. Brazhnik, "Dynamic compressibility and equation of state for iron under high pressure," *Soviet Physics - JETP*, vol. 34, pp. 874–885, 1958. 1, 3

[3] L. Al'tshuler, S. Kormer, A. Bakanova, and R. Trunin, "Equation of state for aluminum, copper, and lead in the high pressure region," *Soviet Physics - JETP*, vol. 11, pp. 573–579, 1960. 1, 2.3.1, 6.8

[4] M. Rice, R. McQueen, and J. Walsh, "Compression of solids by strong shock waves," *Solid State Physics IV*, vol. 6, pp. 1–63, 1958. 1, 2.1

[5] W. Herrmann, "Constitutive equation for the dynamic compaction of ductile porous materials," *Journal of Applied Physics*, vol. 40, pp. 2490–2499, 1969. 1, 4, 4.3, 4.3, 4.3, 4.4, 4.3, 4.3, 4.3, 7.3.1, 7.3.2, 7.4.2, 9.1

[6] B. Butcher and C. Karnes, "Dynamic compaction of porous iron," *Journal of Applied Physics*, vol. 40, pp. 2967–2976, 1969. 1, 4.3, 4.3, 7.3.2, 7.4.2, 9.1

[7] R. Boade, "Principal Hugoniot, second-shock Hugoniot, and release behavior of pressed copper powder," *Journal of Applied Physics*, vol. 41, pp. 4542–4546, 1970. 1

[8] P. Lynse and W. Halpin, "Shock compression of porous iron in the region of incomplete compaction," *Journal of Applied Physics*, vol. 39, pp. 5488–5495, 1968. 1

[9] M. Carroll and A. Holt, "Suggested modification of the P-alpha model for porous materials," *Journal of Applied Physics*, vol. 43, pp. 759–761, 1972. 1, 3.4.1, 4.3

[10] M. Carroll and A. Holt, "Static and dynamic pore-collapse relations for ductile porous materials," *Journal of Applied Physics*, vol. 43, pp. 1626–1636, 1972. 1, 3.4.2, 4.3, 4.3, 4.5, 7.3.1, 7.3.2, 7.3.2, 7.4.2, 7.5, 8.1.2, 8.2

[11] V. Nesterenko, Mesomechanics of Porous Materials Under Intense Dynamic Loading, in *Dynamics of Heterogeneous Materials*. New York: Springer, 2001. 1, 3.3.1, 4.3

[12] D. Grady, N. Winfree, G. Kerley, L. Wilson, and L. Kuhns, "Computational modeling and wave propagation in media with inelastic deforming microstructure," *Journal Physics IV France*, vol. 10, pp. Pr9–15–Pr9–20, 2000. 1, 4, 4.4, 4.4, 4.4, 4.4, 4.5, 7.3.2, 9.1

[13] M. Petrie and N. Page, "An equation of state for shock loaded powders," *Journal of Applied Physics*, vol. 69, pp. 3517–3524, 1991. 1, 3.4.1, 3.4.1, 3.15, 3.4.1, 3.4.3, 7.1, 7.3, 7.1, 7.1, 7.2.1.2, 7.3.1, 7.13, 7.14, 7.4.1, 7.18, 7.19, 7.4.1, 7.4.3, 8, 8.1.3, 9.1

[14] G. Simons and H. Legner, "An analytic model for the shock Hugoniot in porous materials," *Journal of Applied Physics*, vol. 53, pp. 943–947, 1982. 1, 3.4.1, 3.4.1

[15] M. Meyers, Shock Waves: Equations of State, in *Dynamic Behavior of Materials*. New York: John Wiley and Sons, Inc., 1994. 1, 2.2, 2.2, 2.2, 2.2, 2.2, 3.13, 3.4.1, 3.14, 7.2.1.2, 7.2.3, 7.3.1, 8.1.3, 9.1

[16] C. Dai, D. Eakins, and N. Thadhani, "Dynamic densification behavior of nano-iron powders under shock compression," *Journal of Applied Physics*, vol. 103, pp. 093503–1–12, 2008. 1, 3.1, 4.3, 8.1.1

[17] R. Bell, M. Baer, R. Brannon, D. Crawford, M. Erlick, E. Hertel, R. Schmitt, S. Silling, and P. Taylor. 1

[18] "Autodyn." 1

[19] W. Tong and G. Ravichandran, Recent Developments in Modeling Shock Compression of Porous Materials, in *High-Pressure Shock Compression of Solids IV*. New York: Springer, 1997. 1, 4.3

[20] H. Fischmeister and E. Artz, "Densification of powders by particle deformation," *Powder Metallurgy*, vol. 26, pp. 82–88, 1983. 1, 3.2, 4, 4.1, 4.1, 4.1, 4.1, 4.2, 7.1, 8.1.2, 9.1, 9.2

[21] A. Ailes, "Modern applications of thermit welding," *Welding and Metal Fabrication*, vol. 32, pp. 9–11, 1964. 1

[22] M. Boslough, "A thermochemical model for shock-induced reactions (heat detonations) in solids," *Journal of Chemical Physics*, vol. 92, pp. 1839–1848, 1990. 1

[23] L. Bennett, Y. Horie, and M. Hwang, "Constitutive model of shock-induced chemical reactions in inorganic powder mixtures," *Journal of Applied Physics*, vol. 75, pp. 3394–3402, 1994. 1

[24] R. Graham, *Solids Under High-Pressure Shock Compression*. New York: Springer-Verlag, 1993. 2.1, 5.1

[25] W. Rankine, "On the thermodynamic theory of waves of finite longitudinal disturbances," *Phil. Trans. Roy. Soc. London*, vol. 160, pp. 277–288, 1870. 2.1

[26] H. Hugoniot *J. L'Ecole Polytech.*, vol. 58, p. 3, 1989. 2.1

[27] W. Gourdin, "Dynamic consolidation of metal powders," *Prog. Mater. Sci.*, vol. 30, pp. 39–80, 1986. 2.1, 3.3.2

[28] M. Meyers, Shock Waves, in *Dynamic Behavior of Materials*. New York: John Wiley and Sons, Inc., 1994. 2.1, 2.1, 2.1

[29] S. Marsh, ed., *LASL Shock Hugoniot Data*. Berkely: University of California Press, 1980. 2.1, 2.1, 2.2, 2.5.5, 6.3, 6.4, 6.8, 6.9.1, A.1, A.1.3

[30] J. Slater, *Introduction to Chemical Physics*. New York: McGraw-Hill, Inc., 1939. 2.2

[31] J. Dugdale and D. MacDonald, "The thermal expansion of solids," *Physical Review*, vol. 89, pp. 832–834, 1953. 2.2, 3.4.2

[32] J. Walsh, M. Rice, R. McQueen, and F. Yarger, "Shock-wave compression of twenty-seven metals. Equations of state of metals," *Physical Review*, vol. 108, pp. 196–216, 1957. 2.2, 2.2, 6.4

[33] L. Davison, Material Response II: Inviscid Compressible Fluids, in *Fundamentals of Shock Wave Propagation in Solids*. Berlin: Springer, 2008. 2.3, 2.3, 2.3, 2.3, 2.3, 2.3, 2.3, 2.3, 2.3.1, 2.3.1, 2.3.1, 2.3.1, 2.4, 2.4

[34] J. Ziman, Phonons, in *Electrons and Phonons*, pp. 52–58. Glasgow: Oxford, 1960. 2.3, 2.3

[35] Y. Zel'dovich and Y. Raizer, Shock waves in solids, in *Physics of Shock Waves and High-Temperature Hydrodynamic Phenomena*, p. 694. New York: Dover, 2002. 2.3.1

[36] Y. Zel'dovich and Y. Raizer, Shock waves in solids, in *Physics of Shock Waves and High-Temperature Hydrodynamic Phenomena*, p. 728. New York: Dover, 2002. 2.4

[37] A. Hall, J. Asay, M. Knudson, W. Stygar, R. Spielman, T. Pointon, D. Reisman, A. Toor, and R. Cauble, "Experimental configuration for isentropic compression of solids using pulsed magnetic loading," *Review of Scientific Instruments*, vol. 72, pp. 3587–3595, 2001. 2.4, 2.4

[38] J. Asay, T. Ao, J.-P. Davis, C. Call, T. Vogler, and G. Gray III, "Effect of initial properties on the flow strength of aluminum during quasi-isentropic compression," *Journal of Applied Physics*, vol. 103, pp. 083514–16, 2008. 2.4

[39] J. Ding and J. Asay, "Material characterization with ramp wave experiments," *Journal of Applied Physics*, vol. 101, pp. 073517–19, 2007. 2.4

[40] V. Zharkov and V. Kalinin, Applications of Equations of State to the Physics of the Earth's Interior, in *Equations of State for Solids at High Pressures and Temperatures*. New York: Consultants Bureau, 1971. 2.4, 2.4, 3.4.2

[41] V. Zharkov and V. Kalinin, Compression of Solids by Strong Shock Waves, in *Equations of State for Solids at High Pressures and Temperatures*. New York: Consultants Bureau, 1971. 2.4, 6.8

[42] P. Bridgman, "Linear compression to 30,000 kg/cm3, including relatively incompressible substances," *Proceedings of the American Academy of Arts and Sciences*, vol. 77, pp. 187–234, 1949. 2.5.2

[43] S. Botsanov, Foundations of the Physics of Shock Waves, in *Effects of Explosions on Materials: Modifications and synthesis under high-pressure shock compression*. New York: Springer-Verlag, 1994. 2.5.3, 2.5.3

[44] B. Krueger and T. Vreeland Jr., "A Hugoniot theory for solid and powder mixtures," *Journal of Applied Physics*, vol. 69, pp. 710–716, 1991. 2.5.4, 2.5.4, 2.5.4, 2.5.4, 2.1, 7.2.1.1, 7.4, 7.2.1.2, 7.4.1, 7.4.1, 7.18, 7.19, 7.4.2, 7.4.3, 8.1.3, 9.1, A.1.3

[45] F. Murnaghan, "The compressibility of media under extreme pressures," *Proceedings of National Academy of Sciences of the United States of America*, vol. 30, pp. 244–247, 1944. 2.5.4

[46] K. Krupnikov, M. Brazhnik, and V. Krupnikova, "Shock compression of porous tungsten," *Soviet Physics - JETP*, vol. 15, pp. 470–476, 1962. 3

[47] E. Santiso and E. Muller, "Dense packing of binary and polydisperse hard spheres," *Molecular Physics*, vol. 100, pp. 2461–2469, 2002. 3.1, 3.1

[48] K. Rietema, *The Dynamics of Fine Powders*. New York: Elsevier Science, 1991. 3.1

[49] A. Rosato, T. Vreelant, and F. Prinz, "Manufacture of powder compacts," *International Materials Reviews*, vol. 36, pp. 45–61, 1991. 3.1, 3.2, 3.9

[50] Y. Lan, *MS Thesis*. NJIT: New Jersey Institute of Technology, 1989. 3.1

[51] R. Yang, R. Zou, and A. Yu, "Effect of material properties on the packing of fine particles," *Journal of Applies Physics*, vol. 94, pp. 3025–3034, 2003. 3.1

[52] R. Yang, R. Zou, and A. Yu, "Computer simulation of the packing of fine particles," *Physics Review E*, vol. 62, pp. 3900–3908, 2000. 3.1

[53] G. Cho, J. Dodds, and J. Santamaria, "Particle shape effects on the packing density, stiffness and strength: natural crushed sands," *Journal of Geotechnical and Geoenvironmental Engineering*, vol. 132, pp. 591–602, 2006. 3.1

[54] T. Nieh, P. Luo, W. Nellis, D. Lesuer, and D. Benson, "Dynamic compaction of aluminum nanocrystals," *Acta Materialia*, vol. 44, pp. 3781–3788, 1996. 3.1

[55] H. Kuhn and D. Medlin, eds., *ASM Handbook: Vol. 8*. Ohio: ASM International, 2000. 3.2, 3.3

[56] S. Tsukerman, Chapter 2, in *Powder Metallurgy*. Oxford: Pergamon Press, 1965. 3.2, 3.7

[57] R. German, *Powder Metallurgy Science*. New Jersey: Metal Powder Industries Federation, 1984. 3.3, 3.2, 3.2, 3.2, 3.2, 3.2, 3.6, 3.2

[58] V. Kenkre, M. Endicott, S. Glass, and A. Hurd, "A theoretical model for compaction of granular materials," *Journal of American Ceramic Society*, vol. 79, pp. 3045–3054, 1996. 3.2, 4, 4.2, 4.2, 4.2, 4.2, 4.2, 4.3, 7.1, 7.1, 9.1, 9.2

[59] E. Artz, "The influence of an increasing particle coordination on the densification of spherical powders," *Acta Metall.*, vol. 30, pp. 1883–1890, 1982. 3.2, 4.1, 8.2

[60] D. Benson, V. Nesterenko, F. Jonsdottir, and M. Meyers, "Quasistatic and dynamic regimes of granular material deformation under impulse loading," *Journal of Mechanical Physics Solids*, vol. 45, pp. 1955–1999, 1997. 3.2, 3.2, 3.3.1, 8.3

[61] D. Kumar, R. Kumar, and P. Philip, "Simulation of dynamic compaction of metal powders," *Journal of Applied Physics*, vol. 85, pp. 767–775, 1999. 3.2, 3.4, 3.5, 8.1.1

[62] D. Cumberland and R. Crawford, *The Packing of Particles*. Netherlands: Elsevier Science Publishers, 1987. 3.2

[63] S. Tsukerman, Chapter 3, in *Powder Metallurgy*. Oxford: Pergamon Press, 1965. 3.2, 3.2

[64] K. Kawikata and K. Ludde, "Some considerations on powder compression equations," *Powder Technology*, vol. 4, pp. 61–68, 1970. 3.2, 3.4.1, 7.1

[65] A. Cooper and L. Eaton, "Compaction behavior of several ceramic powders," *Journal of American Ceramic Society*, vol. 45, pp. 97–101, 1962. 3.2

[66] C. van Buren and H. Hirsch, Hydrostatic pressing of powders, in *New Methods for the Consolidation of Metal Powders*. New York: Plenum Press, 1967. 3.2, 3.8

[67] G. Sethi, N. Myers, and R. German, "An overview of dynamic compaction in powder metallurgy," *International Materials Review*, vol. 53, pp. 219–234, 2008. 3.3, 7.4.1

[68] M. Meyers, D. Benson, and E. Olevsky, "Shock consolidation: microstructurally-based analysis and computational modeling," *Acta Materialia*, vol. 47, pp. 2089–2108, 1999. 3.10

[69] W. Gourdin, "Energy deposition and microstructural modification in dynamically consolidated metal powders," *Journal of Applied Physics*, vol. 55, pp. 172–181, 1984. 3.3.1

[70] R. Schwarz, P. Kasiraj, T. Vreeland, and T. Ahrens, "A theory for the shock-wave consolidation of powders," *Acta Metallurgica*, vol. 32, pp. 1243–1252, 1984. 3.3.1, 3.3.2

[71] R. Williamson, "Parametric studies of dynamic powder consolidation using a particle-level numerical model," *Journal of Applied Physics*, vol. 68, pp. 1287–1296, 1990. 3.3.1, 3.3.2, 8.1.1

[72] N. Thadhani, R. Graham, T. Royal, E. Dunbar, M. Anderson, and G. Holman, "Shock-induced chemical reactions in titanium-silicon powder mixtures of different morphologies: Time-resolved pressure measurements and materials analysis," *Journal of Applied Physics*, vol. 82, pp. 1113–1128, 1997. 3.3.1, 4.5, 7.3.1, 8.1.1

[73] L. Murr and E. Esquivel, "Observations of common microstructural issues associated with dynamic deformation phenomena: Twins, microbands, grain size effects, shear bands, and dynamic recrystallization," *Journal of Materials Science*, vol. 39, pp. 1153–1168, 2004. 3.3.1

[74] P. Kasiraj, T. Vreeland Jr., R. Schwarz, and A. T.J., "Shock consolidation of a rapidly solidified steel powder," *Acta Metallurgica*, vol. 32, pp. 1235–1241, 1984. 3.3.2

[75] O. Roman, V. Nesterenko, and I. Pikus, "Influence of the powder particle size on the explosive pressing process," *Translation from Fizika Goreniya i Vzryva*, vol. 15, pp. 102–107, 1979. 3.3.2

[76] R. Rusnak, "Energy relationships in the high velocity compaction of copper powder," *Intnational Journal of Powder Metallurgy*, vol. 12, pp. 91–99, 1976. 3.3.2

[77] D. Benson, "An alalysis by direct numerical simulation of the effects of particle morphology on the shock compaction of copper powder," *Modelling and Simulation in Materials Science and Engineering*, vol. 2, pp. 535–550, 1994. 3.3.2, 3.11

[78] N. Thadhani, A. Advani, I. Song, E. Dinbar, A. Grebe, and R. Graham, *Shock wave and high strain rate phenomena in materials*, pp. 271–282. New York: Marcel Dekker, 1992. 3.3.2

[79] D. Eakins and N. Thadhani, "Mesoscale simulation of the configuration-dependent shock-compression response of Ni+Al powder mxitures," *Acta Materialia*, vol. 56, pp. 1496–1510, 2008. 3.3.2, 3.12, 5.1, 8.1.3, 8.3

[80] Y. Horie and A. Sawaoka, Thermomechanics of Powder Compaction and Mass Mixing, in *Shock Compression Chemistry of Materials*, p. 128. Tokyo: KTK Scientific Publishers, 1993. 3.4.1

[81] Y. Zel'dovich and Y. Raizer, Shock waves in solids, in *Physics of Shock Waves and High-Temperature Hydrodynamic Phenomena*, p. 715. New York: Dover, 2002. 3.4.1, 3.4.1

[82] K.-H. Oh and P.-A. Persson, "Equation of state for extrapolation of high pressure shock Hugoniot data," *Journal of Applied Physics*, vol. 65, pp. 3852–3856, 1989. 3.16, 3.4.2, 3.4.2, 3.17, 7.2.1.2

[83] Q. Wu and F. Jing, "Thermodynamic equation of state and application to Hugoniot predictions for porous materials," *Journal of Applied Physics*, vol. 80, pp. 4343–4349, 1996. 3.4.2, 3.4.2, 3.18, 3.4.2, 3.4.2, 3.4.3, 4.3, 7.2.1.2, 7.3.1, 7.3.1, 7.13, 7.14, 7.3.2, 7.15, 7.3.3, 7.16, 7.4.1, 7.18, 7.19, 7.4.1, 7.4.3, 7.5, 8, 8.1.2, 8.1.3, 8.4, 8.1.3, 8.1.3, 8.2, 8.2, 9.1, 9.2

[84] F. Giordano and M. Weir, The Modeling Process, in *A First Course in Mathematical Modeling*. Monterey, California: Brooks/Cole Publishing, 1985. 4

[85] M. Meyers, S. Shang, and K. Hokamoto, The Role of Thermal Energy in Shock Consolidation, in *Shock Waves in Materials Science*. Tokyo: Springer-Verlag, 1993. 4.1, 4.1, 4.1, 8.1.2, 8.2

[86] A. Mehta and S. Edwards, "Statistical mechanics of powder mixtures," *Physica A*, vol. 157, pp. 1091–1100, 1989. 4.2

[87] P. Richet, Entropy and Principles, in *The Physical Basis of Thermodynamics*. New York: Kluwer Academic/Plenum, 2001. 4.2

[88] D. Grady, "P-alpha compaction of sand.". 4.3, 7.3.2, 7.4.2

[89] J. Brown, T. Vogler, D. Grady, W. Reinhart, L. Chhabildas, and T. Thornhill, "Dynamic compaction of sand," in *Shock Compression of Condensed Matter - 2007*, pp. 1363–1366, 2007. 4.3

[90] T. Vogler, M. Lee, and D. Grady, "Static and dynamic compaction of ceramic powders," *International Journal of Solids and Structures*, vol. 44, pp. 636–685, 2007. 4.5, 4.5

[91] "Matlab," 2006. 4.5, 6.2, 7.2.1.1, 7.2.3

[92] D. Eakins and N. Thadhani, "The shock-densificaiton behavior of three distinct Ni+Al powder mixtures," *Applied physics letters*, vol. 92, p. 111903, 2008. 4.5, 8.1.1

[93] D. Benjamin, ed., *ASM Handbook: Vol. 3*, p. 129. Ohio: ASM International, 1980. 4.5

[94] H. Huang and J. Asay, "Compressive strength measurements in aluminum for shock compression over the stress range of 4-22 GPa," *Journal of Applied Physics*, vol. 98, pp. 1–16, 2005. 4.5

[95] K. Walter, D. Pesiri, and D. Wilson, "Manufactureing and performance of nanometric Al/MoO_3 energetic materials," *Journal of Propulsion and Power*, vol. 23, pp. 645–650, 2007. 5

[96] B. Clapsaddle, L. Zhoa, A. Gash, J. Satcher Jr., and K. Shea, "Synthesis and characterization of mixed metal oxide nanocomposite energetic materials," *Materials Research Society Symposium Proceedings*, vol. 800, pp. AA2.7.1–BB3.8.7, 2004. 5

[97] N. Thadhani, "Shock-induced and shock-assisted solid-state chemical reactions in powder mixtures," *Journal of Applied Physics*, vol. 76, pp. 2129–2138, 1994. 5.1

[98] A. Strutt, K. Vecchio, L. Yu, M. Meyers, and R. Graham, "Shock synthesis of nickel-aluminides," in *Shock Compression of Condensed Matter - 1993*, pp. 1259–1262, 1993. 5.1

[99] L. Yu, W. Nellis, M. Meyers, and K. Vecchio, "Shock synthesis of niobium silicides," in *Shock Compression of Condensed Matter - 1997*, pp. 1291–1294, 1993. 5.1

[100] V. Joshi, N. Thadhani, and R. Graham, "Mechanistic study of shock-induced solid-state chemistry in Ti- and Ta-based carbide and boride systems," in *Shock Compression of Condensed Matter - 1993*, pp. 1299–1302, 1993. 5.1, 5.1

[101] N. Thadhani, V. Subramanian, R. Russell, D. Savage, and Y. Gupta, "The effect of pulse duration on shock-induced chemical reaction in Ti-Si powder mixtures," in *Shock Compression of Condensed Matter - 1995*, pp. 709–712, 1995. 5.1

[102] "Standard test method for density of compacted or sintered powder metallurgy products using archimedes' principle," 2008. 6.2

[103] E. Levin and R. Roth, "Polymorphism of bismuth sesquioxide. I. Pure Bi_2O_3," *Journal of Research of National Bureau of Standards - A*, vol. 68A, pp. 189–195, 1964. 6.2, 6.2, 6.3

[104] P. Sang Jun Lee. personal communication, 2010. School of Electrical and Computer Engineering. 6.2

[105] W. Cousins, R. Armstrong, and W. Robinson, "Young's modulus of lignin from a continuous indentation test," *Journal of Materials Science*, vol. 10, pp. 1655–1657, 1975. 6.2

[106] G. Dieter, *Mechanical Metallurgy*, pp. 49–51. New York: McGraw-Hill Book Company, 1986. 6.2

[107] D. Wackerbarth, M. Anderson, and R. Graham, "A PC-based computer program to reduce Bauer PVDF stress-rate gauge data," *Sandia Report, SAND92-0046*, pp. 5–14, 1992. 6.2, 7.2.3

[108] F. Birch, "Finite elastic strain of cubic crystals," *Physical Review*, vol. 71, pp. 809–824, 1947. 6.2, 7.2.1.1

[109] M. Martin, *Dynamic mechanical behavior and high pressure phase stability of a zirconium-based bulk metallic glass and its composite with tungsten*. PhD thesis, Georgia Institute of Technology, 2008. 6.2

[110] M. Yashima and D. Ishimura, "Temperature dependence of lattice parameters and anisotropic thermal expansion of bismuth oxide," *Journal of the American Ceramic Society*, vol. 88, pp. 2332–2335, 2005. 6.2, 6.3

[111] C. Anderson, "The heat capacities of bismuth and bismuth trioxide at low temperatures," *Journal of the American Chemical Society*, vol. 52, pp. 2720–2723, 1930. 6.2, 6.3

[112] R. Liebermann and E. Schreiber, "Elastic constants of polycrystalline hematite as a function of pressure to 3 kilobars," *Journal of Geophysical Research*, vol. 73, pp. 6585–6590, 1968. 6.3, 6.3, 6.4

[113] C. Briant and D. Lassila, "The effect of tungsten on the mechanical properties of tantalum," *Journal of Engineering Materials and Technology*, vol. 121, pp. 172–177, 1999. 6.3, 6.3

[114] Y. Hidaka, T. Anraku, and N. Otsuka, "Tensile deformation of iron oxides at 600-1250 °C," *Oxidation of Metals*, vol. 58, pp. 469–485, 2002. 6.3, 6.3

[115] L. Palmeiri, "Ultrasonic measurements of elastic moduli of polycrystalline tantalum and niobium," *Applied Materilas Research*, vol. 3, pp. 139–143, 1964. 6.3, 6.3

[116] A. Chijioke, W. Nellis, and I. Silvera, "High-pressure equations of state for Al, Cu, Ta, and W," *Journal of Applied Physics*, vol. 98, pp. 073526–1–8, 2005. 6.3

[117] K. Katahara and M. Manghnani, "Pressure derivations of the elastic moduli of niobium and tantalum," *Journal of Applied Physics*, vol. 47, pp. 434–439, 1976. 6.3

[118] T. Massalski, ed., *Binary Alloy Phase Diagrams, Vol. II*. Ohio: American Society for Metals, 1986. 6.3

[119] R. Austin, D. McDowell, and D. Benson, "Numerical simulations of shock wave propagation in spatially-resolved particle systems," *Modeling and Simulation in Materials Science*, vol. 14, pp. 537–561, 2006. 6.3

[120] A. Mitchell and W. Nellis, "Shock compression of aluminum, copper, and tantalum," *Journal of Applied Physics*, vol. 52, pp. 3363–3374, 1981. 6.4, 6.8, 6.9, 6.9.1, 6.9.2, 6.9.2, 6.9.2, 6.9.2

[121] S. Jones and Y. Gupta, "Refractive index and elastic properties of z-cut quartz shocked to 60 kbar," *Journal of Applied Physics*, vol. 88, pp. 5671–5679, 2000. 6.7.2.2

[122] D. Strange, "High Strain Rate Impact Facility," tech. rep., Physics Applications Inc., 1993. 6.12

[123] R. McQueen and S. Marsh, "Equation of state for nineteen metallic elements from shock-wave measurements to two megabars," *Journal of Applied Physics*, vol. 31, pp. 1253–1269, 1960. 6.8

[124] R. Trunin, ed., *Experimental data on shock compression and adiabatic expansion of condensed matter*. Sarov: RFNC-VNIIEF, 2001. 6.8

[125] M. Yoshida, "Program MIXTURE," tech. rep., CERT Report, New Mexico Institute of Mining and Technology, 1986. 6.8

[126] Y. Beers, *Introduction to the Theory of Errors*, p. 40. Massachusetts: Addison-Wesley, 1957. 6.9.1, 6.9.1

[127] Y. Beers, *Introduction to the Theory of Errors*, p. 42. Massachusetts: Addison-Wesley, 1957. 6.9.1, 6.9.1

[128] P. Denny, "Compaction equations: a comparison of the Heckel and Kawikata equations," *Powder Technology*, vol. 127, pp. 162–172, 2002. 7.1

[129] "Plotdata," 2004. 7.2.3

[130] D. Eakins and N. Thadhani, "Shock-induced reaction in a flake nickel + spherical aluminum powder mixture," *Journal of Applied Physics*, vol. 100, p. 113521, 2006. 7.3.1, 8.1.1

[131] S. Batsanov, D. G.S., and A. Klochkov, S.V. Teut, "Syntiesis reactions behind shock fronts," *Fizika Goreniya i Vzryva*, vol. 22, pp. 134–137, 1986. 7.3.1

[132] J. Borg and T. Vogler, "Mesoscale calculations of the dynamic behavior of a granular ceramic," *International Journal of Solids and Structures*, vol. 45, pp. 1676–1696, 2008. 8.1.1, 8.3

[133] S. Chen and G. Gray, "Constitutive behavior of tantalum and tantalum-tungsten alloys," *Metallurgical and Materials Transactions A*, vol. 27A, pp. 2994–3006, 1996. 8.1.1, 8.1.3

[134] N. Thadhani and T. Aizawa, Materials Issues in Shock-Compression-Induced Chemical Reactions in Porous Solids, in *High-Pressure Shock Compression of Solids IV*. New York: Springer, 1997. 8.1.2

[135] W. Kingery, H. Bowen, and D. Uhlmann, Plastic Deformation, Viscous Flow, and Creep, in *Introduction to Ceramics*. New York: Wiley-Interscience, 1976. 8.1.2

[136] G. Johnson, J. Hoegfeldt, U. Lindholm, and A. Nagy, "Response of various metals to large torsional strains over a large range of strain rates - Part 1: ductile metals," *Transactions of the ASME*, vol. 105, pp. 42–47, 1983. 8.1.3

[137] G. Johnson, J. Hoegfeldt, U. Lindholm, and A. Nagy, "Response of various metals to large torsional strains over a large range of strain rates - Part 2: less ductile metals," *Transactions of the ASME*, vol. 105, pp. 48–51, 1983. 8.1.3

[138] N. Thadhani, K. Vandersall, R. Russell, R. Graham, G. Holman, and M. Anderson, "Shock compression of Al+Fe_2o_3 powder mixtures of different volumetric distributions," in *Shock Compression of Condensed Matter - 1997*, pp. 553–556, 1997. 8.2, 8.2, 8.13, 9.1

[139] S. Du and N. Thadhani, "Impact initiation of pressed Al-based intermetallic forming powder mixture compacts," in *Shock Compression of Condensed Matter - 2009*, pp. 470–473, 2009. 8.3

[140] D. Benson, I. Do, and M. Meyers, "Computational modeling of the shock compression of powders," in *Shock Compression of Condensed Matter - 2001*, pp. 1087–1092, 2001. 8.3

[141] D. Benson, "The calculation of the shock velocity - particle velocity relationship for a copper powder by direct numerical simulation," *Wave Motion*, vol. 21, pp. 85–99, 1995. 8.3